DEPARTAMENT DE FÍSICA ATÒMICA, MOLECULAR I NUCLEAR

INSTITUTO DE FÍSICA CORPUSCULAR

DOCTORAT EN FÍSICA

Characterization of the optical properties at the ANTARES site using the Optical Beacon system. Influence on the detector performance

Ph.D. thesis dissertation by

Harold Yepes Ramírez

València, Mayo 2014

D. JUAN JOSÉ HERNÁNDEZ REY, Investigador Científic del C.S.I.C. i D. JUAN ZÚÑIGA ROMÁN, Professor Titular de la Universitat de València,

CERTIFIQUEN:

Que la present memòria, **Characterization of the optical properties at the ANTARES site using the Optical Beacon system. Influence on the detector performance**, ha sigut realitzada baix la seua direcció en el Institut de Física Corpuscular (Centre Mixt Universitat de València - CSIC) per D. Harold Yepes Ramírez i constitueix la seua Tesi Doctoral en el Departament de Física Atòmica, Molecular i Nuclear de la Universitat de València, per a optar al grau de Doctor en Física.

I per a que conste, en compliment de la legislació vigent, signem el present certificat a Paterna a 13 de Mayo de 2014.

Signat: Juan José Hernández Rey

Signat: Juan Zúñiga Román

Als meus pares ...

Acknowledgements

More than the 50% of this thesis is merit of who supported my crazy adventure to meet and live a different experience out of my country, what converged in a life surrounded by a phd thesis...difficult to predict it!

Primero que todo gracias a mis padres Rodrigo Yepes y Maria Doriam Ramírez, mi hermana Natalia Yepes, unas de mis razones de ser y a mi familia en general. Gracias por soportar cantidad de situaciones encadenadas al desafío de la distancia, por apoyar y aguantar en todo sentido cada una de las decisiones que tomé. Gracias a mi "segundo padre" Jorge Iván Ramírez y Ana María Serna, Giovanny Ramírez, Nancy Vásquez y Francisco Pérez, Alex Serna y Elizabeth. Gracias en un muy alto porcentaje a mi amada esposa Yuliana Maria López, mi otra razón de ser, quien siempre estuvo conmigo en la distancia y en la cercanía de su tiempo en España, su sacrificio, paciencia, sabiduría y energía nos permitieron conspirar con el universo, conservando y fortaleciendo nuestra poderosa unión.

Gracias a todos mis amigos desde tiempos inmemorables, gracias a Alejandra Baena, Jorge Mario Gil, David Oliveros, Julián Márquez, por todos los momentos de crecimiento que hemos compartido en América y Europa. Gracias a la música que tuvo que esperar este largo tiempo para retomar ambiciosos e inconclusos proyectos, mi otra razón de ser. Gracias a Juan José Hernández Rey por apoyar mi entrada en ANTARES, por su tiempo y paciencia, pero sobre todo por confiar en mí y presionarme a ser mejor. Agradezco especialmente a Juan Zúñiga Román, un ejemplo de profesional y persona que ha marcado esta etapa de mi vida, gracias por ser un excelente jefe, por dirigirme con paciencia,

Contents

Chapter 1

The birth of a new age in astronomy

If you're not failing every now and again, it's a sign you're not doing anything
very innovative
Woody Allen

The advancement of astronomical sciences has followed an interesting and revolutionary path as long as the sky has been observed. The scientific merits of Galileo could establish the basis of a well defined orderliness in the astronomy research by using amazing engineering tools for that epoch. In the case of the telescope, his optical engineering skills played an important role in its development into a successful instrument, what was even recognized by the Senate of Venice in May-June 1609. In particular, due to the discovery of four of the 67 moons of Jupiter, he became increasingly convinced that the Copernican, heliocentric system of the world was correct.

Most of the knowledge about the universe comes from the information carried by photons. Lots of valuable information is extracted thanks to their particular features as stability and electric neutrality which allow to detect them in a wide range of energy and find out the physical and chemical properties of the source. However, astronomy by using photons has some constraints when dense and distant regions of the stars, Active Galactic Nuclei (AGNs) or other astrophysical energy sources are studied.

In order to explore the most dense and distant Galactic and Extra-galactic systems, a stable and electrically neutral cosmic messenger is required so that its

trajectory will not be deflected by magnetic fields, and its small interaction cross section favours to get information from distant regions opaque to photons. The particle that overcome these constraints and fulfils the mentioned requirements is the neutrino, which can come from the core of astrophysical objects.

1.1   Cosmic rays astronomy

The discovery of extra-terrestrial particles goes back to the beginning of the last century when Victor Francis Hess set that "the results of my observations are best explained by the assumption that a radiation of very great penetrating power enters our atmosphere from above". Hess, by using a dedicated electroscope systematically measured the radiation rates at altitudes up to 5.3 km during 1911-1912 using an aloft balloon. The results of Hess were published by the Viennese Academy of Sciences where it was explained in detail that the level of radiation decreased up to an altitude of about 1 km, but above it, the level of radiation increased hugely, being the radiation detected at 5 km about twice that of the sea level (1). The Sun was discarded as the sole cause since the effect was produced both by day and night.

The work performed by Hess about this high-energy penetrating radiation particles was confirmed some years after by Robert Andrews Millikan who called them "Cosmic Rays (CRs)". Hess and Millikan researches opened the gates to many discoveries in the Nuclear Physics field. These CRs are technically "primary" particles such as electrons, protons and helium, as well as carbon, oxygen, iron and other nuclei synthesized in celestial bodies. The "secondary" particles are those produced in the interaction of primary particles with stellar gas including the Earth's atmosphere.

In 1938 Pierre Auger discovered particle "showers" which come from the striking of primary high-energy particles with the Earth's atmosphere as shown in Figure 1.1. Muons and neutrinos produced in the interaction of secondary CRs at the top of the atmosphere are result of the decay of charged mesons, while electrons and photons come from decays of neutral mesons.

The origin of CRs in still unclear. Several efforts on space-based or ground-based techniques have been developed in order to study the Galactic or Extra-Galactic origin of such particles.

Development of cosmic-ray air showers
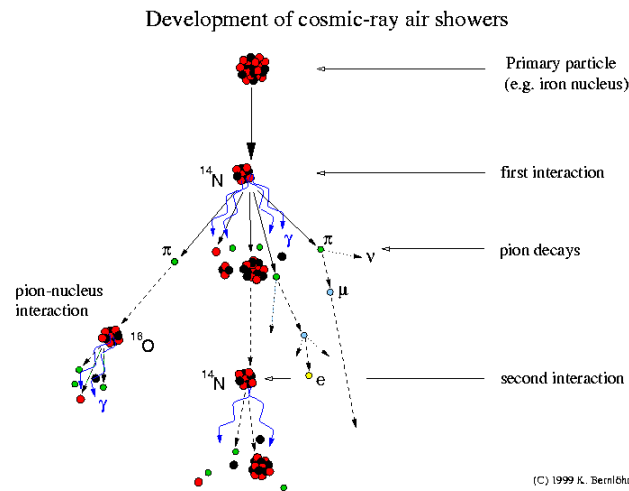
Figure 1.1: Development of CR air showers - Several interactions due to a primary particle are indicated. Its development along the atmosphere is represented taking place the emission of several kind of particles.

Most CRs are the nuclei of atoms ranging from the lightest to the heaviest elements in the periodic table. It goes from high-energy protons (89%), Helium (10%) and heavier nuclei (1%). The observed energy spectrum from non-thermal origin goes from 10^9 eV up to 10^{20} eV. Figure 1.2 shows the energy measurements by several experiments (2) (3) (4). The CR energy spectrum (dN/dE) follows a broken power law as $K \cdot E^{-\alpha}$ where α represents the differential spectral index (power index). The CR spectral index α changes from 2.7 up to 3.0 (transition in the slope in Figure 1.2) at energy close to 3×10^{15} eV, effect known as the "knee" of the spectrum. A second "knee" is seen close to 4×10^{17} eV. In addition, close to the energy region at 3×10^{18} the value of γ is again 2.7. This region is known as the "ankle" of the CR spectrum. The Very-high-energy (VHE) CRs are usually defined for kinetic energies below 10^{18} eV. Up this energy and below 10^{19} eV there are of Ultra-high-energy (UHE), and larger than 10^{19}, the ankle energy, there are of Extreme-energy (EE).

The origin of CRs include three questions: the origin of particles, the origin of energy and the site of acceleration. By assuming the Galactic origin of CRs below 10^{18} eV, the knee can be related to the maximum energy that cosmic accelerator in the Galaxy can achieve. It is the case for expanding Super Nova Remnants (SNRs) for which proton acceleration is not predicted above energies $\sim 10^{15}$ eV, where
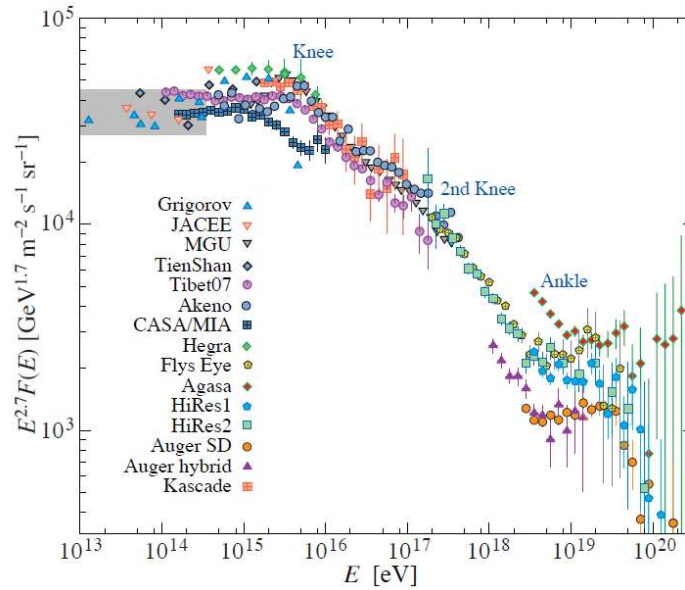
Figure 1.2: Energy and rates of the CR particles - Measurements performed at ground and atmospheric level are shown for several experiments.

propagation and confinement effects in the Galaxy are considered (5). Actually the Fermi Large Area Telescope suggest the direct evidence of SNRs as acceleration site for CRs protons (6), results supported by the characteristic pion-decay feature in the γ-ray spectra of the IC443 and W44 SNRs. The origin of CRs with energies between the knee and the ankle is more unclear. The determination of the chemical composition equivalent to the energy spectra estimation of the CRs for both regions is crucial to fit the theoretical models with the results of the experiments. Most authors agree that, up to the knee, protons and He primaries follow the standard composition, between the first and second knee the composition is mainly iron-based, finally above the ankle the composition should to be made of extra-galactic protons without a clear site of acceleration.

There are several guesses about the Galactic origin (E$\leq 10^{15}$ eV) of high-energy protons and other nuclei, but it is not possible to correlate its direction on Earth to astrophysical sources since CRs experience deflections in their trajectories due to the Galactic magnetic fields. At Very-high energy, a cut-off is expected due to the interaction of high-energy CRs with the Cosmic MicroWave Background (CMB), effect known as the "Greisen-Zatsepin-Kuzmin (GZK) effect" (7). The propagation of the highest CRs rays is then limited by the GZK effect which produces a cut-off in the spectrum of primary cosmic rays and above 6×10^{19} eV.

It suggests that no source of high-energy protons can be detected farther than 50 Mpc (7). A pion production by delta resonance takes place due to the GZK effect as

$$p + \gamma_{CMB} \rightarrow \Delta^+ \rightarrow \pi^+ + n \quad . \tag{1.1}$$
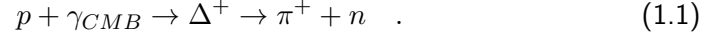
The goal of this section on CRs is to briefly present the proposed mechanism to explain the origin of such cosmic particles as sites of acceleration, followed by a review on the main detection techniques and sources detected.

1.1.1 Shock acceleration mechanisms

High-energy cosmic particles are produced by astrophysical acceleration mechanisms that are supposed to take place in SNRs in the Galaxy, and AGNs and Gamma-Ray Bursts (GRBs) outside our Galaxy.
The stochastic acceleration process of CRs was first explained by Enrico Fermi in 1949 (8) as consequence of iterative scattering processes of charged particles in a shock-wave along their trajectories into cosmic magnetic fields. The Fermi mechanism assumes the origin of shock-waves in environments of huge gravitational forces such as regions close to black holes in stellar gravitational collapses. If a particle is accelerated into the inhomogeneity of a magnetic field, its energy increase should be proportional to its energy as a function of the gain due to the movement into the magnetic field. Two approaches are used to describe the stochastic acceleration process, the so-called "second" (original theory) and "first" order Fermi acceleration mechanisms.
The second order Fermi acceleration mechanism depicted in Figure 1.3-left uses a moving gas magnetic cloud model where the particles are scattered elastically in non-homogeneous locations in the magnetic field, their trajectories being randomized into the cloud. The particles can go out from the cloud to whichever direction carrying an average gain in energy $\langle \Delta E \rangle / E \simeq (4/3)\beta^2$ proportional to the squared cloud velocity (β=v/c) (9).
The first order acceleration mechanism considers a plane infinite shock front where the particles do not come into a moving gas magnetic cloud model but go back and forth across the shock-wave front. The particles crossing the cloud are then accelerated with an average gain of $\langle \Delta E \rangle / E \simeq (4/3)\beta$ (9). The first order Fermi acceleration mechanism is depicted in Figure 1.3-right.
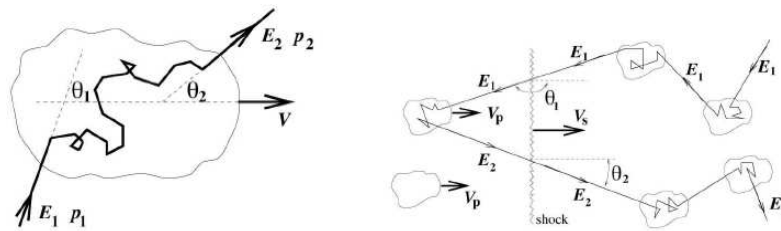
Figure 1.3: Second and first order Fermi acceleration mechanisms - Left: second order Fermi acceleration where a cosmic particle with energy E_1 crosses a cloud with velocity V_1. Right: first order Fermi acceleration. The plane shock velocity is labelled as V_s.

In 1984 Michael Hillas proposed a schematic description of the main acceleration sites as a function of their size and magnetic field. The energy losses are not included in this approach, but the sizes of the bodies are included allowing to be confined in the magnetic field. In this framework, the maximum energy can be defined as

$$\frac{E_{max}}{1EeV} = Z \times \frac{L}{1kpc} \times \frac{B}{1\mu G} \quad , \tag{1.2}$$

where L is the estimated size of the cosmic region. Figure 1.4 shows the Hillas clasification for some celestial bodies in particular AGNs and GRBs.
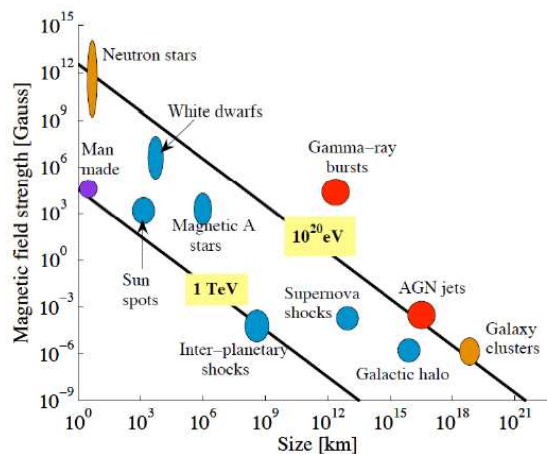
Figure 1.4: Hillas diagram for celestial bodies - The figure shows the classification of Galactic systems based on the sizes and the magnetic field strength in a Fermi acceleration scenario.

1.1.2   Detection and sources of Cosmic Rays

Two principles are used to determine the direction of UHE CRs: Surface Detection (SD) and Fluorescence Detection (FD). The SD consist of wide horizontal plane surface arrangement which detects the secondary particles. The direction of the primary can be inferred from the reconstruction of the measured arrival time of the secondaries. The FD technique takes advantage of the fluorescence light released by excited atmospheric nitrogen molecules (10) (11) and the Cherenkov photons induced by secondary particles. The aim of the FD technique is to estimate the longitudinal profile of showers collected by the SD. The integral of this longitudinal profile allows to compute quantities such as the shower energy and the speed of the shower development (related to the primary particle mass). The combination of the FD and SD techniques is the so-called "hybrid" detection scheme (2).

The most relevant discoveries on UHE CR energy spectrum and CR chemical composition come from experiments as the Pierre Auger Observatory (PAO) (2) and the Telecope Array (TA) experiment (3). The PAO is a surface array of almost 1600 water Cherenkov detectors spread over along 3000 km^2 on the vast plain known as "Pampa Amarilla" in the west of Argentina. It consists also of 4 FD stations equipped with six fixed telescopes each for air-fluorescence light detection. The TA experiment, located in the central western desert of USA is composed by a triplet of FD stations located in the surroundings of a ground grid of 507 SD stations, with 38 fluorescence telescopes in total for the triplet.

The inference about CR composition by indirect detection of primaries comes from observables of the Extensive Air Showers (EAS). In the FD technique the relevant observable is the atmospheric depth at which the maximum number of secondary particles is reached. It is proportional to the amount of energy deposited in the atmosphere and to the UV light collected in the telescope. The average depth of the shower maximum $\langle X_{max} \rangle$ is related to the energy E and the mass A of the primary particle as

$$\langle X_{max} \rangle \propto D_{10} \cdot log(\frac{E}{A}) \quad , \tag{1.3}$$

where D_{10} is known as the elongation rate which in physics terms represents the change of $\langle X_{max} \rangle$ per decade of energy and it is sensitive to changes in composition with energy. This longitudinal development of the CR air showers

represents the distance between the point of impact of the primary particle at the higher level of the atmosphere and the point of the primary track where the shower reaches its maximum number of secondary particles. Figure 1.5 shows the latest PAO results for $\langle X_{max} \rangle$ (12) and Figure 1.6 the updated results for TA (13). The solid lines in Figure 1.5 correspond to the Monte Carlo simulations for protons (top line) and Fe nuclei (bottom line).
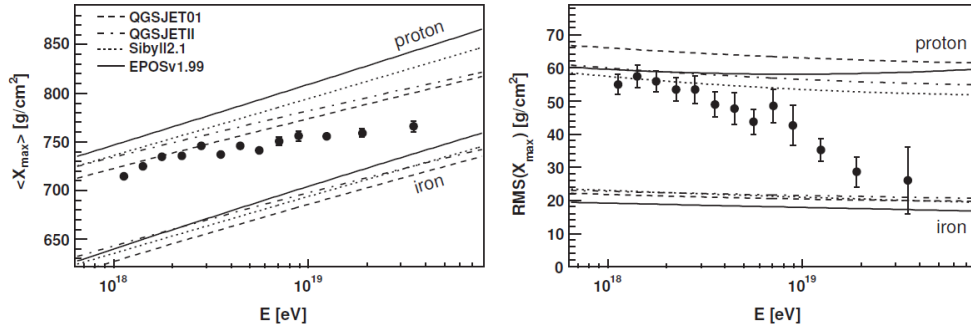
Figure 1.5: Average depth of shower maximum (left) and its fluctuations RMS (right) reported by the PAO as a function of the energy - Simulations with a set of hadronic interaction models are indicated in the plot for proton (top) and iron showers (bottom).

For the TA experimental results, one single line can explain the D_{10} contribution which is in contradiction with the PAO results, however, consistent to the prediction for proton primaries at all energies as Figure 1.6 shows. The data matches with the predictions for the pure proton model, as a very light dominated process.
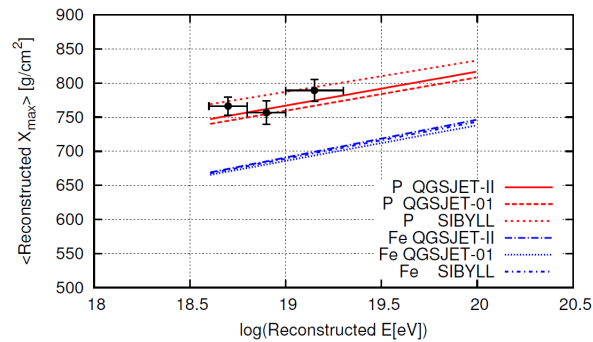
Figure 1.6: Comparison of the average reconstructed X_{max} for each energy between data (black points) and Monte Carlo for the TA experiment - The red and blue lines are the predictions of the pure proton and pure iron compositions respectively with the interaction models of QGSJET-II, QGSJET-01 and SIBYLL (13).

The PAO results by using FD technique in coincidence with at least one SD device have allowed to correlate almost 69 observed events with a list of AGNs candidate sources (14). The skymap in Figure 1.7 represents the location of the 69 events observed by PAO.
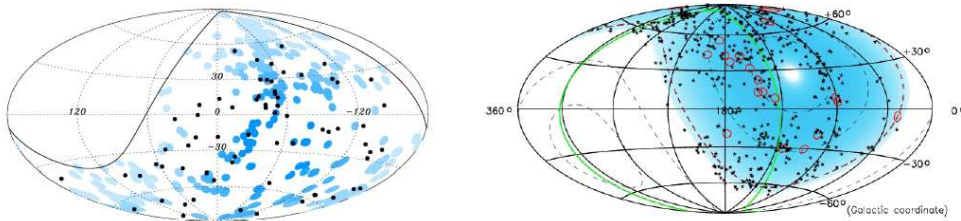
Figure 1.7: Skymap of the PAO and TA events in Galactic coordinates - Left: PAO events, the black dots correspond to the arrival directions of CRs with E > 55 EeV, the blue circles (3.1° radius) represent the AGNs candidates from the Veron-Cetty catalogue (14). Right: TA events, red circles (3.1° radius) at E > 57 EeV. The blue color intensity is related to the visibility of the source.

The experimental procedure for understanding where the UHECR come from is based on the idea of searching for small and large-scale anisotropies in their direction. The solid line drawn in Figure 1.7-left traces the visible region for PAO for zenith angles less than 60° (15). The correlation studies between the anisotropy in the arrival directions of UHE CRs and the AGNs gave the most significance for 27 CR with E > 55 EeV and AGNs located at a distance L< 75 Mpc (15), with a total fraction of correlating events of 33%. Likewise, the TA experiment has tested this correlation with their own data for the SD stations and has found a fraction of 40% of correlated events. The skymap of the events above E > 57 EeV and AGNs on both hemispheres is depicted on Figure 1.7-right.

1.2   Cosmic photons and gamma astronomy

The gamma astronomy uses photons at energies larger than the X-ray radiation. By using this kind of particles, several extreme and violent cosmic bodies can be studied. It is mostly supported by space-based experiments since γ-ray radiation is absorbed by the atmosphere, however, several kind of techniques have been developed in order to measure high-energy γ-ray at ground. This section presents some basic insights about the mechanism of production of high-energy γ-rays, their detection techniques and an updated skymap with some cosmic sources.

1.2.1 Production mechanisms

Two mechanisms are considered for the γ-ray production: the leptonic (16) and the hadronic (17) mechanisms which refer respectively to the acceleration of electrons or protons and other nuclei. The relevant processes in leptonic acceleration models are the Inverse Comptom (IC) scattering, *bremsstrahlung* and the synchrotron radiation. The interaction of ultra-relativistic electrons with the celestial photon fields produces IC γ-rays. The energy spectra shows a double bump shape with one peak on the IR/X-ray band due to the synchroton radiation, and another peak on the γ-rays energy due to IC (16). In hadronic processes, photons are generated by the decay of neutral pions produced by the interaction of extremely energetic protons with the matter or radiation at the source. This also implies the production of charged pions and therefore high-energy neutrinos. The link between VHE γ-ray sources and neutrinos is the meson-decay channel. The energy spectra of γ-rays sources follows a similar behaviour than that of the CR sources, i.e. a power law energy spectrum, $E^{-\alpha_\gamma}$, where $\alpha_\gamma \sim 2.0 - 2.5$.

1.2.2 Detection techniques and sources of γ-rays

Most of the detection techniques of primary photons in the MeV to GeV energy range are space-based experiments. At higher energies, the detection of Cherenkov light induced by charged particles produced in the interaction photons-atmosphere is the most efficient technique for γ-rays studies. The technique is known as Imaging Atmospheric Cherenkov Telescopes (IACTs) used in experiments as HESS, MAGIC and VERITAS. The IACTs allow to detect γ-rays between 50 GeV and 50 TeV. Other ground based experiments detect the light using Water Cherenkov EAS as CANGAROO and HAWC.

The High Energy Stereoscopic System (HESS) (18) (Namibia) is one of the latest generation instruments for VHE γ-ray astronomy and comprises several telescopes installed in several stages. The first phase consisted of four large Cherenkov telescopes with about 100 m^2 mirror area able to cover an energy range up to 100 GeV providing large event statistics for high-energy phenomena. The IACT stereoscopy requires at least two telescopes to improve the angular reconstruction, energy reconstruction and background suppression. Figure 1.8 shows the last results of the minimal detectable flux for HESS as a function of the energy threshold.
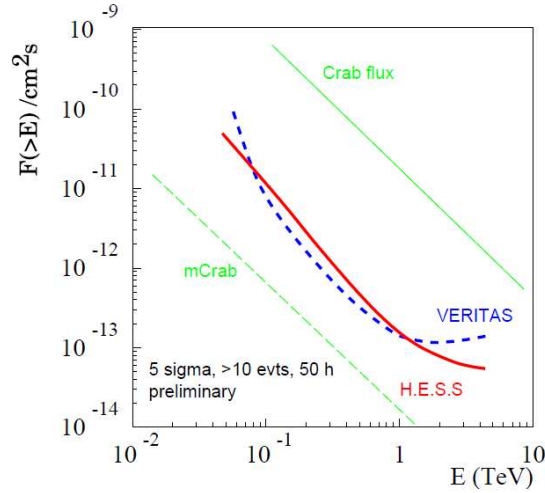
Figure 1.8: Minimal detectable flux as a function of the energy threshold for different γ-ray experiments for 50 hours of exposure time - A comparison for Crab Nebula flux levels is also shown.

The Major Atmospheric Gamma-ray Imaging Cherenkov (MAGIC) project ([19]) consists of a set of two telescopes 85 metres away designed for γ-ray astronomy able to be configured for lower energy studies with high sensitivity. MAGIC-I, operative since 2004, and MAGIC-II, operative since 2009, are a system of two 17 metres Cherenkov telescopes sensitive to VHE radiation above a energy threshold of 50 GeV. The stereoscopic mode (MAGIC-I + MAGIC-II) improves the sensitivity and its energy range (20% at 100 GeV, 15% at 1 TeV) and angular resolution ($\sim 0.1°$ at 100 GeV, $\sim 0.05°$ at 1 TeV).

The MAGIC physics goals span several high-energy astrophysics topics from Galactic and Extra-galactic objects, fundamental physics studies on the origin of CR, Dark Matter searches and tests of Lorentz invariance violation. Using the IACTs technique, MAGIC may distinguish showers from electrons or positrons coming from the background of hadronic CR showers through the image shape. For a 14 hours of Extra-galactic observations, the e^-/e^+ spectrum was measured in the energy range 100 GeV - 3 TeV. An extension of this and other interesting studies in MAGIC can be found in ([20]).

The Very Energetic Radiation Imaging Telescope Array System (VERITAS) ([21]) is a ground-based γ-ray instrument operating at the Fred Lawrence Whipple Observatory (FLWO) in southern Arizona, USA. It consists of an array of four 12 metres (aperture) atmospheric Cherenkov optical reflectors with 350 individual mirrors in

each telescope reflector and 499-pixel Photo Multiplier Tube (PMT) camera in each covering a field of view of 3.5°. The telescopes were arranged in a such a way that they can obtain the best sensitivity in the VHE energy band, 50 GeV - 50 TeV with maximum sensitivity from 100 GeV to 10 TeV, reaching an angular and energy resolution of about 0.1° and 15% respectively.

One of the main scientific results of VERITAS was the detection of 21 blazars (a kind of AGN), one radio Galaxy (M87) and one starbust Galaxy (M82) (22). The current VERITAS program is directed to the objects detected by FERMI-LAT multi-wavelength observations. The combined results of HESS, MAGIC and VER-ITAS provided a more complete catalogue of TeV blazars represented in Figure 1.9.
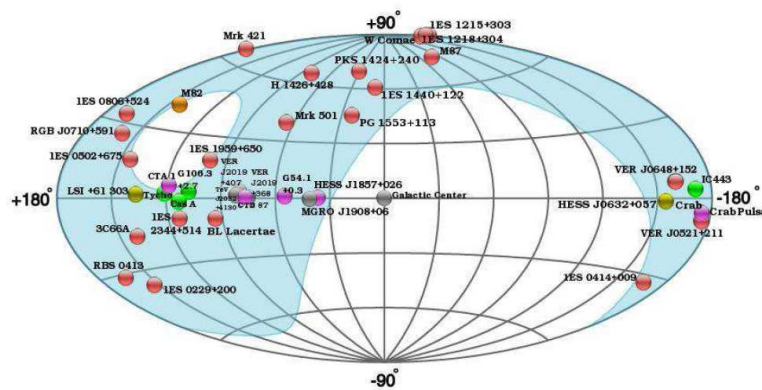
Figure 1.9: VERITAS skymap in Galactic coordinates, July 2011 - The TeV mixed blazar catalogue has been completed by several observations of experiments as HESS and MAGIC with addition of new classes of objects concerning last catalogues before 2011.

The results achieved by the experiments described before, are expected to be overcome by the next Cherenkov Telescope Array project (CTA). It foresees a factor of 5-10 improvement in sensitivity in the current energy domain of about 100 GeV to 10 TeV and an extension of the accessible energy range below 100 GeV and above 100 TeV (23).

Contrary to the ground-based experiments, satellite-based detectors can not be designed for large effective areas (< 1 m^2). The most relevant experiment which used this kind of technique was the Compton Gamma Ray Observatory (CGRO). The most energetic part of the electromagnetic spectrum (up to 30 GeV) was studied with the Energetic Gamma-Ray Experiment Telescope (EGRET) that detected

271 γ-ray sources with high significance, with almost 170 unidentified sources (the third EGRET catalogue). Figure 1.10 shows the final EGRET skymap catalog.
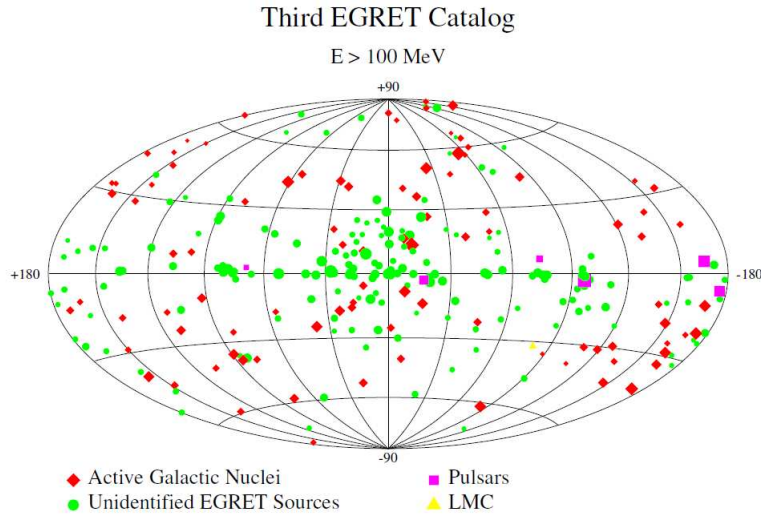
Figure 1.10: Third EGRET catalog for E>100MeV - The figure shows different sources with energies higher than 100 MeV in Galactic coordinates.

Being launched in June 2008, Fermi Gamma-ray Space Telescope, reached the same EGRET sensitivity after one week of observation as the EGRET operation along 9 years. The Fermi range of operation exceeds considerably the EGRET energy threshold, typically from 30 MeV to more than 300 GeV including the gap between previous satellites and ground-based experiments with a resolution better than one arc-minute.

Based on FERMI Large Area Telescope (LAT) results, Table 1.1 (24) shows the high-energy γ-ray sources detected for a period of almost two years from the beginning of the scientific mission.

The Fermi-LAT 2FGL catalogue includes 1873 sources, from which 127 are certainly identified and 1171 of the remaining ones are associated with complements of known sources of γ-rays. The 2FGL label corresponds to the 2nd catalogue and FGL represents Fermi Gamma-ray LAT. The range of energy where the sources where detected and characterized goes from 100 MeV to 100 GeV covering the whole sky with reduced bias effect in observations.

Description	Identified Label	Number	Associated Label	Number
Pulsar, identified by pulsations	PSR	83	...	...
Pulsar, no pulsations seen in LAT yet	...	...	psr	25
Pulsar wind nebula	PWN	3	pwn	0
Supernova remnant	SNR	6	snr	4
Supernova remnant / Pulsar wind nebula	...	...	†	58
Global cluster	GLC	0	glc	11
High-mass binary	HMB	4	hmb	0
Nova	NOV	1	nov	0
BL Lac type of blazar	BZB	7	bzb	423
FSNRQ type of blazar	BZQ	17	bzq	353
Non-blazar active Galaxy	AGN	1	agn	8
Radio Galaxy	RDG	2	rdg	10
Seyfert Galaxy	SEY	1	sey	5
Active Galaxy of uncertain type	AGU	0	agu	268
Normal Galaxy (or part)	GAL	2	gal	4
Starburst Galaxy	SBG	0	sbg	4
Class uncertain	...	...		1
Unassociated	...	...	...	572
TOTAL		127		1746

Table 1.1: The LAT 2FGL source classes. The † symbol means potential association with SNR and Pulsar Wind Nebulae (PWN), capital letters for solved sources and lower case letters for associations.

1.3   Neutrino astronomy

The only sources of extra-terrestrial neutrinos confirmed up to now are the Sun and the SN1987A, detected by the KAMIOKA Nucleon Decay Experiment (KAMIOKANDE) (25), the Irvine-Michigan-Brookhaven (IMB) detector (26) and the Baksan Neutrino Observatory (27). Nonetheless, less than one year ago, at mid of 2013, the IceCube collaboration (28) announced the observation of 28 very-high energy particle events with a clear fingerprint differing of the atmospheric muon and neutrino backgrounds features, representing the first solid evidence of high-energy neutrinos coming from outside the solar system (29). The energy of such neutrino events are above several tens of TeV, and one million times those observed in the SN1987A in the large Magellanic Cloud. A slightly broad information about this result is given in the next section (neutrino telescopes), where the IceCube neutrino telescope is explained.

In addition, neutrinos are produced in accelerators and nuclear reactors and on the atmosphere as secondaries of CR interactions. The Figure 1.11 shows the estimation of fluxes for natural and artificial neutrino sources.

Neutrino telescopes behave as a "telescope" when the neutrino direction can
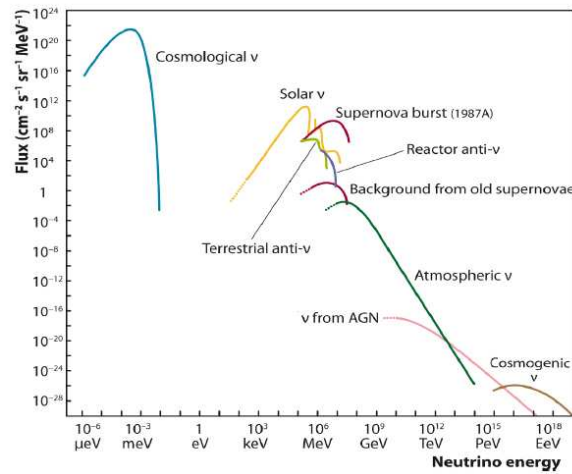
Figure 1.11: Measured and expected fluxes of artificial and natural neutrino fluxes - The figure shows the estimated flux as a function of neutrino energy from non-cosmic, cosmic and other neutrino fluxes.

be reconstructed with an angular resolution tenths of a degree. Nowadays the efforts have been directed to the high-energy cosmic neutrino detection from extra-terrestrial sources as GRBs, AGNs and the ones from the interaction of ultra-energetic protons with the CMB.

Neutrinos are electrically neutral and can only interact weakly with the surrounding matter. Therefore, they can travel along the cosmos without undergoing absorption or reflection, pointing back to the origin of the source. Unfortunately, this low interaction cross-section requires massive detection systems of the order of km^3 volumes.

The neutrino astronomy is the backbone framework about this thesis was developed. This section will review the particle physics phenomenology associated to neutrinos and several innovative techniques ongoing and operative looking for the cosmic neutrino hunting will be commented. Some hypothetical sources of cosmic neutrinos will be commented also.

1.3.1 Neutrino phenomenology

In 1930, Wolfgang Pauli postulated the existence of a neutral particle in order to explain the conservation of energy, momentum and angular momentum in the beta decay of a nucleus. In 1932 James Chadwick discovered a massive neutral particle that he called neutron. Three years later Enrico Fermi developed a theory of beta

decay that contained the lightest of the "neutrons", that he called "neutrino". Twenty years later Clide L. Cowan Jr and Frederick Reines detected the neutrino in a nuclear reactor experiment (discovery awarded with the Physics Nobel prize in 1995).

Some time later it became clear that more than one type of neutrino existed associated with each type of charged lepton. This was experimentally proven in 1962, by Leon M. Lederman, Melvin Schwartz and Jack Steinberger showing that the lepton produced in muon neutrino interactions was always a muon. When the third type of lepton, the tau, was discovered in 1975 at the Stanford Linear Accelerator Center, it was expected to have an associated neutrino (the tau neutrino). The first detection of tau neutrino interactions was done by the DONUT collaboration (30) at Fermilab in 2000; its existence had already been inferred by both theoretical consistency and experimental data from the Large Electron–Positron collider (LEP).

Neutrinos can also change flavour or "oscillate", what explains the reduction on solar electron neutrino and the missing atmospheric muon neutrino flux. The origin of this oscillation among neutrino eigenstates comes from the fact that the flavour states produced by the weak interaction (ν_α) are not eigenstates of the mass matrix (ν_i), instead they are a linear combination of them:

$$|\nu_\alpha\rangle = \sum_{i=1}^{3} U_{\alpha i}|\nu_i\rangle \quad , \tag{1.4}$$

where $\alpha = e, \mu, \tau$ are the neutrino flavours and $i = 1, 2, 3$ correspond to the mass eigen-states. If the time evolution is added, the Equation 1.4 can be written as

$$|\nu_\alpha(t)\rangle = \sum_{i=1}^{3} U_{\alpha i}|\nu_i(t)\rangle = \sum_{i=1}^{3} U_{\alpha i}e^{-iE_i t}|\nu_i\rangle \quad . \tag{1.5}$$

In the approximation that oscillations between only two states dominate, the oscillation probability can be deduced as (31)

$$P_{\alpha\beta} = \sin^2(2\theta)\sin^2(1.27\frac{L}{E}\triangle m^2) \quad , \tag{1.6}$$

where $\triangle m^2 = (m_\alpha^2 - m_\beta^2)$ in eV^2, L is the distance between the neutrino source and the detector in metres and E is the neutrino energy in MeV. The Equation 1.6 suggests that at least two of the neutrino states should have mass since $\triangle m^2$ could

not be zero. The oscillation probability depends on two fundamental unknowns θ and Δm^2. In the three-flavour treatment of neutrino oscillations, there are three mixing angles θ_{12}, θ_{13} and θ_{23}, a CP-violating phase δ, and two independent squared mass differences, Δm_{12}^2 and Δm_{23}^2. In this case the Pontecorvo-Maki-Nakagawa-Sakata (PMNS) mixing matrix can be expressed as (31)

$$U = \begin{pmatrix} 1 & 0 & 0 \\ 0 & c_{23} & s_{23} \\ 0 & -s_{23} & c_{23} \end{pmatrix} \begin{pmatrix} c_{13} & 0 & s_{13}e^{-i\delta} \\ 0 & 1 & 0 \\ -s_{13}e^{i\delta} & 0 & c_{13} \end{pmatrix} \begin{pmatrix} c_{12} & s_{12} & 0 \\ -s_{12} & c_{12} & 0 \\ 0 & 0 & 1 \end{pmatrix} \quad , \quad (1.7)$$

where $c_{ij} \equiv \cos\theta_{ij}$ and $s_{ij} \equiv \sin\theta_{ij}$. The first matrix can be studied with atmospheric neutrinos and LBL (Long-Base-Line) accelerators, the second one with SBL (Short-Base-Line) reactors and the third one with solar neutrinos and LBL reactors. The quantity δ is expected to be small and the results from the Daya Bay experiment (32) demonstrate that $\sin^2(2\theta_{13}) = 0.092 \pm 0.017$ with statistical inference of 5.2σ. In the limit where θ_{13} and δ are zero, the central matrix in Equation 1.7 reduces to the identity matrix, and the experimental case can be explained by means of two decoupled oscillations. The first one, $\nu_e \to \nu_\mu$, is responsible of the solar neutrino oscillations (31), whereas the second decoupled oscillation, $\nu_\mu \to \nu_\tau$, is responsible for atmospheric neutrino oscillations (31).

The experimental signature for neutrino oscillations consists on the disappearance of one neutrino flavour, the corresponding appearance of neutrinos of a different flavour and evidence for an oscillatory pattern.

1.3.2   Detection techniques of cosmic neutrinos

The main challenge of a neutrino detector is to achieve the required mass to be sensitive enough to the expected low fluxes, since the more matter used the more neutrinos will interact. Taking into account that the funding of neutrino facilities is limited, natural environments are used as detection media for neutrino detectors. Reference experiments uses large array of sensors following geometrical patterns looking for detection of the Cherenkov light. As the neutrinos are electrically neutral they are not light emitters. Instead, charged particles produced in its interaction with the environment do it. Other innovative detectors record radio and acoustic waves emitted in the neutrino interaction. In this point the reason about use radio, acoustic or Cherenkov light, relies on the attenuation length

of the media and the neutrino energy threshold. The Table 1.2 compares some methods for neutrino detection installed in several detection media as a function of the neutrino energy threshold and the attenuation length (λ_{att}) at the peak of the spectra (33).

Detection technique	Detection media	$E_\nu^{threshold}$	λ_{att}
Cherenkov	Pure water	> GeV	≈70 m
	Natural lake	> GeV	≈20 m
	Deep ocean	> GeV	≈40 m
	Polar ice	> GeV	≈20 m
Radio Cherenkov	Polar ice	> 5 PeV	≈1 km
	Moon	> 100 EeV	≈10 m
	Salt	> PeV	≈1 km
Acoustic	Water	> PeV	≈5 km
	Ice	> GeV	≈1 km
EAS	Air	> 10 PeV	≈1 km
N_2 fluorescence	Air	> EeV	≈10 km
EAS radar	Air	> EeV	≈100 km

Table 1.2: Relevant parameters of the detection for large neutrino detectors and detectable neutrino energy.

As it can be seen, the radio and acoustic waves can travel much longer in matter before to be absorbed allowing larger detector volumes, but energy threshold is higher. The Cherenkov telescopes are the best option to study neutrino events above GeV threshold. The ground-breaking techniques used presently in the cosmic neutrino search can be named as follows:

- *Detection via Cherenkov light water-based environments*.
  The cosmic neutrino hunting in water-based detection media (artificial or natural environment) is actually a feasible technique with large experience from the commissioning of prototype detection systems and engineering. The artificial environment is commonly a large and carefully chamber (or vessel) filled with ultra-pure water as in the Super-Kamiokande (Super-K) detector. In Super-K, the chamber where particles are detected is filled with $\sim$ 50k tons of water and buried at 1 km, where $\sim$ 12k PMTs surrounding the 2 concentric walls of the chamber detect the Cherenkov light (as ring) emission by particles crossing the detector. The array of PMTs sample the projection of the distinctive ring pattern, used to determine the direction

of the particle. Electrons create electromagnetic showers and leave a fuzzy ring pattern, but muons which do not make showers give a clear ring. For both kind of events the parameters of the Cherenkov cone as vertex position, number of rings, direction, particle type and momentum are possible from charge and hit timing information from the PMTs. A hit is defined as the combined data of arrival time and charge information of the signals from the PMT, recorded as single photo-electron or complete waveform. The Ring Imaging water CHerenkov (RICH) technique used by Super-K offers a good tracking specially at 1 GeV or less, with a particle identification close to 99%, a energy resolution for e and $\mu \sim 3\%$ and an energy threshold 14-16 MeV for solar and super-nova neutrinos (34).

On the other hand, natural environments are used by experiments as ANTARES in the case of deep-sea water and IceCube in deep glacial ice, where a grid of PMTs are uniformly throughout the detector collecting the Cherenkov light induced by particles. In this kind of detectors the reconstruction of the track of the particle is also carried out from the timing and positioning of the hits in the PMTs of the detector. From optimization studies of the 3D-grid of light sensors as well as from current physics studies in these neutrino telescopes, it has been possible to show that above 1 TeV, the direction of the incoming neutrino can be determined better than $0.5°$ for deep sea neutrino detectors (35). In the case of deep glacial ice, the method allows the detection of neutrinos above 100 TeV with an angular resolution better than $0.6°$ (36).

- *Detection via air showers*.

  Detection via air showers is the working mode for the PAO and TA experiments. In this case, horizontal air showers induced by neutrino interactions at energies above E$> 10^{17}$eV can be studied. The optimum sensitivity for this method is between 1 EeV to 100 EeV and the effective target mass $\simeq$ 20 Gigatons. The sensitivity could be improved for ν_τ scratching the Earth and interacting close to the array. The charged τ lepton produced in the Charged Current (CC) interaction can escape from the deeper rocks surrounding the array. Most of the time its decay is in hadrons (branching ratio $\sim$ 65%) and the event can be recorded if it happens close to the field

of view of the fluorescence telescopes. For a energy scale of 1 EeV, the current ν_τ limit for a E^{-2} flux is $E^2\phi < 10^{-7} \text{GeVcm}^{-2}\text{s}^{-1}\text{sr}^{-1}$ (37).

- *Radio detection*.

  This technique is used in the ANtarctic Impulsive Transient Antenna (ANITA) experiment and it is carried out in Antarctic ice or atmosphere environments. When the UHE neutrino strikes the ice it creates an electron-photon shower featured by the excess of the number of electrons in the shower concerning the number of positrons. By this fact, the shower develops a negative charge imbalance and the emission of a coherent Cherenkov light takes place proportional to the square of the electric net charge. In ice, attenuation lengths greater than 1 km are observed for radio signals, depending on the frequency band and the ice temperature, which suggests that for E>10 PeV this technique becomes competitive or even better than the optical detection ($20 \leq \lambda_{att}[\text{m}] \leq 70$). The ZeV range is the aim of the Goldstone Lunar Ultra-high energy neutrino Experiment (GLUE) (38). Other reference experiment is the Extreme Universe Space Observatory on the Japanese Experiment Module (JEM-EUSO) to be located in the International Space Station (ISS), expected to be installed in 2017. JEM-EUSO will use the Earth atmosphere as detection media for UHE particles able to detect particles with E$> 10^{19}$ eV. When these particles occasionally break through the atmosphere, they collide with nucleus of air atom and produces a detectable EAS.

- *Acoustic detection*.

  This technique takes advantages of the production of pressure waves by charged particles depositing energy in liquid or solid media. For a particle cascade, its full energy is attenuated into the media mostly through ionisation and transformed to heat in a very short time compared to the time scales for the generation and propagation of acoustic pulses. As a consequence, a bipolar acoustic pulse with a width of a few tens of microseconds in water or ice is produced corresponding to a peak signal power of 20 kHz (37). The acoustic pulse is propagated into the media transversely to the pencil-like cascade within a disk-shaped volume with thickness corresponding to the cascade length of about 10 m.

1.3.3   Cosmic neutrino sources

Cosmic neutrinos can be produced through hadronic acceleration processes by $\pi^{\pm}$ decay produced in the interaction of a proton with other proton or atomic nuclei, or with a photon as

$$
\begin{array}{cccccccc}
pp/p\gamma \rightarrow & \pi^0 & + & \pi^+ & + & \pi^- & + & ... \\
 & \downarrow & & \downarrow & & \downarrow & & \\
 & \gamma + \gamma & & \mu^+ + \nu_\mu & & \mu^- + \bar{\nu_\mu} & & \\
 & & & \downarrow & & \downarrow & & \\
 & & & e^+ + \nu_e + \bar{\nu_\mu} & & e^- + \bar{\nu_e} + \nu_\mu & &
\end{array}
\tag{1.8}
$$
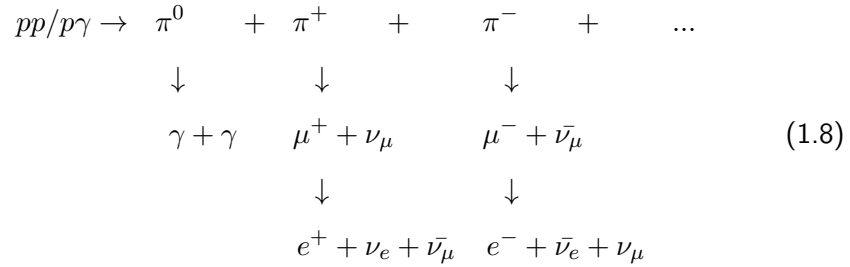
These decay channels produce neutrinos in a flavour ratio $\nu_e : \nu_\mu : \nu_\tau = 1 : 2 : 0$. Neutrino oscillations turns this ratio to $1 : 1 : 1$ for cosmic neutrinos which have travelled long distances before arriving to Earth.

Accelerated protons in Galactic systems are mostly unable to reach the Earth with a good pointing accuracy due to their interaction with the Inter-galactic magnetic field. Nonetheless, some low detectable flux of protons with energies up to 10^{20}eV can be expected ([4]). In the case of CR accelerated in regions of high magnetic fields near black holes, their interactions with the surrounding matter and radiation produce neutral and charged pion secondaries via delta resonance and as it is indicated in Equation [1.8]. The π^0 emission carries a secondary proton which can be trapped in the high magnetic fields, whereas the emission of the π^+ is released together with a neutron which can escape as well as the decay products of neutral and charged pions. Therefore, all the energy released by the source is kept by the particles ejected out the magnetic region namely CRs, γ-rays and neutrinos result of the decay of neutrons, neutral pions and charged pions respectively. The neutrino sources can be classified as Extra-galactic and Galactic. Some of the most studied are the following:

- **Extra-Galactic sources**

  - *AGNs*

    A typical Active Galactic Nuclei has a volume less than 1 pc^3 located at the center of young galaxies (active galaxies), a luminosity around 10^{48} erg/s, and the energy spectrum covering several tens orders of

magnitude. They are classified as radio-quiet and radio-loud depending of their radio emission: thermal-like spectrum or radio and X-ray range. The core of the AGN is a super-massive black hole with 10^6-10^9 solar masses. The accretion disk is made of several Galactic materials such as gases, stellar dust and stars. The energy released by an AGN is mainly due to accretion of the material into the black hole by gravitational interaction which give very efficient conversion of potential and kinetic energy to radiation. The plasma created in the AGN keeps an angular momentum which creates magnetic fields pushing out particles to the Galactic media by means of two jets perpendicular to the Galactic plane. AGNs are classified according to the angle between the axis of rotation and the direction of the observer as:

* Blazar: an AGN is a blazar when the rotational axis (direction of the relativistic jets) is pointing in the direction of the observer.

* Seyfert Galaxy: the observation axis is between the rotational axis of the AGN and the Galaxy plane.

* Radio Galaxy: the observer axis matches with the Galactic plane.

If the AGNs constitute a site of acceleration of particles above 1 TeV, it can be argued that such particles can be primary protons which by proton - proton or proton - photon interaction lead neutrino emission in the same energy range and able to be detected by neutrino detectors.

– *GRBs*

Gamma Ray Bursts are the most violent and brightest sources of γ radiation in the Universe, supposed to be produced by the collapse of a massive star into a black hole or the collapse of two massive stars. They can be classified depending on their emission time as long GRBs (above 2 ns) and short GRBs (below 2 ns) duration, the latter are the candidate source of cosmic neutrinos. The "Fireball model" is the reference framework used to study the phenomenon which is explained from considerations on the total energy released and the variability time of the GRB during the collapse. Result of this is the emission of blast waves propagated along the stars at velocities close to the speed of light. These blast waves or fireballs are expanded

at constant energy by conversion of entropy into kinetic energy. In addition to the emission of the fireball, two jets are released in opposite direction located in the hemispheres of the accretion disk and when the matter is accelerated in the jets consecutively reaching larger velocities forming shells with different speeds. The interaction between shells and the external medium or shell-to-shell leads a kinetic energy re-convert into internal energy which is translated into γ-ray radiation or energy transference to baryons by a baryon-to-photon coupling.

The dissipation of the kinetic energy of the relativistic fireball described before is expected to be converted to neutrino flux of energies close to 10^{14} eV by photo-meson production, what could be detected by km^3 neutrino detectors in a quantity up to several tens of events per year. Most optimistic models are being constrained by the most recent results of the IceCube neutrino observatory ([36]).

– *Starburst galaxies*

The central regions of the Starburst galaxies have an emission of a kind of Galactic-scale wind by means of the joint effect of supernova (SN) explosions and winds from the massive stars. The γ-ray flux detected is in the MeV energy range and suggests CR densities of 2-3 times above that in our own Galaxy. The cumulative neutrino flux of all Starburst galaxies could be detected by km^3 detectors ([37]).

- **Galactic sources**

  – *SNRs*

  A SN is the result of the explosion of a massive super-giant star. A SNR is the structure that remains from the explosion of such star in a supernova. The supernova remnants are postulated as accelerators of CRs ([39]). This assumption is based on considerations of energy losses of CRs from the Galaxy which can be compensated by assuming that each new SNR transforms a small fraction of its kinetic energy into CRs ([40]). In such processes, large amounts of protons are converted, by the absorption of electrons, into neutrons, and then the subsequent emission of neutrinos. During the core-collapse supernovae all the

gravitational energy released in the process is ejected as intense neutrino fluxes coming from the newly-born neutron star. This neutrino signal is emitted promptly, contrary to photons which take hours or days for emerging from the stellar envelope.

– *PWNe*

A Pulsar Wind Nebula is an interstellar cloud made of dust, hydrogen, helium and other ionized gases (all the aggregate known as nebula) driven by a pulsar wind, which is a flow of energetic particles escaping a pulsar (pulsating neutron star). Young pulsars of less than 10^6 yr are able to accelerate protons at relativistic energies above the polar cap region for cases when the spin axis is anti-parallel aligned (expected in half of the total neutron stars) with the pulsar magnetic moment. The high-energy neutrino emission (TeV range) in that process takes place when the relativistic protons interact with the soft X-rays photons released from the neutron star surface, what is carried out as photo-meson production. Together with neutrino emission, the interaction gives TeV γ-rays produced by IC scattering of high-energy electrons on the synchrotron radiation. However, both γ-ray and neutrino fluxes can be estimated by several hadronic models proposed by several authors (41) coming from high-energy nuclei and via decay of pions (both charged and neutral). The most studied PWN is the Crab nebula, for which 1.9 to 5.8 neutrinos can be expected with energies from 1 TeV to 5 TeV for km^3 detectors (42). Other studies suggest a no detectable neutrino event rate coming from PWNe (43), except that of the Crab Nebulae.

– *Micro-quasars*

Micro-quasars are X-ray binary systems (XRBs) made of a compact central object like a neutron star or a black hole, as accretion system of matter from a close star as part of the scheme. The physics laws that explain the mass accretion of matter into the black holes is assumed to be the same as for other systems as AGNs and GRBs. They are classified as "High-Mass X-ray binaries" (HMXBs) when the mass of the companion star is larger than ten solar masses or "Low-Mass

X-ray binaries" (LMXBs) when the companion star is less than the so-lar mass. The mechanism of the mass transfer can be explained from the "Roche lobe" overflow and stellar wind dynamics (44). Collimated relativistic jets are obtained as result of the gravitational energy re-leased by the dropped matter into the system. These jets are ejected on perpendicular directions to both sides of the accretion disc in the binary system. Up to now it is still unclear the hadronic component of the jets (44). There are some models which predicts the neutrino emission from micro-quasar jets (45) (46). Such studies assume the dissipation of energy of the acceleration process due to internal shock waves giving a non-thermal power law distributions for protons up to large energies, thus, their interaction with X-rays from the accretion disk or synchrotron photons produced into the jet by thermal electrons release neutrino fluxes (prior pion production and decay). Neutrinos are expected to carry ~5% of the initial protons energy, i.e., neutrinos of TeV energy range should be produced (44). When HMXBs are consid-ered, neutrinos and γ-rays can be produced by means of the interaction between the hadrons in the relativistic jet and the clumps of the stellar wind of what the massive micro-quasars are made of. Some common micro-quasars (HMXBs type) have been already detected by using high and very-high γ-ray energies, as the LS5039 and LSI+61°303, detected by HESS and MAGIC respectively and confirmed by Fermi-LAT, or the CyG X-1 detected by MAGIC and AGILE, CyG X-3 by AGILE and Fermi-LAT (44).

– *Galactic Centre (GC)*
Galactic sources in the centre of the Milky Way Galaxy are also con-sidered as candidates for high-energy neutrino detection. The emis-sion of CRs arriving from the GC direction enlarges the assumptions of neutrino fluxes in the TeV to PeV energy range from the decay of pions or neutrons due to proton-proton collisions from the same shock-accelerated, GC population with ambient photons (47). The most studied sources of TeV γ-rays in the direction of the GC are HESS J1745-290, the Galactic super-massive black hole and the SNR SgrA East reported by HESS. The expected number of neutrino events

coming from the GC for a five years of observation are between 2 to 3 for energies above 1 TeV and 5 TeV respectively for a km^3 detector (42). The expected neutrino flux can be normalized to the γ-ray and neutron fluxes due to the common origin of such particles.

– *Fermi bubbles*

This is a particular source discovered by the FERMI-LAT detector with a hard and almost uniform energy spectrum. They are visible in the Galaxy as two bubble-shaped region centred just in the core of the Milky Way, perpendicular to the Galactic plane and extending up to 10 kpc from the center of the Galaxy. Fermi bubbles have being postulated as a promising source of HE neutrinos with fluxes (~ 0.4 times γ-flux) reaching $\mathrm{d}\phi_\nu/\mathrm{dE} \sim 1.2 \cdot 10^{-7} \mathrm{E}^{-2} \mathrm{GeVcm}^{-2}\mathrm{s}^{-1}\mathrm{sr}^{-1}$ (48).

Other possible signals in neutrino telescopes are the neutrinos produced in dark matter particle annihilations and relic particles such as magnetic monopoles and nuclearites:

- *Dark matter particles*

  Weakly Interactive Massive Particles (WIMPs) are considered as the most feasible candidates for Dark Matter. These particles are trapped in the most inner regions of large mass celestial bodies like the Sun, the GC or the Earth itself. In agreement to the Minimal Super-Symmetric Standard Model (MSSM) (49) the favorite candidate as Dark matter particle is the neutralino, whose annihilation products could produce detectable rates of flux of high-energy neutrinos (model-dependent). Other proposed particles as the Lightest Kaluza-Klein (LKK) particle is also widely studied (49).

- *Magnetic monopoles*

  Magnetic monopoles are hypothetical particles predicted from the Grand Unified Theories (GUT) (50) which have only one pole of magnetic charge instead of the known two magnetic poles. The detection of magnetic monopoles in neutrino detectors is based on the same principle as the detection of high-energy muons. The Cherenkov light emission by using $z = ng/e$ as charge of the particle can describe the phenomena. In this sense, a fast monopole with $g = g_D = (\hbar c)/2e$ is expected to emit about 8550 times

more Cherenkov light than muons of the same velocity. Below the Cherenkov threshold $\beta_{th} = 0.74$, a magnetic monopole of velocity $\beta \geq 0.51$ ionizes sea water releasing indirect Cherenkov emission from δ-rays electrons produced along its trajectory.

- *Nuclearites*

  The nuclearites also known as "strangelets", result of aggregates of u, d, s-quarks and electrons produced in the early universe or in strange star collisions. Nuclearites are also referred to as nuclear SQM (Strange Quark Matter) nuggets with masses similar to that of heavy nuclei. They have typical Galactic velocities $\beta \approx 10^{-3}$ under a dominant interaction of elastic collisions with atoms in the media. Nuclearite detection in neutrino detectors is possible from the energy released through elastic collisions giving the over-heating of the nuclearite track in matter. If the media is water, a fraction of $\eta \simeq 3 \times 10^{-5}$ of the energy loss is dissipated as visible black body radiation emitted by the expanding cylindrical shock wave (51).

1.4   Neutrino telescopes

The neutrino telescopes are the main facilities for detecting high-energy neutrinos from extra-terrestrial origin. A 3D-array of PMTs allows the detection of the Cherenkov light released by ultra-relativistic particles crossing the detector. The beginning, present and future prototypes of neutrino telescopes will be presented as well as their fundamentals, detection principle and performance.

1.4.1   Neutrino interactions and Cherenkov radiation

Neutrino telescopes consist of a three dimensional grid of PMTs arranged in several detection lines anchored to the seabed or buried in deep ice. The PMTs collect the Cherenkov light produced by relativistic charged muons produced by the interaction of neutrinos with the detector surroundings. The reconstruction of the neutrino-induced muon trajectory is carried out from the timing and location of the PMT hits. The high-energy neutrino interaction with a nucleon N by means of CC or via Neutral Current (NC) weak interactions yields respectively

$$\nu_l + N \rightarrow l + X \qquad \nu_l + N \rightarrow \nu_l + X \quad . \tag{1.9}$$

For the range of energies considered in neutrino astronomy, the differential cross section for CC interactions can be expressed as (52)

$$\frac{d^2\sigma_\nu N}{dxdy} = \frac{2G_F^2 m_N E_\nu}{\pi} \frac{M_W^4}{(Q^2 + M_W^2)^2} \times [xq(x,Q^2) + x(1-y)^2 \bar{q}(x,Q^2)] \quad , \quad (1.10)$$

where $x = Q^2/2m_N(E_\nu - E_l)$ and $y = (E_\nu - E_l)/E_\nu$ corresponds to the Feynman-Bjorken variables, Q^2 refers to the square of the momentum transferred between neutrino and lepton, m_N is the nucleon mass, M_W is the mass of the W boson and G_F is the Fermi coupling constant. The represented functions by $q(x,Q^2)$ and $\bar{q}(x,Q^2)$ correspond to the parton distributions for quarks and antiquarks. Interaction cross sections for ν_μ and $\bar{\nu}_\mu$ are depicted in Figure 1.12 as a function of the neutrino energy.
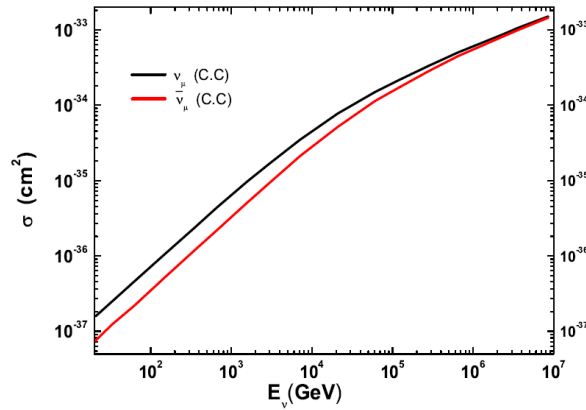
Figure 1.12: ν_μ **and** $\bar{\nu}_\mu$ **cross sections** - The cross section measurements use models based on parton distributions referred in (52)

As it can be deduced from the Figure 1.12, at lower energies the neutrino cross section behaves linearly with E_ν up to $\sim 10^4$ GeV. For higher energies the invariant mass $Q^2 = 2m_N E_\nu xy$ could get values larger than the W-boson rest mass being reduced the total cross section.

The Cherenkov radiation is the response of the polarization and relaxation of atoms along the path of a charged particle whose speed exceeds the speed of light propagation in the media (53). The Cherenkov angle (θ_c) is given by

$$\theta_c = \cos^{-1}(\frac{1}{n\beta}) \quad , \quad (1.11)$$

where n is the refractive index of light in the media and $\beta = v/c$ is the velocity of the particle divided by the speed of light, $\beta = 1/n$ represents the Cherenkov threshold. Fast charged particles will emit Cherenkov radiation such as $\beta > v/c$, leaving a light wake of constant angle. The radiation per unit length x and wavelength λ can be estimated from the Frank-Tamm equation (54)

$$\frac{d^2N}{dxd\lambda} = \frac{2\pi\alpha z^2}{\lambda^2}(1 - \frac{1}{\beta^2 n^2}) \quad , \tag{1.12}$$

where z is the charge of the particle and α is the electromagnetic coupling constant. The effective wavelength interval for water and detectors is typically between 310 and 500 nm and the effective number of radiated quanta per unit distance is around 200 Cherenkov photons every centimetre. If an energy loss rate in pure water of 1.99 MeV/cm is assumed for a minimum ionizing particle, Cherenkov radiation contributes for only 5.9×10^{-5} of the ionization energy loss (33).

1.4.2   The muon neutrino ν_μ and other neutrino flavours

For neutrino energies typically larger than 1 TeV, the great penetrating power of the ν_μ crossing the Earth can generate an interaction outside the detection array. There is no other particle than neutrinos that can penetrate through the Earth and enter the detector from below. The muon coming from the ν_μ CC interaction enters the detector from this direction. The average angle $\theta_{\nu-\mu}$ between the incident neutrino and the out-going muon can be estimated as

$$\theta_{\nu-\mu} \sim \frac{0.6°}{\sqrt{E_\nu(TeV)}} \quad . \tag{1.13}$$

High-energy muons lose energy due to several processes namely ionization, pair production, *bremsstrahlung* and photo-nuclear interactions. A parametrization of that energy loss per unit length can be expressed as

$$\frac{dE_\mu}{dx} = \alpha(E_\mu) + \beta(E_\mu)E_\mu \quad , \tag{1.14}$$

where $\alpha(E_\mu)$ includes the ionization energy loss and $\beta(E_\mu)$ represents the sum of pair production, bremstrahlung and photonuclear reactions (55) which contributes to the detectable signal. For water the ionization loss is roughly given by $\alpha(E_\mu) = 2$ MeV/cm and $\beta(E_\mu)_{tot} = \beta(E_\mu)_{pair} + \beta(E_\mu)_{brems} + \beta(E_\mu)_{phonuc} = (1.7 + 1.2 +$

$0.6) \times 10^{-6}$ g·cm^{-2} = $(3.5) \times 10^{-6}$ g·cm^{-2} (56). The range after which a muon of initial energy E_μ has still a residual energy E_μ^{thr} at the detector can be quantified by the "effective muon range" represented in Figure 1.13-left as a function of the initial muon energy.

The multiple scattering experienced by the muon is an important issue to take into account. The deviation for muons can be quantified for a distance x as (57)

$$\theta_{ms} = \frac{13.6(MeV)}{E_\mu} \sqrt{\frac{x}{X_0}} [1 + 0.0038 \log(\frac{x}{X_0})] \quad , \qquad (1.15)$$

where X_0 is the radiation length of the media. For the typical energies considered in neutrino telescopes, $\theta_{ms} < \theta_{\nu-\mu}$ and the influence is minimal. There are other channels or signatures than can be detected in neutrino telescopes as

- *Electron-neutrinos* ν_e: high-energy ν_e leave almost the 0.8% of its energy into an electromagnetic shower which has been started by the leading final state electron. The remaining energy is released as fragments of the target giving a secondary shower. The size of the shower is of the order of metres in water or ice and it is not large enough compared to the distance between PMTs, therefore, to a good approximation it can be seen as a point-like source of Cherenkov photons radiated by the shower particles. These photons trigger the PMT at the single photo-electron (p.e.) level over a spherical volume whose radius scales linearly with the shower energy. The measurement of the radius of the sphere in the PMTs array let to compute its energy and makes possible to consider neutrino telescopes as total energy calorimeters. The direction can be reconstructed with an angular resolution of less than 10° only (58).

- *Tau-neutrinos* ν_τ: one of the interests of ν_τ detection is the fact that half of the ν_μ convert to ν_τ over cosmic distances. For ν_τ CC interactions the produced τ-lepton travels some distance before it decays and releases a second shower. The τ-lepton in fact has a short lifetime and for energy ranges of interest in neutrino astronomy, it only can travels some metres before the decay.

  In this way, if the track of the τ-lepton is long enough to distinguish between the primary interaction of the ν_τ and the decay of the τ, the expected

signature will be for: shower + track + shower, which is known as "double-bang event" (58). If the τ-decay starts or ends out of the detection array, the event will have one shower less than the double-bang event and it is known as "lollipop event" (58).

The processes described above are seen in Figure 1.13-right where the path length for other neutrino flavours for a water media is shown.
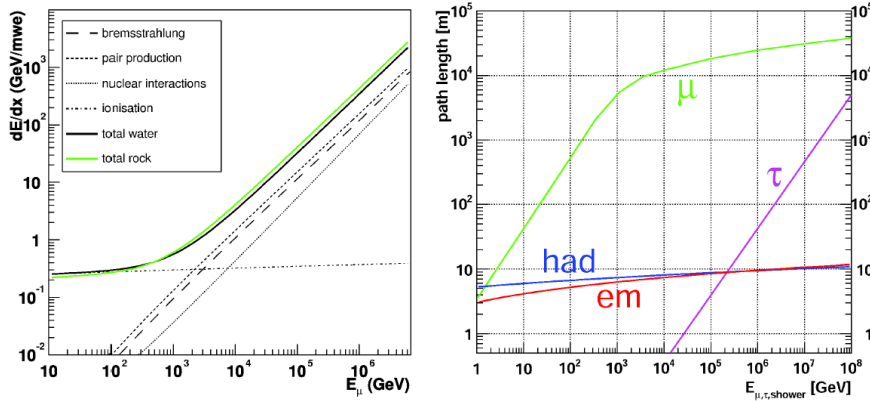
Figure 1.13: Energy loss and range of muons in water - Left: average energy loss per metre water equivalent for muons in water and rock. Right: range of muons or path length of particles by neutrino interactions in water.

Back to the NC interactions, is important to remark that this channel gives the same signature for all neutrino flavours. For the NC channel a fraction of the interaction energy is carried away unseen by the outgoing neutrino, what gives an increasing error on the reconstructed energy of the primary neutrino.

1.4.3   First generation neutrino telescopes

The exciting road of neutrino astronomy can be divided in two periods, the one when the viability of the technology was tested and the first hints of the physics arose, and that of the consolidation of km^3 infrastructures with the capability to cover several physics programs in particle, astroparticle and even Earth science studies. The first generation neutrino telescopes includes the pioneer DUMAND experiment, the precursor Baikal observatory, the large volume AMANDA and Mediterranean infrastructures. Such projects will be briefly described in this section, except the Mediterranean ANTARES telescope which will be broadly described in Chapter 2 as main subject of this thesis.

- **The DUMAND project**

  The Deep Underwater Muon And Neutrino Detector (DUMAND), which was located closed to Hawaii, USA, can be considered the origin of the neutrino telescopes concept. Around 1975 the consortium was created, the decision to begin deployment activities was taken and the commissioning of the project started. Several drawbacks due to financial policies and technical matters limited the original scheme of at least a 20k PMTs grid to a final configuration of 216 PMTs array. This was the concept of DUMAND-II (37) with eight strings at the corners of an octagon and one in the center, 100 metres of diameter and 230 metres of height. The pressure housing of the first string broke during its deployment in 1993 and the communication to shore was cut. The most relevant advance was to obtain with a 7-PMT test string, the muon intensity as a function of the depth for only a few hours from a ship. The project was cancelled in 1995 due to the lack of funding.

- **The Baikal telescope**

  The Lake Baikal in Siberia, Russia, houses the first operative neutrino telescope, "the Baikal telescope", located at 3.6 km from the shore at a depth of around 1.1 km (37). Baikal reported the first atmospheric neutrino flux detected underwater.

  The core of the detection scheme called NT200, was a grid of 192 optical modules (OMs) arranged in eight vertical strings anchored to the lake floor with height around 72 m. The OMs consisted in glass spheres housing QUASAR-370 PMTs grouped in pair-wise along the strings. The basic detection unit comprises the pair of OMs plus an electronics module for time and amplitude conversion and slow control.

  The deployment campaign was carried out in six weeks between February and April 1998 when the lake is often covered by a thick ice layer used as an stability scaffolding. The connection to shore was done by means of long copper cables. The data stream from all channels was handled at the bottom of the NT200 array by a special electronics module less than 100 m away from the optical modules allowing the synchronization at nanosecond level over transmission copper cable. The distance between OMs ($\sim$ 6.5

m) in Baikal leads to a comparable low energy threshold of around 15 GeV for muon detection, the distance between lines was around 100 m. Up to 400 up-going muon events were collected for a period of 5 years of data taking. An angular resolution between $3°$-$4°$ for Baikal neutrino telescope was estimated (37).

- **The AMANDA telescope**

  The Antarctic Muon And Neutrino Detection Array (AMANDA), was the first neutrino telescope deployed totally under ice, few hundred metres away from the Amundsen-Scott station in the South Pole. The strings deployment was performed by introducing several detection lines equipped with OMs into holes of 60 cm diameter drilled with pressurized hot water, with a careful strategy for cooling the melted water inside the holes. The deployment campaign was mostly during November to February in the early 90's and later on maintenance activities.

  The shallow grid AMANDA-A was installed in the early phase of the experiment between 800 and 1000 m as a prototype. The AMANDA-B10 (10-strings) array was deployed deeper between 1500 and 2000 m (37). The detector was finally commissioned in February 1997 and extended to 9 detection strings more in January 2000, for a total 19 strings of OMs in the final array AMANDA-II. The total diameters for the detection array from AMANDA-A, AMANDA-B10 to AMANDA-II were 60, 120 and 200 m respectively of instrumented volume. The digitization of the signals were not performed *in-situ*, since the reduced distance ($\sim$ 2 km) between the electronics top array and the OMs allowed the subsequent data processing and digitization. Nonetheless, it required a large output signal of the PMT as the Hamamatsu R5912-2 8-inches (14 dynodes, 10^9 of gain) used by AMANDA.

  Concerning physics performance, AMANDA achieved an angular resolution for muon tracks of $2°$-$2.5°$ with a lower energy threshold of 50 GeV. For cascades a value close to $25°$ (37) was obtained.

- **The Mediterranean neutrino telescopes**

  - NEMO:
    The NEutrino Mediterranean Observatory (NEMO) located at 3.5 km

of depth and 100 km off the Capo Passero at the southern-eastern coast of Sicily (Italy), has made significant advances on alternative technology for deep-sea neutrino astronomy. The innovative concept in NEMO concerning other experiments is the detection strings based on "flexible towers" with horizontal bars of ~ 15 m long linked by ropes in a tetrahedral structure in such a way that the consecutive bars are placed orthogonal to each other. An electro-optical cable connects the shore station with the detector site. Several advantages can justify this detection scheme. First at all, detection towers can be folded together and deployed to the seabed as a dead weight being later on unfurled. Secondly, mechanical tension is carried out by the ropes and not by the electro-optical backbone cable. Third, the 3D array of PMTs per detection tower favours the local reconstruction of muon directions. One of the main NEMO results is the estimation of the atmospheric muon flux in agreement with the expected results from the simulation (37).

The construction of NEMO was split in two stages. The NEMO phase-1 allowed to install the electro-optical cable for connection to the shore station and it operated for several years. Some time after, a mini-tower with four bars was deployed, connected and it was operative only few weeks due to technical problems, but showing reliability of their components for deep-sea neutrino technology. For the NEMO phase-2 a mechanical test tower (600 m of height) of reduced size was successfully deployed and unfurled (late March 2013), and it is taking data since April 2013 (59). The main design includes 8 floors (8 m in length, 40 m vertical distance) equipped with 32 OMs (4 per floor) and 16 hydrophones (2 per storey) plus LED and laser as calibration sensors and the full communication protocol

– <u>NESTOR:</u>

The Neutrino Extended Submarine Telescope with Oceanographic Research (NESTOR) is located on the sea floor off the Pylos Coast in Greece. Around March 2003 a test floor of a detection tower scheme (12 m diameter) was deployed at the site equipped with twelve OMs, electronics and environmental sensors. The basic detection unit in

NESTOR is an hexagonal floor or star of six arms made of titanium tubes to form lightweight array with two OMs (15'' diameter PMT) attached to the ends of the arms looking upwards and downwards (60). The electronics of the floor (control and trigger) is contained into a titanium sphere (1 m diameter) within a central wrapper. The atmospheric muon flux estimations were in agreement to the Monte Carlo predictions (60). The NESTOR project has been focused to the site characteristics as optical properties studies (60).

1.4.4   Second generation of neutrino telescopes

The ongoing neutrino telescope projects aim for an extension of the physics potential of the precursors described in the last section. In addition, they are strategically placed along the Earth hemispheres in order to form a global neutrino observatory covering the whole sky. The ongoing observatories in the Mediterranean Sea, the Lake Baikal and the South Pole are briefly described.

- **The KM3NeT project**

  The KM^3 Neutrino Telescope (KM3NeT) collaboration formed by the Mediterranean telescopes ANTARES, NEMO and NESTOR have joint efforts (hardware, software, simulations, etc.) and operative experience to set the deep-sea technology and physics potential to observe large fluxes of astrophysical high-energy neutrino sources. In addition, it will be also a deep-sea research infrastructure for Earth sciences.

  The Detection Units (DU) in KM3NeT will be strings mainly composed by 18 storeys with one OM each spaced 30-36 m and 100 m of distance between the anchor and the first storey (61). Around 115-120 DU are expected to be installed. The Digital Optical Module (DOM) will be a 17-inch high pressure resistant sphere equipped with 31 3-inch PMTs, high-voltage bases and the digitization electronics. The PMTs inside the DOM will be looking from vertically downwards to about 45° upwards and supported by a foam structure fixed to the glass sphere by a special optical gel. The most relevant improvements comparing with ANTARES, NEMO and NESTOR technologies include:

– the overall photocathode area of the 31 PMTs is three times higher than the one for a 10-inch PMT. An additional increase is possible by using reflective rings being possible to extend the light collection (37),

– the number of container electronics, penetrators and other equipment is hugely reduced,

– the PMTs readout is performed individually, then, an improved p.e. resolution is achieved,

– Some directional sensitivity is provided.

KM3NeT will have around 600 DUs and its geometrical layout is still under optimization studies. Two electro-optical cables to shore are expected to be installed with their corresponding junction boxes (one primary and a set of secondary ones). Other option to take into account is the possibility to have a cable ring surrounding the detector with several primary junction boxes connected directly to the DUs. The installation of the first DU is expected in 2014 and the data taking will start since the installation of the first line will be operational. Recent progress was the installation of a fully equipped DOM with 31 PMTs, acoustic positioning sensors and a LED. It was mounted in the ANTARES instrumentation line, re-connected around April 2013 (61).

- **The IceCube telescope**

The IceCube neutrino telescope was conceived under the operative and physics experience of AMANDA. It consists of 5160 DOMs deployed at the South Pole with 86 strings at depths between 1450 and 2450 m. AMANDA itself is embedded into the IceCube detection array. IceCube also uses a top array called IceTop where there are 320 additional DOMs, ordered in an array of detection stations above the deeper strings array.

At the beginnings, AMANDA was running as a sub-array of IceCube as a low-threshold array but it was replaced by a high-density sub-array of six strings called "DeepCore". By using this particular configuration, a low threshold of 10 GeV can be achieved, important for neutrino oscillation and indirect Dark Matter studies.

Each IceCube string has 60 DOMs with 30 copper pair of cables for power

and communication duties, and the neighbour DOMs shared the same pair which allows a fast local coincidence triggering on ice.

The DOM is a 13-inch spherical glass frame housing a 10-inch Hamamatsu R7081-02 PMT (10^7 of gain) equipped with a μ-metal cage as shield from Earth's magnetic field. A system of LEDs is used for calibration using pulses at 405 nm with a variable intensity up to 10^{11} photons. All the DOMs are equipped with quartz oscillators for local clock signals stamps, synchronized every few seconds to a central GPS clock, reaching a resolution close to 2 ns ([37]).

Concerning to detector performance, the angular resolution reached by the IceCube reconstruction software is about $1°$ for $E > 1$ TeV muons. If the full waveform is used, the angular resolution could be improved up to $0.5°$ for $E > 10$ TeV. For cascades at large ice depths, an angular resolution between $10°$-$30°$ is only reached being worst that the one reached for water-based neutrino detection techniques mainly due to the short scattering length in ice.

Around April 2012 the IceCube collaboration reported the discovery of two > 1 PeV (ever seen in man-made accelerators) neutrino cascades in two years of data of the IC79+IC86 configuration. An extended search to lower energies for the same data set gave evidence of 26 additional events (data collected until May 2013) with energies above 30 TeV ([62]). The total data collected to study the 28 events spans about two years, from May 2010 - May 2012. The results of this analysis about the evidence of high-energy astrophysical neutrinos from cosmic accelerators, constitutes the first high-energy neutrino flux ever observed, with a high statistically significant signal ($>4\sigma$) ([29]). These 28 events have flavours, directions, and energies clearly inconsistent with what is expected for atmospheric muon and neutrino backgrounds. Nowadays, the improve of the significance is an ongoing work, as well, as the understanding what this signal means and where it comes from.

- **The GVD telescope**

  The Gigaton Volume Detector (GVD) pretends to be the abidance of the Baikal telescope neutrino physics program. The detection units will be 27 clusters of 8-strings detection modules. The GVD clusters have a flexible structure and makes easy the deployment and recovery activities. Each

string consists of 4 sections with 48 OMs uniformly spaced at a depth between 600 to 1300 m. The modules will house a 10-inch Hamamatsu R7081-HQE PMTs with a peak quantum efficiency $\sim$35%. A time accuracy of 2 ns has been reached by activities carried out by prototype strings in previous campaigns between 2009-2010 (37).

By means of a dedicated Monte Carlo simulation for a specific GVD design (96 strings, 12 clusters and 2304 OMs) a compromise between large volumes for cascade detection and reasonable efficiency for muons was found for a instrumented height of 345 m, cluster diameter of 120 m and vertical distance between optical modules of 15 m. The effective area for muons was also estimated at trigger level for $E > 1$ TeV as 0.3-1.8 km^2, and for cascades above 10 TeV as 0.4-2.4 km^2 (63). The angular resolution for muons and cascades has been recently estimated as 0.25$°$ for muons and 3.5 to 5.5$°$ for cascades (63). Ongoing activities on GVD includes a 3 full-scale strings of 72 OMs with its corresponding electronics, taking data since April 2013, what comprises $\sim$ 106 m^3 of instrumented volume.

1.4.5   Detector performance: angular resolution and effective area

The capability to resolve neutrino point-sources depends on the effective area and on the angular resolution of the detector. These main concepts are studied in this thesis as a function of the detection media description, and described in this section focused to the current knowledge on the ANTARES neutrino telescope (fully described in Chapter 2) performance.

For a neutrino flux dN_ν/dE_ν the number of neutrino events that can be seen by the detector is just computed from its integral as (64)

$$N_\nu = V \int_{\Delta T} dt \int_{E'}^{+\infty} dE_\nu A_{eff}^\nu \frac{dN_\nu}{dE_\nu} \quad , \qquad (1.16)$$

where $V, \Delta T, A_{eff}^\nu$ represents the visibility (fraction of one sideral day when a source is in the field of view of the telescope), the data taking period (or lifetime) and the detection effective area respectively.

The angular resolution is defined as the median value of the distribution of the

difference in absolute value between the reconstructed direction (θ_{rec}) and the true MC direction (θ_{true}) of the track:

$$\alpha = |\theta_{rec} - \theta_{true}| \quad .\qquad\qquad (1.17)$$

This magnitude can only be estimated by Monte Carlo simulation. The angular resolution for data collected during 2007-2010 period can be seen in Figure 1.14-left. From its cumulative distribution is it possible to conclude that more than the 80% of the signal events can be reconstructed with an angular error better than 1° (35). The median value of the distribution is 0.46±0.10° by considering a E^{-2} neutrino flux. The associated systematic uncertainty on angular resolution has been estimated varying the hit time resolution which is a function of the PMT transit time spread, mis-calibrations of the timing system and possible spatial misalignments of the detector (35).
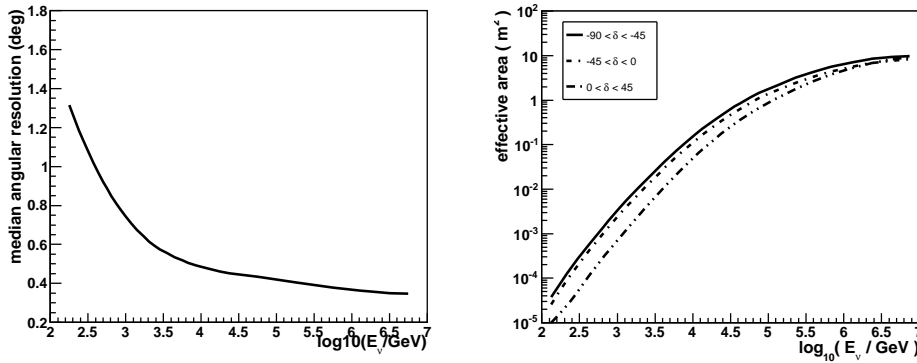
Figure 1.14: Angular resolution and effective area estimated for ANTARES for 2007-2010 data - Left: median angle of the angular resolution as a function of the neutrino energy E_ν. Right: neutrino effective area as a function of the neutrino energy E_ν. Some cuts on the quality parameter of the track and the associated angular error have been applied.

On the other hand, the effective area is defined as the equivalent surface perpendicular to the incident particle beam which is 100% efficient and detects the same number of particles (neutrinos or muons) than the detector. It depends on the energy and the direction of the incident neutrino. It can also be defined as the ratio of the rate of selected events to the total incident neutrino flux detected at the Earth ($A^\nu_{eff}(E, \nu) = R^\nu_{det}(E_\nu)/J_\nu(E_\nu)$). The cosmic neutrino flux is assumed

to be equal both for neutrinos and anti-neutrinos. The effective area is calculated as (64)

$$A_{eff}^{\nu, \Delta E} = \sum_{i=1}^{n_{\Delta E}} \frac{w2_i}{N \cdot I_\theta \cdot I_E \cdot E_i^\Gamma \cdot t} \cdot \frac{1}{F_{\Delta E}} \quad , \tag{1.18}$$

where

$$I_E = \int_{E_{min}}^{E_{max}} E^{-\Gamma} dE = \frac{E_{max}^{1-\Gamma} - E_{min}^{1-\Gamma}}{1 - \Gamma} \quad , \tag{1.19}$$

represents the energy phase space factor and

$$F_{\Delta E} = \frac{1}{I_E} \int_{\Delta E} E^{-\Gamma} dE \quad , \tag{1.20}$$

the fraction of simulated events in a energy interval ΔE. The remaining factors represent

- $w2_i \Rightarrow w3_i / (d\Phi/dE) [GeV \cdot m^2 \cdot sr \cdot s \cdot yr^{-1}]$. Where $w3_i [yr^{-1}]$ is the weight of the event i per one year and $d\Phi/dE$ is the signal neutrino differential flux in $[GeV^{-1} \cdot m^{-2} \cdot sr^{-1} \cdot s^{-1} \cdot yr^{-1}]$ (65),

- N is the total number of simulated events,

- Γ is the generated energy spectrum index,

- t corresponds to the time window of the simulation,

- I_θ relates to the angular phase space factor,

- $n_{\Delta E}$ gives the number of reconstructed events in ΔE (the true neutrino energy bin) which pass the quality cuts.

The Figure 1.14-right shows the neutrino effective area for three different declination angles (35). The impact of the water optical properties in these main detector performance parameters as well as the main reconstruction track parameters will be part of the work of this thesis and it will be treated in detail in Chapter 5 (complementary studies on optical properties with reconstructed track).

Chapter 2

The ANTARES neutrino telescope

Tell me and I forget. Teach me and I remember. Involve me and I learn

Benjamin Franklin

ANTARES (Astronomy with a Neutrino Telescope and Abyss environmental RE-Search) is a large-area water-Cherenkov neutrino detector and actually the largest neutrino telescope in the Northern Hemisphere. Located at 2.5 km of depth into the Mediterranean Sea at 40 km off the Toulon coast in France (42° 48'N 6° 10'E) it consists of a 3D array of 885 PMTs arranged in 12 detection lines, able to detect the Cherenkov light induced by up-going relativistic leptons produced in the interaction of high-energy cosmic neutrinos with the detector surroundings.

The 40-km ANTARES Main Electro Optical Cable (MEOC) connecting the shore station and the detector was succesfully deployed in October 2001 off "Les Sablettes" beach in La Seyne-Sur-Mer near Toulon, France and the data transmission started in December 2002. The official inauguration of the ANTARES shore station took place in November 2003. A special Mini Instrumentation Line equipped with Optical Modules (MILOM) was installed in March 2005 at the ANTARES site, with the aim of testing the set of OMs, front-end electronics and read-out and calibration systems to be definitively used in the final ANTARES detection lines. The installation of the first detection line equipped with the corresponding instrumentation for positioning, monitoring and calibration took place in February 2006 (66). The measurements carried out with the first line included the measurement of the atmospheric muon flux (66), the muon angular distributions and the depth

profile of the muon intensity. The installation of the rest of the lines was carried out from March 2006 until May 2008, and the first neutrinos were detected in 2007. In June 2008 a power distribution failure of the detector took place due to a problem in the MEOC, 25 km away from the shore. The damaged part of the cable was replaced successfully and ANTARES restarted data taking in September 2008. Nowadays, the final octagonal sketch of the position of the detection lines in the seabed is depicted in Figure 2.1.
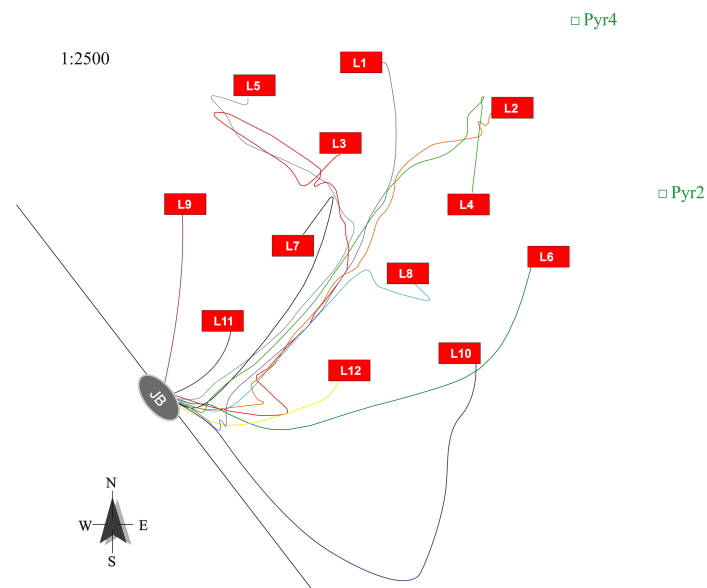
Figure 2.1: Detector layout at the seabed - The colour lines indicate the position of the interlink cables between the bottom of the lines and where they converge. Acoustic pyramids (Pyr) are located surrounding the lines and used for positioning.

Currently, more than 7000 up-going tracks have been well reconstructed and selected for dedicated physics analysis. This chapter will cover several aspects related to the design of the OMs and the detection lines as well as the architecture of the data acquisition, readout systems and its performance. Forthcoming the impact on the ANTARES calibration systems it will be showed and how these results allow ANTARES an angular resolution of a few tenths of degree.

2.1 Detector architecture. Main elements

The ANTARES detection lines comprise 25 storeys per line where OMs are coupled in triplets (looking downwards at $45°$), the lines are anchored to the seabed by the

Bottom String Socket (BSS). The OM is a high-pressure resistant glass sphere housing a 10" Hamamatsu PMT (14 dynodes). Consecutive storeys are separated by 14.5 m and the average distance between adjacent lines is 60 m. Every storey is equipped with a triplet of PMTs for light collection, the electronics container called the Local Control Module (LCM) and in some of them, a set of light/sound devices for calibration. A typical ANTARES storey is represented in Figure 2.2.
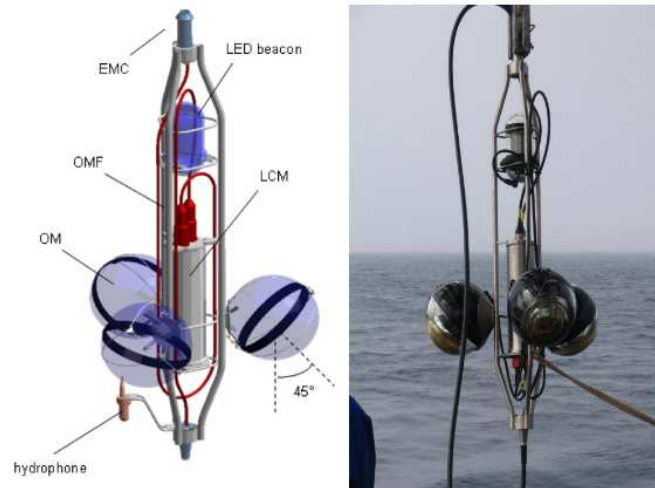
Figure 2.2: An ANTARES storey - Left: a schematic view with its main components. Right: a picture of one storey. Optical beacons (4 per line) are installed along the lines for time calibration and measurements of water optical properties.

At the bottom of each line is installed the String Control Module (SCM), which collects the data stream from the line and send them to shore by means of the MEOC connected to the Junction Box (JB) where the detector lines converge. Every five storeys, a Master Local Control Module (MLCM) with some special and extra devices is installed instead of the conventional LCM. A basic scheme of the ANTARES neutrino telescope is depicted in Figure 2.3.

The detector is supplied with 4400 V of AC at 10 A through the MEOC from the power hut on-shore. This current reaches a transformer in the JB where it is distributed to the lines. The String Power Module (SPM) at the bottom of each line provides every five storeys with up to 400 V of DC (67). The MLCM and the LCMs of the sector are fed in parallel, the Local Power Box (LPB) in the LCM distributes low power voltages to the electronics boards.

The ANTARES components undergo challenging environmental conditions: a
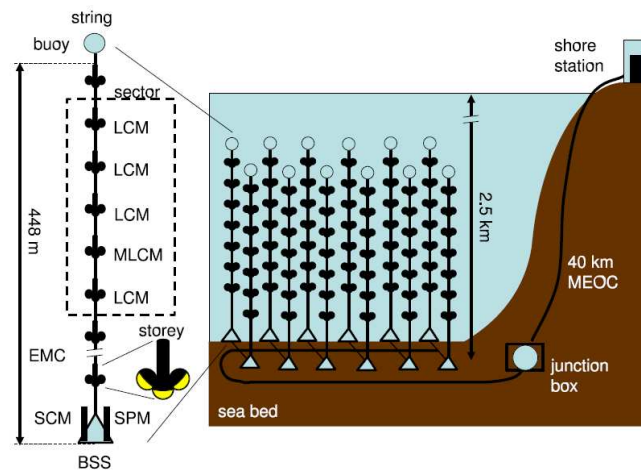
Figure 2.3: ANTARES detector at the Mediterranean Sea - Scheme of the detector and data transport between off-shore and on-shore.

pressure between 200 and 260 bars and high corrosion due to sea water (a conductivity of 46 mS cm^{-1}). To endure these severe conditions and ensure a lifetime of at least 10 years, materials with known resistance to corrosion were selected: glass, titanium alloys, anode protected carbon steel, polyethylene, polyurethane, aramid and glass-epoxy (67).

A detailed description of the OMs and the particular devices forming the detection lines is presented below.

2.1.1 The Optical Module

The ANTARES OM contains a large area hemispherical PMT glued to a high pressure-resistant glass sphere with optical gel, a μ-metal cage used as Earth's magnetic field shield, the OM electronics, the PMT high-voltage power supply and the LED system for internal monitoring. A schematic view of the ANTARES OM and its main components are depicted in Figure 2.4.

The final choice for the ANTARES PMTs was a large photo-cathode area ($\sim$ 500 cm^2) PMT (Hamamatsu R7081-20), with quantum efficiency > 20%, collection efficiency > 80% and Transit Time Spread (TTS) (fluctuation in the p.e. pulse Transit Time (TT)) < 3 ns. The dark count rate should be < 10 kHz for a threshold of 0.3 p.e. (68). Figure 2.5 shows the main parameters for the optical design of the OM.
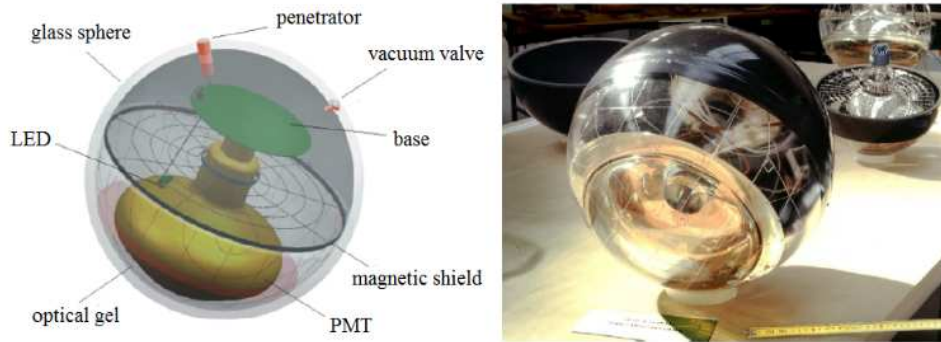
Figure 2.4: The ANTARES OM - Left: schematic view and main components of the OM. Right: the large photo-catode PMT in the complete OM mounting.
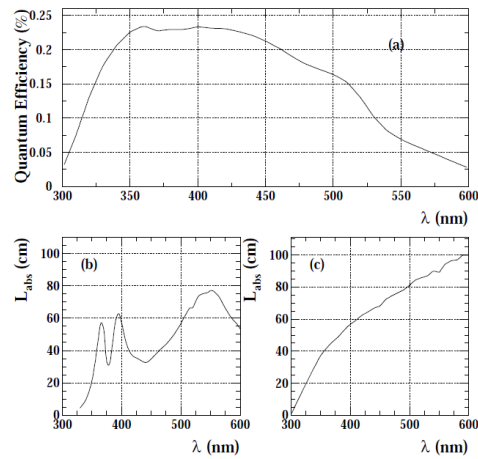
Figure 2.5: Optical properties of the OM - a) Combined quantum and collection efficiency of the PMT, b) Absorption length of the glass sphere and c) Absorption length of the coupling gel.

A good peak-to-valley ratio of the PMT is necessary to isolate the single p.e peak from the pedestal. A value $P/V \approx 2$ was required and achieved in the ANTARES PMTs.

The glass sphere (69) is the PMT envelope which ensures a good light transmission between 400 and 500 nm. The glass sphere features are shown in Table 2.1.

Paramater	Equivalence
Material	Vitrobex 8330 (low-activity borosilicate glass)
Outer diameter	432 mm
Thickness	15 mm (minimum)
Refractive index	1.47 ($300 < \lambda$ [nm] < 600)
Transmission	$> 95\%$ above 350 nm
Depth rating	6.7 km

Table 2.1: Main design features of the optical module glass sphere.

Earth's magnetic field can deviate the electron trajectory in the PMT and degrade the TTS and the peak-to-valley ratio (68). A shield against Earth's magnetic field effects consisting on a semi-spherical grid layout made of wires of high magnetic permeability μ-metal was installed in the OM surrounding the bulb of the PMT. The optical silicon gel is an optical coupling between the glass sphere and the PMT. It is used for two purposes: as optical link between the glass-sphere and the PMT, and as a mechanical position fixer of the different elements inside the OM (67).

The task of the internal LED system inside the OM is the monitoring of the TT of the PMT. It is a fast blue LED (470 nm at peak) located in the rear part of the bulb which flashes the pole of the photo-cathode along an aluminium coating used as a filter of large optical density (≈ 5). The system is completed with an external driven pulser circuit (68). The communication between the OM and the LCM is performed by a "penetrator", which is a Ti socket with polyurethane over moulding (67).

2.1.2 Detector lines

The LCM is a titanium container which houses all the readout electronics of the storey and consisting in a hollow cylinder (179 mm outer diameter, 600 mm long and 22 mm of wall-thickness) and two end-caps (30 mm of thickness) (67). The top end-cap houses the two penetrators in the storey connected in turn to the

upper and lower adjacent storeys. The bottom end cap allows the link between the LCM itself and the three OMs of the storey by means of three connectors. There is another additional connector used for additional equipment in the storey. The LCM crate houses circular-shaped electronics boards plugged into a backplane which distributes the signals and the DC power. If the storey is equipped with acoustic instrumentation, there are three additional electronics boards installed for signal pre-amplification, CPU duties, and for independent signal processing. The common devices installed in the LCMs are:

- *The Local Power Box (LPB).* The LPB distributes the power voltages to the electronic boards of the storeys, as commented before.

- *The clock board (CLOCK).* A clock reference signal is sent from the shore to each LCM. In this process the CLOCK card receives the clock signal from the lower LCM and send it to the upper LCM of the sector.

- *The compass motherboard (COMPASS).* The heading, pitch and roll of each LCM is governed by means of a TCM2 electronic compass sensor installed on a COMPASS motherboard. The TCM2 combines a three-axis magnetometer and a high-performance two-axis tilt sensor.

- *The DAQ/Slow-Control board.* The DAQ/SC card hosts the local processor and memory. Its duties are related to the data handling of the main front-end electronics motherboard in ANTARES (ARS chip) and those concerning the slow-control respectively.

The MLCM is equipped with extra devices for signal multiplexing, communication and electrical-optical conversion by means of a Dense Wavelength Division Multiplexing (DWDM) and a BIDICON (BI-DIrectional CONversion) motherboard respectively (67). An Ethernet SWITCH connects the processor of the MLCM-BIDICON card via the backplane. These devices play an importat role in the data stream handling coming from each independent LCM which form the sector.
The BSS acts as an anchor at the seabed for the line structure and is strategically designed to make possible its recovery.
The SCM is installed at the bottom of each line. The SCM collects the data stream from the line and sends it to shore by means of the MEOC connected to the JB (67). The SCM/SPM electronics container is embedded into the BSS in

two independent cylindrical-shaped crates vertically fixed. The SCM container is also equipped with devices common to the LCM, such as COMPASS, CLOCK and DAQ cards.

The JB is a high-pressure resistant container (1 m diameter) whose main function is the interlink (16 sockets) between the detection lines through the SCM and the MEOC for communications to the shore. It also acts as a power transforming housing, as a line over-current protection and as a remote diagnostic system. The JB internal pressure is around 1 bar, and the external water pressure close to 250 bar. The lower hemisphere contains a transformer immersed in oil and the upper hemisphere the power system slow control electronics (67).

The MEOC provides the optical data and electrical power link between the shore station and the JB (67). The special structure of the MEOC is based on 48 monomode optical fibres in a stainless steel tube covered by a "pressure vault" of two windings of steel armour wires. The overall weight of the whole cable has been estimated $\sim$ 88 tons with a total length of 41.3 km. The total electrical power transmitted by the MEOC goes from 400 AC V at 50 Hz in the detector shore power supply to the 3700-4100 V converted in the local power hut where the MEOC-detector link starts.

2.2   The background at the detector site

Two kinds of background are present in an underwater neutrino telescope as ANTARES: one comes from the optical activity from the detector environment and the other is the result of physical processes at the atmosphere releasing muons and neutrinos. These two kinds of sources are described in this section.

2.2.1   Optical background

The optical background light at the ANTARES site comes mainly from two different sources: the bioluminescence emission by some micro and macro-organisms and the two modes of radioactive decay of ^{40}K. The bioluminescence emission has two components, one is a continuous baseline and the other one is a random component of spontaneous emission. The random component is responsible for the sudden increase of background counting rates registered in ANTARES up to 1 MHz, non-constant in time. This light is produced by a chemical reaction into

the organisms ([70]), mainly in the blue region but also emission shifted towards the green in some sea creatures and into red in some fishes.

On the other hand, the sea water contains about 4.5×10^{-5} g/L of potassium in ^{40}K radioactive isotopes with activity above 14 kBq/m^3, which emits β and γ particles when it decays through β-decay and e-capture respectively

$$^{40}K \to {}^{40}Ca + e^- + \nu_e^- \quad (89.3\%) \qquad ^{40}K \to {}^{40}Ar^* + \nu_e \to {}^{40}Ar + \gamma \quad (10.7\%) \quad . \tag{2.1}$$
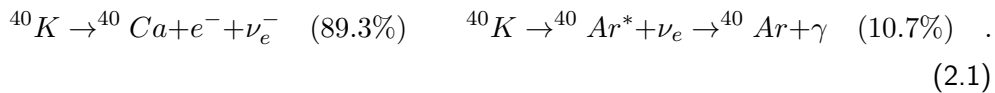
The β-decay releases a free electron with energy ~ 1.3 MeV, enough to produce Cherenkov light (above 100 photons), the Cherenkov threshold at the ANTARES site is about 0.25 MeV ([71]). By e-capture it is possible to produce photons with an energy of about 1.46 MeV. Compton electrons produced by γ-ray scattering can release Cherenkov light. The ^{40}K contributes to the continuous optical background component on the ANTARES PMTs as part of the baseline commented for the biological activity. The continuous baseline is typically estimated close to 60 kHz for the ANTARES photo-cathode diameter. The Figure 2.6 shows all the optical background activity for above 3 years of constant monitoring in the ANTARES site.
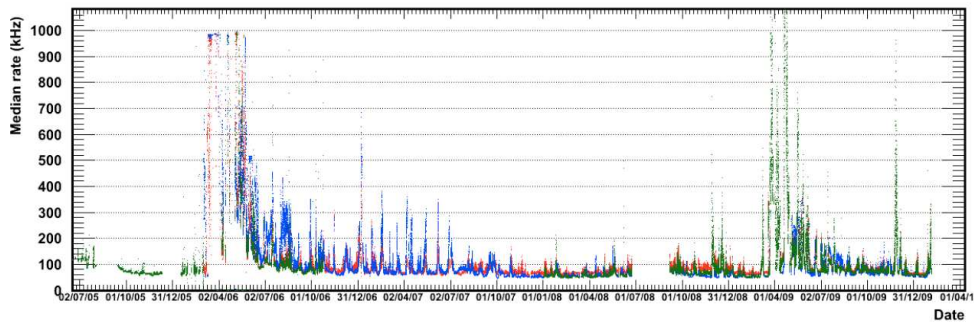
Figure 2.6: Optical background registered as a function of time - Median PMT counting rate. Green indicates measurements by the earlier MILOM and IL07 (Since December 2007, currently inactive) lines, red for L1F1, blue for L1F25.

As seen in Figure 2.6, several periods of high and low optical background can be observed. There is not a clear season when the mean rates in the detector trend to be constant. Nonetheless, as operative experience, the data taking is favoured for seasons different to spring and beginning of summer when apparently such rates increases. The number of triggers and type in ANTARES are switched on

depending of the level of optical background reported in averaged measurements at top, middle and bottom sections of the detector.

2.2.2 Physical background

There are two kinds of physical background reaching the detector: a "reducible background" coming from atmospheric muons and the "irreducible background" of atmospheric neutrinos. Atmospheric muons are produced by the high-energy CRs striking the nucleons at Earth's atmosphere. Figure 2.7 shows such contribution as a function of their zenith arrival direction.
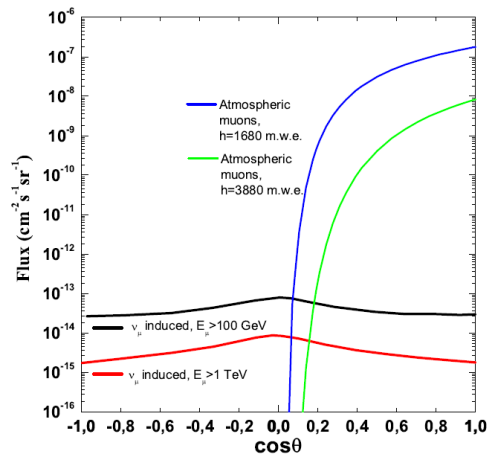
Figure 2.7: Zenith angle distribution for atmospheric muons - Muons at two different depths and atmospheric neutrino-induced muons at two different energy thresholds are compared.

High-energy muons can cross the whole atmosphere, going through the detection media of the detector and produce a track throughout the detector. A muon created by an atmospheric neutrino can not be distinguished from a muon created by a cosmic neutrino. The flux of down-going atmospheric muons is several orders of magnitude higher than the atmospheric neutrino signal (see Figure 2.7). The atmospheric muon background is highly reduced in two ways: first by the deployment of the detector at large depths and second locating the PMTs looking downwards $45°$ favouring the efficiency for up-going tracks collected in the detector. In addition, this background can be rejected by means of a proper reconstruction of the track direction and quality cuts when physics analysis are done. It consists in restricting the search for signal solely for up-going events, taking into account

that up-going muons are only possible be produced by interaction of up-going neutrinos. Sometimes, mis-reconstructed down-going muons (in particular muons bundles, parallel muons produced in the same cascade) can lead to an up-going track reconstruction, therefore a cut based on the quality of the reconstruction is used to purify the data sample. On the other hand, at large energies, the cosmic neutrino diffuse flux may dominates over the atmospheric neutrino background and they can be identified by their harder and softer energy spectrum respectively. For cosmic neutrino point-like sources the background can only be discriminated by looking for clustering of events at a given direction in the sky. The peak at the horizon in Figure 2.7 for neutrinos is the result of the "secant theta effect", what is an excess of neutrinos due to that pions and kaons generated skimming the Earth have more flight time in low dense atmospheres, in such a way that the probability to decay and produce neutrinos increases.

2.3 Data acquisition and readout

The Analogue Ring Samplers (ARSs) motherboards (housed into the LCM) are the heart of the signal digitization process of the analogue PMTs signals from the OMs. The performance of this device, its acquisition protocol, as well as the time-stamp, charge measurement and triggering of the signal are commented in this section.

2.3.1 Front-end electronics

The signals of each PMT (time and charge) are digitized *in-situ* by two ARSs working in a token ring configuration in order to decrease the electronics dead-time. If the storey contains an optical beacon for timing calibration, an additional ARS is installed to digitize the signals sent by the internal PMT inside the device. The ARS has two modes of operation: single photo-electron (SPE) signals and multi-form waveform (WF) signals. An analogue Pulse Shape Discriminator (PSD) performs the selection (72). The SPE signals are compatible signals in time width and amplitude with the single p.e. profile. Figure 2.8 shows the working principle of the PSD.

In the SPE mode the digitization of the signal is carried out when the electrical signal exceeds a low threshold of 1/3 of the SPE average amplitude (L0 level ~ 0.3
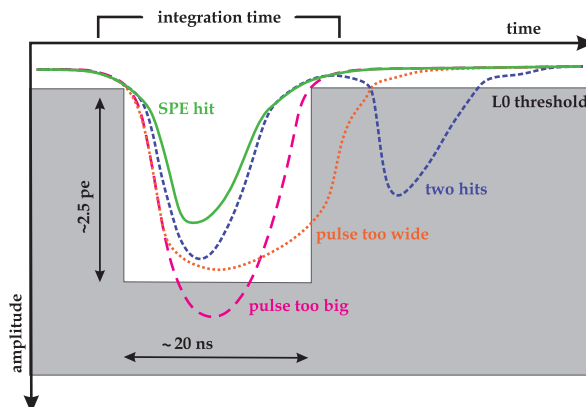
Figure 2.8: PSD principle - Three different criteria are represented: time width, pulse height and multiple hit during integration. Signals fulfilling the SPE pattern are selected.

p.e.). If the SPE profile matches, the signal is time-stamped (TS) with a master clock signal and the TVC and integrated by the AVC in a 35 ns time window (72). In the WF mode the PMT signal is sampled by means of a set of 128 switched capacitors running between 0.15 and 1 GHz, 128 times every 1.6 ns. This mode is mainly used for calibration and detector tuning purposes. Its good resolution lets to distinguish between two consecutive pulses (72), however, due to the amount of data collected in WF mode, only SPE signals are currently recorded for physics analysis in ANTARES.

The time information is recorded by the TVC (an 8-bits Time-to-Voltage Converter) where a ramp generator furnishes a voltage proportional to the time within two subsequent clock pulses ($\sim$ 50 ns). When the signal reaches the L0 level, the ramp voltage is frozen and recorded with its TVC value. Since the fallback to the base voltage is not immediate, a flip-flop scheme based on two TVC ramps is used (72).

To minimize charge losses, the charge measurement by the AVC (an 8-bits Amplitude-to-Voltage Converter) is done in several steps by means of three switched capacitors: integration (signal from the anode is integrated), memorization (integrated charge is recorded in the pipeline memory) and charge erasing (pipeline memory is reset) (72). Such phases are carried out in a cycle of period between 8–30 ns. Once the L0 level is reached, the time integration is increased in order to cover all the signal pulse shape (between 17–50 ns). The integrated charge is the result of the addition of the collected charge in the two capacitors of the integration and

memorization phases. After integration, the charge is digitized by the AVC and the PSD returns a binary result if the pulse is SPE or WF type, afterwards, the data is stored with their corresponding AVC-TVC, TS-PSD respectively.

2.3.2 Data handling and triggering

The data is digitized *in-situ* and its transmission to shore is based on the "all-data-to-shore" concept. The all-data-to-shore scheme implies that all signals exceeding the L0 level are digitized, sent to shore (700 Mb/s per line) and processed in real time by a farm of PCs. Due to the large amount of data, several levels of multiplexing are required. The first level is carried out in the LCM of each storey, where the FPGA (Field Programmable Gate Array) and the microprocessor in the DAQ card outputs the digitized data of the three OMs. In the second level, the MLCM of a sector gathers the data from the local OMs and from the other four connected storeys by means of the Ethernet SWITCH and sends the data stream to the third multiplexing level through the DWDM, which is performed at the bottom of the line at the SCM. Here, multiplexers and de-multiplexers pack the data of the line and send it to shore via the MEOC connected to the JB. The last level is the de-multiplexing in the shore station where the data are processed and filtered by a PC farm and sent by optical fibre to the computer centre to be stored and made available for analysis (72). An on-line trigger selects events according to the physics under study (muon events, OB events, etc.) The different multiplexing/de-multiplexing stages are depicted in Figure 2.9.

The digitized data processed by the OMs are packed as arrays of hits of predefined time frame duration, typically of 100 ms and a size between 60 to 200 kB, being recorded in a 64 MB SDRAM. Aftwerwards, the total data collected in the detector are sent in packages to a single data filter process in the on-shore data processing system. This collection of time frames in the same time window are called "time slices". The maximum manageable photon detection hit rate by the DAQ is 300 kHz per PMT.

The standard data trigger aims for a hit selection due to Cherenkov photons by rejecting the optical background or Cherenkov scattered hits. It is based on the arrival time of the hits, the distance between PMTs and the speed of light. Two
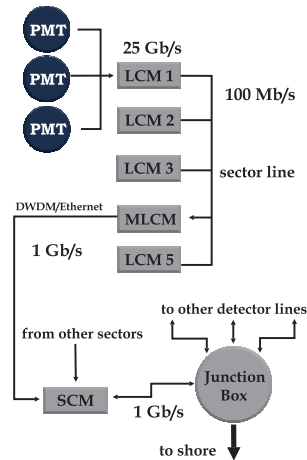
Figure 2.9: DAQ system - Multiplexing levels in each detector element in the OM to the shore station path. Three levels are performed at LCM (first), MLCM (second) and the shore station (third).

hits in any location in the detector are causally related if their time and position follows the causality relation

$$| \Delta t | \leq \frac{n_g}{c} d \quad , \tag{2.2}$$

where Δt is the time difference between hits, n_g/c the group velocity of light in sea water, and d the distance between the two hit storeys. An additional 20 ns for the trigger selection are added for compensating the uncertainty of the storey position, as well as the time calibration and light scattering.

In order to avoid constraints due to accidental correlations, an increase of purity of event samples is mandatory and the pre-selection of the sample requires additional trigger levels after L0 level: L1 trigger level and T3 trigger level. As commented, the L0 level is reached when the electrical signal exceeds a threshold of 0.3 p.e. and it is digitized by the ARS. The L1 trigger level is achieved when a high threshold (usually 3 p.e.) is exceeded or a coincidence of at least two L0 levels from different OMs is found inside a 20 ns time window on the same storey ([67]). The T3 trigger is a cluster of L1 of two types: the coincidence of 2 L1 in 80 ns and other of 2 L1 in 160 ns time window. There are several refined trigger algorithms in ANTARES set for different physics analysis. Some of the used triggers are:

- 3N: which requires at least 5L1 in time windows corresponding to a muon track.

- GC: is a directional trigger looking for maximizing neutrinos coming from the Galactic Center direction. This trigger requires 1L1 and 4L0 levels.

- K40: which is used for *in-situ* calibration, it requires 2L0 on two OMs of the same storey within a time window of 50 ns.

There are other triggers which operate jointly with networks of experiments for multi-messenger approach in ANTARES. Example of this is the TST trigger that is switched on when an alert is sent by γ-ray satellites as SWIFT of Fermi via the GCN network of NASA. In this particular trigger, 2 minutes of data around the trigger are recorded without any filter (64).

2.4   The Optical Beacon system

The Optical Beacon system (OBs) consists of a set of pulsed light sources strategically located throughout the detector. There are two kinds: the LED OB and the laser OB. The system is mainly used for time calibration (73) but can also be used as a tool to study the water optical properties and their stability (74) as it will be shown in Chapter 4 (Estimation of the optical properties with the OB technique). The standard OBs will be described in the following subsections, as well as some modified devices specially designed and installed during recovery campaigns or maintenance operations.

2.4.1   The LED Optical Beacon

The LED OB is a cylindrical high-pressure borosilicate container (210 mm diameter, 443 mm length) inside which an hexagonal frame houses six electronic cards (one per face) with several LEDs able to flash with a well known emission time (see Figure 2.10). Each card is equipped with six LEDs, one pointing upwards in the top and five pointing radially outwards.

Each LED (RMS rise-time $\sim$0.15 ns) flashes at an energy per pulse $\sim$150 pJ ($\sim 4 \times 10^8$ photons for a 24 V of applied voltage), being the emission time recorded by means of an internal PMT (RMS rise-time $\sim$ 0.8 ns, TT $\sim$ 5.4 ns). The emission time of the 36 LEDs is synchronized using a variable capacitor ($\sim$200 ps) in each pulser circuit.

As previously said, if the storey contains an OB, an additional ARS card is installed
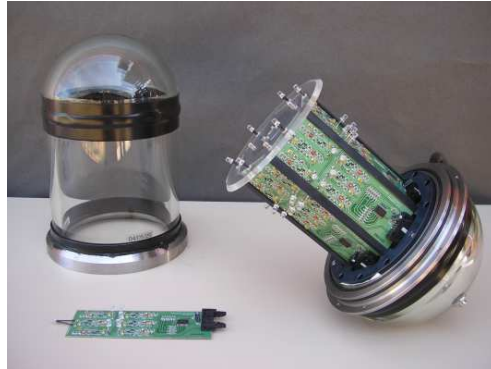
Figure 2.10: ANTARES LOB - The borosilicate container protects the internal LOB structure which holds the electronics boards and internal devices. The distribution of the LEDs in the LOB faces is seen in the top and middle of the electronic cards.

in the LCM to readout the signals sent by the internal PMT. By means of its internal clock it is possible to multiply its nominal flashing rate from 30 Hz up to a factor ten. Figure 2.11 shows the rise-time distribution of the electronic signal of an LOB flash in the ARS of the internal PMT.
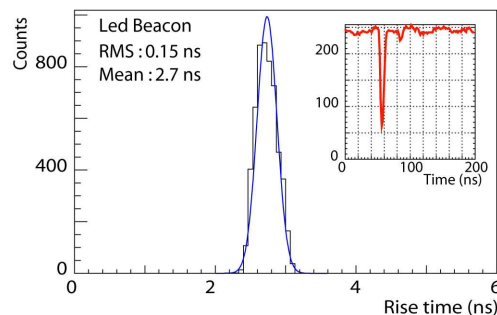
Figure 2.11: Rise-time distribution of a LOB - The rising edges measurements show a resolution ∼0.15 ns. Inset the waveform of the readout of the internal PMT in the ARS.

There are four LOB strategically placed per line (storeys 2, 9, 15 and 21) in such a way that almost all the line can be illuminated. The faces of the LOB are mechanically fixed to a hollow nylon frame which houses the internal 8-mm photo-cathode diameter Hamamatsu H6780-03 PMT. A flat acrylic disc is used as light-guide at the top of the nylon frame structure with the purpose of increasing the light collection. Its edges are bevelled at 45° to improve collection of the light from the horizontal LEDs. The electronic boards required to release the operating

voltages and enable the LEDs flashing by external slow control commands are found at the bottom of the OB structure (75). Their faces can be flashed/triggered independently.

Based on his amplitude and rise-time properties, the LED model Agilent HLMP-CB15-RSC00, was selected. The wavelength peak is around 472 nm with a spectral half-width of 35 nm. A rise-time between 1.9 and 2.2 ns was measured (75). The fastest ones were placed in the top where the uncertainty in the calibration is mainly due to the rise-time, not by the light propagation effects. In addition, all the caps of the LEDs were machined-off in order to extend the angular occupancy of the emitted light, initially fixed at $15°$. Several depths of cuts were tested to find an optimum flat angular distribution of the light output. A cut of 3 mm provided an emission distribution flat within $\pm 10\%$ for angles up to $35°$ and within a factor two up to $55°$ (Figure 2.12).
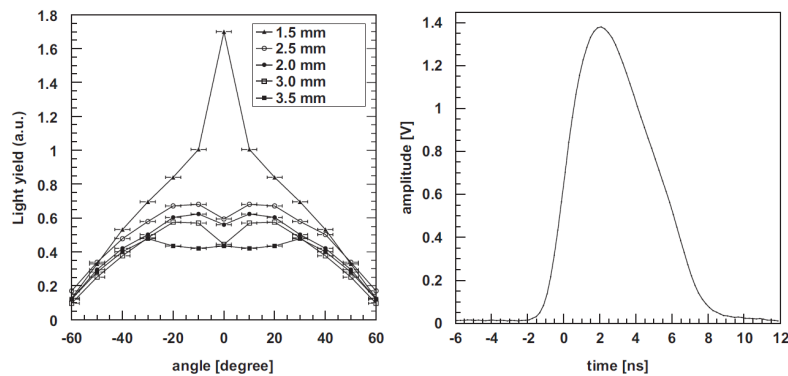
Figure 2.12: Emission profile and time distribution for LEDs in the OB - Left: light amplitude as a function of the azimuth angle for different cut depths of the cap. Right: time distribution of a single LED pulse.

2.4.2 The multi-wavelength LED Optical Beacons

Two modified OBs with multi-wavelength LEDs (MW-LOBs) were specially designed to study the light propagation as a function of the wavelength. They were installed during the line recovery and redeployment campaigns in 2008 for the MW-LOB in Line 12 Storey 2 (L12F2), and in 2010 for the MW-LOB in Line 6 Storey 2 (L6F2).

- **The MW-LOB in L12F2**:
  The layout of the L12F2 LOB is identical to that of the "standard LOB",
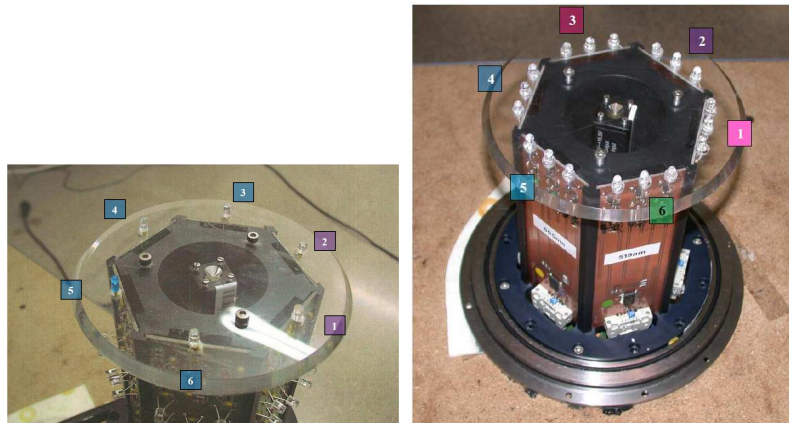
Figure 2.13: The modified OBs in ANTARES - Left: MW-LOB installed in L12F2 storey. Two different wavelengths were used: Ultra Violet for faces 1-2, blue for faces 3-6. Right: MultiWavelength LOB in L6F2. Triplets of LEDs pointing up-wards with different wavelengths are installed in the top cap.

the main differences rely on the LEDs models mounted in the LOB: different models at two different wavelengths (400 and 470 nm). Unique standalone LEDs are mounted in the top of the electronic cards forming the faces as Figure 2.13-left shows.

The aim of the L12F2 OB was to test different LED models to study their viability as a time calibration and water optical properties monitoring tool for KM3NeT. They were selected based on the amplitude and rise-time of the emitted pulses and the angular distribution of light. Such LEDs features are described in Table 2.2.

Model	HUVL400-5x0B	HLMP-CB26	HLMP-CB30-K000	HLMP-AB87	NSPB500S
Face in the OB	1,2	3	4	5	6
Wavelength [nm]	400	470	472	470	470
Angular occupancy (FWHM)	20	23	28	51	20
Rise-time [ns]	1.9-2.2	2.4	2.0	2.4	3.2
Intensity [pJ]	-	150	90	130	170
Distance range at 0.1 PE	130	230	195	235	250

Table 2.2: Main design parameters for blue LEDs selection installed in MW-LOB L12F2.

The wavelength peak for the two UV LEDs is around 400 nm with a spectral half-width of 20 nm and a rise time of the LEDs pulses between 1.9 and 2.2 ns (76) and they were also machined-off (76). The same kind of LEDs with

the same features were installed in L11F2 but they have not been operative due communication failures from the shore station.

The blue LEDs in L12F2 have a wavelength peak between 470-472 nm and spectral half-width around 20-51 nm (76). The light emitted by the new LEDs covers a more longer range along the line than the standard ANTARES LED, but a lower opening angle since blue LEDs were not machined-off (77). Figure 2.14 shows the average number of hits per flash as a function of the distance for the different prototype LEDs for the different LED models.
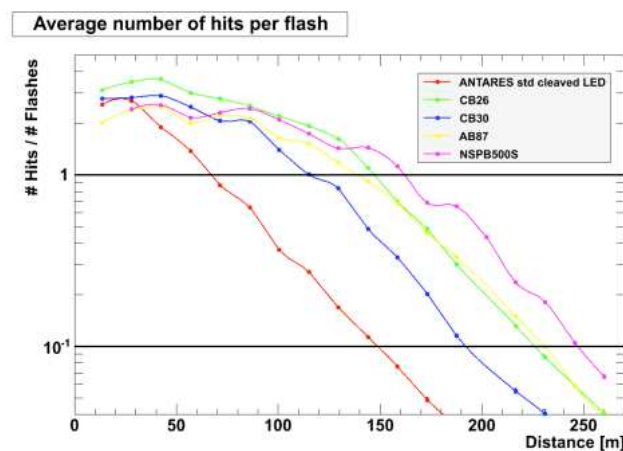
Figure 2.14: Relative light intensity for the prototype LEDs for KM3NeT installed in ANTARES - The comparison with the standard ANTARES LED is shown. Larger distances can be reached with the new LEDs.

The maximum distance reached by the light pulse both at 1 p.e. (1 hit per flash) and 0.1 p.e. (0.1 hit per flash) level is also shown. The LEDs were successfully tested *in-situ* at the ANTARES site and some of them installed in other detection line as OM-embedded LEDs (Nano-Beacon) for specific studies such as the influence of biofouling on the detection units and for water optical properties studies.

- **The MW-LOB in L6F2**:
  Concerning the MW-LOB in L6F2, the integration tests were performed in November 2009 on-shore in the main ANTARES headquarters at CPPM (Centre de Physique des Particules de Marseille). Its integration was carried out in March 2010. It was sucessfully deployed in April 2010 and the data taking period began in November 2010. As in the L12F2 LOB, the MW-

LOB in L6F2 has different LED models and different wavelengths at the top of the device, which can be flashed independently. The MW-LOB in L6F2 was strictly designed for water optical properties studies (78). A total of 6 different wavelengths for 6 different LED models were installed in triplets (to check LED systematics) in the upper part of the OB as shown in Figure 2.13-right. Neither the central radial LED nor the group of four were present in any of the faces and their labels were used in the DAQ to reference the new left and right LEDs at the top. The main features for the LEDs of L6F2 MW-LOB are shown in Table 2.3.

LOB face	LED MODEL	λ [nm]†	FWHM [nm]†	λ [nm]‡	FWHM [nm]‡
1	VAOL-5GUV8T4	385	5	384	9
2	HUVL400-5x0B	400	20	400	10
3	ETG-5AX440-15	440	-	447	13
4	HLMP-CB15-RSC00	472	35	469	13
4	HLMP-CB30-K000	460	35	458	19
5	HLMP-CE36-WZ000	505	30	494	18
6	SLA580ECT3F	518	35	518	25

Table 2.3: Main MW-LOB L6F2 features. Measurements provided by the manufacturer (†) and laboratory (‡) (IFIC, Valencia) are indicated. A high-resolution HR4000CG-UV-NIR calibrated spectrometer from Ocean Optics (79) was used.

2.4.3 The laser Optical Beacon

The laser OB is a cylindrical titanium container 705 mm of length and 170 mm in diameter housing a diode pumped Q-switched Nd-YAG laser which produces very short light pulses ($\sim$1 ns). An inner structure made of aluminium is used to hold the laser and its electronics. After extensive studies of different kind of lasers, the selected model was Nanolase NG-10120-120 (80). Figure 2.15 shows the typical laser OB.

There are two laser OBs at the BSS of L8 and L7. The laser OB in L7 was only operative few days since its deployment. Then, communication with the on-shore station was lost (due to a power failure supply). As L7 laser OB has not been recovered, a dedicated diagnosis has not been possible. The wavelength peak of the light pulse is 532 nm after frequency doubling of the original wavelength of 1064 nm. It has a very narrow emission, 1 nm of FWHM, and an energy per pulse around 1μJ (75).

The laser beam is emitted upwards and leaves the titanium container through an
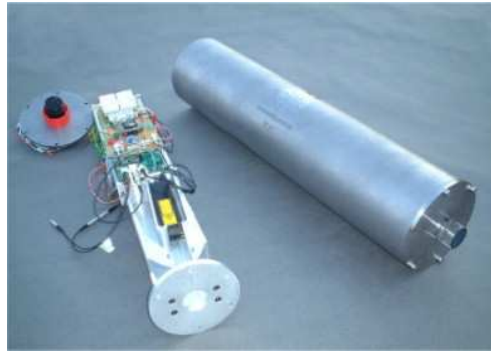
Figure 2.15: The Laser OB - Internal and external frames of the mounting. The device is mainly used for inter-line time calibration, but it is also a cross-check tool for positioning and for optical properties studies (78).

opening in the top end-cap. The laser OB can operate at variable light intensity by means of a crystal liquid attenuator system, working jointly with a crystal quartz rod and a diffuser (optical flat disk) of 2.2 mm of thickness and 255 mm of diameter (75). The function of the latter element is to spread out the light beam according to a cosine distribution such that it is possible to flash up the neighbouring lines.

The crystal quartz rod (40 mm diameter, 47 mm in length) was bonded to the upper surface of the diffuser, the rod was coated with a black water resistant epoxy layer. This layout is used to minimize light transmission losses due to underwater sedimentation and biofouling, since the light comes out from the cylinder along the vertical walls where biofouling is negligible (75). Due to Snell's law, the cosine distribution is conserved when the light leaves the cylinder through its vertical walls. The minimum and maximum angle of the light output depends on the refractive index of the crystal quartz rod ($n = 1.54$) and the refractive index of water ($n = 1.34$) and on the dimensions of the rod.

The laser OB is able to operate in triggered (variable frequency) or non-triggered mode (fixed frequency at around 15 kHz). In the triggered mode, which is the one used for the standard calibration in ANTARES, the laser OB is triggered when a TTL (Transistor-Transistor Logic) signal arrives to the emission unit along a connection in the rear panel of the power supply. As the laser is Q-switched, the time delay between the trigger signal and the light pulse emission is at the μs level and the pulse-to-pulse jitter is of the order of a few hundred nanoseconds. The emission time of the light pulse is recorded by an internal fast photodiode

integrated in the laser head ([75]). When the laser pulse is emitted, the photodiode sends back a signal which is received by an ARS chip housed in the SCM of the line. Then, the electrical current which feeds the photodiode is switched off and the next trigger signal is ready to be readout.

2.5   Calibration systems

The amplitude, time and positioning calibration is crucial to carry out the physics program in ANTARES. The accuracy on the charge calibration is relevant in order to have a good estimation of the neutrino energy, this energy information helps on the discrimination of the effective rejection of atmospheric neutrinos which shown a soft energy spectra, different to the hard spectra of cosmic neutrinos. Concering the time calibration of the OMs for the arrival of the Cherenkov light we can distinguish between an absolute and a relative calibration. The absolute time calibration is relevant since it is linked to the required time to correlate detector events with astrophysical phenomena. The required accuracy is of the order of $\sim$1 ms and the main uncertainty come from the electronic path common to all the OMs. The relative time resolution is performed to measure the time offsets between OMs. This is meant as the capability for measuring the same time for an identical hit, not depending on which OM the hit is recorded. The nanosecond level of uncertainty reached by the relative time calibration system allows to estimate an unprecedented angular resolution in ANTARES. The exact knowledge of positioning of each OM or pointing accuracy is in turn relevant to reach the desirable detector performance. The main features of ANTARES calibration systems and their performance are the main subject of this section.

2.5.1   Amplitude calibration

The amplitude calibration relies on the measurement of the corresponding p.e. peak and the pedestal value of the AVC channel. The measurement of the charge is performed in three stages (integration, memorization and erasing) for minimizing charge losses as explained previously. Three main parameters are responsible of a good charge calibration: the discriminator threshold (start the integration), the pedestal plus the p.e. peak and the "cross-talk" information ([72]). Before lines immersion the discriminator threshold is estimated by computing efficiency curves

at different test voltages, what allows to obtain the response function of the AVC in such a way that the suitable voltage can be chosen. Once *in-situ*, these thresholds are measured again by using the signals recorded from the ^{40}K decay in the sea water as p.e. pulses. Concerning pedestal and p.e. peak, the PMTs current is recorded at random times in special data taking runs and giving the estimation of the pedestal. The p.e. peak is obtained during observations of minimum bias events since, as commented, the optical activity due to ^{40}K produces single photons as well as the bioluminescent bacteria present in the ANTARES site.

The charge measurements in the ARS are affected by a "cross-talk" effect due to the influence of the TVC ramp values on the analogue memory of the AVC during the ARS signal digitization. However, TVC values are not affected by the AVC digitization. A small slope close to the 10% for the AVC channel is arisen as result of such effect (72). The deviation due to the cross-talk effect over TVC range is calculated from a linear fit to the measurements *in-situ* of the AVC against TVC values (72).

Non-uniform bin sizes or "Differential Non-Linearities (DNL)" are seen as empty channels in TVC/AVC distributions (inhomogeneous ADC bin sizes). The DNLs effect is due to an ARS comparator imperfection when the input signal is converted into an output binary signal. It appears when a given reference voltage is growing too slow and does not reach the final expected value, giving wrong ADC channels (72). A way to reduce this effect is to treat the TVC and AVC distributions as cumulative distributions, but actually is not included in the time calibration and it is considered as a second order correction.

Once these effects have been corrected, all hits which exceed the L0 level are parametrized in charge distribution according to the Equation 2.3 (72)

$$\frac{dN}{dx} = A\exp^{-\alpha(x-x_{th})} + B\exp^{-\frac{(x-x_{pe})^2}{2\sigma^2}} \quad , \tag{2.3}$$

where x is the charge, x_{th} the effective threshold and x_{pe} the p.e. peak, all of them in ADC units. The dark current of the PMT and the p.e. distribution are taking into account in the first and second term respectively. The charge calibration is applied to reconstruct the amplitude of the individual signals from the OMs. In this sense, the distribution is peaked at 1 p.e. as it is expected for the optical activity signals as can be seen in Figure 2.16-right.
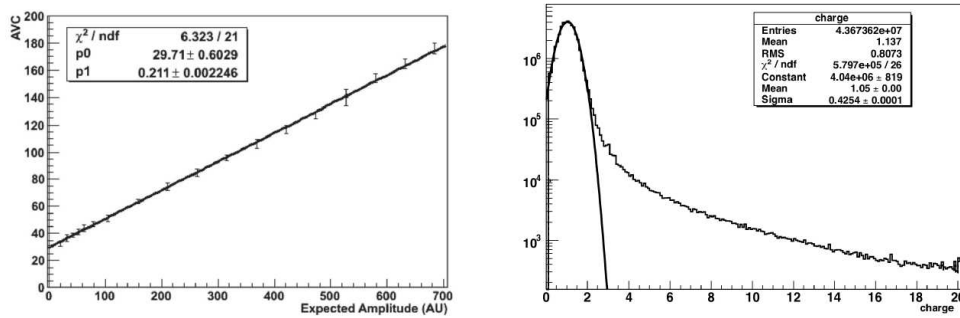
Figure 2.16: Charge parametrization - Left: measurement of the AVC linearity by estimations of the input (expected) amplitude. Right: calibrated charge distribution for all PMTs in the detector.

The linear response integrator-ADC as shown in Figure 2.16-left, provides the equivalence of ADC counts into p.e. units (what is required for the physics analysis) computed as

$$Q_{pe} = \frac{AVC - AVC_0}{AVC_1 - AVC_0} \quad , \qquad (2.4)$$

where AVC_0 and AVC_1 are the values that match the pedestal and the p.e. peaks respectively.

2.5.2 Time calibration

The time calibration is carried out before and after lines immersion in order to verify and tune time offsets of the OMs. The tools to make possible this, goes from the echo-based clock system (enable measurement of the time delay of the signal from the clock board in the LCM to the shore station), a set of devices on-shore known as "dark-room" assembly (for relative time calibration), the OBs which carry out the *in-situ* time calibration and the ^{40}K calibration method (a cross-check method for OBs time measurements).

2.5.2.1 Time calibration before lines immersion

Before immersion several tests are carried out with a dedicated calibration set up in a dark-room in order to estimate the time offsets between detection units, by means of a laser and a clock system. The on-shore calibration starts by flashing simultaneously groups of OMs (a sector) by short laser pulses in the dark room. The propagation times from the SCM to each LCM are known from the clock

system calibration ([73]). With this experimental setup, the contribution of cable linking the LCM to the OM, the TT of the PMT and the front-end electronics time delay can be deduced. The dark-room setup is depicted in Figure 2.17.
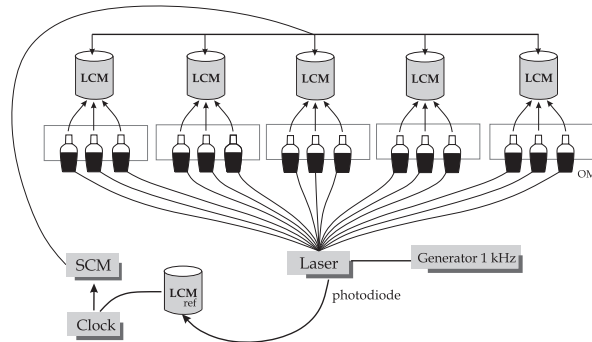
Figure 2.17: On-shore calibration in the dark room - A common laser signal is distributed to the whole sector where the time offsets for each detection unit is computed.

The laser used is almost identical to that used in the laser OB which is externally triggered at a frequency of 1 kHz. The light output is distributed to each OM of the sector through optical fibres using a 1-to-16 optical splitter. Each optical fibre contains a Lambertian diffuser which spreads the light over each PMT photocathode area. The length of the fibres has been determined in such a way that the corresponding time differences are less than 0.3 ns. The time reference comes from the laser internal photodiode, whose signal is digitized by the reference LCM ([73]). From the difference between the time of the signal registered in the OM and the emission time of the laser photodiode pulse, it is possible to extract a time offset between each OM of the line and the first OM of the lowest storey (chosen as reference) with a precision of 0.5 ns. An example of this measurement is shown in Figure 2.18.

As seen in Figure 2.18, there is a small spread (less than 3 ns) in the offsets. This spread comes from the difference in the internal cabling of the OMs to the storey electronics and also from the difference in the TT of the PMTs. The measurements of the time offsets are recorded in the ANTARES data base and used as initial values in the analysis after the line deployment and connection.

Once at the site, the relevant constants measured on-shore are re-computed since they could change due to temperature changes, stretching of cables due to transport and deployment activities, and also when high voltages applied to the PMTs
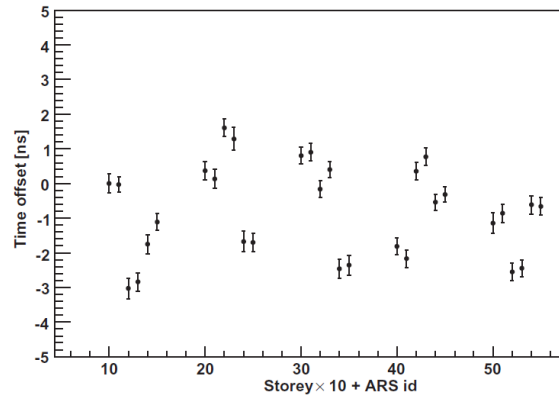
Figure 2.18: Time offsets measured for the 30 ARS of a given sector - The measurements are relative to the first ARS of the first OM of the lowest storey.

are modified (73). This is carried out by the OB system and cross-checked by alternative methods such as coincidence analysis of ^{40}K decays and time residuals computed from muon tracks.

2.5.2.2 Time calibration after lines immersion

The absolute time calibration aims at the assignment of a universal time to each event. This is achieved by interfacing the shore station master clock to a card receiving the Global Positioning System (GPS) time, that has an accuracy of about 100 ms respect to the Universal Time Coordinated (UTC). The time measurement of the PMT hits is made by a self-calibrated 20 MHz master clock system generated on-shore. This is done from the shore station to the JB and then to the SCM and LCM of each line, and from there to the ARS chips of each detection unit. A schematic representation of the clock distribution network can be seen in Figure 2.19.

The independent time offsets for each specific detection unit are calibrated *in-situ* by the OBs. The difference between the signal time recorded in the OM and the emission time of the corresponding LED flash is measured. Taking into account the time offsets measured on-shore, and once the nominal travel of the light from the LOB to the OM has been subtracted, the time distribution of these "time residuals" should be center at zero. An example of the distribution for time residuals OB-OM is depicted in Figure 2.20.
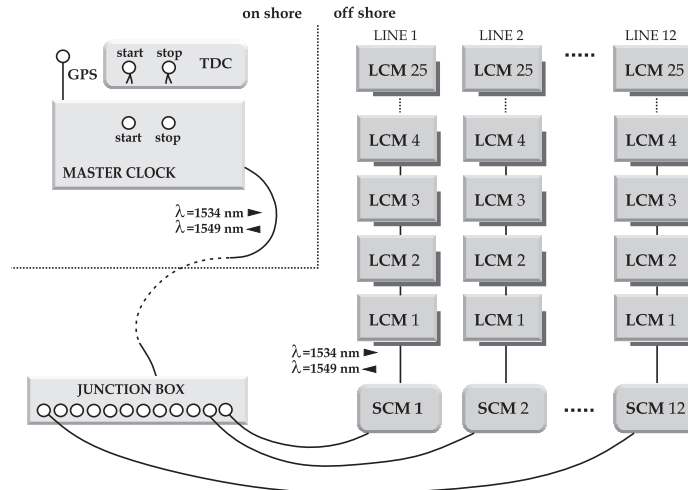
Figure 2.19: Layout of the master clock system - The system is based on a bi-directional optical communication system using infra-red signals for transmission in the two opposite directions.
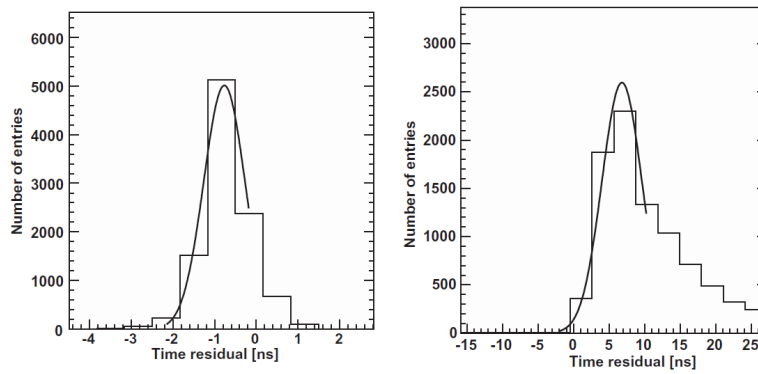
Figure 2.20: Time residuals distribution OB-OM - Signal time residuals are measured in two OMs. Left: separated two storeys above (~ 30 m) the OB. Right: separated seven storeys above (~ 105 m) the OB.

The tail seen in Figure 2.20-right corresponds to the effect of light scattering in water. The peak value of the distributions as that of Figure 2.20 is represented in Figure 2.21-left for several distances.

The increase of the time residual with distance is a well-known effect in ANTARES and referred to as "early-photon" effect. This effect appears due to the duration of the light pulse and the fact that the first photons detected by the OMs determine the recorded time of the pulse. In this way, the PMTs near to the LOB record the time of the first arriving photons of the pulse, due to the inability to treat the big amount of light released by the source of light.
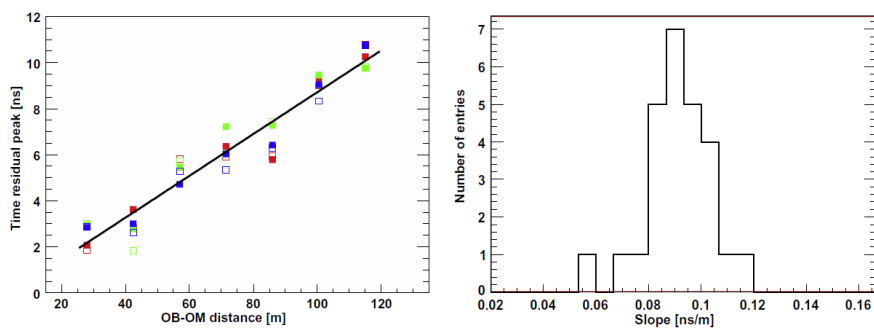
Figure 2.21: Early-photon effect - Left: time residual peak position as a function of the distance OB-OM for the ARSs of seven storeys. For each distance six values are represented (2 ARS/OM, 3 OM/storey). Right: distribution of the slopes of the fits to the time residuals peak position as a function of the OB-OM distance for all the OBs.

The resulting deviations from the linear fit are used to obtain the time offsets corrections, see Figure 2.21-right. These corrections for all the OMs can be calibrated with the OBs.

Figure 2.22 compares the times measured by two OMs in the same storey when it is illuminated at maximum light intensity. As it can be seen, by means of these considerations a resolution above 0.5 ns is reached $(\sigma(0.7)/\sqrt{2})$, which is enough to achieve an angular resolution (angle between real and reconstructed track) in the detector less than $0.5°$ for neutrino energies above 10 TeV (35).

The laser OB is used to compute relative time offsets between lines since its light can reach all the detector lines. In this case, the early-photon effect correction is not needed since only distances where the OMs are illuminated below the 1 p.e. level are considered. Therefore, the time residuals do not depend on the distance to the source, and the relative time offsets between lines are estimated as the
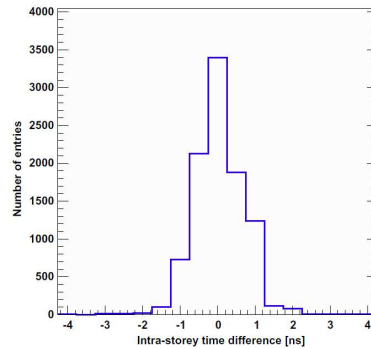
Figure 2.22: Intra-storey time difference - Hit time differences for a pair of OMs in the same storey when are illuminated by the same OB.

average of the time residuals peak measured every month. The distribution of the inter-line offsets measured by the laser OB of L8 are shown in Figure 2.23.
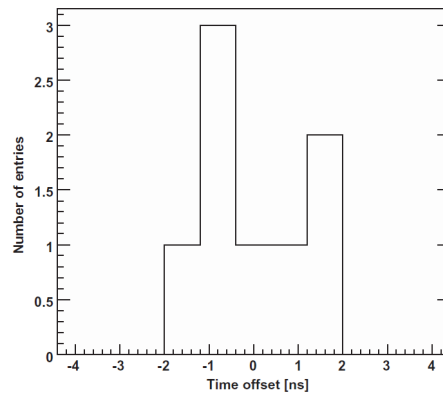
Figure 2.23: Inter-line time offsets - The distribution shows the measurements made with the laser OB of L8. Each offset is calculated as the average of the time residuals peak.

On the other hand, the ^{40}K present in the sea water is used for time calibration and PMT efficiency of the detector by using the Cherenkov light induced by the electron released in the β-decay and e-capture (71). When the ^{40}K decay takes place some few meters from the storey it is possible to obtain coincidence signals on the OMs which are completely independent of the bioluminescence in the sea water and isotropic along the detector. The distribution of the measured time differences between hits in two OMs of the same storey for one particular case can be observed in Figure 2.24.

The peak seen in Figure 2.24-left is due to single ^{40}K decays detected in coinci-
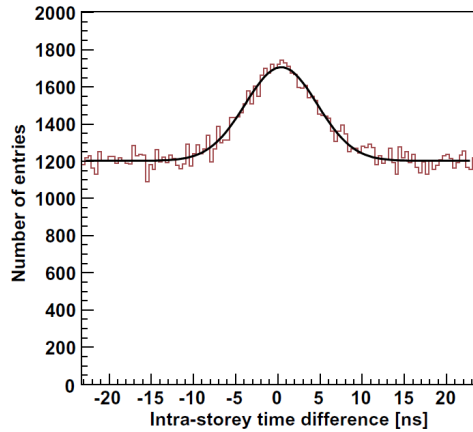
Figure 2.24: Calibration with ^{40}K - Intra-storey time difference for one pair of OMs in the same storey.

dence by two OMs. The distribution is fitted to the convolution of a Gaussian plus a flat background and the width of the distribution is due to the distance from the point where the decay occurs to each of the OMs of the pair. In this sense, the time offsets computed on-shore in the dark-room as well as the ones obtained from the *in-situ* OB calibration can be cross-checked by means of the identification of the position of the peak within each storey. An incorrect OM time offset of the pair should be seen as a displacement from the zero position.

2.5.3 The positioning system

The movement of the lines due to the sea current is an important factor since affects the positioning of the detector and thus the detector performance. The ANTARES acoustic positioning system includes 1 transceiver/receiver (T_x/R_x) at the bottom of the lines, 5 hydrophones (R_x) per line at specific heights for signal receiving, plus a set of autonomous transponders anchored at known positions on the seabed.

The measurements of the OM positions are performed every two minutes by means of the measurement by triangulation of the travel time of the acoustic signals exchanged between receivers hydrophones and transponders emitters.

On the other hand, each storey is equipped with a commercial compass-tiltmeter sensor (the commented TCM2) (one per storey) which estimates the inclination of the storey respect to the horizontal plane in two perpendicular axis, based on the movement of an internal fluid in the sensor. As it is done for tiltmeters, compasses

are properly calibrated. The heading of the ANTARES storeys are computed based on the Earth's magnetic field component in the horizontal plane at the detector position.

For the reconstruction of the line shape a global χ^2 fit is performed to a model based on the mechanical behaviour of the line (weights and drag coefficients) due to sea water flow. This mechanical model provides the radial displacement of the line as a function of the vertical coordinate z. The Figure 2.25 shows the positions of the 25 storeys of a given line as a function of several sea current velocities.
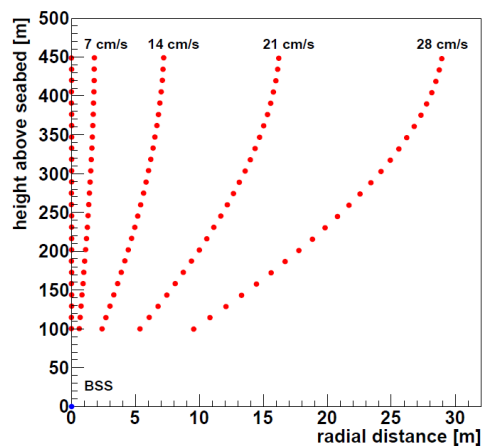
Figure 2.25: Height and radial displacement of a line - The line position is referred to the BSS at the bottom of each line. Storeys are represented by the red dots.

The typical velocities registered in the ANTARES site do not exceed 7 cm/s. For a extreme case of velocities above 20 cm/s, more than 10 m of radial displacement can be expected. The Figure 2.26 shows the difference between the triangulated positions of a storey using its hydrophone and the positions measured from the alignment fit. The mean of the distribution is 0.8 cm and the width 4.5 cm. These results suggest the absence of systematic errors present in the line shape model and shows that this system provides a precision better than 10 cm (81) enough to achieve the physics goal from the accurate detector positioning requirements.
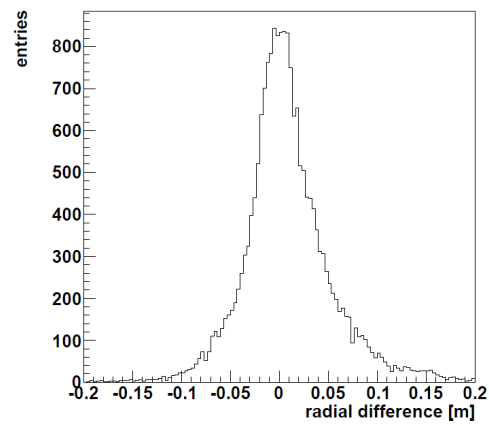
Figure 2.26: Radial difference between hydrophones - The alignment fit measurements are those of that March 2010 estimations. It showed a precision ~ 10 cm for the positioning system.

Chapter 3

The detection medium description for deep-sea neutrino detectors

An expert is a man who has made all the mistakes which can be made, in a narrow field

Niels Bohr

In order to detect the correct signal from a neutrino point-like source, a good angular resolution and effective area of the detector are mandatory. Both angular resolution and effective area depend on the optical properties of the detection medium. This chapter aims to show the basic concepts of the propagation of light in water, and how the relevant optical parameters of the medium are extracted from the studies performed by the oceanographic community and astrophysicists working on neutrino observatories. In addition, the parameterized water model (as detection medium) used in ANTARES will be commented, and the past and status of the optical characterization of the site are reviewed, setting the foundations of the work developed in this thesis to be shown in the Chapters 4 and 5.

3.1   An introductory overview

High-energy neutrinos coming from astrophysical sources can be detected in the Earth by identifying the small fraction of up-going high-energy muons produced in the CC interactions of such neutrinos with the detector environment. When

relativistic muons crosses a transparent medium as water, they can be detected by the Cherenkov light emission if their trajectory intersects the instrumented volume of the detector. The Cherenkov light induced by particles crossing the detector has an optical region of interest between $320 \leq \lambda \, [\text{nm}] \leq 620$. At $\lambda < 320$ nm light is absorbed by the glass and the silicon gel of the OM. At $\lambda > 620$ nm the quantum efficiency of the PMT is not high enough. The light propagation through the water is mainly affected by the convolution of two phenomena: absorption (photons disappearance) and scattering (change of direction of photons). The angular distribution of scattered photons becomes quite relevant as well. In this way, the total number of detected Cherenkov photons is deeply linked to the absorption in the medium while the arrival time of such photons from the point of emission in the track to the OMs, is critically affected by the scattering properties of the medium. With high density of absorption centres in the medium, large fractions of photons will be lost before reaching the OMs. The larger the scattering, the larger the number of delayed photons that will reach the OMs.

Previous studies in ANTARES with a less detailed simulation software and reconstruction algorithms showed that an uncertainty of the $\pm 25\%$ in the scattering can change the event rate by 5-10% (82) (83). The scattering effect on angular resolution was found most significant at large energies (~ 100 TeV) where the quality of the reconstruction dominates. At lower energies the angular resolution is governed by the uncertainty in the neutrino-muon angle at the interaction vertex (83). The ignorance on the accuracy of scattering suggested variations and uncertainties about 30% and $0.2°$ for the detector efficiency and detector angular resolution respectively (83). Photons scattered at large angles are lost, therefore more scattering and less photons will be detected, what reflects a decrease in the detector efficiency. A similar reasoning is applicable for the angular resolution of the detector, since the number of useful photons for reconstruction is reduced for large scattering in the medium, therefore degrading the detector performance for short scattering lengths.

Concerning the absorption effects on the detector performance, for the average distance between detector lines of 60 m, changes in absorption length of $\pm 10\%$ reduce the number of detected photons between 10-20% (83). At larger energies the performance of the detector should be less impacted by the absorption length uncertainty since the number of photons increase with energy.

This chapter aims to identify the basic tools to comprehend the interaction light and matter, and how the optical properties of the environment can be extracted. The impact of the optical properties of the water on the ANTARES detector performance is the final goal of this thesis, what will be the last topic of Chapter 5.

3.2   Light propagation and interaction with matter

The optical properties of the water are mainly represented by the attenuation, absorption and scattering phenomena. A general review about such concepts and how they are linked to the radiative transfer equation for the medium is presented. The Beer-Lambert law used for most of the transmission and absorption parameterizations is roughly deduced. The determination of the scattering requires a different rigorous treatment.

3.2.1   Fundamental concepts: transmission, absorption and scattering

The study of the interaction between light and matter is associated to the understanding of the properties of the medium. A saline natural water as the ANTARES environment, is composed both by dissolved and particulate matter which are variable in type and concentration, therefore, impacting on the optical properties of the medium. In this way, it may lead to temporal and spatial variations in the detector. The optical properties are in turn linked to biological activity, chemical and geological constituents of the water.

The optical properties of the water are classified as Inherent Optical Properties (IOP) when depend only upon the medium and as Apparent Optical Properties (AOP) when depend both of the medium and on the geometrical (directional) structure of the ambient light field, as well that shows regular features and stability in order to be used as fingerprints of the water body ([84]). IOP are mainly the absorption coefficient and the volume scattering function, and in second order, the scattering coefficient, the refractive index and the beam attenuation (or transmission) coefficient. For AOP are often cited the irradiance reflectance, the average cosines and the diffuse attenuation coefficients. The radiative transfer theory is the connection between IOPs and AOPs. The results in this thesis are

focused to IOPs of the medium namely, transmission, absorption and scattering. When a narrow and collimated incident beam of monochromatic light $\Phi_i(\lambda)$ crosses a small fraction of volume of water ΔV of thickness Δr, one part of the beam is absorbed $\Phi_a(\lambda)$, other part is scattered out $\Phi_s(\psi, \lambda)$ at angle ψ ($0 \leq \psi \leq \pi$) and the rest is transmitted along the volume unaltered in direction. This phenomenology is graphically represented in Figure 3.1.
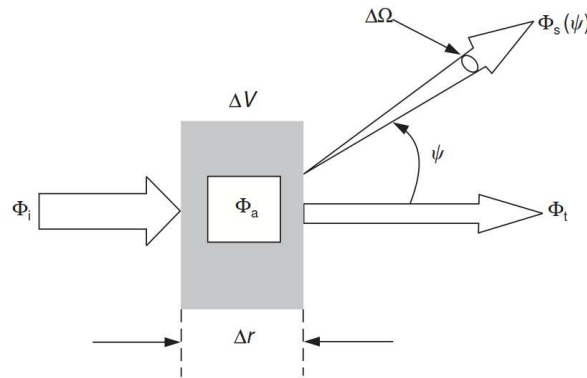
Figure 3.1: Geometrical inference for IOPs determination - The total effect when a incident beam crosses a section of matter is summarized by the transmission of light plus absorption and scattering response of the medium, as conservation of energy. The solid angle where the light is scattered out is defined as $\Delta\Omega$ at a wavelength λ and angle ψ is measured relative to the direction of the incident beam. The volume illuminated by the incident beams is $\Delta V = \Delta r \Delta A$, ΔA being the area.

By assuming scattering in all directions and considering only elastic scattering (no changes of wavelength, no loss of energy) what will be justified in the next subsection, it is possible by means of conservation of energy set that

$$\Phi_i(\lambda) = \Phi_a(\lambda) + \Phi_s(\lambda) + \Phi_t(\lambda) \quad . \tag{3.1}$$

If Equation 3.1 is divided into $\Phi_i(\lambda)$ the absorptance $A(\lambda)$, scattereance $B(\lambda)$ and transmittance $T(\lambda)$ are obtained. If such quantities are evaluated in the limit when the thickness Δr of the volume of water is so small, what is obtained are the absorption and scattering coefficient represented by the attenuation coefficient as

$$c(\lambda) = a(\lambda) + b(\lambda) = \lim_{\Delta r \to 0} \frac{A(\lambda)}{\Delta r} + \lim_{\Delta r \to 0} \frac{B(\lambda)}{\Delta r} \quad [\text{m}^{-1}] \quad . \tag{3.2}$$

The radiant intensity I [W/sr] defines the spectral (radiant) power Φ [W] from a source that is directed into a particular direction along the center of a cone encom-

passing a solid angle Ω [sr]. In general, by assuming absorption and scattering, a beam of photons of radiant intensity I going to some propagation direction (i.e. x-direction) is altered by the attenuation effects as (85)

$$\frac{dI}{dx} = -I \cdot c(\lambda) \quad . \tag{3.3}$$

If Equation 3.3 is integrated the Beer-Lambert law is obtained

$$I = I_0 e^{-c(\lambda)x} = I_0 e^{-[a(\lambda)+b(\lambda)]x} \quad . \tag{3.4}$$

Often Equation 3.2 is represented in terms of the inverse of such quantities as

$$\frac{1}{\lambda_{att}} = \frac{1}{\lambda_{abs}} + \frac{1}{\lambda_{sca}} \quad . \tag{3.5}$$

In Equation 3.5 the attenuation, absorption and scattering (att, abs, sca) refers to c, a, b respectively in Equation 3.2. These quantities in turn represent the distance into a material (i.e. in the volume of water) at which the probability that a particle (i.e. the Cherenkov photon) has not been attenuated, absorbed or scattered has dropped to $1/e$ respectively. In other words, the "attenuation length" is defined as the average distance between photon attenuation events (absorption and/or scattering). In this way, the "absorption length" is defined as the average distance travelled by the photons before being absorbed. The "scattering length" represents the average distance between two consecutive photon scattering events. Equation 3.5 is only valid if a collimated beam of light is considered, for isotropic sources the scattering length has to be re-defined as it will be showed in forthcoming sections.

On the other hand, the volume scattering function $\beta(\psi, \lambda)$ or differential scattering cross section per unit volume which takes into account the angular distribution of the scattered light, can be expressed in terms of the radiant intensity I_s $(\Phi_s(\psi, \lambda)/\Delta\Omega)$ as

$$\beta(\psi, \lambda) = \lim_{\Delta V \to 0} \frac{I_s(\psi, \lambda)}{E_i(\lambda)\Delta V} \quad [\mathrm{m}^{-1}\mathrm{sr}^{-1}] \quad , \tag{3.6}$$

where $E_i(\lambda)$ is the incident irradiance equal to $\Phi_i(\lambda)/\Delta A$. The "irradiance" term is used when the electromagnetic radiation is incident on the surface. In turn, the

scattering coefficient can be obtained by integration of $\beta(\psi, \lambda)$ over all possible directions as

$$b(\lambda) = 2\pi \int_0^\pi \beta(\psi, \lambda) \sin \psi d\psi \quad . \tag{3.7}$$

The integral in Equation 3.7 is often divided into two components: forward scattering ($0 \leq \psi \leq \pi/2$) and backward scattering ($\pi/2 \leq \psi \leq \pi$), each characterized by their corresponding scattering coefficients $b_f(\lambda)$ and $b_b(\lambda)$ respectively. The function $\beta(\psi, \lambda)$ is normalized by the scattering coefficient $b(\lambda)$, and the elastic scattering phase function $\tilde{\beta}(\psi, \lambda)$ is obtained (84)

$$\tilde{\beta}(\psi, \lambda) = \frac{\beta(\psi, \lambda)}{b(\lambda)} \quad [\text{sr}^{-1}] \quad . \tag{3.8}$$

According to the previous definition, the following normalization condition is preserved

$$2\pi \int_0^\pi \tilde{\beta}(\psi, \lambda) \sin \psi d\psi = 1 \quad . \tag{3.9}$$

The scattering phase function is often characterized by the average over all scattering directions of the cosine of the scattering angle ψ as

$$g \equiv 2\pi \int_0^\pi \tilde{\beta}(\psi) \cos \psi \sin \psi d\psi \quad , \tag{3.10}$$

what is known as the average cosine or the asymmetry parameter. In this way, g is close to 1 when $\tilde{\beta}(\psi)$ is very large for small ψ. A value $g = 0$ is reached when $\tilde{\beta}(\psi)$ is symmetric about $\psi = 90°$. Other important IOP parameter used in the optics of natural waters is the "single-scattering" albedo or the probability of elastic scattering (84)

$$w_0 = \frac{b}{c} \equiv \frac{b}{a + b} \quad , \tag{3.11}$$

as well as the probability of back-scattering

$$B(\lambda) = \frac{b_b(\lambda)}{b(\lambda)} = 2\pi \int_{\pi/2}^\pi \tilde{\beta}(\cos \psi, \lambda) \sin \psi d\psi \quad . \tag{3.12}$$

3.2.2   Radiative transfer equation and optical parameters

The Beer-Lambert law is commonly used by the oceanographic community and
neutrino observatories to extract optical parameters of the environment, the ex-
traction of these optical parameters is in turn linked to the scalar radiative transfer
theory (84). Based on such formalisms, the absorption and scattering spectra are
built and used as reference for the characterization of the detection media for
neutrino detection facilities. The scalar radiative transfer equation can be set as
(86)

$$[\frac{1}{v}\frac{\partial}{\partial t} + \vec{n}\bigtriangledown + c(\lambda, \vec{x})]L(\lambda, \vec{x}, \Omega) = Q^E(\lambda, \vec{x}, \Omega) + Q^I(\lambda, \vec{x}, \Omega) \quad , \qquad (3.13)$$

where $L(\lambda, \vec{x}, \Omega)$ is the total spectral radiance of light in water as a function of
the solid angle $\Omega = \Omega(\theta, \phi)$. The "radiance" or "spectral radiance" [W·sr^{-1}·m^{-2}]
describes the amount of light that passes through or is emitted from a particular
area and falls within a given solid angle in a particular direction. The spectral
radiance is often defined as (84)

$$L(x, y, z, t, \theta, \phi, \lambda) = \frac{\Delta Q}{\Delta t \Delta A, \Delta\Omega\Delta\lambda} \quad , \qquad (3.14)$$

where ΔQ is the amount of radiant energy incident in a time interval Δt over a
surface ΔA located in x, y, z at wavelength λ. The quantity $c(\lambda, \vec{x})$ as a function
of the wavelength and the spatial and time coordinates $\vec{x} = (\vec{r}, t)$ is the attenuation
coefficient. The v is the speed of light in water, and $\vec{n}$ refers to a unit vector in
the propagation of the photon direction. The right part of Equation 3.13 takes
into account the source of both elastic (E) and inelastic (I) scattering of light.
The elastic source can be described by

$$Q^E(\lambda, \vec{x}, \Omega) = \int_{4\pi} d\Omega' \beta(\lambda, \vec{r}, cos\psi)L(\lambda, \vec{r}, \Omega') \quad . \qquad (3.15)$$

The inelastic scattering expression takes into account inelastic processes of Raman
scattering, red fluoresence by chlorophyll and blue fluorescence by yellow substance
also known as Gelbstoff, or coloured dissolved organic matter or CDOM present
in sea water (86) (84). The probability of Raman scattering in water is one tenth
of the probability of occurrence of elastic scattering in water (87), therefore, this
component is not included in the analysis of this thesis. In addition, at very larger

depths in the sea (i.e. ANTARES site) the presence of chlorophyll and yellow substance should be highly reduced, as the sunlight does not penetrate, there is no phytoplankton and then chlorophyll. Their associated fluorescence process takes place when a molecule absorbs the incident photon and shortly thereafter emits a photon of greater wavelength. This photon emission is carried out at microsecond scale ([84]), since the experimental procedure used in this thesis record the light emitted into a nanosecond time interval, the contribution of fluorescence is excluded also from this work.

In the photon interaction with an atom or molecule, the photon can be absorbed leaving the atom or molecule in a state with higher energy (excited state), named electronic, vibrational or rotational. If the atom or molecule promptly comes back to its original internal state (ground state) with a photon emission of the same energy as that absorbed, it defines the "elastic scattering". If the excited molecule or atom emits a photon of less energy than the incident photon, it is at longer wavelength, it defines a "inelastic scattering". This occurs because the molecule or atom remains in an intermediate excited state and afterwards, may emit another photon and go back to its original state, or even, the retained energy could be converted to thermal or chemical energy. A fraction or the total energy of the absorbed photon may be converted into thermal energy (kinetic) or chemical energy (i.e. formation of new compounds), and the conversion of this photon energy in a non radiant form is what is known as the true "absorption". The opposite process is called true "emission" and takes place when the chemical energy is converted into light.

The radiative transfer equation indeed requires considerations of elastic scattering, inelastic scattering, true absorption and true emission. The above assumptions are the basis to set the energy balance equation for beam photons represented by the radiative transfer equation.

3.3 Absorption of light in natural waters

Several factors are responsible of absorption of light in the sea water namely water molecules, coloured dissolved organic matter (yellow substance) and different kinds of chlorophyll molecules grown in phytoplankton cells in natural waters ([86]). The absorption of light by pure water is associated to electronic transitions within

the water molecule as commented. By considering pure water, at wavelengths $370 < \lambda[\text{nm}] < 450$, the molecular scattering provides 20 to 25% of the total beam attenuation $c(\lambda)$ (84). At all visible wavelength range scattering effects can dominate absorption in water with large particulate loads. At wavelengths larger than 450 nm the energy of the photons is transferred to more than one of the vibrational modes of the O-H bond in the water molecule (88). The true absorption of a photon is translated into a non-radiative energy scheme; thermal energy dissipation takes place as commented before.

As a reference model in the oceanographic community the absorption coefficient in natural waters as a function of the wavelength for a given depth can be expressed as (86)

$$a(\lambda) = a_W(\lambda) + a_Y(\lambda) + a_C(\lambda) \quad , \tag{3.16}$$

where $a_W(\lambda)$ corresponds to the absorption coefficient of pure water, $a_Y(\lambda)$ relates to an specific absorption coefficient of yellow substance and $a_C(\lambda)$ the specific absorption coefficient for chlorophyll (84). The specific absorption coefficients in Equation 3.16 are, therefore, due to three main factor sort as

- **Absorption by pure water:**

  The contributions by Smith & Baker (89) have been of great interest. They performed an indirect determination of the upper bound of the spectral absorption coefficient of pure sea water $a_W(\lambda)$ in a wavelength range of $200 < \lambda[\text{nm}] < 800$. In their study, they assume that for the clearest natural waters absorption by salt or other dissolved substances is negligible, the scattering is only present for water molecules and salt ions, and no inelastic scattering is considered. This assumption leads a inequality for the absorption of pure sea water such as

  $$a_W(\lambda) \leq K_d(\lambda) - \frac{1}{2} b_m^{sw}(\lambda) \quad , \tag{3.17}$$

  where $b_m^{sw}(\lambda)$ represents the spectral scattering coefficient for pure sea water available in tabulated data from Morel & Loisel (84). Their estimations as well, are based in measured values of the diffuse attenuation function $K_d(\lambda)$ for very clear waters (89). By having these two contributions, the value of $a_W(\lambda)$ is easily extracted. As such values for $a_W(\lambda)$ are consider upper

bounds, the true value of absorption for pure water should be somewhat lower at least at violet and blue wavelengths. The uncertainties reported by Smith & Baker arise from $K_d(\lambda)$ due to the fact that it is an AOP, therefore influenced by environmental conditions. In addition, they remark that at $\lambda < 300$ nm their values are closely an "educated guess". The accuracy of their measurements of $a_W(\lambda)$ are within +25 and -5 percent for $300 < \lambda$ [nm] < 480 and +10 to -15 percent between $480 < \lambda$ [nm] < 800. Other numerical solutions as that by Gordon (84) consider a more restrictive inequality corrected by effects of sun angle and sea state on $K_d(\lambda)$. By using this, the Smith & Baker estimations could be reduced by up to 20% at blue wavelengths. As the measurements were made based on the clearest natural waters, a small amount of dissolved or particulate matter are present and may contribute both absorption and scattering.

- **Absorption by yellow substance (CDOM):**
  The contribution of the CDOM to the absorption is reasonably well described by Equation 3.18

$$a_Y(\lambda) = a_Y(\lambda_0)e^{-0.014(\lambda-\lambda_0)} \quad , \tag{3.18}$$

along the wavelength range $350 < \lambda$[nm] < 700, where factor λ_0 is the reference wavelength and $a_Y(\lambda_0)$ is the absorption due to yellow matter at λ_0 and, dependent on the concentration, values for the exponent between -0.014 to -0.019 are in turn reported (84).

- **Absorption by chlorophyll in phytoplankton:**
  Phytoplankton has a stronger contribution than CDOM to absorption. They are absorbers of visible light where the absorption by chlorophyll is characterized by strong absorption bands in the blue and red region, at 430 nm and 665 nm respectively in the case of the "chlorophyll *a*" (main pigment in phytoplankton cells), with very short absorption in the green region. The concentration of chlorophyll *a* can reaches up to 0.01 mg·m^{-3} in the clearest open ocean waters. Its distribution along the phytoplankton cell is not random, what means that the spectral absorption in water is flatter with less-pronounced peaks and reduced overall absorption (84). A typical source

of variability is the pigment composition since each pigment displays a typical absorption curve. The chlorophyll specific spectral absorption curve for phytoplankton for different pigment composition could be approached by Equation 3.19

$$a_C(\lambda) = \frac{a_i(\lambda) - a_i(737)}{C_i} \quad ,$$

(3.19)

where i denotes each specie of pigment composition and C_i the concentration. The subtraction $a_i(737)$ is done in order to remove the effects of absorption due to constituents different to phytoplankton pigments. The assumption is not absorption by pigments at 737 nm and that residual absorption is wavelength independent. Nonetheless this approach, an average specific absorption curve was done by Morel by averaging over 14 different cultured phytoplankton species.

The determination of absorption by pure water is a difficult task because the preparing or obtaining uncontaminated samples with unaltered physical and chemical properties once removed from the site. Several $a_W(\lambda)$ data sets from different authors have been produced by using different techniques. One of the widely reference data sets come from the Smith & Baker observations (89) derived from radiative transfer theory approximations.

The common experimental procedure to measure $a_W(\lambda)$ for oceanic water consists of the filtering of a water sample in order to retain particulate matter on a filter pad. Once the sample is prepared, the absorption by the particulate matter $a_p(\lambda)$ is determined via spectrometry, then by adding the absorption by pure water $a_W(\lambda)$ to the particulate matter contribution, is obtained the global absorption by oceanic water. This procedure involves many systematic errors from the determination of the particulate matter contribution (84), in addition it assumes a negligible contribution due to yellow substance absorption. If the contribution of yellow substance $a_Y(\lambda)$ is wanted, the absorption of the "filtrate" $a_{filtrate}(\lambda)$ is measured in such a way that $a_Y(\lambda) = a_{filtrate}(\lambda) - a_W(\lambda)$. The *in-situ* measurements become to be a more difficult task, due to the technical challenge what it involves.

Other interesting absorption coefficient measurements are those by Pope & Fry (90) for $380 < \lambda[nm] < 700$ range, by using integrating cavity measurements

(the ICAM device). An integrating cavity is just a spherical frame that can be uniformly illuminated by a monochromatic light from outside and whose internal walls are made of a diffuse reflecting material of very high reflectivity ($>$99%). This feature provides an isotropic illumination of the sample once introduced in the cavity, which allows to make absorption measurements independently of the scattering effects. The integrating cavity is made of two concentric cavities enclosed by the diffuse reflecting wall: the outer filled with air, and the inner filled with the sample. The high reflectivity of the cavity walls provides a long effective optical path length in a small sample volume. The energy is lost from the radiation field and transferred to heat, what lead to a reduction of the outward irradiance at the inner surface of the cavity. By comparing the outward irradiance from both empty and full cavity, the absorption coefficient can be extracted. The Figure 3.2 shows the absorption estimations by Pope & Fry compared with that obtained by Smith & Baker.
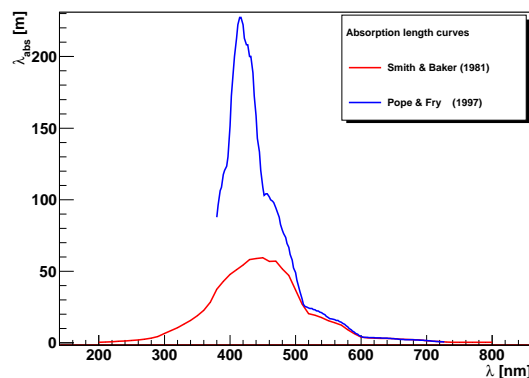
Figure 3.2: Representative absorption length spectra in oceanography - Smith & Baker estimations differs systematically Pope & Fry measurements exceeding up to 3 times in the UV and more than three times up the 500 nm, then both spectra trend to match.

As seen, the Pope & Fry measurements differ from the Smith & Baker data systematically, for instance, the absorption length close to the UV showed to be 3 times lower. By means of the ICAM instrumentation of Pope & Fry, it was possible to obtain an absorption spectrum which differs for wavelengths less than 490 nm respect to several authors including Smith & Baker. The main differences are attributed to more effective water purification by Pope & Fry, the absence of scattering effects in the ICAM, and the greater sensitivity of the ICAM (90).

The Smith & Baker model for the clearest natural waters is the reference spectra for the ANTARES absorption parametrization of the detection media giving acceptable results in the detector performance. The clearest natural waters as the deep oceanic one should not be confused with pure water, which is water triply distilled.

3.4   Elastic scattering of light in natural waters

The global effect of the elastic scattering mainly comes from two contributions. The first one is due to density fluctuations of water molecules and it is known as "Einstein-Smoluchowsky" or "Rayleigh scattering". In this case, the size of this fluctuations is small enough to consider the electromagnetic field uniform over all the extension of the scattering centre being the angular distribution of the scattered photons forward-backward or symmetric. The second type of scattering is due to suspended particulate on the water whose size is much larger and producing a very complex angular distribution peaked on the forward direction. The total scattering coefficient can be expressed as the addition of those two contributions as (86)

$$b(\lambda) = b_{Ray}(\lambda) + b_{Mie}(\lambda) \quad , \qquad (3.20)$$

where each scattering contribution is explained in detail as follows.

- **Scattering by small centres: "Einstein-Smoluchowsky" or "Rayleigh" scattering**

  This kind of scattering is experienced by particles with radius smaller than the wavelength of light (typically $\sim \lambda/20$). The small scattering centres in natural waters are divided into local fluctuations in the density of the water and very small impurities. The Einstein-Smoluchowsky theory if a formalism based on the statistical analysis of the random motion of the water molecules in a given volume of water, which causes local fluctuations in the molecular number density and, therefore, fluctuations in the index of refraction which give rise to scattering. Before the development of such formalism, Rayleigh proposed an independent theory for scattering for small spherical particles.

The angular distribution of the scattered radiation and wavelength dependence by both approaches are the same. By comparing the expressions of the number of scattered photons given by the Einstein-Smoluchowsky and Rayleigh theory, it is possible to observe that the intensity of the scattered light is proportional to λ^{-4}, and depends on the cosine of the scattering angle ($\cos\psi$). The exponent for λ can slightly change as a function of the empirical models used for the relation between the dielectric constant of the water, density and refractive index. The best average value is about -4.32 ± 0.31. Based on the above considerations, the volume scattering function either for pure water or pure sea water get the form (91) (84)

$$\beta_{Ray}(\psi,\lambda) = \beta_{Ray}(90°,\lambda_0)\left(\frac{\lambda_0}{\lambda}\right)^{4.32}(1+0.835\cos^2\psi) \quad . \qquad (3.21)$$

The normalized phase function of scattering of pure water from Equation 3.21 can be written as

$$\tilde{\beta}(\psi) = 0.06225 \cdot (1+0.835\cos^2\psi) \quad , \qquad (3.22)$$

where the 0.835 factor is due to the anisotropy of the water molecule (84) and $0.06225 = \tilde{\beta}_{Ray}(90°)$. In addition, the total scattering coefficient can be obtained from

$$b_{Ray}(\lambda) = 16.06\left(\frac{\lambda_0}{\lambda}\right)^{4.32}\beta_{Ray}(90°,\lambda_0) \quad . \qquad (3.23)$$

The values of $\beta_{Ray}(90°,\lambda_0)$ and $b_{Ray}(\lambda)$ both for pure water and pure sea water can be obtained from tabulated data (84). The values for pure sea water exceed in 30% those of pure water for all the wavelength range.

- **Scattering by large centres: "Mie" scattering**

  Particle sizes which are larger than a wavelength (typically $> \lambda/20$) can not be considered as simple small spheres subject to a uniform electromagnetic field. Mie proposed an analytical solution of such equations for an arbitrary geometry and electronic composition (85). The Mie theory is a generalization of the Rayleigh theory leading to the same result in the limit where

the particle sizes are small. In this case, the choice to treat the problem goes to the solution of the Maxwell equations with the dedicate boundary conditions. Mie showed that the larger the scattering centres, the more forward-peaked scattering angular distribution is expected. The solutions for the scattering angular distribution is complex and depends on the different sizes and density distributions of particles. One of the most common analytical model proposal is based on the normalized Henyey-Greenstein (HG) volume scattering function as (85)

$$\tilde{\beta}_{HG}(\cos\psi, g) = \frac{1}{4\pi}\frac{(1-g^2)}{(1-2g\cos\psi+g^2)^{3/2}} \quad . \tag{3.24}$$

In Equation 3.24 the relative amount of forward or backward-scattering determined by the distribution of particle size densities in the water, can be governed by the parameter g which is simply the average cosine of the scattering angular distribution

$$g = -2\pi\int_{-1}^{1}\tilde{\beta}_{HG}(\psi, g)\cos\psi d\cos\psi \quad . \tag{3.25}$$

In addition the HG function has the advantage that is easily invertible, what it is so useful in the sampling of such distribution in Monte Carlo simulations such as (83)

$$\cos\psi = 2r\frac{(1+g)^2(1-g+gr)}{(1-g+2gr)^2} - 1 \quad , \tag{3.26}$$

where r is just a random number between 0 and 1. In principle, the knowledge of these distributions is needed, but on practice, the scattering angular distribution is either measured experimentally or approximated by some analytical model which can reproduces the global shape of Mie scattering angular distribution. More refined treatments based on HG functions can be found in Haltrin's studies (86) (85). These approaches include the addition of extra-terms, the usage of Legendre expansion approaches and the usage of delta-hyperbolic approximations in order to extract the most accurate scattering behaviour by large centres.

- **Petzold measurements and scattering phase functions**

  Concerning experimental scattering measurements, Petzold, by using a device with spectral response centered at 514 nm and bandwidth 75 nm of FWHM, was able to extract a widely referenced data (84) (86). Petzold's measurements include volume scattering functions $\beta(\psi, \lambda)$ for three kind of oceanic waters in a scattering angle range $0.1 < \psi$ [deg] < 180. The behaviour of the volume scattering functions of these three oceanic water showed to be consistent in their shapes, but not for their corresponding scattering coefficients differing by a factor of 50 (84). From the uniform shapes is then possible to define a typical particle phase function $\tilde{\beta}(\psi, \lambda)$. Such estimation was possible by using three set of Petzold's data from water with a high particulate load (84). The volume scattering function for pure sea water is determined by using Equation 3.21 (with tabulated data of $\beta_{Ray}(90°, \lambda_0)$ (84)).

  A generalization of the scattering models described before can be given by a linear combination what is a weighted sum of the particle-scattering phase function $\beta_{Mie}(\psi, \lambda)$ and the molecular scattering $\beta_{Ray}(\psi, \lambda)$ phase function. The average cosine $\langle \cos \psi \rangle$ of the global distribution can be expressed in turn as

$$\langle \cos \psi \rangle = \eta \langle \cos \psi \rangle_{Ray} + (1 - \eta) \langle \cos \psi \rangle_{Mie} \quad , \qquad (3.27)$$

  where η is the ratio of molecular scattering to total scattering ($\eta = b_{Ray}/(b_{Ray} + b_{Mie}) = b_{Ray}/b$) coefficients.

  There are two different models which can be used in ANTARES simulations for modelling scattering: the "Partic" model (this thesis) where the scattering angular distribution is fixed to that of the experimental measurements by Petzold with a high particle load and the analytical "MedSea" model where the scattering angular distribution is the sum of two "Henyey-Greenstein" functions which give the strongly forward-peaked particle contribution (representing the Mie scattering) and a smaller back-scattering component (representing the Rayleigh scattering). Figure 3.3 shows their scattering phase functions estimated for $\eta = 0.17$, the Partic model with the typical Rayleigh

and Mie scattering shapes (plus the global distribution) and the MedSea or Mediterranean Sea model.
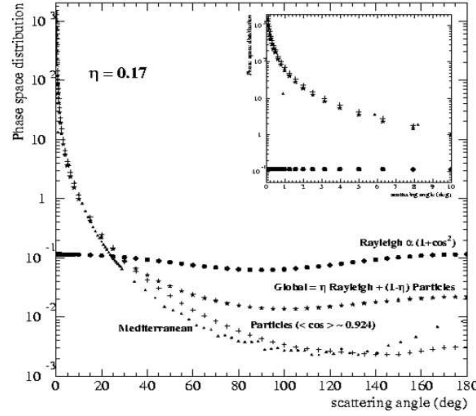
Figure 3.3: Scattering phase functions of molecular and particles for $\eta = 0.17$
- The isotropic trend of the Rayleigh scattering is clearly seen, the Mie (particles) strong forward peak distribution gives mainly the overall shape labelled as global. A comparison with the global distribution in the Mediterranean Sea is showed.

The Partic model data is the average of 3 similar measurements with very different particle densities and it is considered as typical of particles scattering in water. This particle scattering is strongly forward peaked with $\langle \cos \psi \rangle_{Mie} \sim 0.924$. Considering that $\langle \cos \psi \rangle_{Ray} \approx 0$ for the symmetrical phase function of water molecule (92) (Figure 3.3), the resulting average cosine of the global distribution can be then reduced to $\langle \cos \psi \rangle = (1 - \eta)\langle \cos \psi \rangle_{Mie} = (1 - \eta) \cdot 0.924$ (84). The MedSea model is adapted from the HG theoretical approximation as Equation 3.24 where as commented, the g parameter gives the average cosine of the global distribution. The Equation 3.27 can be also defined in terms of HG functions by changing η by α and the average cosines at right in Equation 3.27 by g_1 and g_2 respectively.

Additionally, the work performed in this thesis uses not collimated light sources (i.e. ANTARES OBs). Considering that $\langle \cos \psi \rangle_{Ray} \approx 0$, the scattering length should to be re-defined as an effective scattering length as

$$\lambda_{sca}^{eff} = \frac{\lambda_{sca}}{1 - \langle \cos \psi \rangle} = \frac{\lambda_{sca}}{1 - (1 - \eta)\langle \cos \psi \rangle_{Mie}} \quad . \qquad (3.28)$$

- **Wavelength dependence of scattering: Kopelevich parameterization**

  The $\lambda^{-4.32}$ wavelength dependence commented before for pure water scattering is not seen for natural waters, due to the diffraction from polydisperse particles largely impacting on scattering, often larger than the wavelength of visible light. Morel studies from the determination of volume scattering functions (84) show an evident dependence of the shape of $\beta(\psi, \lambda)$ on the wavelength. This diffraction depends on the particle size-to-wavelength ratio.

  The Kopelevich physical model of elastic scattering relates the volume scattering functions $\beta(\psi, \lambda)$ with the wavelength and parameterizes large number of marine water bodies from the estimation of the particle size distributions (93) (84). This model is composed by three different contributions: the volume scattering functions of pure water, large "L" (biologic particles larger than 1μm in size) and small "S" particles (mineral particles less than 1μm in size) such as

$$
\beta(\psi, \lambda) = \beta_{Ray}(\psi, \lambda) + \left(\frac{550}{\lambda}\right)^{0.3} \beta_L^*(\psi) v_L + \left(\frac{550}{\lambda}\right)^{1.7} \beta_S^*(\psi) v_S \quad ,
$$
(3.29)

  where the concentration-specific volume scattering functions for small $\beta_S^*(\lambda)$ and large $\beta_L^*(\lambda)$ particles as a function of the scattering angle ψ can be found in tabulated data (84). The typical concentration of small and large particles ranges from $0.01 \leq v_S$ [ppm] ≤ 0.20 and $0.01 \leq v_L$ [ppm] ≤ 0.40 respectively. Nonetheless v_S, v_L are in turn parameterized in terms of the total volume scattering function at 550 nm (84). By means of the Kopelevich studies it was also possible to determine several parameters as the density of the large particles, the relative refractive index and the size distribution for large and small particle fraction (86). By integration over ψ Equation 3.29, we obtain the formalism in terms of the scattering coefficient as (86)

$$
b(\lambda) = \frac{1}{\lambda_{sca}(\lambda)} = 0.0016(\frac{550}{\lambda})^{4.3} + 0.312 v_L (\frac{550}{\lambda})^{0.3} + 1.34 v_S (\frac{550}{\lambda})^{1.7} \quad .
$$
(3.30)

Figure 3.4 shows the scattering length as a function of the wavelength (Equation 3.30) according to the Kopelevich model for three different values of v_L, v_S such as $v_L = v_S$.
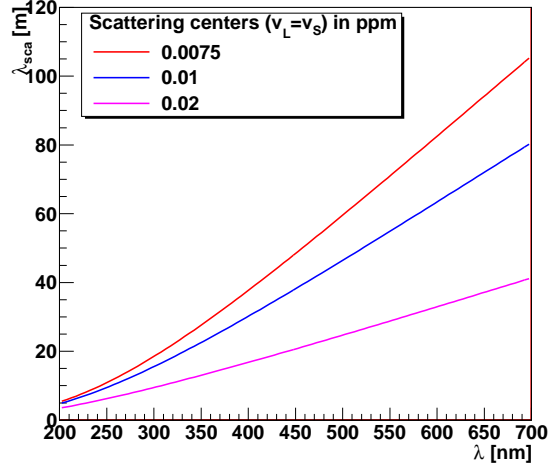
Figure 3.4: Scattering length spectrum based on Kopelevich model - For equal volume concentration of scattering centres, the low concentration of scatterers is traduced into large values of scattering lengths.

The accuracy of the model is of the 30% as Kopelevich set it (84). This model is used to parametrize the scattering features of the ANTARES detection media and which is used in the reconstructed track analysis for optical properties studies to be presented in Chapter 5.

3.5   Group velocity of light and refractive index

As commented before, the refractive index is another important IOP of the sea water. The group velocity of light crossing a given environment is defined as

$$v_{gr} = \frac{d\omega}{dk} \quad , \tag{3.31}$$

where ω is the angular frequency and $k = 2\pi/\lambda$ refers to the wave-vector. Taking into account that $\omega/k = c/n_{ph}$ where n_{ph} is the phase velocity refractive index, the group velocity can be expressed as

$$v_{gr} = \frac{c}{n_{ph}} - \frac{ck}{n_{ph}^2}\frac{dn_{ph}}{dk} = \frac{c}{n_{ph}}\left(1 + \frac{\lambda}{n_{ph}}\frac{dn_{ph}}{d\lambda}\right) \quad , \tag{3.32}$$

which allows us to define the group velocity refractive index as

$$n_{gr}(\lambda) = \frac{c}{v_{gr}} = \frac{n_{ph}(\lambda)}{1 + \frac{\lambda}{n_{ph}(\lambda)} \frac{dn_{ph}(\lambda)}{d\lambda}} \quad . \tag{3.33}$$

Looking for velocity of light signals in deep underwater neutrino experiments, the group velocity of light and not the phase velocity has to be used. The use of phase velocity instead group velocity for Cherenkov light signals and pulses of light from calibration sources in neutrino detectors, leads to errors in track reconstruction and horizontal distance measurements (94). The phase and group velocity of light do not coincide in a medium with dispersion leading to an additional delay of about 10 ns for a typical distance of $\sim$ 100 m between light source and OMs (94).

The phase refractive index n_{ph} of water depends on the wavelength, temperature and salinity (84) (95). It is well known that n_{ph} decreases with increasing wavelength. This dependence is well approximated by the Cauchy Equation on the visible region as (85)

$$n_{ph} = P + \frac{Q}{\lambda^2} + \frac{R}{\lambda^4} \quad , \tag{3.34}$$

where P, Q, R are expansion coefficients. At a fixed wavelength, n_{ph} decreases approximately gradually with the temperature at constant salinity and increases linearly with the salinity of sea water at constant temperature.

A representative approach for refractive index parameterization for pure and sea water, is given by Millard & Seaver where an expression with 27 expansion coefficients by using four experimental data sets (96) was used. This approximation formula takes into account the wavelength λ of light dependence, salinity S, temperature T and pressure P, with a valid range of $500 \le \lambda$ [nm] ≤ 700 nm, $0 \le$ T [°C] ≤ 30, $0 \le$ S [ppt] ≤ 43 and $0 \le$ P [dbar] ≤ 11000. The accuracy is of the order of part-per-million over most of the parameter range. The complete Millard & Seaver expression and the whole set coefficients can be found in (96) (85).

Another referenced model for refractive index of sea water is the Quan & Fry parametrization, which takes well-known the Austin & Halikas experimental data

set and fits to polynomial approximation as (95)

$$n_{ph}(\lambda, T, S) = n_0 + (n_1 + n_2 T + n_3 T^2)S + n_4 T^2 + (n_5 + n_6 S + n_7 T)\lambda^{-1} + n_8 \lambda^{-2} + n_9 \lambda^{-3} \quad .$$
(3.35)

The Equation 3.35 was set under hydrostatic pressure of 0 in the range intervals 0 < T[°C] < 30, 0 < S[%] < 35, and 400 < λ[nm] < 700. The complete data set can be found in (85) (95). The Figure 3.5 shows the Quan & Fry refractive index parametrization as a function of the wavelength with its corresponding pressure corrections with a linear interpolation between the extreme values of the pressure (97) (98). The two lines in Figure 3.5 for each case represent the extremes values of pressure.
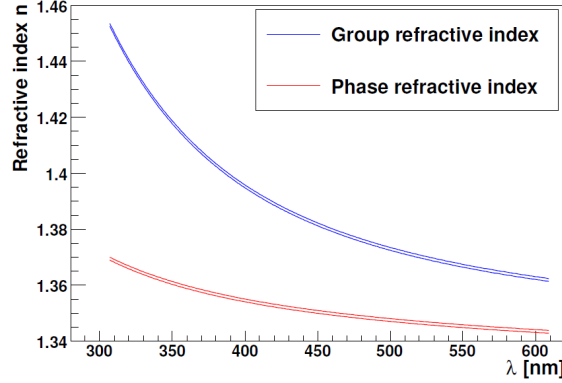
Figure 3.5: Refractive index by Quan & Fry - Conditions correspond to the typical environment of the ANTARES site between 2 to 2.4 km of depth, λ[nm](307,610), S[ppm] = 38.44, T[°C] = 13.2, and p[atm](200,240). The blue curve represents the group refractive index n_{gr}, the red curve refers to phase refractive index n_{ph}.

3.6   Optical properties in neutrino astronomy experiments

The high-energy neutrino detection is linked to the collecting ability of the Cherenkov light induced by ultra-relativistic charged leptons crossing the detection environment. Such collection power is dependant on the arrival time and the amount of light recorded in the detections units, and then on the optical properties of the media. The optical properties in deep lakes, oceans or ice are not equivalent. The effective scattering length is large for deep ocean sites, but the absorption

coefficient is an order of magnitude smaller concerning to deep ice. This section will review the knowledge about optical properties for several neutrino observatory sites, from the past to the present of the studies performed in their facilities.

3.6.1   Pioneer studies: the DUMAND site and Baikal lake

The transmission length spectrum at the DUMAND site was measured by free fall of a self-contained transmissometer together with equipment to measure conductivity, temperature and depth, obtaining profile measurements in the deep Pacific Ocean near Hawaii (Keahole point) (99). Concerning Baikal, along March-April 2001 a joint collaboration between Baikal and NEMO tested complementary methods by using dedicated and commercial instrumentation for optical properties measurement: the ASP-15 inherent optical properties meter and the AC-9 device (100). The most relevant details about their sea campaigns and their main results on optical parameters are summarized as follows.

- **Studies at the DUMAND site:**

  The self-contained transmissometer used by Zaneveld (99) with a path length of 1 meter, contained a pulsed Xenon light source and filters to profile the beam attenuation at intervals 50 nm wide from 400 nm to 650 nm at depths to $\sim$ 4500 m. A decrease on attenuation at all wavelengths as a function of the depth was found. After correction for the scattering length, the Figure 3.6 shows the absorption length spectrum extracted from the DUMAND site (101).

  The absorption spectra for DUMAND showed in Figure 3.6 was constructed by other author (101) by scattering correction as $b_p(\lambda) = A(400/\lambda)^{1.7}$ where the exponent 1.7 is taken for small suspended particles in the shallow ocean and valid along the wavelength region $400 < \lambda$ [nm] < 650. The only absorption measurement at the DUMAND site was estimated by Bradner and Blackington giving a value of $\lambda_{abs} = 25 \pm 1$ m (99). This measurement was estimated by using an uncollimated photostrobe with an interference filter to measure the $1/e$ transmission distance of the 480 nm light.

- **Studies in Baikal lake:**

  The ASP-15 meter was designed and developed by the Baikal collaboration. It has two receiving channels, one with a wide aperture for absorption and
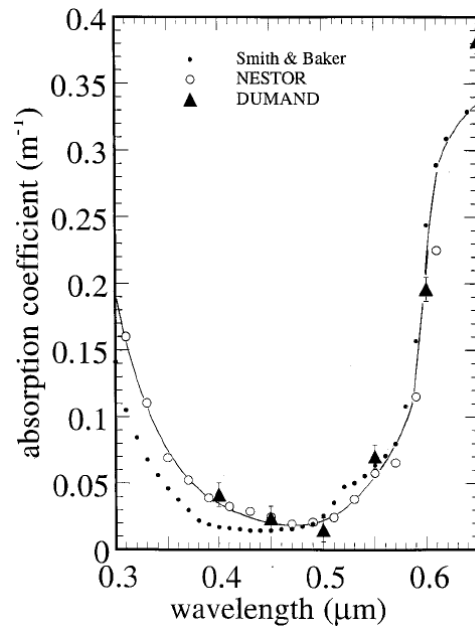
Figure 3.6: Absorption length spectra at the DUMAND site - The DUMAND
spectra (solid triangles) is compared with measurements from the early phase of
NESTOR experiment before 1997 (only for reference) and in turn with the spectrum
of the clearest natural water by Smith & Baker.

scattering coefficient estimation, and other equipped with a rotation mirror
and a narrow angle collimator for measuring the phase scattering function.
The ASP-15 meter operates in the range $369 < \lambda[\text{nm}] < 691$, the uncer-
tainties for absorption and scattering coefficients are close to the 5% and
10% respectively (100). The AC-9 device (to be described latter) by the
NEMO collaboration was used simultaneously to the ASP-15 measurements.
The Figure 3.7 shows the absorption length spectra estimated by the both
devices (100).

Based on Figure 3.7, the agreement of the results is quite nice independently
of the intrinsic systematic errors of each device (100). The spread between
both data sets can be related to local changes in optical and hydro-physical
properties of the water column (100). The peak of the spectra is located
$\sim$490 nm with a mean value of $\lambda_{abs} = 28.3 \pm 1.5$ m for the ASP-15. This
updated value is in agreement to previous results in the Baikal collaboration
(102).

Concerning scattering spectrum, Figure 3.8 depicts what is obtained from
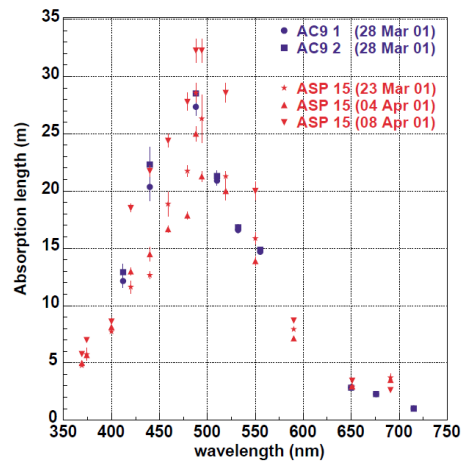
Figure 3.7: Absorption length spectra measured at Baikal lake - The data set was computed in a depth in Baikal lake of 1000 m by using the ASP 15 and AC9 devices.

the ASP-15 and AC-9 measurements for the scattering coefficient at ~ 1 km of depth. As seen, the agreement between the experimental data set extracted from both devices is quite good. The measured value for scattering length at its maximum transparency ($\lambda \sim 488$ nm) is $\lambda_{sca} = 58.8 \pm 3.5$ m. More details on the experimental setups, data sets and other related issues can be found in (100) (103).
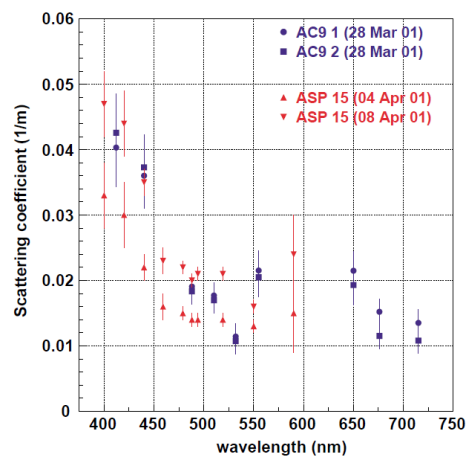
Figure 3.8: Scattering spectrum in terms of $b(\lambda)$ measured at Baikal lake - The data set was estimated at 1000 m of depth with the ASP 15 device between March and April 2001 campaigns.

3.6.2   Estimations in deep ice: the AMANDA and IceCube case

The optical characterization of the AMANDA site was done by using pulsed and continuous light sources (lasers and LEDs) along the detector (104) in the wavelength range $313 < \lambda$ [nm] < 560 and depth range $1.1 < z$[km] < 2.4. These devices included a frequency-doubled Nd-YAG laser flashing light pulses at 532 nm with a pulse width of 4 ns located in the counting house on the ice surface. The laser light was conduced by optical fibres to diffuser balls installed in specific locations in the detection strings, following an isotropic emission pattern. Other two nitrogen lasers flashing at 337 nm, 3 ns width pulses located on different strings near the centre of the detector were used. A diffusive filter was used to generate an upward peaked intensity pattern almost proportional to the cosine of the angle from the vertical. In addition, a variable light attenuator controlled from the surface was used reaching up to seven decades of attenuation. Apart from the laser sources, there were eight OMs equipped with six LEDs flashers of 470 ± 30 nm. These blue flasher modules were located at different depths on the detector in two of the three longest detection strings. Each LED had a lambertian light output profile and was mounted with its symmetry axis pointing vertically up. Other UV flashers at 370 ± 12 nm were used as well in 41 OMs on one of the strings.

The optical properties of the South Pole are not homogeneous along the depth, due to the concentration of lots of impurities (dust particles) embedded into the ice layers. Therefore, the average cosine of the global scattering has several contributions from dust components as salt, minerals, acids and soot. An average cosine of 0.94 of the global scattering distribution was estimated (105).

For the most densely instrumented depth range, typically between 1530-2000 m it was possible to measure the scattering at four different wavelengths and to fit the wavelength dependence to a power law such as $b_{sca}^{eff} \propto \lambda^{-\alpha}$ where a factor $\alpha = 0.90 \pm 0.03$ was extracted, as Figure 3.9 shows.

The experimental data points are wavelength averages normalized to $b_{sca}(532)$. The shaded curve represents the one-standard deviation uncertainty including systematics (104). The error in α covers a 5% of systematic uncertainty added in quadrature to the statistical error of each data point.
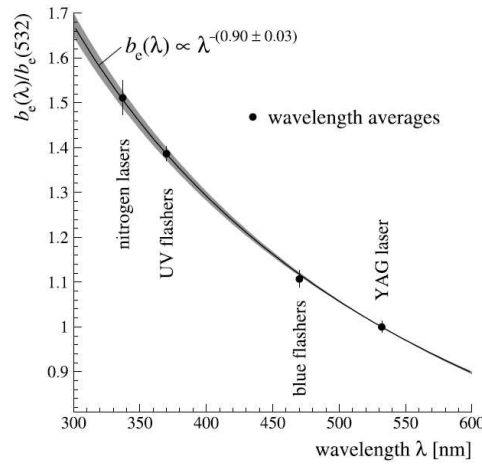
Figure 3.9: Effective scattering coefficient wavelength dependence in the South Pole - The spectrum was built by using pulsed light sources at four different wavelengths.

On the other hand, the absorption estimation in ice is modelled empirically with three main contributions as a function of the wavelength (104)

$$a(\lambda) = A_U e^{-B_U \lambda} + C_{dust}\lambda^{-\kappa} + A_{IR}e^{-\lambda_0/\lambda} \quad , \tag{3.36}$$

where the two exponential terms govern light absorption by ice in the UV and infrared respectively due to molecular absorption by pure ice (104), and the second takes into account absorptivity by insoluble dust particles in ice. The absorption length spectrum obtained at the South Pole at different depths between 830 and 1755 m is seen in Figure 3.10.

Other extended studies systematically performed between the deepest region from 1400 to 2400 m in deep glacial ice have been recently reported at 400 nm (106) by the IceCube observatory, what extends the research performed by AMANDA. As commented in Chapter 2, the IceCube detector is a large array of optical sensors (DOMs) including LEDs as *in-situ* light sources for calibration.

In the case of IceCube optical characterization, each DOM is equipped with 12 LEDs on a flasher board able to produce detectable light by adjacent DOMs up to 0.5 km away. The LEDs are addressed in six different azimuth angles 60°-spaced and two different zenith angles. In this way, the charge and time distribution of light is recorded throughout all detector depths and sections. Then, a global fit approach (likelihood-based) is carried out and the result is a set of absorption and
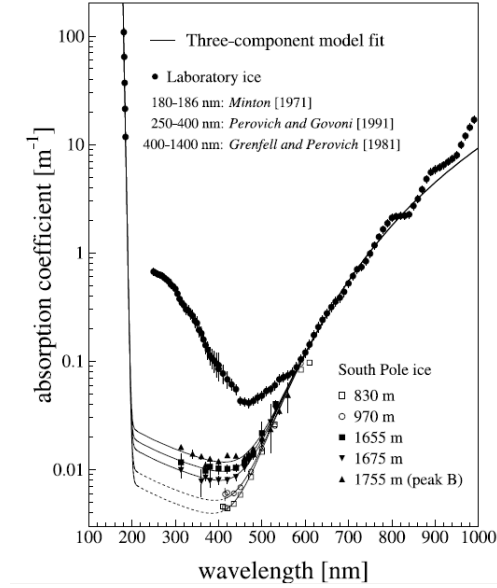
Figure 3.10: Absorption coefficient as a function of the wavelength in the South Pole - Ultraviolet region up to infrared region are compared with laboratory ice grown estimations. Measurements between 800 and 1000 m ($\circ$, $\square$) are from previous studies (104).

scattering parameters in 10 m layers at depths from 1450 to 2450 m.

The ice parametrization used in these updated IceCube studies (106) follows a six-parameter model. The effective scattering coefficient dependence on wavelength is computed as a power law normalized to 400 nm as in AMANDA studies. The total absorption coefficient is described as the sum of two components, one due to dust and other being a temperature dependant variable component for ice. The effective scattering and absorption formalism used in IceCube analysis are

$$b_e(\lambda) = b_e(400) \left(\frac{\lambda}{400}\right)^{-\alpha} \quad a(\lambda) = a_{dust}(400) \left(\frac{\lambda}{400}\right)^{-k} + Ae^{-\frac{B}{\lambda}}(1+0.01\delta\tau) \quad ,$$

$$(3.37)$$

where $\delta\tau$ represents the temperature difference relative to the depth of 1730 m (the center of AMANDA).

The dashed line in Figure 3.11 represents the updated measurements of the Additionally Heterogeneous Absorption (AHA) model for AMANDA. The uncertainties of the AHA model for depths between 1730±225 m are a 5% for scattering and close to the 14% for absorption measurements. The values for the effective scattering length at large depths where the increase of the transparency of the ice is
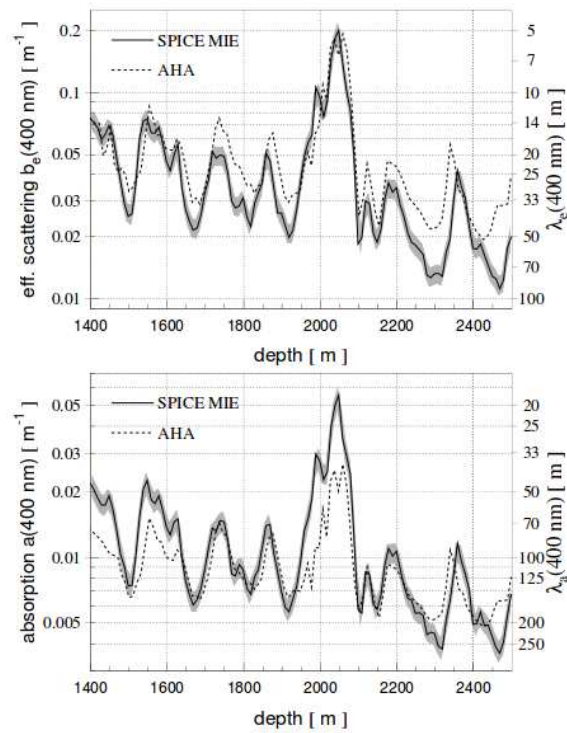
Figure 3.11: Scattering and absorption coefficients at 400 nm as a function of depth in IceCube - The grey band correspond to $\pm 10\%$ of systematics equivalent to $\pm 1\sigma$ combined statistical and systematic uncertainty at most depths.

expected, can reach up to 50 m. For the absorption case, lengths better than 100 m are estimated. These results confirm the shortest scattering lengths and large absorption lengths achieved in deep ice environments, what is the opposite case of deep-sea or water based environments for neutrino facilities. Such absorption lengths have been also achieved in water-based environments as in the Super-Kamiokande experiment which have reported values of attenuation length exceeding 100 m in better agreement to Pope & Fry measurements than for Smith & Baker predictions (107).

3.6.3 Contribution of NEMO and NESTOR at the Mediterranean Sea

The highly-sensitive AC-9 transmissometer (manufactured by WETLabs (108)) used for NEMO characterization of the Capo Passero site as commented before, can operates in the range $412 < \lambda[\text{nm}] < 715$. Its accuracy is about 1.5×10^{-3} m^{-1} both for absorption and transmission coefficients estimation (100), and the scattering coefficient can be obtained as the difference between transmission and absorption coefficients. The set of measurements were performed for visible light wavelengths. The attenuation coefficient was measured with a collimated source of light with angular acceptance of $\sim 7°$. Both attenuation and absorption measurements are done independently by using two different light paths extending the light spectra at eight different wavelengths. The Figure 3.12 shows the absorption and attenuation length spectra for several sea campaigns at the NEMO site.

The NEMO site inherits a water transparency comparable to the clearest natural waters reported in results from Smith & Baker. At distances larger than 2000 m the absorption and transmission coefficients measured in different seasons are compatible within their experimental errors. The complete data set reported by NEMO can be found in (109), obtained as the weighted average values of the absorption and attenuation coefficients as a function of the wavelength. The weighted average is computed from the values of absorption $a(\lambda)$ and transmission $c(\lambda)$ measured in each instrumentation deployment at distances range between 2850 m and 3250 m. The experimental errors are treated as the RMS of the distribution of such parameters. As summary, the absorption and attenuation lengths obtained close to the maximum (~ 440 nm) were $\lambda_{abs} = 66.5 \pm 8.2_{stat} \pm 6.6_{syst}$ m and $\lambda_{att} = 34.7 \pm 3.3_{stat} \pm 1.8_{syst}$ m respectively. These estimations were obtained by
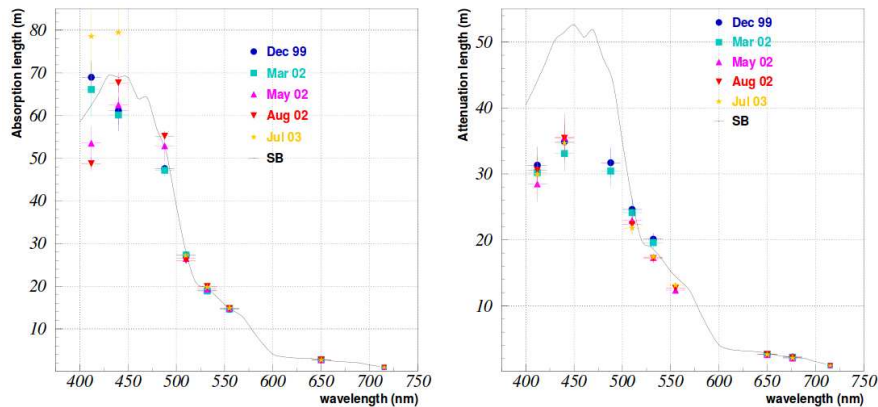
Figure 3.12: Absorption and attenuation length spectra for several sea campaigns by NEMO - Left: averaged values of absorption length along $\sim$ 3 years in Capo Passero. Right: averaged values of attenuation length estimations at Capo Passero along $\sim$ 3 years. Absorption measurements show nice agreement with the Smith & Baker spectrum for the clearest natural waters, and attenuation for $\lambda >$ 500 nm.

using a collimated beam and not an isotropic source as for DUMAND, NESTOR or ANTARES, which prevent us from a direct comparison (109).

On the other hand, the studies on optical properties in the deep Ionian Sea (NESTOR site) have been performed by using diverse kinds of devices. They have showed the consistency of the results along 20 years of research and sea campaigns. The most recent results were obtained by means of the Long Arm Marine Spectrometer (LAMS) (110) for transmission length measurements (May 2009). The LAMS uses eight groups of isotropic light sources in the range between $370 < \lambda[\text{nm}] < 530$ which it can be deployed at several depths and recovered to perform new measurements at other sites. Due to its open geometry, it can collect both direct photons and a fraction of scattered photons in the surrounding water (110). The light intensities of the LED sources located in one of the endings of the LAMS are detected by a photodiode in the opposite ending. The transmission length coefficient is computed directly from the Beer-Lambert Equation. The most updated transmission and attenuation length spectra by NESTOR is shown in Figure 3.13.

The difference between both curves for transmission and attenuation length measurements comes from the very steep slope of both curves, plus the small uncertainty in the wavelengths of the different kinds of sources considered at 1992 and
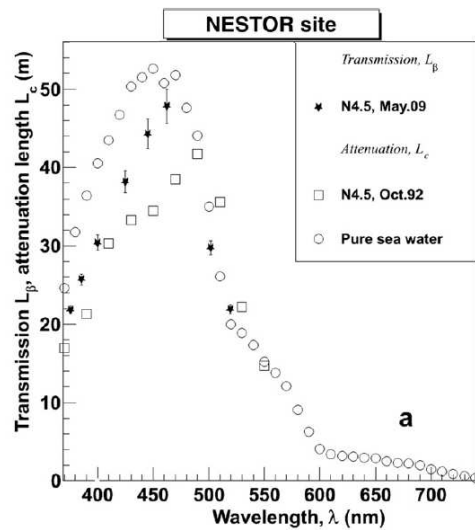
Figure 3.13: Transmission length spectra for several sea campaigns by NESTOR - The difference between transmission and attenuation concepts comes from the kind of light source used, attenuation (well-collimated beam) and transmission (isotropic source of light).

2009 sea campaigns. The variation of the transmission length measurements as a function of depth is above 2-5 m with shorter transmission lengths for shallower water (110). The maximum of such measurements are reached at depths between 3000 m and 4000 m. Transmission and attenuation length measurements have been reported but no absorption length nor scattering studies have been given yet, except for the ones reported in old sea campaigns in 1992 (101), where corrections by scattering effects were done, but built up by other author (101).

3.7 Optical parameters in ANTARES R&D phase and status

The ANTARES R&D phase was crucial in order to find the relevant hints towards an optical characterization of the site. There were several campaigns in order to characterize the ANTARES site: the "test 1" looking for study the optical background, the "test 2" in order to study the biofouling and the "test 3" and "test 3'" focused to study the optical properties of the site by means of a continuous and pulse source respectively. This section will describe briefly the results obtained in the test 3, and more in detail those obtained in the test 3'. From these studies some

contributions to the characterization of the optical properties of the site have been done in the past (111) (83) (82). More recently, some measurements have been started by using the ANTARES OBs for measuring transmission, absorption and scattering parameters (74) (78), and other already published as the measurement of the group velocity in the ANTARES site (112).

3.7.1 Experimental setups

The light propagation experiments known as test 3 and test 3', used a gradually improved mooring line immersed at the ANTARES site, by means of which several data sets were obtained in the sea campaigns between 1997-2000. The first set (test 3) included a continuous and collimated DC source and a detector located at several distances away from it with the aim to get the light attenuation dependence on distance (111). The second setup (test 3') allowed to compute transmission, absorption and scattering contributions (111). The full improved device used finally is depicted in Figure 3.14 what represents the test 3' itself.
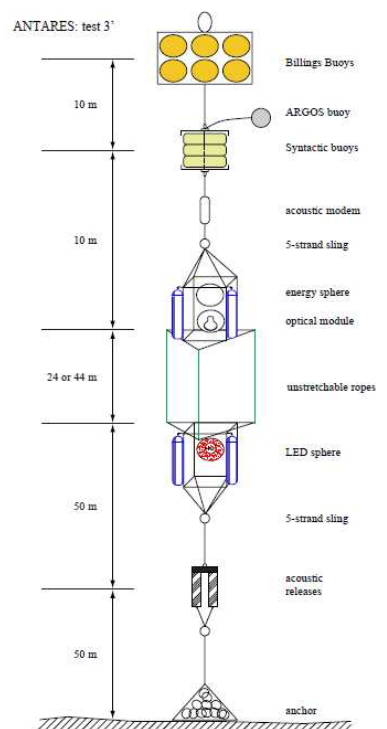
Figure 3.14: Sketch of the mooring line used in ANTARES test 3' - A flexible structure was gradually improved for light propagation studies at the ANTARES site, the figure corresponds to the test 3' experimental set.

The test 3' was basically a standalone experiment equipped with a PMT able to measure *in-situ* the distribution of the arrival times of photons emitted at several distances by means of isotropic pulsed light sources. The final mooring line used in test 3' housed a pulsed isotropic LED source (six LEDs, 10-cm side-length cube, at 473±29 nm and 375±10 nm) housed in a high-pressure resistant sphere (111). In addition, the LED intensity was fixed to reach a detection efficiency of about 1 detected photon per 100 triggers for the shortest source-detection distance, working within the SPE regime. The discriminator threshold was set at a pulse height close to 0.3 times the amplitude of the SPE peak (111). In the upper part of the structure there were buoys to keep it taut and vertical, and fixed at the bottom by means of a heavy anchor. Electronics were put inside a high-pressure resistant vessel or "energy sphere" which provided a 6 kHz trigger signal which was fed to the LED pulsers and through a delay to a TDC, started by the delayed trigger signal and stopped by the first PMT signal above the discriminator threshold. One of the advantages of this final configuration was that the relative large distances used in the experiment make possible discriminates between several optical parameters, since it is possible to take into account long absorption or scattering lengths with different setups (83). The main disadvantage is the use of analytical approximations for the scattering angular distribution of large scattering centres since the angular distribution was not measured (83).

3.7.2 Attenuation, transmission, absorption and scattering of light

As commented, two campaigns or tests were used in order to extract optical parameters from the ANTARES site. The first set or test 3 used a continuous source and was possible to extract the attenuation length of light at 473 nm. The second set or test 3' was carried out by using a pulse light source and transmission, absorption and scattering parameters were estimated with the associated systematics at 375 and 473 nm. The measurements obtained in each campaign are summarized as follow.

- **Effective attenuation length:**
  Based on December 1997 setup (test 3) with the continuous collimated source of light at 473 nm, for each chosen distance D between the light source and the detection unit (from 6 to 27 m), the luminosity of the beam

Φ_{LED} was adjusted to yield a constant current I_{PMT} on the PMT (111), calibrated in air environment. The emitted intensity and the current I_{PMT} in the PMT can be then related by

$$I_{PMT} \propto \frac{\Phi_{LED}}{D^2} \cdot e^{-\frac{D}{\lambda_{att}^{eff}}} \quad , \tag{3.38}$$

which allows to extract the effective attenuation length parameter from the dependence between the LED intensity and the distance to the source (Figure 3.15). As this method used a collimated beam, special attention should to be paid when compares to other measurements with different light output (i.e. isotropic).
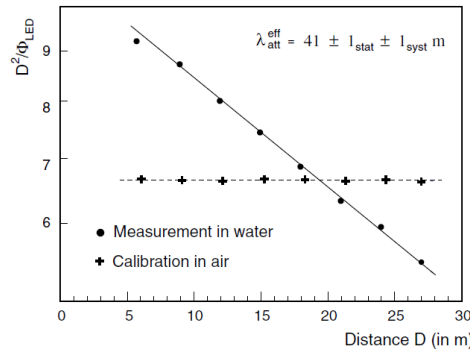
Figure 3.15: Effective attenuation length extracted from test 3 (1997 setup) - Statistical and systematic errors are indicated, a value ~ 41 m can be extracted for a wavelength of 470 nm for the case of a collimated beam.

A dedicated Monte Carlo simulation reproducing such experimental set differs in 3 meters the estimation from Figure 3.15 of λ_{att}^{eff} (blue, collimated) $= 41 \pm 1$(stat.) ± 1(syst.) m, being the statistical and systematics unchanged (111).

To disentangle the absorption and scattering lengths from such estimation a more rigorous procedure is needed. Both standalone contributions are extracted as will be explained in brief from the measurements made with the test 3', being actually the reference values for the spectra in ANTARES site (111) (113).

- **Transmission, absorption and scattering length:**
  The final sketch of the test 3' mounting (Figure 3.14) allowed to extract

the official values used in ANTARES as optical properties of the site at 375 and 473 nm, computed by using isotropic sources of light. Again, it is important to remark that measurements of test 3 (December 1997) and test 3' measurements (1997-2000) for attenuation and transmission length can not be directly compared due to the kind of light output of the source. For isotropic sources of light (test 3'), the time distributions shown in Figure 3.16 have a clear peak coming from the direct photons and a tail extended to larger delays due to scattered photons.
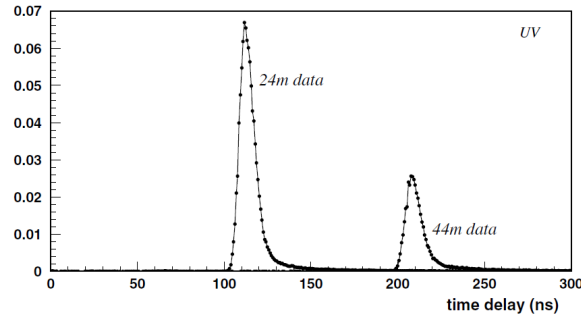
Figure 3.16: Time distributions for a UV LED pulse light - Two source-detector distances are indicated: 24 m data is normalized to the unit and 44 m data normalized to the 24 m one in addition to a factor $(44/24)^2$, so that the difference only comes from the exponential attenuation factor.

The effective transmission length can be determined from the ratio of the integrated time distributions measured at two distances as

$$\frac{\int N_{d_1}(t)dt}{\int N_{d_2}(t)dt} = \frac{d_2^2}{d_1^2} \cdot e^{-\frac{d_1-d_2}{\lambda_{tr}^{eff}}} \quad , \tag{3.39}$$

where d_1, d_2 are the light source - detection unit distances and N_{d_i} is the time distribution at a distance d_i after background suppression and multi-photon event correction (111). It leads to the extraction of transmission lengths for 375 and 473 nm showed in Table 3.1.

Such estimations mismatch within their statistical errors. The systematic uncertainties due to LED luminosity are not monitored and assumed to be the same for the time distributions collected at the distance where the measurements were performed.

The way to extract the absorption and scattering parameters is based on

Epoch (wavelength [nm])	λ_{tr}^{eff}
July 1998 (473)	60.6±0.4
March 1999 (473)	51.9±0.7
July 1999 (375)	21.9±0.8
September 1999 (375)	22.8±0.3
June 2000 (375, 473)	(26.0±0.5, 46.4±1.9)

Table 3.1: Such estimations were performed by using an isotropic pulse light source. The blank in table corresponds to no measurements in that epoch, the error is that of the statistical.

a global fit of the experimental time distributions to Monte Carlo distributions (111), including the geometry of the experiment as well as the optical properties of the medium (λ_{abs}, λ_{sca}, η), the light source - detection unit distance d_i, the origin of time of each distribution and the collection efficiency for each distribution (111).

In the Monte Carlo simulation, probability distribution both for absorption and scattering are used (111), which are proportional to $e^{-x/\lambda_{abs}}$ and $e^{-x/\lambda_{sca}}$ respectively. Weights were applied to take into account the dependence of the PMT detection efficiency on the incidence angle of photons (111). The final Monte Carlo spectrum can be associated to a low intensity light source generated in a non-noise environment. Multi-photons event correction is applied since the TDC is working in single-hit mode where only the first one is detected (111). Both results for λ_{abs} and λ_{sca} extracted from the global fit method are represented in Figure 3.17.

The horizontal error bars in Figure 3.17 refer to the spectral resolution of the source ($\pm 1\sigma$) and the vertical ones for statistical errors. The circles represent measurements in pure sea water found in the literature (i.e. as (84)). The scattering length for pure water is used as an upper limit for sea water measurements. The measurements of the scattering length at the ANTARES site both for 375 and 473 nm are roughly compatible with the Kopelevich parametrization for small scattering centres concentrations at $v_L \approx v_S \approx 0.0075$ (113) and in agreement with reference values for the clearest natural waters ($v_L \approx 0.01$) (84).
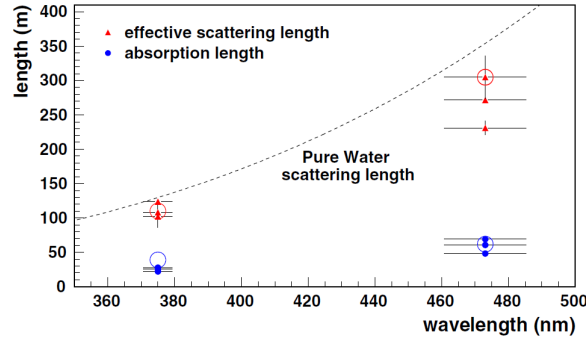
Figure 3.17: Absorption and effective scattering lengths (mean values) at the ANTARES site during the R&D phase - A dedicated simulation was needed due to the difficult of disentangle both parameter from *in-situ* transmission/attenuation data. Each set of three measurements comes from the data summarized in Table 3.1.

3.7.3 Group velocity of light

The group velocity of light can be estimated by means of Equation 3.32 using empirical models for the refractive index and evaluated for the parameters of the ANTARES site: $p = 230$ atm, S = 38.44 % and T = 13.2°. The refractive index model of Millar & Seaver nicely agrees with Quan & Fry parametrization at the ANTARES site natural conditions. Figure 3.18 shows the set of experimental points at 375 and 473 nm for the refractive index computations at the ANTARES site that were obtained with data from the test 3'. The parameterizations by Millar & Seaver (MS) and Quan & Fry (QF) for the phase and group velocity of light are also shown.

The experimental measurements were done by estimating the group velocity of light as $v_g = \Delta d/\Delta t$ where Δd corresponds to the difference between the light source and the detection unit, and Δt represents the time difference between the times at which the direct photons flashed by the light source reach the detection units at two different distances from the source. The values for the group velocity of light obtained were

$$v_g(\text{experimental}) = \begin{cases} 0.2185 \pm 0.0015 & \text{m/ns} \quad \text{blue} \\ 0.2153 \pm 0.0015 & \text{m/ns} \quad \text{UV} \end{cases} . \quad (3.40)$$

The main systematic error comes from the length of the cables linking the source to the detection unit. As it can be seen (Figure 3.18), the experimental formalism
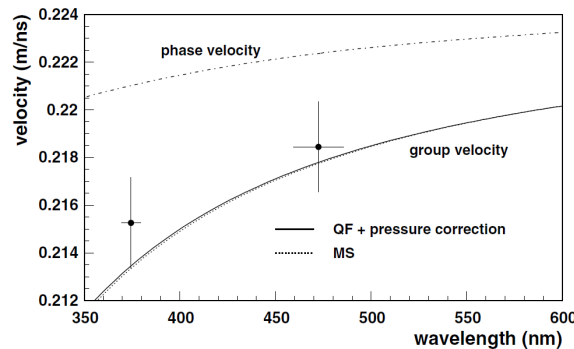
Figure 3.18: Group velocity of light in ANTARES R&D - Data points correspond to ANTARES measurements at 375 and 473 nm from the test 3'. Comparison with Quan & Fry (QF) and Millar & Seaver (MS) are indicated, as well as the phase velocity of light. The experimental measurements in ANTARES R&D lies on the predictions for the group velocity.

(Millar & Seaver) and analytical values are in good agreement.

Recently, a new sort of measurements of the group velocity have been performed using the LEDs of the multi-wavelength OB (112) whose results are summarized in Figure 3.19.

The new measurements on the group velocity of light in sea water is measured by registering the time delay of the photons arriving at the OMs at different distances from the OB along the same line. The time distributions on each storey are fitted by the convolution of a Gaussian and an exponential function and the peak time is plotted as a function of the distance to the OB. Its slope is related to the group velocity of light. The group velocity of light in sea water was parameterized by Quan & Fry based on *in-situ* measurements performed by Austin & Halikas (95). The parameterization as a function of the wavelength and pressure includes the dependence on the temperature and the salinity of the ANTARES environment. Measurements of the refractive index at different wavelengths from the multi-wavelength OB data are compatible with the Quan and Fry predictions within its systematic uncertainty.

3.7.4 Status and prospects about water optical properties estimation

The role of the knowledge on the optical properties in underwater neutrino observatories, as well as its continuous monitoring aims at knowing its impact on the
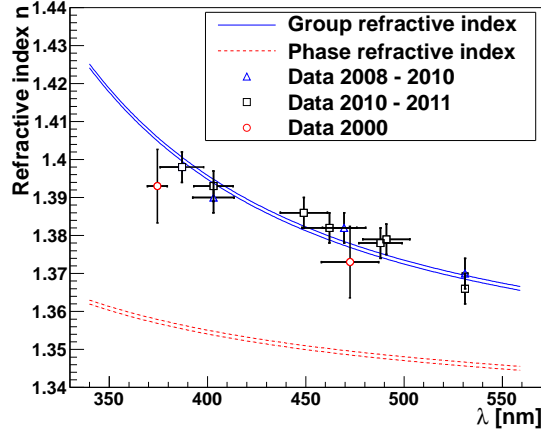
Figure 3.19: Updated refractive index estimations at different wavelengths - The data sets indicate the measurements performed along the period when the kind of source was fully available for measuring, except 2000 data what concerns to ANTARES R&D showed before. Such estimations covers the usage of the standard ANTARES OB and the multi-wavelength OB.

detector performance.

In the ANTARES R&D phase important advances were reported inside the collaboration as the works done in (111) (83) (82).

In addition to the results obtained during the R&D phase, a first attempt to measure and monitor the water optical properties in ANTARES by using its own instrumentation is reported in (114) where the transmission length of light is obtained by fitting to the Beer-Lambert law, data obtained from OBs calibration runs. The main conclusion extracted from this preliminary study was the feasibility to estimate the transmission length of light at 470 nm as an average value equal to $\lambda_{tr}^{eff} = 43.00 \pm 1.1(stat)$ m, the reproducibility of the measurement in time was left as a work to be continued. In addition, the depth influence was roughly estimated.

The statistical errors in the test 3' (115) for the different optical parameters, as well as the concerning to the preliminary OB studies commented before, are matter of study on this thesis. Other systematics (115) as the source anisotropy, noise subtraction, stability of LED intensity and PMT efficiency, angular distribution of light output, ARS calibration, seasonal and depth variations are matter of review also.

The main subject of this thesis leads to the determination of the main IOP of

the water named transmission, absorption and effective scattering length looking for their impact on the detector performance. The estimation of such parameters by using the OBs are determined by using the Beer-Lambert law (transmission length) and a dedicated data - Monte Carlo time residuals comparison for OBs data through a robust χ^2-minimization. The result of these experimental procedures are connected to their evaluation in the ANTARES track reconstruction chain and the validity of the minimization by using and independent technique based on raw comparisons of data - Monte Carlo distributions for different track reconstruction parameters. The impact of the results on the main track reconstruction parameters and detector performance, and their discussion with previous and less detailed results in ANTARES is performed.

Chapter 4

Estimation of the optical properties with the OB technique

Hard work defeats natural talent

Rock Lee

Several efforts have been done in the past to characterize optically the ANTARES detection environment. Results in the test 3' ([113](#)) were relevant, but their reproducibility was not possible and their systematics a matter of review. A monitoring from online measurements is needed in order to know its possible seasonal variation or stability. Very preliminary studies of the ANTARES detection environment with its own instrumentation ([116](#)) gave some hints in the past towards a more detailed study performed in this thesis.

This chapter presents one of the two strategies developed to determine the water optical properties at the ANTARES site by means of its own instrumentation. The first one is based on the Optical Beacon data analysis (OB technique) and the second one is based on the analysis of reconstructed track data (reconstructed track technique). The OB technique is presented in this Chapter 4 and the reconstructed track technique in the final Chapter 5. In the OB technique two independent methods are considered, one to measure the transmission length and other for absorption and scattering length measurements.

The transmission length of light is obtained from an exponential fit (Beer-Lambert equation) to the decrease of signal hits along a target line and at three different

wavelengths (402, 470 and 531 nm). The absorption and scattering lengths are computed from the arrival time distributions of the OB light at 470 nm comparing real data with Monte Carlo samples generated with different optical parameters, namely absorption, scattering and the contribution of Rayleigh scattering. The absorption and scattering lengths are determined from a modified Pearson's χ^2-test.

This chapter is structured in three parts. First, several issues common to both methods, such as data selection and quality, signal extraction and handling, noise subtraction, PMT efficiency and systematic effects, are explained. Secondly, the method to estimate the transmission length as well as the analysis of the precision achieved, the quality of the fit and the evolution of this parameter in time are described in detail. Finally, concerning the extraction of the absorption and scattering lengths, the development, optimization and results of the method are presented. After analysing data and Monte Carlo arrival time distributions, the method to discriminate the optical parameters based on a modified Pearson's χ^2-test is set and tested with Monte Carlo samples and extended to real data. All the experience in the method leads to the use of a "run-by-run" simulation taking into account the most realistic conditions during data acquisition.

4.1   Data handling and systematics

The data quality and good acquisition conditions are relevant to obtain the best estimation of the optical parameters in ANTARES. The use of the Beer-Lambert equation and a modified Pearson's χ^2-test are the basis for transmission, absorption and scattering lengths determination, respectively. To reach the most reliable results, appropriate data run selection, signal filtering and handling are mandatory. These considerations and the treatment of some identified systematics are presented in this section.

4.1.1   Data run acquisition, signal extraction and run selection

More than 250 special OB runs for optical properties studies with the OB technique have been taken in about four years, for all types of OBs described in Chapter 2. In these OB runs, light pulses are flashed from a single or set of LED(s) of a given OB and recorded by the OMs throughout the detector. In each storey there are six

ARSs (2 per OM) numbered from 0 to 5. If the storey contains an OB, its ARS is labelled as 6. An OB event is identified by means of an algorithm which looks for the `ARS_6` label corresponding to signals in the small PMT in the case of the LED OB, or the built-in photo-diode in the case of the laser OB. The data stored in such OB events are the time and charge information of the hits recorded (`ROOT TTree` structure) in all the lines, storeys, OMs and ARSs along the detector. As mentioned in Chapter 2, a hit is a pulse, time and charge, in one OM processed by one of its ARSs. A special set of programs for OB data analysis has been developed by the calibration group in Valencia called `HistoFiller` which sorts all the information in histograms and `ROOT TNtuples`, which are easily handled. Figure 4.1 shows a typical hit time residual distribution (difference between the emission time of the OB light and the time recorded by the OM when the flash arrives) as an example. The hit time residual distributions are shifted by the direct time taken by photons to arrive at each OM. The measurement of the group velocity of light (112) is used as an input for `HistoFiller`. In addition, the positions of the OMs and time calibration constants in the detector are extracted directly from the ANTARES database.
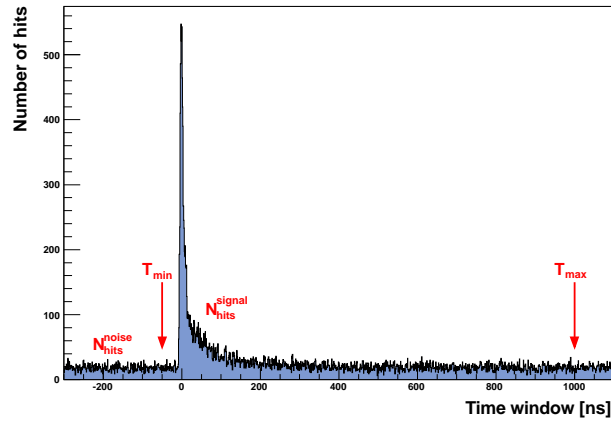
Figure 4.1: Time information extracted from OB runs - Example of hit time residual distribution. The time window where the OB technique is carried out is restricted to the time range [T_{min}, T_{max}] described in the text.

As seen in Figure 4.1, there is a clear signal fingerprint (N_{hits}^{signal}) formed by the peak and the tail of the time distribution associated to direct and scattered photons, respectively. Before the signal arrival as well as for very long times, the

counting rate on the OM is entirely due to the optical background hits (N_{hits}^{noise}) (bioluminescence + ^{40}K).

The first step to extract the signal is to determine the noise contribution per storey/OM/ARS due to this optical background. This is evaluated as the mean baseline in the noise region defined before the signal arrives, typically 10 ns before the peak, T_{min}, as indicated in Figure 4.1. Once the background contribution has been estimated, the signal is obtained by computing the difference between the contribution of all the hits contained in the time interval [T_{min}, T_{max}] and the estimated background. Here, T_{max} is typically set to 1000 ns after the first signal arrival, where most of the hits come from the optical background.

The level of optical background is used as an indicator of the quality of the run. The OB runs have been rigorously performed when the optical background in the detector is low enough ($<$ 100 kHz). At very high background rates, the `HistoFiller` code gets in trouble to find the signal peak biased by noise fluctuations, since the statistics at large distances from the OB becomes too low. In order to avoid this, low background conditions and moderately high statistics for OB runs are required. About six minutes of data taking enable to obtain nearly 100k light flashes which are found to be enough to perform suitable optical properties measurements. In this way, the "golden runs" to be used in the OB technique are featured by:

- a background rate below 100 kHz,

- a flat-shape trend along the line,

- $N_{flashes} > 100$k.

A typical example of golden run is shown in Figure 4.2-left.

In the selection of golden runs, runs with an increasing background along the line reaching 100 kHz rates are discarded. Likewise, runs with very low $N_{flashes}$ are also rejected, these runs are called "copper runs" (see Figure 4.2-right).

On the other hand, some OMs have a counting rate outside the nominal values, or they can be inactive during acquisition. A cut in the minimum number of hits per OM, $N_{hits}^{OM} > 500$, is applied, in such a way that it ensures the rejection of very low counting OMs and guarantees minimum statistics.

For the blue LEDs in the standard OBs, several configurations and OBs in the
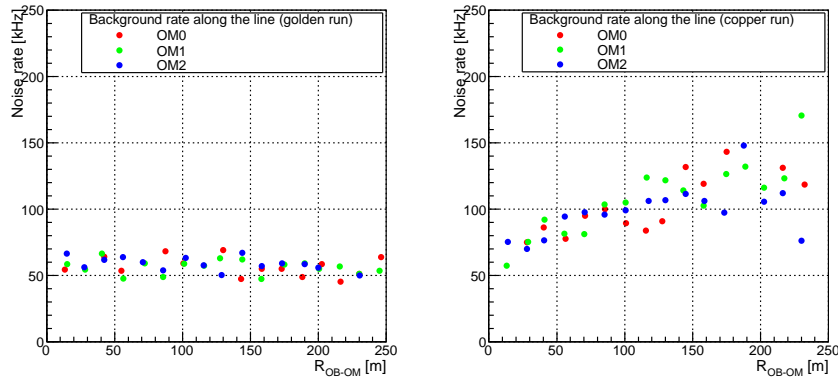
Figure 4.2: Background rate as a function of the OB-OM (R_{OB-OM}) distance for two different periods of data taking - Two kinds of behaviour are shown. Left: the "golden run" with low values of background rate and a flat-shape. Right: the "copper run" where the background rate is high and increases along the line.

detector were used to test different issues: different light intensities (reduced scattering), several heights in the line (deep relation studies) and different lines (homogeneity). If the light intensity of the LED is decreased, it leads to work at closer distances from the OB position, thus the number of scatterings is reduced and the transmission length is closer to the absorption length. However, as there were not enough available runs, the studies related to low LED intensity and the OB position for deep relation studies could not be done and are not included in this thesis. The homogeneity of the measurement by using several lines in the detector is, nonetheless, included.

Most of the runs were taken with the "single top-LED" configuration for the modified OB with UV LEDs (L12F2f1-f2), the OB with multi-wavelength LEDs (L6F2f1-f6) and the standard OB equipped with blue LEDs. As commented in Chapter 2, "L", "F", "f" denote the line of the detector, the floor where the OB is located in the line, and the face of the OB, respectively. Other runs with "all top-LEDs" (only top LEDs switched on) or "full OB" configuration (top, middle and four LEDs groups switched on) were performed.

The data for optical properties measurements with the OB technique includes the high intensity runs performed with L12F2 (faces 1-2, UV), L6F2 (face 2, UV), L1F2-L2F2-L4F2 (face 1, blue), L2F2-L4F2 (all top-LEDs, blue) and L8 (laser, green). These data runs were filtered and 35% (92/263) of the total data

collected along the last 4 years survived the quality requirements and availability for the analysis. The final data set for optical properties measurements with the OB technique are summarized in Table 4.1.

Line (L)	OB position (F)	face (f)	Wavelength [nm]	Number of runs
6	2	2	406	10
12	2	1-2	406	22
				<u>32</u>
1	2	1	470	9
2	2	1	470	16
2	2	all top	470	1
4	2	1	470	5
4	2	all top	470	3
				<u>34</u>
8	BSS	-	531	26
				<u>26</u>
All OBs				92

Table 4.1: The data used in the OB technique was filtered and 35% (92 runs) collected along the last 4 years was considered suitable for the analysis. It includes 32 runs at 406 nm, 34 runs at 470 nm and 26 runs at 531 nm.

4.1.2 Systematic effects

The time distributions of the hits are a convolution of different physics phenomena as absorption and scattering, and diverse detector features related to the geometry and the acquisition system of the detector. In order to minimize the impact of some systematics on the detector some considerations for the OB technique have been taken into account:

- **Shadowing effect due to upper structures above the OB**

    Intermediate OMs and other detector components can prevent direct photons from reaching the OM of the same line where the OB is located. This effect reduces the number of direct photons and distorts the angular distribution of the light measured at the OMs depending of the line considered.

    Figure 4.3 shows the arrival time distributions for the OMs located at floor 16 either in the neighbouring line (L4) and the emitter line (L2). As seen, the number of collected photons is significantly smaller when it is evaluated
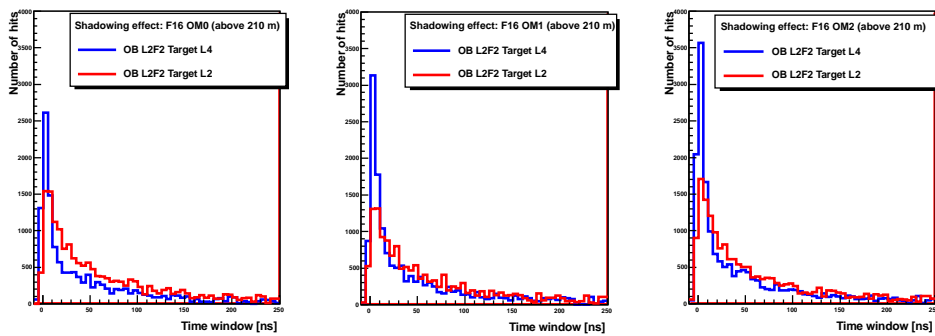
Figure 4.3: Shadowing effect - Number of hits collected in the same (red) and neighbouring (blue) line at the same height for several OMs. Left: OM0. Center: OM1. Right: OM2. The measurements are shown for the storey 16 (F16 $\sim$ 210 m up the OB) with the lowest OB of the emitter line L2.

along the same line where the OB is placed, which shows a different attenuation of light along the light paths between the OB and OMs depending of the line considered. By measuring along the same line where the OB is placed, mechanical structures forming the upper storeys above the OB plus the water environment are present. However, measuring along a neighbouring line only the sea water environment is responsible of the attenuation of light. The loss of direct photons due to intervening material is called "shadowing effect". This effect is present no matter the line, light output profile, OB configuration or wavelength. The shadowing effect is not strong enough at the tails where scattered photons are expected, which shows that the impact is only on the direct light detected. In Figure 4.3, the relative difference between the amount of direct photons detected in each of the three OMs of the same storey is due to the relative orientations of the OM-axis in the storey with respect to the OB-OM direction.

In order to avoid the shadowing effect only measurements in neighbouring lines to the emitter OB are used in the analysis, both for transmission and absorption-scattering measurements.

- **The PMT efficiency**

At the beginning of the development of the OB technique, a noise-based efficiency correction for PMTs calibration was tried. This method assumed that the number of noise hits was proportional to the efficiency of the PMT,

with the idea of normalizing the PMT signal to their own noise. However, as the noise-based efficiencies could introduce correlations due to noise subtraction in the OMs along the line, an independent method for PMT calibration was needed. In this sense, the coincident signals due to ^{40}K decay close to a given storey can be used to compute the sensitivity for each OM. The coincidence rate is proportional to the sensitivity of both OMs as

$$r_{ij} \propto s_i s_j \quad , \quad i = 1, 2, 3 \quad , \tag{4.1}$$

where r_{ij} is the coincidence rate between the i-th and j-th OMs and s_i, s_j are the sensitivities of the i-th and j-th OM, respectively. By means of the proportionality constant r_0 (71) the rate of genuine coincidences for two nominal OMs is obtained. The rate of genuine coincidences from ^{40}K decays is represented by the integral of the peak in the coincidence time histograms after subtraction of the flat pedestal of random coincidences, r_0 $\sim$ 16 Hz. Therefore, Equation 4.1 can be written as

$$r_{ij} = r_0 s_i s_j \quad . \tag{4.2}$$

The solution of such three equation system allows to know the sensitivity (or efficiencies) for each of the three OMs of the storey:

$$s_1 = \sqrt{\frac{1}{r_0} \frac{r_{12} r_{31}}{r_{23}}}, \quad s_2 = \sqrt{\frac{1}{r_0} \frac{r_{23} r_{12}}{r_{31}}}, \quad s_3 = \sqrt{\frac{1}{r_0} \frac{r_{31} r_{23}}{r_{12}}} \quad . \tag{4.3}$$

The sensitivity of the detector channel includes the intrinsic detection efficiency of the OM and the electronics threshold. Figure 4.4-right shows the relative sensitivity computed for a particular detection line in a standard physics run. In Figure 4.4-left the correlation with the noise-based sensitivities is shown.

When one of the three OMs is not properly working in the storey, only one coincidence rate can be measured, not enough to estimate the other two remaining sensitivities. In such cases, equal sensitivities for the other two OMs are assumed. If two OMs were missing in a ^{40}K + physics data taking run, efficiencies are set to 0 for the corresponding storey.
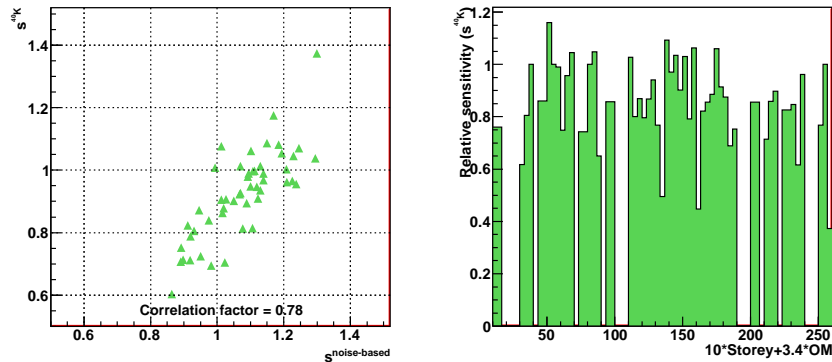
Figure 4.4: Relative sensitivities computed for ANTARES detection line 2 - Left: correlation between noise-based and ^{40}K sensitivities for those OMs above the OB. Right: ^{40}K efficiencies for all active OMs in the line.

The choice of ^{40}K efficiencies plays a sanity role in order to avoid correlated errors from the noise treatment. This method is not affected by time variations of the background since the light output of ^{40}K per unit volume is constant over depth ([71]).

The OB technique both for transmission and absorption-scattering measurements uses the ^{40}K PMT efficiency.

- **The LED position in the OB and the OB-OM orientation**

The relative position of the top LEDs inside the OB can produce a bias. In Figure 4.5, the amount of light collected by several target lines (except that of the emitter OB) when each of the six top LEDs of a given OB flashes, is shown.

When one single top LED of the lowest OB in the line flashes upwards, the amount of light recorded in the neighbouring lines can differ significantly. For instance, when the top LED of the face 1 in L2 is flashing, the target lines L3 and L4 register the same amount of light in average, whereas line L1 collects smaller amounts of light in the region of interest, i.e., where there is no more saturation of the PMTs (the saturation is reached when the output signal, the anode current in the PMTs, is no longer proportional to the incident light intensity).

This effect appears when only one top-LED is flashing and can be explained
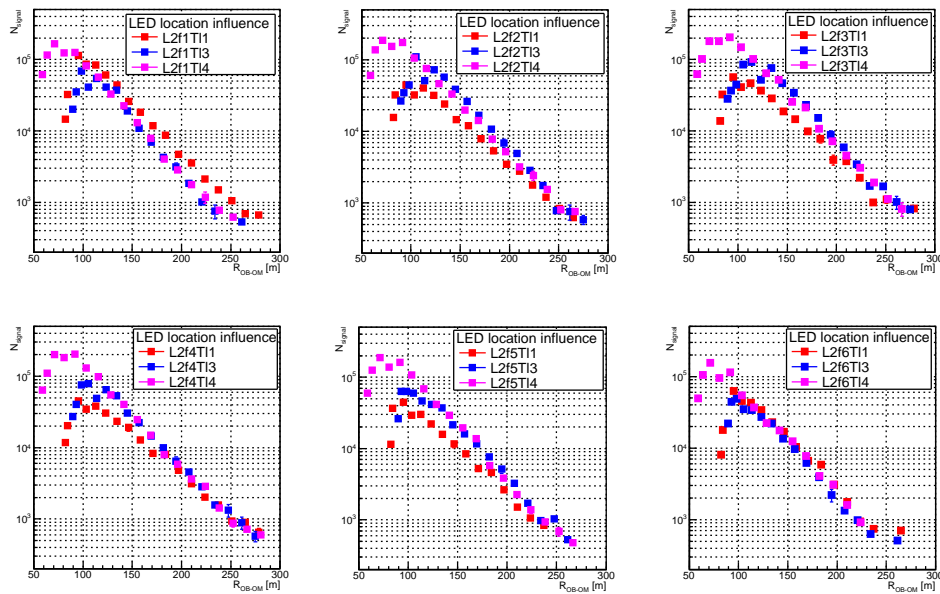
Figure 4.5: Light collected in several target lines where each LED of the OB in L2F2 is flashing - Each plot corresponds to one of the six top LEDs (1-6, from top-left to bottom-right) of the L2F2 flashing OB, where the closest neighbouring target lines Tl1 (red), Tl3 (blue) and Tl4 (pink) collect the light.

by the different trajectories of the light on the interface air-glass-water depending on the LED position in the OB, in such a way that the light distribution in the azimuth angle is not uniform. This anisotropy mainly affects the normalization or total light of the curve in Figure 4.5. Changes in the slopes are linked to the uncertainty of the transmission of light. In general, the LED that produces more light in one line gives the smallest amount the opposite line. It is the case for face 1 (f1) and face 4 (f4), or face 3 (f3) and face 6 (f6) in Figure 4.5.

A way to avoid this effect is to use the "all top-LEDs" or "full OB" OB configurations, covering a more uniform solid angle. Figure 4.6 depicts what is obtained for several neighbouring lines with these two configurations.

As seen in Figure 4.6-left, the isotropy of the light recorded by the OMs in most of the neighbouring target lines is confirmed. Practically, all the lines surrounding the emitter line (L4) collect the same amount of light in average. On the other hand, if the "full OB" configuration is used (see Figure 4.6-right), there are no differences: all the neighbouring lines collect
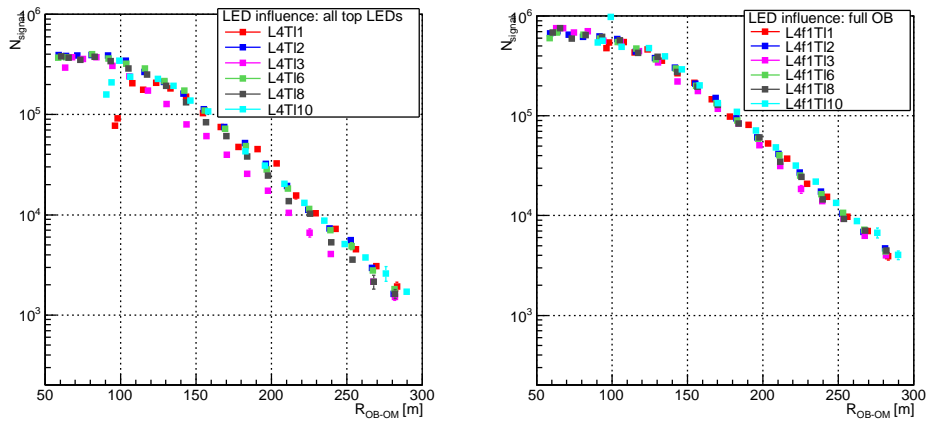
Figure 4.6: Uniform light output configuration of the OB - Left: number of signal hits collected by several target lines with the "all top-LEDs" OB configuration. Right: number of signal hits collected by several target lines with the "full OB" configuration.

in average the same number of signal hits along the line. In this case, a factor ~ 1.5 of light (normalization constant) is gained compared to the "all top-LEDs" configuration.

The OB technique for transmission length measurements uses the neighbouring line with the maximum number of signal hits for "single top-LED" and the few "all top-LEDs" runs available. For absorption and scattering lengths measurements all the neighbouring lines are considered. The "single top-LED" configuration is only used for testing the method, but the final results are obtained with the "all top-LEDs" configuration of the OB.

On the other hand, the relative orientation between the OM-axis and the OB-OM line of sight influences the amount of light detected. Due to the translation and rotation of the lines because of sea water currents, this relative orientation can change and the OM could receive the OB light forward looking (facing) or slightly deviated from its line of sight. When measuring in neighbouring lines, the symmetry of flashing the same line where the OB is located is lost, thus the analysis is very sensitive to the orientation of the OM-axis with respect to the OB-OM line of sight and the LED position in the OB.

• **Angular distribution of light and the width of the arrival time distri-**

bution

In order to see the impact of the LED angular distribution, two different
emission profiles were tested with Monte Carlo: an isotropic distribution
and the real angular distribution measured in the laboratory. In both cases,
the azimuthal angle distribution of light was assumed to be uniform. Regard-
ing the zenith angle, the distribution of light can be chosen: OB_UNIF (an
isotropic single LED distribution), OB_LABO (single LED distribution mea-
sured in air) and OB_6TOP (convolution of six distribution measurements).
The refraction of light in the physical borders of the OB and its environ-
ment, air-to-glass and glass-to-water, is taken into account in all the cases.
The angular distribution in the laboratory was found to be isotropic within
$\pm 10\%$ up to $30°$ and decreasing a factor 2 down to $60°$. In the Monte
Carlo simulation, the isotropic distribution and that measured in the labo-
ratory used the same number of photons. Figure 4.7 shows the arrival time
distribution of hits obtained for the two different emission profiles.
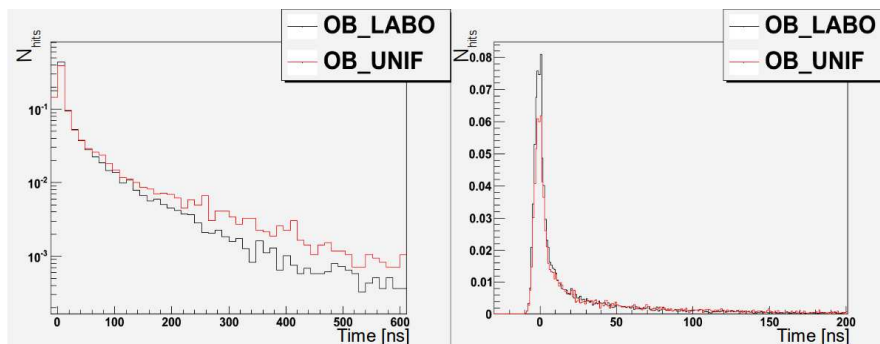
**Figure 4.7: Example of arrival time distribution of the hits for two different
LED angular distributions** - Left: two time distributions are compared in logarithmic
scale, an isotropic distribution (OB_UNIF and a non-uniform distribution (OB_LABO).
Right: a zoom in a reduced time window for the such isotropic and non-uniform
distributions and represented in linear scale. Both distributions are scaled to the
area.

As it can be seen in Figure 4.7-left, the long tail in the isotropic distribu-
tion (OB_UNIF) due to scattered photons is higher since more photons are
expected at high angle ($\theta > 60°$). However, non large effects are expected
whether a non-uniform or isotropic light emission is used to be modelled in
Monte Carlo since a zenith angle up to $30°$ showed to be enough to repro-

duce the same emission features of the LEDs, and sufficient to cover the active area of the OMs of the neighbouring lines. A suitable cut in $\theta < 50°$ allows to reduce the PMT acceptance uncertainty. Nonetheless, in order to have a more realistic approach of the light emission the non-uniform distribution (`OB_LABO`) was adopted.

The arrival time distribution of light is a convolution of the time width of the LED pulse, the TTS of the PMT and the optical properties of the water. The leftmost part of the time distributions can be approximated to a Gaussian whose width (σ) is governed by the above parameters $\sigma^2 = \sigma_{LED}^2 + \sigma_{TTS}^2 + \sigma_{OP}^2$.

By measuring one single LED time distribution in the laboratory, it was possible to find a value for $\sigma_{LED} \sim 2$ ns (FWHM, ~ 4.8 ns, risetime 1.7 ns). The contribution from the TTS of the PMT was estimated to be $\sigma_{TTS} \sim 1.5$ ns. Therefore, the contribution due to the optical properties could be evaluated. To do this, several Monte Carlo simulations with different optical parameters were generated. By varying λ_{sca}^{eff}, the change in σ of the Gaussian was evaluated at several distances between OB and OM. Due to the optical properties the width of the distribution is enlarged between $2 \leq \sigma$ [ns] ≤ 2.5 depending on the effective scattering, the shorter the λ_{sca}^{eff}, the wider σ.

- **The ARS token ring effect and noise fluctuations at large distances**

  As commented in Chapter 2, the readout of every PMT is performed by two ARS chips using a token ring protocol in order to minimize the dead-time in the data processing. The digitization of the signal allows to obtain the time and integrated charge information of each PMT, defining the SPE hit. The charge is integrated along a time window of ~ 35 ns and digitized by the AVC. Afterwards, the ARS chip is idle for about 200 ns, and passes the job onto the second ARS about 10 ns after the SPE hit integration, being the tail of the analogical signal processed as a new hit. This leads to a broad enhancement starting at 45 ns, when the token is passed to the second ARS, that is seen as a dip in Figure 4.8-left, more striking the shorter one distance to the OB.
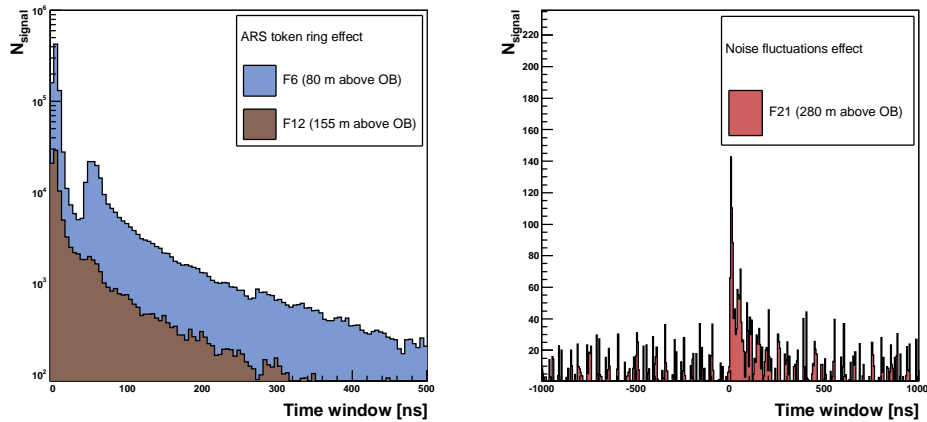
Figure 4.8: ARS token ring and noise fluctuation effects on arrival time distributions - A particular example in L4 when the OB in L2F2 flashes. Left: the ARS token ring effect is evident at shorter distances from the OB (i.e. 80 m), at larger distances (i.e. 155 m) the effect becomes negligible. Right: the signal fingerprint close to 0 is highly contaminated by noise fluctuations at large distances from the OB, as seen here at $\sim$ 280 m.

The dip at 45 ns in Figure 4.8-left is, therefore, due to the loss of the time information of a second pulse arriving either before the 35 ns integration gate or during the 10 ns dead-time that the swapping from one ARS to the other takes place. The small dip at 280 ns is consequence of the time integration gate cycle (35 ns + 35 ns), the time after SPE integration (10 ns) and the dead-time (200 ns).

In order to avoid saturation effects and the small dead-time effect due to the token ring mechanism in the ARS, the OB technique for optical properties determination is performed in the photo-electron region, avoiding any influence coming from the electronics. As defined in Chapter 2, the photo-electron region the region where the probability to get more than one photon per flash is negligible. Therefore, the single photo-electron profile analysed, no double pulses are recorded and no loss because of dead-time effects is present. Requiring a rate of 0.1(0.35) hits per flash, the probability of having two o more hits is smaller than 1(5)% according to Poisson statistics. At 470 nm and maximum LED intensity this rate is achieved at $R_{min} \sim 125$ m in the same line where the OB is located. When neighbouring lines are considered, the optimum distance to start the analysis is estimated as

$R_{min} \sim 165$ m (high intensity at 470 nm). This value slightly differs for the other wavelengths used in the analysis. At 402 and 531 nm, R_{min} is about 150 and 220 m respectively.

On the other hand, when the distance R_{OB-OM} is large enough, the signal peak is comparable to the noise fluctuations (see Figure 4.8-right) and the `HistoFiller` code is not able to find the correct peak. An educated approach is to take distances for which the signal is several times greater than the noise fluctuations such as $N_{signal}/\sqrt{N_{noise}} > 6(5)$. Typically this condition leads to consider maximum distances $R_{max} \approx 1.5(1.6)R_{min}$.

Both transmission length and absorption-scattering estimations by using the OB technique minimize the ARS token ring effect and avoid the noise fluctuations at large distances performing the analysis in the interval [R_{min}, R_{max}].

- **Wavelength spectra of the sources**

  The measurements of the LED light spectra of the OBs (UV, multi-wavelength and standard OBs) were performed by using a high-resolution calibrated spectrometer from Ocean Optics (79) whose main parameters are summarized in Table 2.3 (Chapter 2). As Figure 4.9-top shows, the typical width of each spectrum is about 10 nm except that of the LED emitting at 518 nm (L6F2f6) which is larger, and the laser spectrum which is practically monochromatic (532 nm).

  Due to the wavelength dependence on the absorption of light in water, the wavelength spectra of the light change as a function of the distance travelled by the light. The expected wavelength distributions at a given distance from the OB have been estimated by using a dedicated Monte Carlo consisting in the convolution of the LED light spectra with the absorption length spectrum from Smith & Baker. Figure 4.9 shows the evolution of the source spectra along several distances of the light propagation path. The shift of the peaks and the distortion of the shapes of the distributions can be observed except for the laser which is almost monochromatic. As the distributions have been renormalized to unity for each peak at each distance, the relative effect of absorption between sources is not observed. The uncertainty linked to each
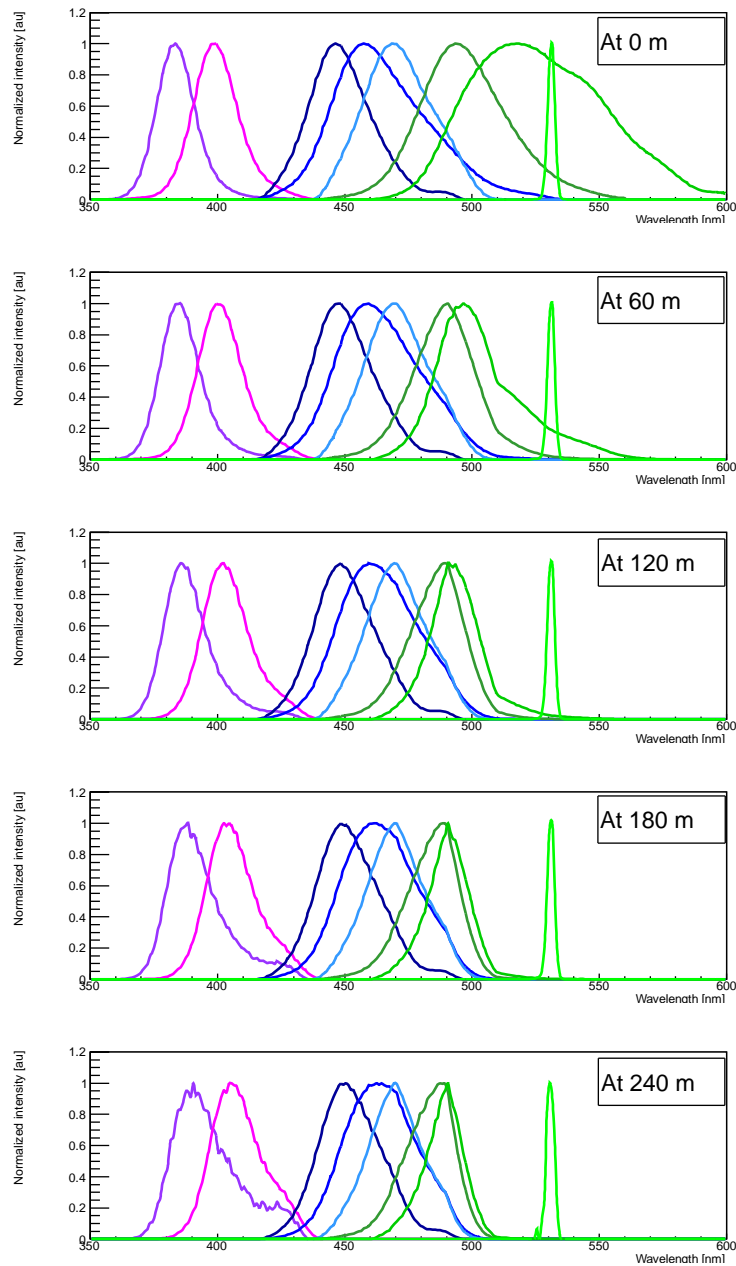
Figure 4.9: Spectra for all available sources of light in the ANTARES OBs (8 in total) - The evolution of the spectra as a function of distance as obtained by a Monte Carlo simulation which includes the spectra measured in the laboratory and the effect of absorption as described by Smith & Baker. Data points have been smoothed and the highest value of each spectrum has been normalized to unity for each distance.

wavelength is defined from the RMS of the wavelength distribution given by the simulation.

As a summary of this section, the data runs acquisition, signal extraction, runs selection and systematics commented before apply both for transmission and absorption and scattering measurements by using the OB technique. However, there are some slight differences concerning how the systematics are treated in each independent analysis, which are summarized in Table 4.2.

Cuts/corrections for OB data	Transmission analysis	Absorption - scattering analysis
Shadowing effect	neighbouring line with maximum N_{signal}	all neighbouring lines
PMT efficiency	no cuts	$0.5 < S^{40K} < 1.5$
LED position in the OB	single + all top-LEDs	single (trial) + all top-LEDs (final)
Angular distribution of light	no cuts	$\theta < 50°$
ARS token ring effect	$R_{min}(406,470,531) \geq (150,165,220)$ m	$R_{min}(470) \geq 165$ m
Noise fluctuation effect	$R_{max}(406,470,531) \approx (1.6,1.5,1.3)\ R_{min}$	$R_{max} \approx 1.6\ R_{min}$
Wavelength spectra of sources	yes	yes

Table 4.2: Description of the main cuts used in the measurements of the water optical properties with the OB technique. Most of the cuts used in transmission length measurements are in turn used for absorption and scattering estimations.

All the measurements listed in Table 4.2 are performed in neighbouring lines, avoiding shadowing effects in both measurements. By measuring in the neighbouring line with the maximum number of signal hits (N_{signal}), enough statistics are obtained to safely perform the transmission length measurements. The PMT efficiency cut is used since it slightly improves the accuracy of the absorption and scattering determination. The cut $\theta < 50°$ allows to reject the backward looking OMs by having most of them inside a large cone aperture solid angle. The cuts for the ARS token ring and noise fluctuation effects ensure that both analysis are

done in the photo-electron region with an acceptable amount of signal hits in the interval [R_{min}, R_{max}]. These cuts are implemented in a general analysis script. However, some details of the time distributions in the OMs are visually inspected and rejected when rare failures of the OMs give strange shapes in the arrival time distributions of light.

4.2   Estimation of the transmission length

As previously commented, the transmission length of light is computed by fitting the decrease of signal hits of the target line as a function of the distance to the Beer-Lambert equation. The transmission length measurements made at several wavelengths from the LEDs installed on the OBs throughout the detector and the uncertainty of the measurements are showed and discussed. Afterwards, the quality of the fits is evaluated by means of the analysis of the χ^2-probabilities and the analysis of pulls. The time stability of the transmission length and the comparison with other sites, concludes the results of the OB technique for transmission length estimations to be shown in this section.

In order to avoid the shadowing effect described before, the transmission and absorption-scattering measurements are performed in neighbouring lines. In transmission length estimation, for each calibration run the number of signal hits in all the lines is evaluated and the one with the maximum signal hits is picked to carry out the measurement. In this way, the more forward looking oriented line (faced) to the OB emitter face, considered as target line, is chosen. In the following, the target line should be meant as the neighbouring line with the largest amount of signal hits collected.

4.2.1   Fit and estimation of the optical parameter

The first proposal for transmission length measurements with the OB technique was based on the "single top-LED" setup. Nonetheless, as commented in the previous section, a few runs performed with the "all top-LEDs" configuration are in turn used. In the transmission length estimation, the lowest OB (F2) in the line flashes upwards and the amount of light collected in the upper storeys of the target line is plotted as a function of the distance. Afterwards, these measurements are fitted to the Beer-Lambert equation in the fit interval [R_{min}, R_{max}]. In this way,

it is possible to obtain an optical parameter related to the transmission length of light which describes the convoluted effect of absorption and scattering. Figure 4.10 shows an example of the number of signal hits collected along the line as a function of the distance. The signal hits along the distance include the geometric factor R^2 related to the OM and it is normalized to the number of flashes of light ($N_{flashes}$) fired in the calibration run.
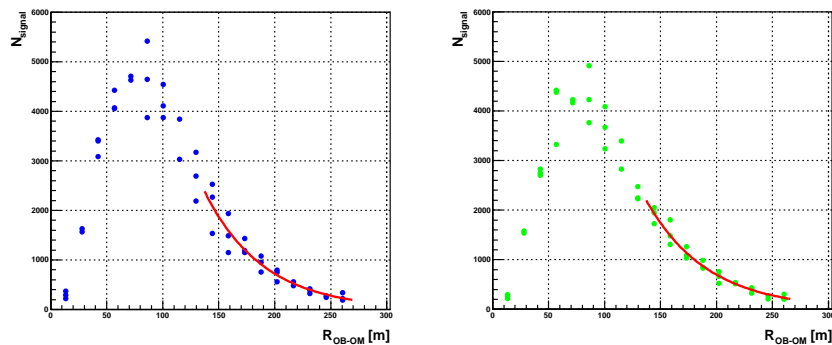
Figure 4.10: Exponential decrease of signal hits as a function of the distance between OB-OM - Left: non-corrected by the PMT efficiency. Right: corrected by the PMT efficiency. The measurements are made on the neighbouring line which collects the largest number of signal hits, designated as "target line".

The OMs not depicted in Figure 4.10 were not properly working during data acquisition. Signal hits are corrected by the PMT efficiency. As seen in Figure 4.10-right, once the correction by the PMT efficiency is done, the number of signal hits given by each OM of the storey becomes to be close enough to be considered safety inside its statistical error (not depicted here).

As seen, three different intensities are registered in each storey, one by each of the OMs. Instead of using the values separately in the fit, a good alternative to treat such intensities is to assume that they are independent measurements and Gaussian distributed. Therefore, we can consider one signal intensity per storey computed as the sample mean of the three OMs. The most suitable method to compute the error of the sample mean is from the "t-statistics". In this sense, when the mean and the standard deviation of a Gaussian distribution are not known, the Student's t-distribution formalism can be used to test the hypothesis

that $\bar{x} = \mu$ in such a way that the error of the sample mean can be taken as

$$\sigma(\bar{x}) = t\frac{s}{\sqrt{n}} \quad , \qquad (4.4)$$

where the sample mean from the group of intensity observations is an estimate of the population mean, and s represents the estimator of the standard deviation (for sample standard deviation). In order to have 68.27% confidence level errors ($\pm 1\sigma$), the one side tail of cumulative Student's function must be 84.13% and thus $t = 1.32$ for n = 3 (2 dof) and $t = 1.83$ for n = 2 (1 dof) (117) (118). In the case where only one OM is working ($n = 1$) in the storey, the point is not used for the exponential fit. The total error assigned to the storey is the sum in quadrature of the statistical error of the storey and the value of the error in terms of t defined in Equation 4.4. The statistical error per storey per OM for each detector line, arises from the fluctuation in the number of signal hits per bin in the time distributions and by assuming a 10% of error for the PMT efficiency. Having the error of the mean from Student's t-distribution and the statistical error in the number of signal hits, the quoted signal for each storey of the line is finally expressed as

$$N_{signal} = \bar{x} \pm \sigma = \bar{x} \pm \sqrt{\sigma_{stat}^2 + \sigma_{(\bar{x})}^2} \quad . \qquad (4.5)$$

The transmission length of light is extracted from the slope of the exponential fit which is strictly done in the interval [R$_{min}$,R$_{max}$], defined in the previous section. It comprises the photo-electron region, thus, the ARS token ring and noise fluctuations effects are largely reduced. The fit range covers $\sim$ 100 m for most of the wavelengths considered. Figure 4.11-center-right (non-corrected and corrected by PMT efficiency) shows the exponential decrease of signal hits fitted to the Beer-Lambert equation for a "single top-LED" of the L2F2 OB (470 nm) flashing and L4 collecting the light. The transmission length obtained is labelled as "L". The signal hits are thus normalized to the geometric factor related to the OM and the number of flashes of light fired in the data run.

The plateau of the signal hits shown up to 100 m obeys to a saturation effect of the PMTs (as previously commented). At higher values the exponential decrease of signal hits starts, however, at such distance the ARS token ring effect is still non-negligible.

The minimum distance to start the fit, R$_{min} \sim$ 160 m ($N_{signal}/N_{flashes} \sim 0.1$),
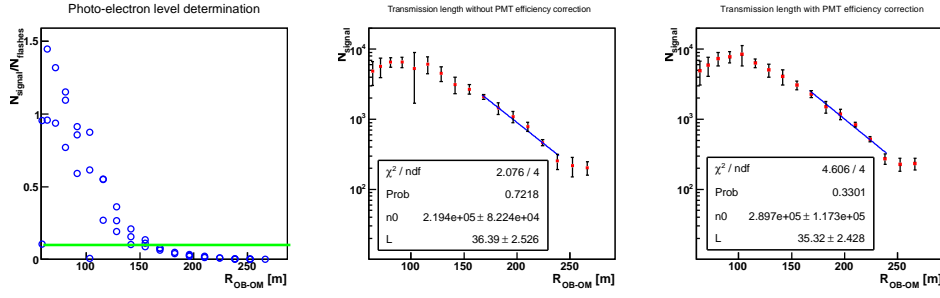
Figure 4.11: The Beer-Lambert equation fitting for the standard OB - Left: estimation of the minimum distance to fit R_{min}. Center: estimation of the transmission length of light "L" without corrections in the PMT efficiency. Right: equivalent measurements including correction by PMT efficiency.

ensures a negligible probability to get more than one photo-electron in each OM of the storey (see Figure 4.11-left). The maximum distance to fit R_{max} is found close to 240 m where $N_{signal}/\sqrt{N_{noise}} > 6$.

In order to show the influence of R_{min} on L, Figure 4.12-left depicts the estimation with four storeys before R_{min} when R_{max} (240 m) is fixed. In Figure 4.12-right, it is represented the effect of changes in R_{max} when R_{min} (160 m) is fixed, for two storeys after the reference value. The reference case is in Figure 4.12-center where there are not changes in the fit interval [R_{min},R_{max}].
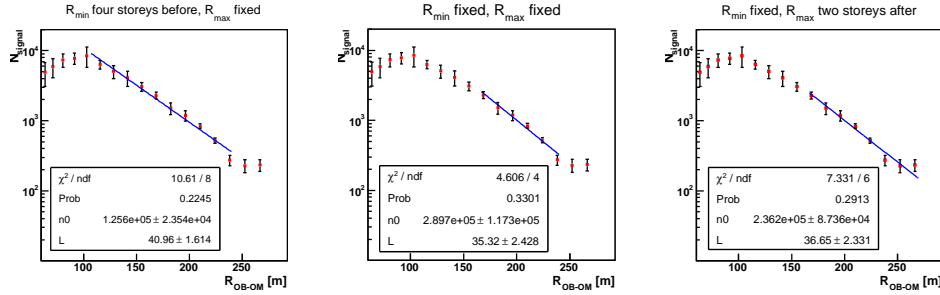
Figure 4.12: The effect of the fit limits in transmission length estimation (470 nm) - Left: evaluation adding four storeys before R_{min}. Center: evaluation inside the fit interval [R_{min},R_{max}] (reference). Right: evaluation adding two storeys after R_{max}.

As Figure 4.12-left shows, the influence of the ARS token ring effect on the choice of R_{min} trends to increase the real value of "L". The impact of noise fluctuations at large distances on R_{max} is not so remarkable sometimes, and leads to transmission length values unchanged as Figure 4.12-right shows. However, the

noise fluctuations can quite often mask the signal extraction, thus impacting on the measurement. By fitting into the interval [R$_{min}$,R$_{max}$] (Figure 4.12-center) a safe estimation of L (label as λ_{tr} afterwards) is achieved.

The fit interval at other wavelengths differs since the light absorption depends on the wavelength. Figure 4.13 shows the fit example for the UV LED (406 nm) in the multi-wavelength OB in L6F2 at high intensity and Figure 4.14 shows the exponential fit at high intensity for the two UV LEDs located in L12F2 OB (406 nm). As observed, no systematic effects are seen, being the measurements compatible within their statistical errors and also compatible with that of the L6F2f2 LED shown in Figure 4.13.
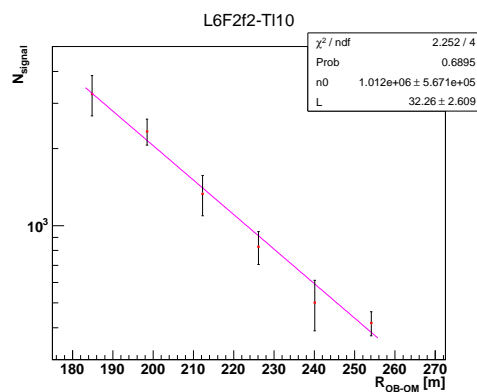
Figure 4.13: The Beer-Lambert equation fitting for the UV LED in L6F2 (406 nm) - Transmission length fit at 406 nm is showed for the face 2 (f2) flashing to the target line (Tl) with the maximum number of hits surrounding the emitter line (L) by using the lowest (F) OB in the line.

Concerning laser OB measurements, Figure 4.15 shows an example of the transmission length fit obtained with maximum light output from the laser.

The transmission length distributions for UV measurements both for L6F2f2 and L12F2f1-f2 OBs faces are shown in Figure 4.16.

The correction by the wavelength spectra of sources previously commented, is taking into account: at R$_{min}$ $\sim$ 150-170 m $\rightarrow$ $\lambda = 406 \pm 10$ nm, a correction in λ of $\pm$ 6 nm, although within its uncertainty. Figure 4.16-left shows the measurements at UV by using the L6F2f2 LED. A value of $\lambda_{tr} = 31.5\pm3.3$ m is obtained for the transmission length. On the other hand, the Figure 4.16-right shows the transmission length distributions obtained with L12F2f1-f2 LEDs with a mean value of $\lambda_{tr} = 31.1\pm2.5$ m. The agreement of both measurements free
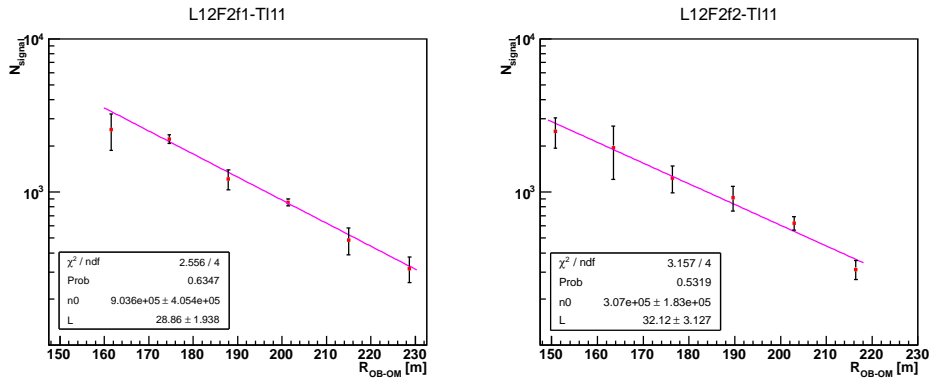
Figure 4.14: The Beer-Lambert equation fitting for the UV LEDs in the L12F2 OB (406 nm) - Left: transmission length fit using face 1 data. Right: transmission length fit using face 2 data.
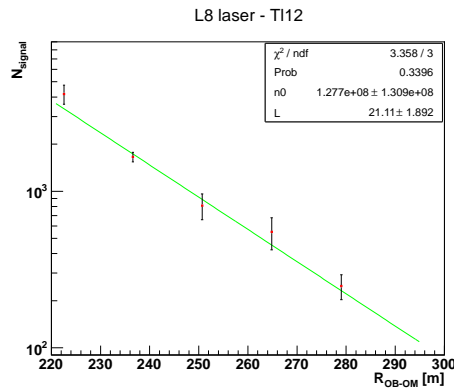
Figure 4.15: The Beer-Lambert equation fitting for the data of the laser OB at bottom of L8 (531 nm) - Measurements correspond to the lowest transmission length able to reach in the ANTARES site.
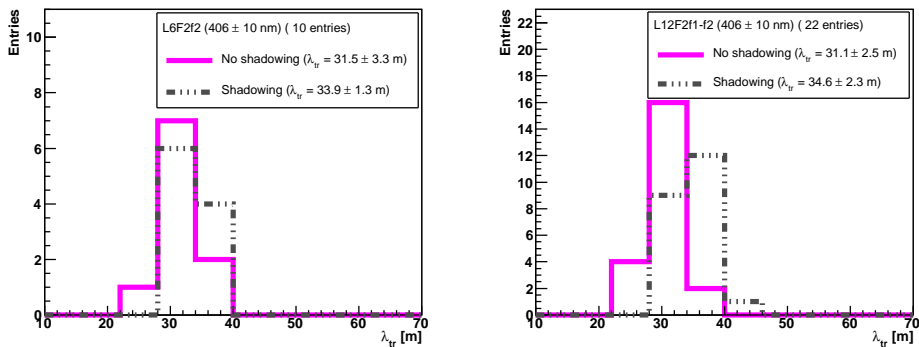
Figure 4.16: Transmission length estimations at the UV (406 nm) - Left: estimations by using the L6F2f2 LED. Right: estimations by using the L12F2f1-f2 LEDs.

of shadowing effect is achieved. Results obtained with measurements along the same line where the OB is placed (shadowing effect) are also shown. In both cases the effect is quite small and of the same order going in the same direction, i.e., increasing the value of the transmission length.

Figure 4.17 shows the transmission length measured with three different lines for the standard OB at 470 nm.
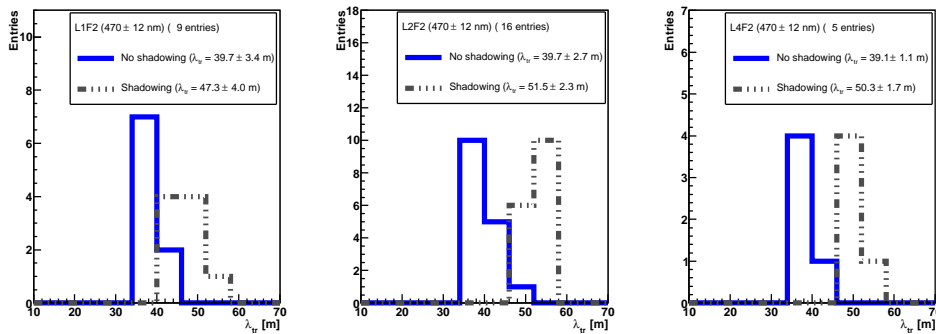
Figure 4.17: Transmission length estimations at the blue (470 nm) - Left: estimation with the L1F2 OB. Center: estimations with the L2F2 OB. Right: estimations with the L4F2 OB.

The correction by the wavelength spectra of sources in this case is negligible: at $R_{min} \sim$ 170-180 m $\rightarrow \lambda = 470 \pm 12$ nm, a correction in λ of ± 1 nm clearly kept into its uncertainty. A value of 40 m for the transmission length free of shadowing is obtained in average. Such measurements are found statistically compatible both for L1, L2 and L4. This result in turn, suggest the homogeneity of the measurement throughout the detector. In this case, the shadowing effect becomes more relevant than in the previous case (406 nm), being bigger than the fit error.

When using the "all top-LEDs" configuration of the OB, the average value of the transmission length free of shadowing effect is found $\lambda_{tr} = 42.1 \pm 3.2$ m for 470 nm with L2F2 and L4F2 OBs, for a total of 4 entries (runs). Such measurements are in agreement with that obtained with the "single top-LED" configuration previously considered. It is also important to remark that the angular anisotropy of the light output is reduced when "all top-LEDs" configuration is used, which is not possible for the multi-wavelength OB in L6F2 and the UV LEDs in the L12F2 OB due to their particular design.

The available set of wavelengths for transmission length estimations is completed with that of the laser OB at the bottom of L8 as can be seen in Figure 4.18, in this case, the shadowing effect does not bias the measurement and a value of $\lambda_{tr} = 20.5\pm2.1$ m is extracted. The correction by the wavelength spectra is not needed because the monochromatic feature for the laser OB.
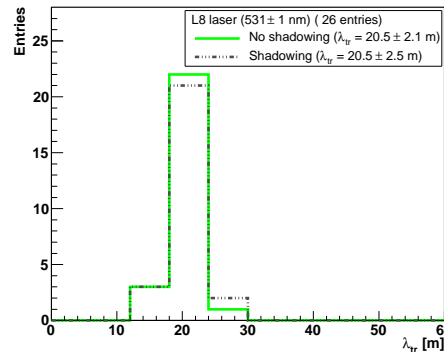
Figure 4.18: Transmission length estimations at the green (532 nm) - Distributions for the laser OB shows the negligible effect due to shadowing effects along the line.

4.2.2   Transmission length and analysis of the error

The distribution of the errors from the fits can be cross-checked with the RMS of the transmission length distributions. Figure 4.19 shows the distribution of the transmission length measurements at 406 nm obtained with the "single top-LED" configuration of L6F2f2 and L12F2f1-f2 OBs and the distribution of errors obtained from each fit.

As can be seen, an estimation of $\lambda_{tr}(406) = 31.2 \pm 2.8$ m is extracted. The mean of the distribution of errors from the fits in Figure 4.19-right is 3.3 ± 0.9 m, which is in agreement with the RMS of Figure 4.19-left.

For the maximum level of transparency at 470 nm, Figure 4.20 shows the equivalent transmission length measurements obtained with L1F2, L2F2, L4F2 "single top-LED" and L2F2-L4F2 "all top-LEDs" configuration of the OBs. As seen, a value of $\lambda_{tr}(470) = 39.9 \pm 2.9$ m is obtained. Having a look to the RMS of the transmission length distribution shown in Figure 4.20-left, it can be noted that the agreement with the mean of the distribution of errors from the fits in Figure 4.20-right (3.3 ± 0.9 m) is reached.
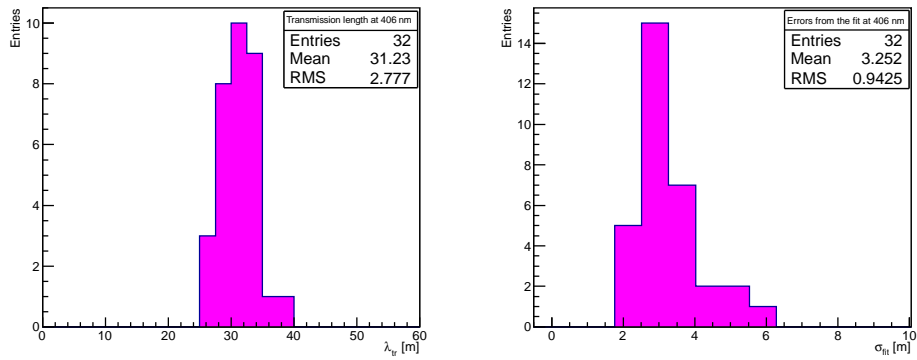
Figure 4.19: Equivalent transmission length at 406 nm and errors from the fit - Left: estimations performed with the face 2 of L6F2 and the two faces of the L12F2 OBs statistically compatible. Right: Distribution of the errors from the fits.
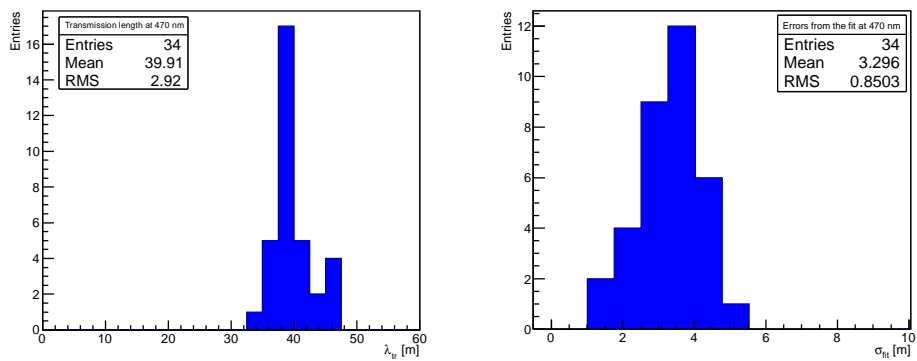
Figure 4.20: Equivalent transmission length at 470 nm and errors from the fit - Left: estimations with "single top-LED" configuration and "all top-LED" configuration statistically compatible. Right: Distribution of the errors from the fits.

Finally, the measurements obtained with the laser OB at 531 nm are shown on Figure 4.21 which constitutes the largest wavelength available in ANTARES to characterize the detection media.
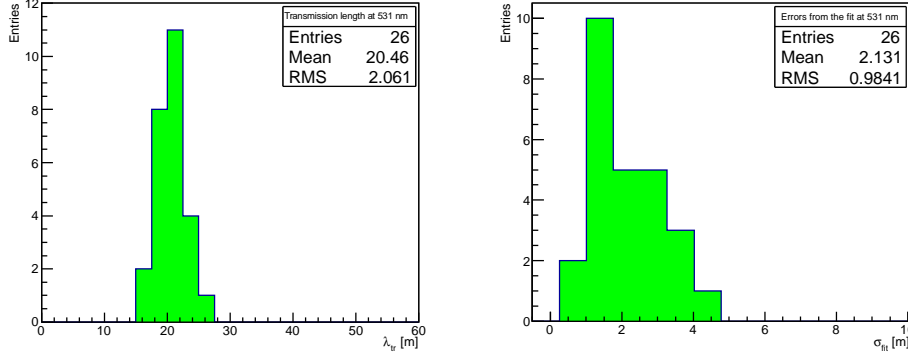
Figure 4.21: Equivalent transmission length at 531 nm and errors from the fit - Left: contribution obtained for measurements carried out by using the laser OB installed in the bottom of L8 at the center of the detector. Right: Distribution of the errors from the fits.

As it can be seen in Figure 4.21, a value of $\lambda_{tr}(531) = 20.5 \pm 2.1$ m is extracted. The agreement between the RMS of the transmission length distribution and the mean of the distribution of the errors from the fit is fulfilled. In this case, the Figure 4.21-left gives an estimation of the RMS compatible with the mean of the errors from the fit in Figure 4.21-right as 2.1 ± 1.0 m.

For all wavelengths, the relative error for the transmission length measurements (σ_{rel}^{tr}) is $\leq 10\%$ (RMS/Mean): 8.9%, 7.3% and 10.0% for 406, 470 and 531 nm respectively.

The distribution of relative or fractional errors of the measurements of each storey (σ_{rel}^{storey}) used in the fit and for all the calibration runs, is a good tool for systematics evaluation impacting the measurement. The Figure 4.22 shows the σ_{rel}^{storey} distributions built with all the points used in the fits, for all the calibration runs used, for each wavelength.

The distribution of relative errors at 406 nm points to an assignment of $\sim 21\%$ of systematics. The estimation of relative errors at 470 nm is smaller being about the 15% and the relative error at 531 nm is found to be $\sim 19\%$. So, the influence of systematics on the transmission length measurements is $\leq 21\%$. As seen, this estimation is just for measuring in the neighbouring target line, where the
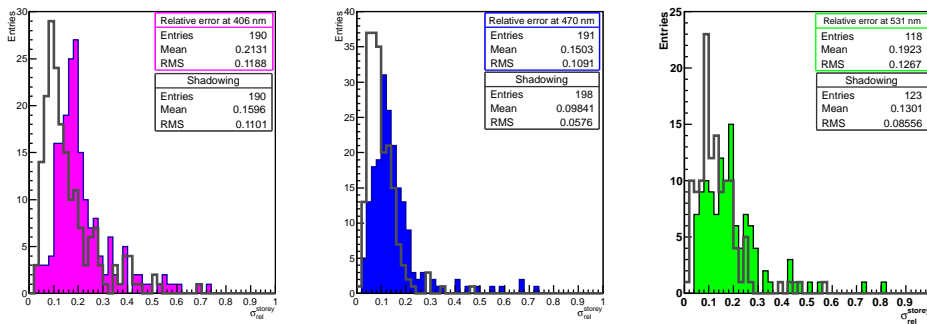
Figure 4.22: Distribution of relative errors for each wavelength in the analysis - Left: estimations at 406 nm. Center: estimations at 470 nm. Right. Estimations at 531 nm. Each entry represents the quotient between the sample error and mean in each storey. Only active storeys in the fit interval are considered.

symmetry of being flashing the same line is lost. The relative error distribution for the storeys of the same line where the OB is located, and thus affected by the shadowing effect is in turn represented in Figure 4.22 (in-grey distributions). As seen from Figure 4.22, the relative errors for storeys are reduced (16%, 9.8% and 13% for 400, 470 and 531 nm respectively) due to the geometrical symmetry that the OMs present to the flashing OB, but unfortunately these measurements are affected by the shadowing effect of the intermediate material. The Table 4.3 summarizes the results.

Wavelength [nm]	$\lambda_{tr} \pm$ **RMS [m]**	Mean σ_{fit} **(RMS) [m]**	σ_{rel}^{tr} **[%]**	σ_{rel}^{storey} **[%]**	$\sigma_{rel}^{storey*}$ **[%]**
406	31.2 ± 2.8	3.3 (0.9)	8.9	21.3	16.0
470	39.9 ± 2.9	3.3 (0.9)	7.3	15.0	9.8
531	20.5 ± 2.1	2.1 (1.0)	10.0	19.2	13.0

Table 4.3: The relative error for transmission length measurements (σ_{rel}^{tr}) is found $\leq$ 10%. The RMS of λ_{tr} distribution is in agreement with the mean of σ_{fit} distributions. Relative errors for measurements in each storey (σ_{rel}^{storey}) for all the wavelengths are found $\leq 21\%$ in average, what can be reduced by recovering the flashing symmetry along the same line where the emitter OB is placed, but affected by shadowing, as represented by $\sigma_{rel}^{storey*}$.

To conclude, the σ_{rel}^{tr} is used for quantifying the variation of the transmission length and the σ_{rel}^{storey} is just for quantifying the variation of the signal intensity in each storey, leading to the evaluation of associated systematics. The identified systematics which impact the analysis based on the OB technique are those described in Table 4.2. As it was shown, some of them become negligible, and

the strongest effect comes from the loss of symmetry when flashing neighbouring lines.

4.2.3   Goodness of the fit: χ^2-test and pulls distributions

In order to test the quality of the fits on the transmission length measurements an analysis of the χ^2-probability $(P(\chi^2))$ and the pulls distribution (117) (119) has been made. The χ^2-test is used to test whether a given data set is well described by some hypothesized function. The pulls (i.e. difference between observations and fitted values, relative to the uncertainty or error) are able to detect various forms of bias.

Figure 4.23-up shows the distribution of the $P(\chi^2)$ for all the runs (entries) used in the analysis at 406 nm. In Figure 4.23-down, a scatter plot of the transmission length versus $P(\chi^2)$ is shown. The $P(\chi^2)$ values for measurements at 406 nm trend to accumulate at high values. As the $P(\chi^2)$ comes from a cumulative integral the distribution has to be uniform over the interval [0,1]. Large $P(\chi^2)$ comes from small χ^2 values of the fit and then from overestimated values of the errors.
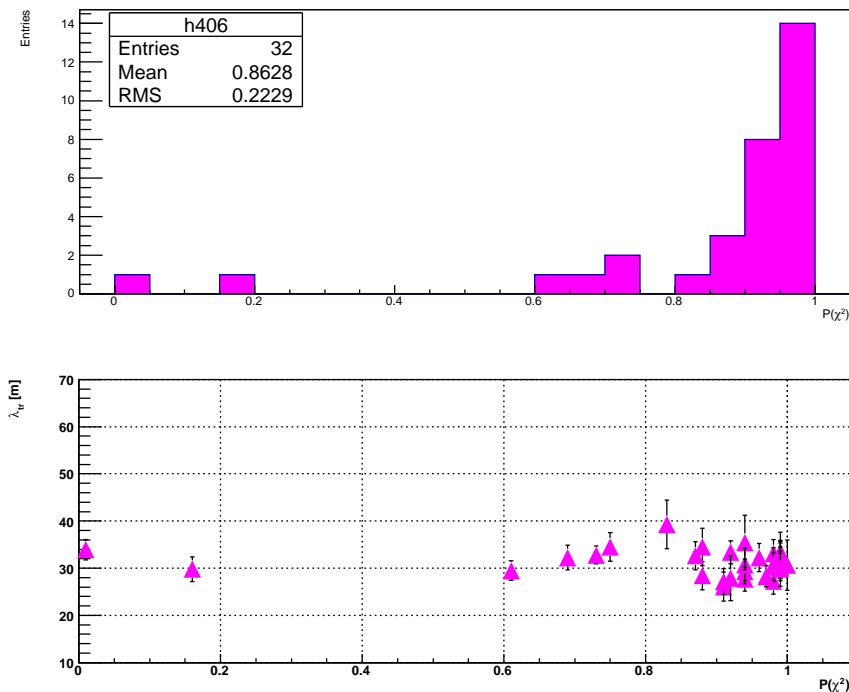
Figure 4.23: $P(\chi^2)$ at 406 nm - Up: χ^2-probability distribution. Down: transmission length versus $P(\chi^2)$.

On the other hand, Figure 4.24 shows the pulls distribution for all the points contained in the fit interval for all the runs considered in the analysis at 406 nm. In agreement to the pulls distribution theory, the pulls should be distributed as a standard Gaussian with mean (μ) zero and unit width (σ). Despite the evident overestimation of errors detected in the $P(\chi^2)$ distribution, what in turn is seen such as $\sigma < 1$ in the pulls distribution, the mean value is centred in 0 as expected. In this way, the deviations between observations and fitted values are minimal, thus, the consistency of an exponential fit to data for transmission length estimation is reasonable.
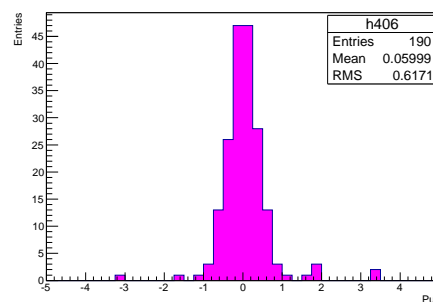
Figure 4.24: Pulls distribution at 406 nm - Pulls distribution for all the points used on the fit to the Beer-Lambert equation.

Concerning the measurement at 470 nm, the Figure 4.25 shows the $P(\chi^2)$ distribution (up) and the scatter-plot of transmission length versus $P(\chi^2)$ (down). Again, there is an accumulation at high values of the $P(\chi^2)$ meaning that the errors have been overestimated. This overestimation is also confirmed on the pulls distribution shown in Figure 4.26. As in the previous case, the width $\sigma < 1$ is observed. However, the mean of the distribution is again centred in 0, and allows to verify the low presence of bias in the exponential fit of the transmission length. For the set of calibration runs at 531 nm, Figure 4.27 shows the $P(\chi^2)$ distribution where a more flat behaviour is obtained according to expectations. Contrary to the previous wavelengths for 406 and 470 nm, in this case almost half of these collected values are greater than the median value (0.5 ± 0.3) and about half being less than the median value. Therefore, the errors assigned to 531 nm become reasonable at this wavelength. The correlation between the impact on the error assigned and the light isotropy reached in the target line, could be explored after the conclusion
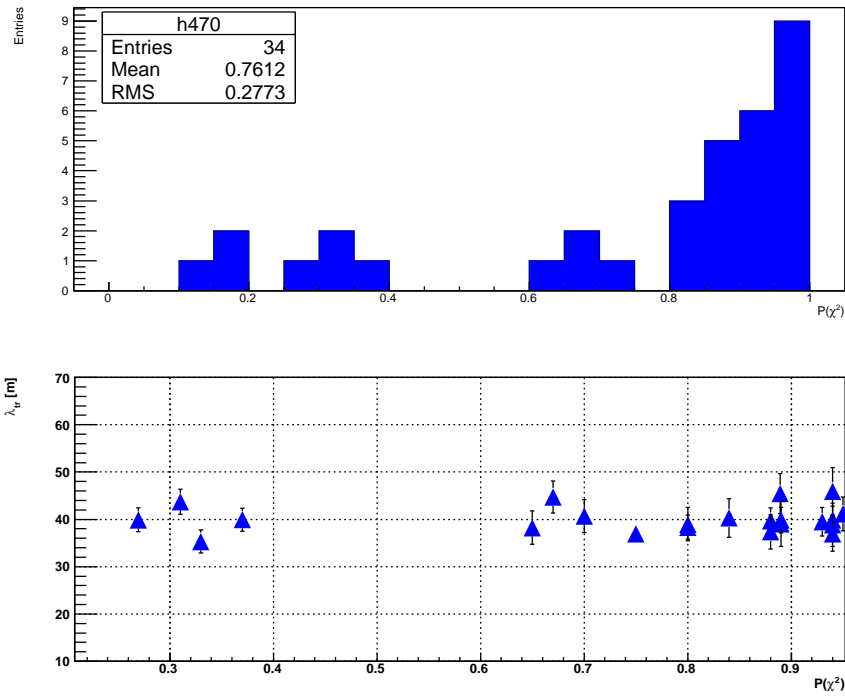
Figure 4.25: P(χ^2) at 470 nm - Up: χ^2-probability distribution. Down: transmission length vs P(χ^2).
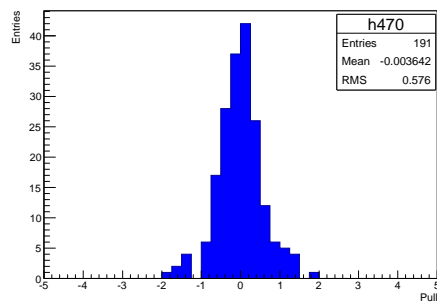
Figure 4.26: Pulls distribution at 470 nm - Pulls distribution for all the points used on the fit to the Beer-Lambert equation.

of this work. Figure 4.28 depicts the pulls distribution obtained for all the points included in the fits at 531 nm.
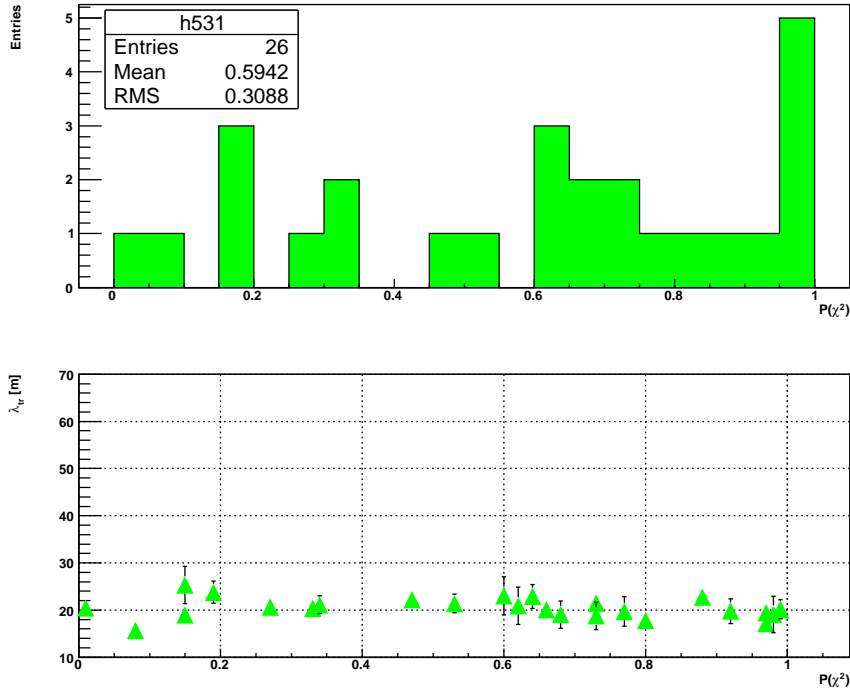
Figure 4.27: P(χ^2) at 531 nm - Up: χ^2-probability distribution. Down: transmission length vs P(χ^2).

As seen the width $\sigma \sim 1$ and mean close centred at 0, evidence the good level of agreement concerning statistical expectations.

Finally, the Table 4.4 summarizes the main statistical results obtained for the three different wavelengths studied in this subsection.

Wavelength [nm]	$\lambda_{tr} \pm$ RMS [m]	Mean Prob(χ^2) (RMS)	Mean Pull (RMS)
406	31.2 ± 2.8	0.9 (0.2)	0.0 (0.6)
470	39.9 ± 2.9	0.8 (0.2)	0.0 (0.6)
531	20.5 ± 2.1	0.6 (0.3)	0.1 (0.9)

Table 4.4: The analysis of the P(χ^2) and pulls distribution evidence the overestimation errors at 406 and 470 nm. Such distributions at 531 nm are fairly close to statistical expectations, and the assignment of errors become reasonable.
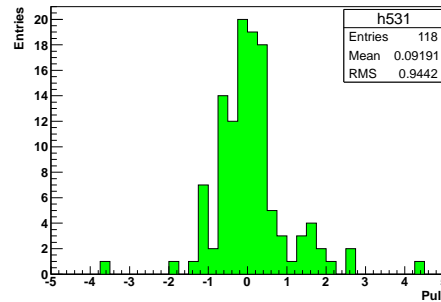
Figure 4.28: Pulls distribution at 531 nm - Pulls distribution for all the points used on the fit to the Beer-Lambert equation.

4.2.4   Time stability of transmission length. Cross-check with other sites

The data taken for the measurement of the optical properties allows to evaluate the time evolution of the transmission length at the ANTARES site. It is known from the oceanographic community and undersea neutrino observatories that for large depths where neutrino telescopes are deployed, the transparency of the water should reach its maximum. In this sense, it is important to check that there are not seasonal, chemical, biological or physical variations in the properties of the water, thus in transmission, absorption and scattering properties of the media. Looking at the stability of the transmission length in time for the three different wavelengths considered in this analysis, Figure 4.29 shows the evolution of these parameters for about 4 years of data taking (06/10/2008 - 11/06/2012, run 36035 - run 64771). As it is observed, the transmission length is maintained almost constant for the three different wavelengths, and its variation is not larger than the $\leq 10\%$ reported before. The measurements depicted in Figure 4.29 suggests that there are not strong changes on the physical, biological or chemical properties that can affect the water transparency along the time. This leads that consequent measurements of standalone contributions of absorption and scattering should be, in turn, maintained stable in time.

Finally, Figure 4.30 compares the three transmission lengths obtained in this analysis with those reported by the NESTOR collaboration in the N4.5D site commented in Chapter 3. Both measurements were carried out by using isotropic light sources, thus, the comparison of results is valid. The data points for ANTARES correspond to the mean and RMS of the distributions in Figures 4.19, 4.20 and

4.21. The wavelengths as previously commented, are corrected by the wavelength spectra of sources, as well as their spectral width.
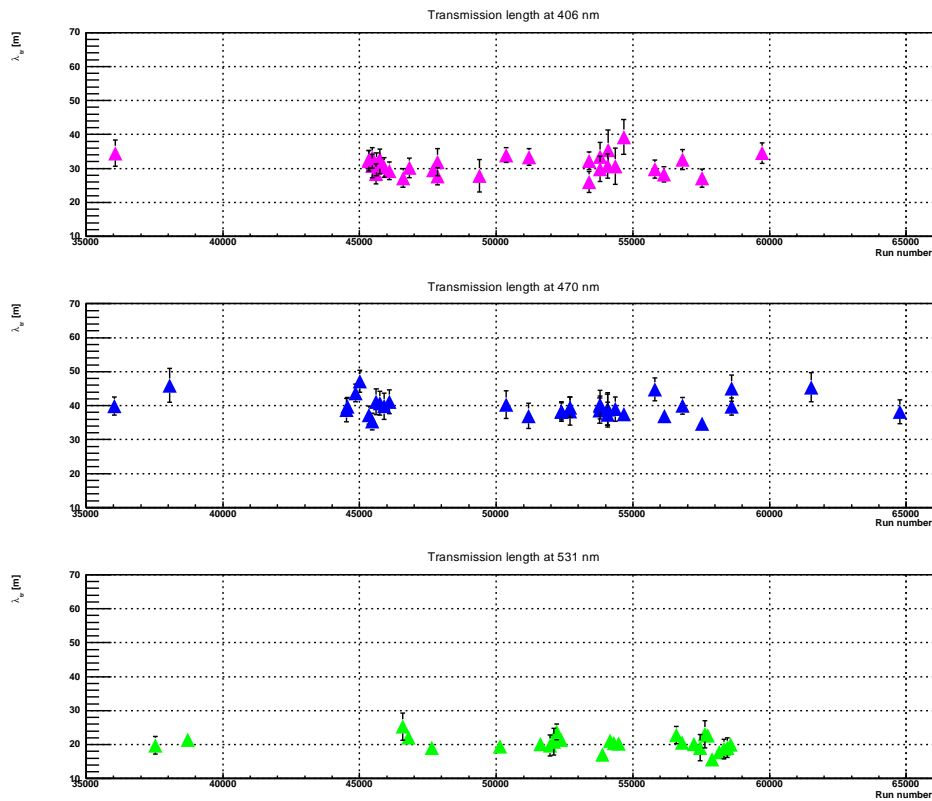
Figure 4.29: Time stability for transmission length measurements - Top: transmission length stability at 406 nm (UV). Middle: transmission length stability at 470 nm (blue). Bottom: transmission length stability at 531 nm (green). For each plot, in the y-axis it is represented the transmission length and in the x-axis the run number. The measurements were carried out along a 4-years period.

The transmission length measurements at the Mediterranean Sea by NESTOR and ANTARES (this thesis) trend to be compatible. The Smith & Baker transmission length spectrum for the clearest natural waters represents a well defined upper limit for such optical parameter. Particularly, at larger wavelengths the measurements reported at the Mediterranean Sea by NESTOR and ANTARES in this work agree with the Smith & Baker curve.
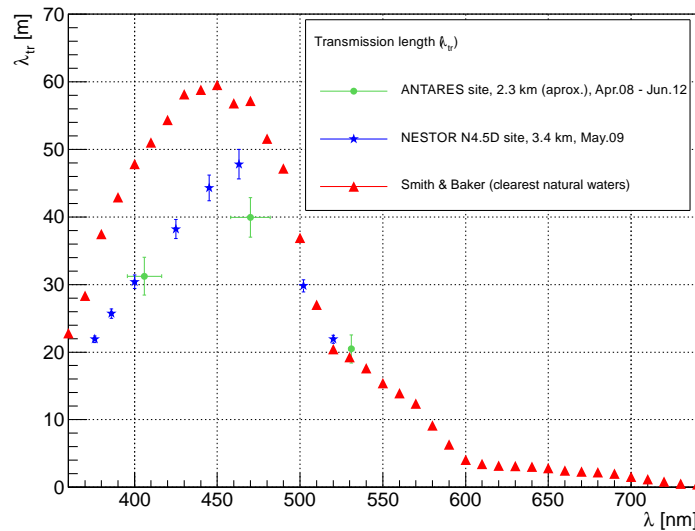
Figure 4.30: Transmission length at the ANTARES site and cross-check with other sites - The comparison with the transmission length spectrum reported by NESTOR at the Mediterranean Sea is showed as well as the transmission length spectrum deduced for the clearest natural waters by Smith & Baker. The measurements in green corresponds to the result of this thesis for 406, 470 and 531 nm.

4.3   Estimation of absorption and scattering lengths

The measurement of the absorption and scattering lengths is performed by means of the comparison of arrival time distributions for data and Monte Carlo. The procedure is based on a modified Pearson's χ^2-test for comparison of weighted histograms. This test is incorporated as a special routine inside the `ROOT` software package via the `Chi2Test` routine ([120]). This is done because the content of each bin in the histograms has been manipulated to suppress the background and correct by PMT efficiencies.

The comparison gives a normalized χ^2 value for each OM which are then grouped into a χ^2 for each line, which determines the level of agreement or discrepancy between data and Monte Carlo. A "run-by-run" Monte Carlo simulation has been gradually improved towards a more realistic comparison of Monte Carlo samples and data, and therefore, the most accurate χ^2-minimization procedure as possible. This section shows all the partial and final results gradually obtained for absorption and scattering parameters in the development of the OB technique.

4.3.1 Monte Carlo simulation for Optical Beacons light

The Monte Carlo simulation package for the OB light is inherited from the general ANTARES simulation framework for Cherenkov light induced by particles crossing the detector, KM3, which uses a full absorption and scattering spectra. The KM3 package (121) (122) is a step-by-step full simulation software for the response of the ANTARES detector to the passage of High-energy muons including the effect of the optical properties of the water. Based on the KM3 structure, a special code to simulate the pulsed light emission from the Optical Beacons, named CALIBOB, was developed for calibration and optical properties analysis. The KM3 and CALIBOB Monte Carlo packages are performed at three different stages: GEN, HIT and KM3MC (CAL for OBs case). In GEN the photons field at several radii from the source of light (electromagnetic shower, muon track or OB) is modelled for a given detector medium description. The HIT code construe the photon fields from GEN into hit probability distributions in a PMT. In the KM3MC stage or CAL for the OBs case, the positions and orientations of the OBs and OMs are evaluated for the detector geometry set by the user. The full description of this simulation chain will be commented in more detail in the next Chapter 5 for the results on optical properties of the reconstructed track technique.

As previously commented, CALIBOB is able to simulate the different angular distributions of light for the LED OB and laser OB. In the case of single or grouped LEDs in the upper part of the OB, the configuration can be set by the user. In addition, the number of photons per pulse and the number of light flashes per run can be also selected. The double refraction through the glass cap of the upper mounting of the LED OB can be taken into account. The photons are propagated from the OB internal region (air environment), going through the glass (barrier) and finally along the water to the OMs. It is assumed that the azimuthal distribution of light from a single LED is uniform. The propagation of light in water is modelled, as commented, in the first stage of the simulation by input of absorption-scattering lengths and the contribution of the Rayleigh scattering.

The different triggers, calibrations and main electronics features are coupled to the final KM3MC and CAL output through the TriggerEfficiency program (123) (124). The PMT and ARS features are modelled based on a hit simulator package which contains different hit generators. The PMT charge of the analogue pulses, are generated following a Gaussian distribution of particular width and relative

gain. In turn, the hit times are modelled from a Gaussian distribution featured by its width (TTS). The coupling of early after-pulses and late pulses can be set with a given probability, typically 0.5% and 1% respectively. In the ARS simulation, the analogue pulses for the PMT are timestamped and interpolated in time by using the TVC calibration values of the ARS for a given period. The charge of consecutive pulses are added during the ARS integration gate. Once the total charge exceeds a pre-set threshold, a hit is triggered and raw data (SPE) are generated, then the integrated charge in the AVC is estimated from the charge calibration of the ARS. The time of the hit is set from the first photon within the ARS gate. These arrival times are offset according to the time calibration of the ARS.

4.3.2   Arrival time distributions for data and Monte Carlo

As mentioned before, there is no analytic formula that from the optical parameters that describe theoretically the physical processes can provide the quantities that are measured in our set-up, i.e. the amount of light and the photon arrival times at the OMs at different distances. To have a rough idea of how the data compares to Monte Carlo and prepare for a more rigurous analysis, several samples with different optical parameters were simulated. They included the testing of five absorption lengths, seven scattering lengths and eight values for the Rayleigh scattering contribution, η, providing a total of 280 ($5\times7\times8$) combinations of optical parameters or water models, which were compared with 28 data runs taken with the "single top-LED" configuration. In this thesis, it is assumed η as a non-wavelength dependant parameter, nonetheless, current studies into ANTARES could lead to rethink this. The goal is to find the simulated water model with the best optical parameters that describes the photon arrival time distributions of as many PMTs observed on data as possible. The Figure 4.31 shows a typical data - Monte Carlo comparison of arrival time distributions at three different distances (storeys or floors) in the line L4 when the OB in L2F2 is flashing. The time distributions are normalized to the peak of the first floor used in the analysis (the analysis starts at floor 12).

For the particular example in Figure 4.31, it is possible to see that the agreement at the tails is better at large distances from the OB where more scattering is expected, despite some deviation at the norm. On the other hand, if the absorption and
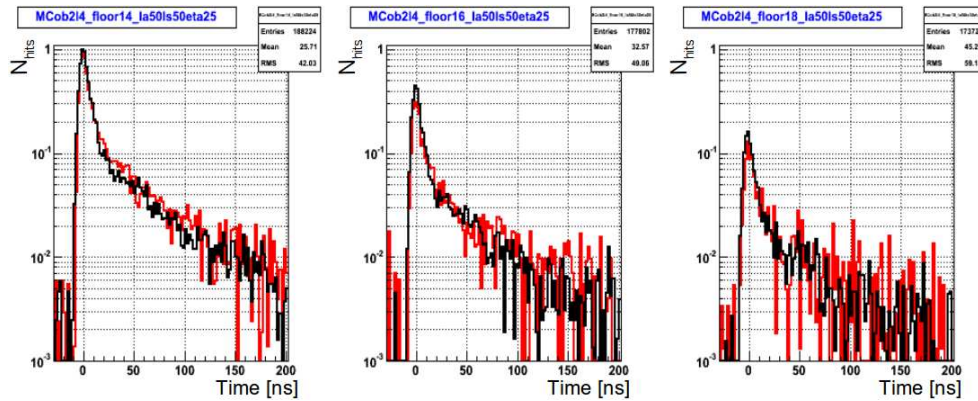
Figure 4.31: An example of data - Monte Carlo comparison for OB data - Photon arrival time distributions at 210 m (left), 240 m (centre) and 270 m (right) from the OB position. The black histogram is data recorded by the OMs of L4 when the OB in L2F2 was flashing. The red histogram is the Monte Carlo simulation with $\lambda_{abs} = 50$ m, $\lambda_{sca} = 50$ m, $\eta = 0.25$ and $\lambda_{sca}^{eff} = 163$ m.

scattering lengths are kept, and η is slightly increased, the agreement in the tails remains but at the peaks it gets slightly worse as Figure 4.32 shows.
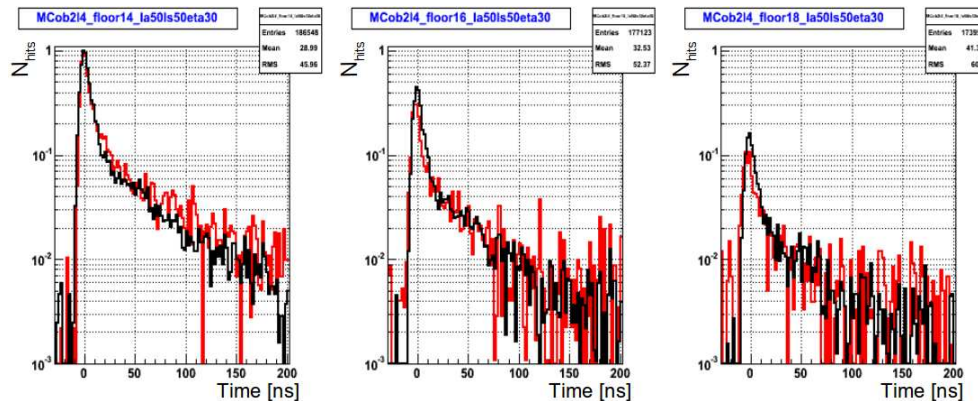
Figure 4.32: An example of data - Monte Carlo comparison for OB data - Photon arrival time distributions at 210 m (left), 240 m (centre) and 270 m (right) from the OB position. The black histogram is data recorded by the OMs of L4 when the OB in L2F2 was flashing. The red histogram is the Monte Carlo simulation with $\lambda_{abs} = 50$ m, $\lambda_{sca} = 50$ m, $\eta = 0.30$ and $\lambda_{sca}^{eff} = 142$ m.

If the values of the λ_{abs} and η are kept as in the first example and λ_{sca} increases in order to enlarge the λ_{sca}^{eff}, what is seen is a very slight improvement of the expected data - Monte Carlo agreement as Figure 4.33 shows.

In particular, if the absorption length is increased five meters respect to this last
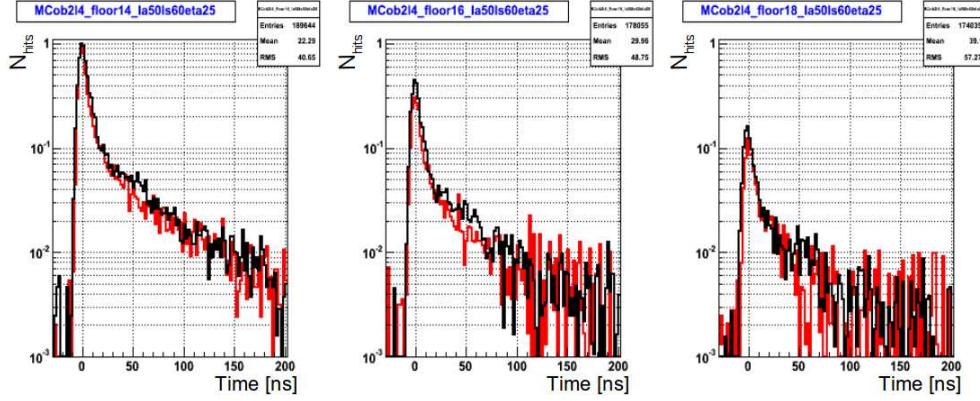
Figure 4.33: An example of data - Monte Carlo comparison for OB data - Photon arrival time distributions at 210 m (left), 240 m (centre) and 270 m (right) from the OB position. The black histogram is data recorded by the OMs of L4 when the OB in L2F2 was flashing. The red histogram is the Monte Carlo simulation with $\lambda_{abs} = 50$ m, $\lambda_{sca} = 60$ m, $\eta = 0.25$ and $\lambda_{sca}^{eff} = 195$ m.

example and the contribution of η is increased a 10% such as λ_{sca}^{eff} reaches 154 m, the agreement is improved as Figure 4.34 shows.

4.3.3   The χ^2-test method

These first observations led to define an adequate estimator of the data - Monte Carlo agreement aimed to confirm such visual inspections. A modified Pearson's χ^2-test was chosen as indicator of the data - Monte Carlo discrepancy.

When comparing two histograms with the same binning and the same number of bins (r), assuming that both histograms represent random distributions from the same parent distribution, the following χ^2 statistics can be defined:

$$\chi^2_{iom} = \frac{1}{MN} \sum_{i=1}^{r} \frac{(Mn_i - Nm_i)^2}{n_i + m_i} \quad , \tag{4.6}$$

where $M = \sum_{i=1}^{r} m_i$ is the total number of events in the first histogram and $N = \sum_{i=1}^{r} n_i$ is the total number of events in the second histogram. In this way, we can compare the corresponding arrival time distribution from data and Monte Carlo for a given OM. However, if we perform this comparison for each OM separately, we are non-sensitive to the light absorption along the line. To include
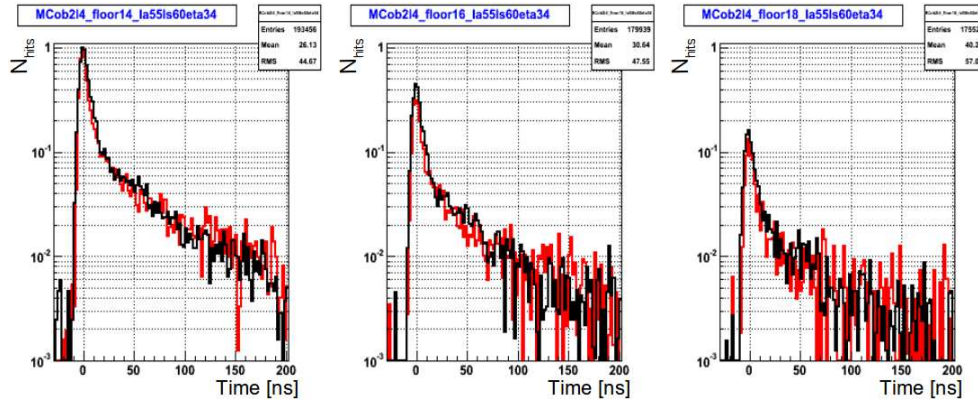
Figure 4.34: Data - Monte Carlo comparison for OB data - Photon arrival time distributions at 210 m (left), 240 m (centre) and 270 m (right) from the OB position. The black histogram is data recorded by the OMs of L4 when the OB in L2F2 was flashing. The red histogram is the Monte Carlo simulation with $\lambda_{abs} = 55$ m, λ_{sca} = 60 m, $\eta = 0.34$ and $\lambda_{sca}^{eff} = 154$ m.

the information of light absorption, the method have to be extended to several OMs of the same line:

$$\chi^2 = \frac{1}{N_{OMs} \cdot r} \sum_{iom=1}^{N_{OMs}} \chi_{iom}^2 = \frac{1}{N_{OMs} \cdot r} \frac{1}{MN} \sum_{iom=1}^{N_{OMs}} \sum_{i=1}^{r} \frac{(Mn_i^{iom} - Nm_i^{iom})^2}{n_i^{iom} + m_i^{iom}} \quad ,$$

(4.7)

where the scale factors M and N are fixed to the average of the integral of the nearest OM distributions to the OB.

In order to test the method, a more wide set of water models was produced. A new simulation composed of 480 (8×6×10) models were generated uniformly distributed in λ_{abs}, λ_{sca}^{eff} and η (see Table 4.5). Again, the Monte Carlo samples were compared with the 28 data runs with "single top-LED" configuration of the OB at 470 nm. In order to test the validity of the method, some Monte Carlo models from Table 4.5 were chosen and handled playing the role of "real data". These models, which were called "trial models", were then compared with the rest of the Monte Carlo samples. To include the trial models, random copies of their time distributions were generated by using the `FillRandom` routine from `ROOT` software analysis.

Two trial models with similar time distributions previously inspected were thus considered:

Optical parameter	Minimum value [m]	Maximum value [m]	Step size [m]
λ_{abs}	35	70	5
λ_{sca}^{eff}	75	575	100
η	0.05	0.95	0.1

Table 4.5: Monte Carlo mass production for OB data used for the testing of a preliminary χ^2-minimization procedure. It includes 8 different values of λ_{abs}, 6 values of λ_{sca}^{eff} and 10 values of η equally distributed.

- T1 $\rightarrow$ $\lambda_{abs} = 50$ m, $\lambda_{sca} = 59$ m, $\eta = 0.15$, $\lambda_{sca}^{eff} = 275$ m.

- T2 $\rightarrow$ $\lambda_{abs} = 55$ m, $\lambda_{sca} = 58$ m, $\eta = 0.25$, $\lambda_{sca}^{eff} = 175$ m.

The contour plots in Figure 4.35 show the result of the χ^2-minimization by assuming the "T1" trial model playing the role of real data and comparing with the Monte Carlo samples previously defined in Table 4.5. Results are shown grouping the Monte Carlo models by the same η value.
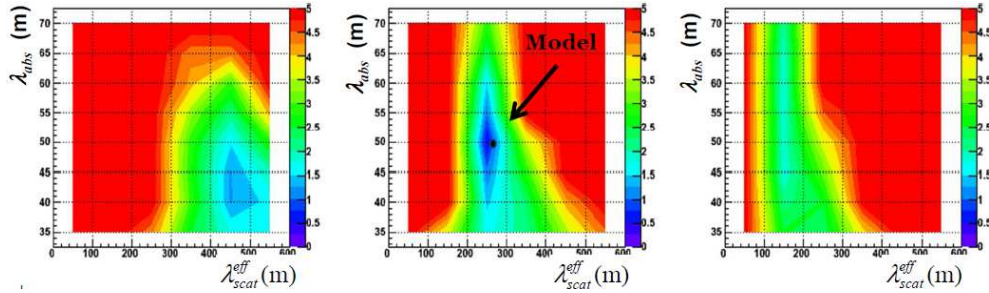
Figure 4.35: χ^2-**minimization for the first trial water model** - The figure shows the results of the χ^2-test as a consequence of the arrival time distributions comparison between the Monte Carlo trial model and the rest of the Monte Carlo samples. Left: comparison with models at $\eta = 0.05$. Center: comparison with models at $\eta = 0.15$. Right: comparison with models at $\eta = 0.25$. The dot indicates the test input water model.

As observed, the method works reasonably well, being able to find a defined χ^2 minimum for the case of the test input model (T1). It also happens for the second test input model (T2) as can be seen in Figure 4.36 where the method converges also to the last model at $\lambda_{abs} = 55$ m and $\lambda_{sca}^{eff} = 175$ m. A small effect of binning and smoothing is seen in the minimization region. The use of Monte Carlo samples as test input models for the validity of the χ^2 method set a good basis for water properties determination.
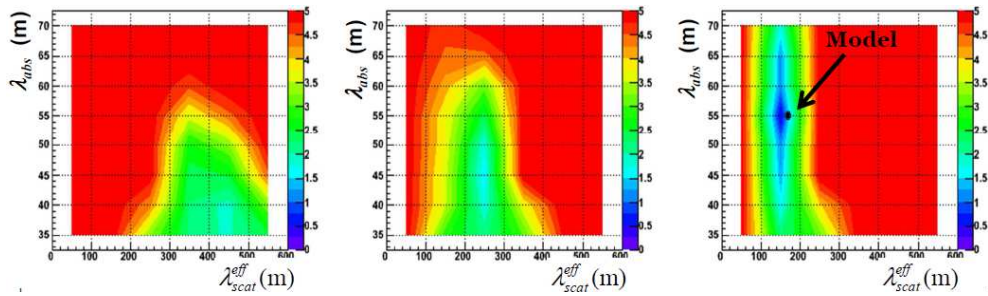
Figure 4.36: χ^2**-minimization for the second trial water model** - The figure shows the results of the χ^2-test as a consequence of the arrival time distributions comparison between the Monte Carlo trial model and the rest of the Monte Carlo samples. Left: comparison with models at $\eta = 0.05$. Center: comparison with models at $\eta = 0.15$. Right: comparison with models at $\eta = 0.25$. The dot indicates the test input water model.

The results obtained from the minimization by using the pair of trial models tested lead to χ^2 values about 2 in each case, what suggested that a little uncertainty was still present in the method. However, it is clear that the minimization is achieved and therefore, it can be considered as a good indicator of the level of agreement for arrival time distributions in our case of weighted histograms. The treatment of this remaining uncertainty is considered from a "run-by-run" simulation to be described in the next subsection. The "run-by-run" simulation is the final bet in the development and full incorporation of a simulation reproducing the same data acquisition features, and thus, the most accurate comparison as possible between them.

4.3.4   The "run-by-run" simulation and final results

Up to this point, the Monte Carlo simulations have used what is known as the "fix geometry" of the detector, which considers the lines as straight-rigid structures. In addition, it assumes identical behaviour (gain, etc.) for all the OMs as well as the same background rate along the line. However, when comparing Monte Carlo with real data several issues have to be taken into account. First of all, we have to be aware that due to the shadowing of frames and intermediate OMs, the arrival time distributions are distorted when the light detection occurs on the PMTs on the same line where the flashing OB is. As this shadowing effect has a great impact on the results of the optical properties, only neighbouring lines are used, where this effect can be considered negligible. But then, the analysis

become more complicated since the symmetry of the geometrical position of the OMs of the same line where the OB is located is lost, and the real OM orientation of the OM axis with respect to the OB-OM line of sight becomes relevant to simulate the correct amount of light in the OMs.

For overcoming such a drawback, a "run-by-run" simulation for OB data where each data file is associated with its "alter ego" in Monte Carlo has been gradually developed. In this "run-by-run" simulation, the real rotation and translation of the OMs are taken into account, by means of a special routine which downloads from the database the alignment table which is closer in time to the mid-time of the considered run. In addition, in these Monte Carlo samples generated in a "run-by-run" mode, the angular sensitivity of the PMTs is modelled according to the description given in (125) and PMT efficiencies are taken into account from ^{40}K measurements offline. Finally, the "all top-LEDs" configuration of the OB is used since the Monte Carlo simulation reproduce better this angular distribution of light output. Nowadays, the analysis has been only done at 470 nm. The final Monte Carlo production is shown in Table 4.6, which constrain the minimization region where the best favoured water model should be represented.

Optical parameter	Minimum value [m]	Maximum value [m]	Step size [m]
λ_{abs}	35	70	5
λ_{sca}	25	81	7
η	0.15	0.40	0.05

Table 4.6: The mass production performed in a "run-by-run" mode includes the largest range of optical parameters looking for the best water model fitting to data. In total 432 models are available for analysis.

The Monte Carlo models are uniformly distributed and form 8×9×6 samples for a total of 432 water models suitable for the analysis.

As previously said, to be sensitive to the absorption length, the comparison of data - Monte Carlo distributions have to be done with several histograms over different distances compared along the same neighbouring line. To do this, several time distribution histograms are merged into one larger one, called hereafter the "super-histogram". The "super-histogram" is the previous step before the final χ^2-minimization, which allow to better visualize the level of agreement between data and Monte Carlo samples. An example of a "super-histogram" is presented in Figure 4.37.
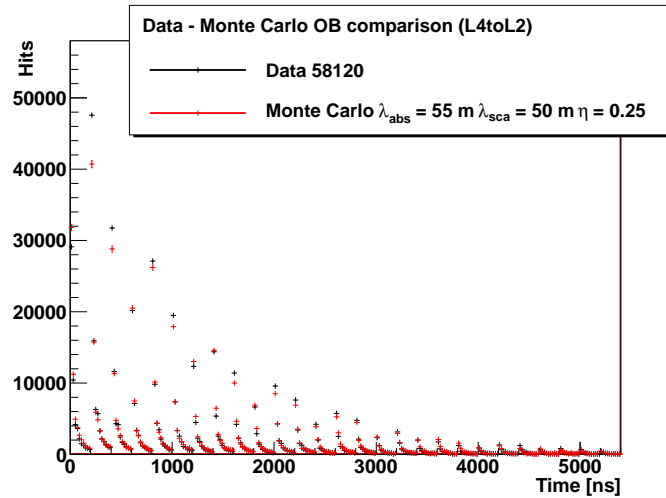
Figure 4.37: A super-histogram for data - Monte Carlo - The number of signal hits is represented as a function of the time window when they are collected. Time distributions of all the PMTs of the same line used in the analysis are merged together to perform the data - Monte Carlo comparison.

In this plot, the number of hits as a function of the photon arrival time is shown for the OMs inside the photo-electron region defined previously (typically from storeys 13 to 21) of line 2 when the OB of line 4 is flashing. The histograms corresponding to different OMs have been artificially separated in arrival time to better show each attenuation curve. Starting from the earliest peak, every three consecutive peaks correspond to the OMs of a given storey. The height of the peaks decrease with distance, as expected due to the attenuation, except for those corresponding to the OMs of the same storey, where the orientation determines their relative height. This is better seen in Figure 4.38, where only three OMs of one storey are plotted. The difference in height is mainly due to their different orientation with respect to the flashing OB. As can be seen, the Monte Carlo simulation with the parameters indicated in the figure describes reasonably well the data.

Before performing the data - Monte Carlo comparison, a visual inspection of the arrival time distributions is done as sanity check to detect bad behaving OMs and remove them from the analysis of the χ^2-minimization.

The procedure to compare data and Monte Carlo is as follows:

- Take a run with a flashing OB and obtain the hit arrival time distributions
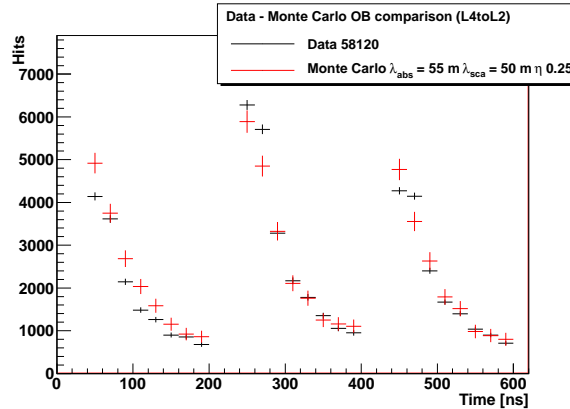
Figure 4.38: Zoomed version of the super histogram - The number of signal hits is represented as a function of the time window when they are collected for three OMs of the same storey. The different heights are related to the orientation of the OM-axis with respect to the OB-OM direction.

for all OMs.

- Simulate many Monte Carlo samples with same data acquisition conditions and different input parameters for λ_{abs}, λ_{sca} and η.

- Loop over the selected floors and OMs which pass the selection criteria for the quality cuts for OB data in Table 4.2.

- Select "good" OMs of one line (sanity check).

- Select a fixed range of hit arrival time distribution where the peak and tail is apparently well defined for each storey. Typically [-10,190] ns with a bin size of 20 ns.

- Merge all the good time distributions of one line (extracted from the above statement for all storeys) in one "super-histogram".

- Compare the super-histogram for data and Monte Carlo with the χ^2-test of the `Chi2Test` routine from `ROOT`, with the Weighted-Weighted option since the arrival time distributions were previously manipulated by subtraction of the noise component and the addition of PMT efficiencies.

- Repeat for all the lines except for the line where the flashing OB is located.

There are two additional factors which impact on the χ^2-test: the histogram binning and the statistics on the Monte Carlo samples. When very small bins are considered, large statistical errors are obtained and χ^2 values turn out to be small. If very large bins are considered, small statistical errors and large χ^2 values are achieved. A bin size of above 20 ns (10 bins in a time window between -10 ns and 190 ns) smooths the impact of the binning giving reasonable values in the χ^2-minimization. The χ^2 values are normalized to the number of degrees of freedom by the `Chi2Test` routine from `ROOT`. Concerning the statistics in Monte Carlo sample, to reach similar statistics at a given distance for each water model, the number of flashes depends on the absorption and scattering lengths of the model. Each Monte Carlo simulation has been produced from the propagation of 2×10^8 photons per flash.

The data runs used to be compared with the Monte Carlo samples are those of Table 4.7

Run number	Events	OB line	OB floor	Date [dd/mm/yyyy]
58120	205161	4	2	17-06-2011
58607	200481	4	2	12-07-2011
58609	200281	2	2	12-07-2011
61518	460000	4	2	12-12-2011

Table 4.7: The set of OB runs used for the final comparison with Monte Carlo samples follows the "all top-LEDs" configuration of the OB. There are three runs of the central line L4 of the detector and one of the peripheral line L2, with more than 200k flashes each.

As an example for a particular special OB run (r58120), Figure 4.39 shows the χ^2-minimization obtained in the different lines of the detector comparing with all the Monte Carlo models defined in Table 4.6 where the value of η is fixed to $\eta = 0.3$. The disposal of the lines in the figure is equivalent to their layout in the detector. As seen in Figure 4.39 all the lines behave similar, however showing slight differences in the values of λ_{abs} and λ_{sca} depending on the closeness to the emitter line (line 4, not shown). For the closest lines (i.e. lines 2, 6, 8 or 3) to the emitter line, the λ_{abs} value is practically unaltered, but the uncertainty on λ_{sca} is something larger. On then other hand, for the farthest lines (i.e. lines 11 or 12), the uncertainty on both magnitudes trends to increase. Figure 4.40 shows the sum of the χ^2 of all the lines of the detector for the calibration run used.
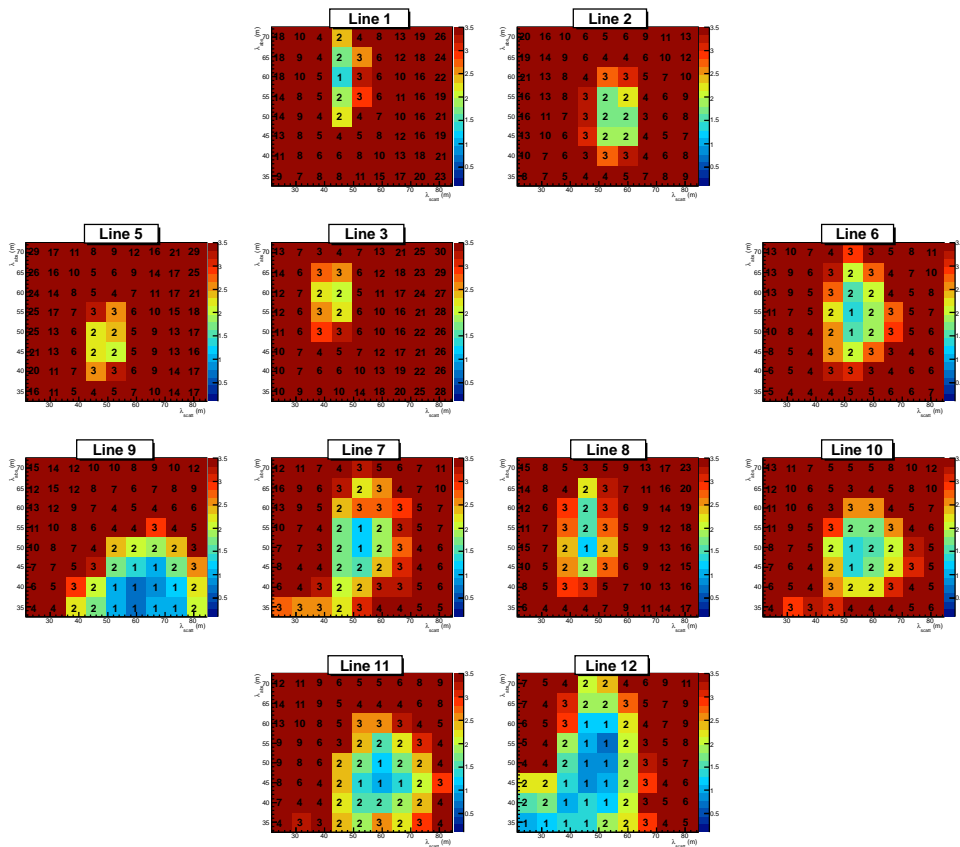
Figure 4.39: χ^2**-minimization, one data run (r58120)** - Each pad corresponds to one line of the detector. The L4 is not shown since it is used as emitter and the shadowing effect spoils the comparison. In the y-axis it is represented the absorption length, in the x-axis the scattering length, and the colour bar the value for the χ^2-test. Only Monte Carlo models with $\eta = 0.3$ are shown.
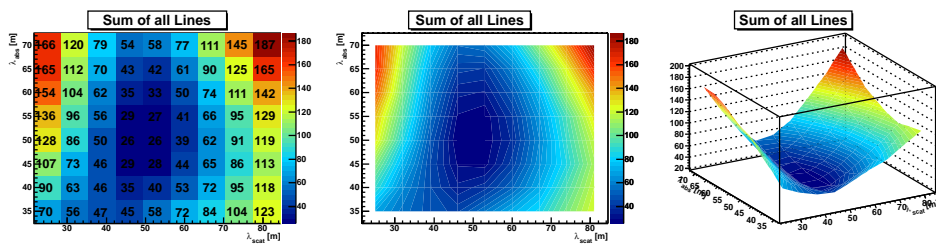
Figure 4.40: Overall χ^2 result, data run r58120, all lines - Left: the sum of the values of the χ^2 tests for all the lines in the detector lines are represented. Center: the corresponding contour plot is shown. Right: surface plot where is clearly seen the minimum achieved. Only Monte Carlo models with $\eta = 0.3$ are shown.

Figure 4.41 represents the χ^2 minimization for a different special OB run (r58607) close in time to the previous one.
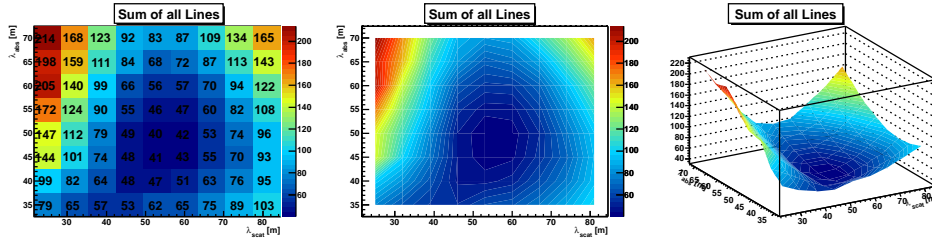
Figure 4.41: Overall χ^2 result, data run r58607, all lines - Left: the sum of the values of the χ^2 tests for all the lines in the detector lines are represented. Center: the corresponding contour plot is shown. Right: surface plot where is clearly seen the minimum achieved. Only Monte Carlo models with $\eta = 0.3$ are shown.

From Figures 4.40 - 4.41, the level of agreement between the results for both OB runs is clearly seen. The technique shows to be a good tool for water models discrimination and the results are reproducible in time. The best data - Monte Carlo agreement concerning the contribution for Rayleigh scattering is particularly seen for values larger than 0.25. Figure 4.42 shows the result obtained when comparing with models with $\eta = 0.15$.
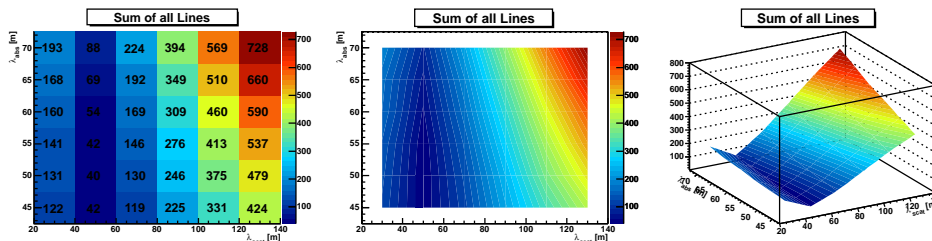
Figure 4.42: Overall χ^2 result, data run r58120, all lines - Left: the sum of the values of the χ^2 tests for all the lines in the detector lines are represented. Center: the corresponding contour plot is shown. Right: the equivalent surface plot is depicted. Only Monte Carlo models with $\eta = 0.15$ are shown.

The best values of the absorption and scattering parameters are taking from the Monte Carlo sample with the smallest χ^2. Afterwards, we put these values for all the 4 special OB runs into an histogram for all the detector lines, excluding the farthest lines to the emitter line. These final results are represented in Figure 4.43.

The absorption and scattering parameters at the ANTARES site measured with
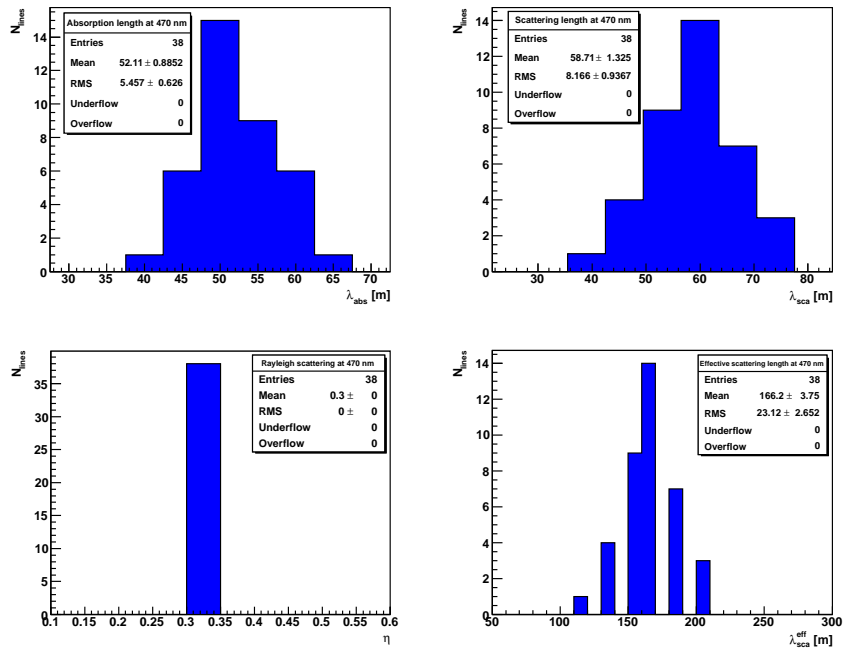
Figure 4.43: Final results on absorption and scattering, OB technique - Top-left: absorption length distribution. Top-right: scattering length distribution. Bottom-left: Rayleigh scattering distribution. Bottom-right: effective scattering length distribution. The number of entries in each histogram correspond to all the active lines (44) evaluated for a total of 4 data runs taken and excluding the lines too distant from the used OB: L9 for OB flashing in L4 (3 runs), and L9, L11, L12 for OB flashing in L2 (one run).

the OB technique gives $\lambda_{abs}(470) = 52.1 \pm 5.5$ m, $\lambda_{sca}(470) = 58.7 \pm 8.2$ m for a $\lambda_{sca}^{eff}(470) = 166.2 \pm 23.1$ m, where the quoted uncertainty are the root mean square of the distributions. If different lines in the detector or different OB light intensity is considered, the impact on the result is inside the quote systematic error ($\pm 10\%$).

Chapter 5

Complementary studies on optical properties with reconstructed track

Education is not the filling of a pail, but the lighting of a fire

William Butler Yeats

As previously commented, two techniques have been developed for optical parameters estimations: the OB technique (presented in Chapter 4) and the reconstructed track technique (this chapter).

The reconstructed track technique is used to quantify the uncertainty in the detector performance (tracks parameters and angular resolution and effective area of the detector) due to the water optical properties estimation and to check the consistency of the results of the OB technique. In this technique, several distributions of physics quantities or magnitudes of real data are compared with the same distributions obtained with Monte Carlo but computed with different values of the optical parameters (absorption length, scattering length and fraction of Rayleigh scattering). Basically, distributions of the quality parameter, directional (i.e., zenith angle) and time information associated to the track are used for data - Monte Carlo comparison.

This chapter is structured as follows. Firstly, the simulation of Monte Carlo events and the reconstruction of tracks are described. Secondly, the data selection procedure is presented, as well as the Monte Carlo production of samples with different absorption and scattering spectra (water models). As before, by water model we

means the values of the inherent optical properties as absorption length, scattering length and fraction of Rayleigh scattering. Afterwards, a preliminary study about how some parameters associated to the track are affected by the optical properties is performed. Then, the quantification of the uncertainty and the estimation of the best model that describes the reconstructed data are carried out. Finally, the effective area and angular resolution of the detector is studied for several water models, including those extracted from the final analysis of the OB and reconstructed track data.

5.1   Event simulation and track reconstruction

An ANTARES physics run consists of Physics events data corresponding to a group of correlated hits in different parts of the detector. In the Monte Carlo simulation of hits, the simulation of the Cherenkov light including photon scattering is taken into account by means of "photon tables" which store the number of photons and distributions of arrival times of PMT hits at different distances, positions and orientations with respect to a given muon track or electromagnetic shower. The reconstruction of the direction of the track which originates such correlated hits is a six-step detailed algorithm involving a pre-selection of hits, linear prefit minimization, maximization and finally a maximum likelihood procedure. The main aspects in the simulation and reconstruction of tracks are presented in this section.

5.1.1   Event generation

The present subsection shows the several stages of the simulation of particle tracks crossing the ANTARES environment. The Monte Carlo physics generators and the simulation of Cherenkov light induced by the relativistic particles crossing the detector environment and the response of the detector are explained as follow.

- **Monte Carlo physics generators:**

  The interaction processes of primary particles with the atmosphere are used in the generation of secondary charged particles. Then, the resulting particles are propagated throughout the detection media reaching the detector sensitive volume. Afterwards, the emission, propagation and detection of

Cherenkov light released by the particles crossing the detector are simulated. Finally, the transformation of photo-electrons into OM "hits" (i.e., the information of charge and arrival times) is performed.

Different codes are used depending on the particles to be simulated. Cosmic and atmospheric neutrinos and their interaction with the Earth are generated with GENHEN (v5r6 this thesis) (126). Atmospheric muons are first simulated in the atmosphere by CORSIKA (127) or MUPAGE (v3r4 this thesis) (128) (129) (130) and then propagated in sea water with MUSIC (126). The Cherenkov light released by the particles and the electromagnetic showers are simulated by the KM3 package (v3r7 this thesis) (121) (122). The light propagation and detector response for hadronic showers is performed by GEASIM (v4r10 this thesis) (131), analogous to KM3 for Cherenkov photons. The propagation of atmospheric neutrinos and muons from the atmosphere to the detector is simulated as follows:

- **Neutrinos:**

    The GENHEN code models the interaction of neutrinos in a chosen energy range $10 \leq E_\nu$ [GeV] $\leq 10^8$ in a large detection volume defined as a function of the maximum muon range for a given energy interval. The simulation includes the deep-inelastic scattering and resonant and quasi-elastic interactions using the LEPTO (132) and RSQ (133) packages respectively. The CTEQ6-D PDF parton distribution is set and the hadronization is carried out by means of the PYTHIA/JETSET (134) physics event generation package. Different models of the atmospheric neutrino flux, as the case of Bartol flux (this thesis) (135) or prompt flux as the RPQM (136) can be chosen to weight the events. The neutrino spectrum is generated as $E^{-1.4}$ but can be weighted after the simulation as atmospheric and signal neutrinos with an isotropic flux as $E_{atm}^{-3.6}$ and $E_{cos}^{-2.0}$ respectively. The neutrino fluxes are simulated in a solid angle of 2πsr as up-going events since down-going atmospheric muons are six orders of magnitude higher, and a cut at zenith $\theta = 90°$ is applied. In this sense, the simulation uses a random time for each event in order to apply a transformation from local to the Equatorial system of reference.

– **Muons:**

The simulation of atmospheric muons is performed at two stages: the tracking of particles from the atmosphere to the sea level (`MUPAGE`), and the propagation below the sea level and to reach the detector (`MUSIC`). The `MUPAGE` package is a muon generator based on parametric formulas from a detailed Monte Carlo simulation of cosmic ray showers releasing muon bundles and reaching the sea level. Afterwards, these muon bundles can be propagated down up to 5 km w.e. (water equivalent) below the sea level with the `MUSIC` package, which consists in a 3D muon propagation code using the cross sections of the muons interaction with water. The muon event kinematics is produced on the surface of the "can" (see Figure 5.1), an imaginary cylinder surrounding the instrumented volume of the detector that defines the volume within the Cherenkov light is generated, i.e., the limit between simple muon propagation and propagation plus Cherenkov light simulation.
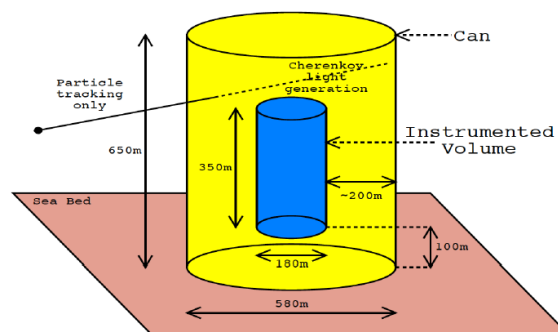
Figure 5.1: Generic detector geometry for Monte Carlo event generation - The so-called "can", is vertically and radially extended about 2.5·λ_{abs} away from the instrumented volume.

The multiplicity of the muons in the bundle, the muon lateral distribution and the energy spectrum can be modelled from the primary CR flux models as HEMAS (this thesis) (137). The muon flux and energy spectrum in `MUPAGE` are parametrized in terms of the vertical depth, the zenith angle, and the bundle multiplicity. For each muon in the bundle, the energy depends as well on the distance of the muon from the shower axis. The atmospheric muon production takes into ac-

count the muon bundle energy threshold and the events are generated following the atmospheric spectra, so no re-weighting is needed.

- **The KM3 code for Cherenkov light induced by particles:**

  A full simulation where every Cherenkov photon is generated and propagated individually is not yet feasible in ANTARES. As alternative, a detailed photon scattering process based on "photon tables" is performed. The KM3 simulation code (121) (122) is organized in three different programs: GEN, HIT and KM3MC. These programs are designed to run in a step-by-step basis. Some introduction about GEN and HIT codes was already explained in Chapter 4, but a slight extended description is as follows:

  - **The GEN package:**

    The GEN code simulates the generation of Cherenkov light by a particle in a given medium (ice, water), including the light coming from secondary particles. The GEN code tracks the Cherenkov photons through space with wavelength-dependent absorption and scattering, recording the position (end point of the track segment), direction and arrival time of photons at spherical shells of various radii centred on the origin, until the photon is absorbed or leaves the volume, as Figure 5.2 indicates.
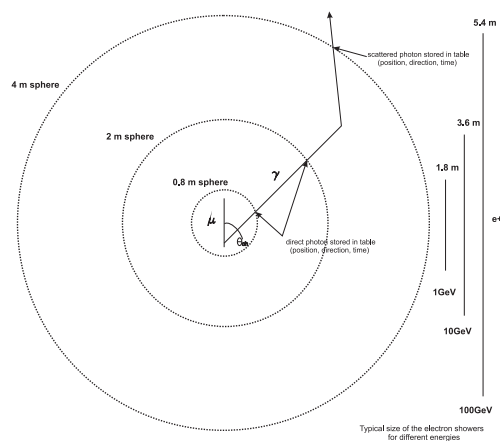
Figure 5.2: The photon tables reference diagram - In the shells scheme, muons and electrons are propagated along the detection medium and the Cherenkov photons are stored in spheres at different distances.

The absorption length spectrum in ANTARES simulations is normalized from *in-situ* data of absorption length measurements at 375 nm and 473 nm (R&D phase) (111). The shape of Smith & Baker spectrum is used, but the normalization is adjusted for tuning the measurements from ANTARES data. The photon scattering in this thesis is described in terms of a linear combination of Rayleigh and Mie scattering, where the Mie angular distribution is fixed to the measurements of Petzold (82). The free parameters are the relative contributions of Mie and Rayleigh scattering and the dependence of the scattering lengths on the photon wavelength, based on the Kopelevich parametrization (86) (84).

– **The `HIT` package:**

This program creates hit probability distributions due to muon track segments and electron showers for the PMT features (i.e., the response for a 10-inch Hamamatsu PMT as gain fluctuation and TTS). The photon fields recorded in shells by `GEN` are read shell-by-shell, converted into hit probabilities and stored in arrays. For each case (muon or electron) probabilities for direct and scattered hits, as well as the cumulative arrival time distributions, are computed as a function of the distance, the angle with respect to the track and the OM orientation.

– **The `KM3MC` package:**

The `KM3MC` code is the detector simulation program which uses as input the hit probability distributions generated in `HIT` for muons and electrons, and the geometrical description of the detector.

The `MUSIC` program is used for muon tracking by iterating through track segments (typically 1 m long) until the muon is stopped or it leaves the detector. A muon is processed if its distance of closest approach to the detector is smaller than 150 m. For each step, the energy lost, the start and end positions, the direction and time of the muon are stored in arrays. If the energy lost by a muon in a segment exceeds the average energy loss by ionization (~0.22 GeV/m), an independent electromagnetic shower is considered in a random location along the segment, it is added to the event particle stack and treated separately as an electron. Once the array with the parameters of each segment

for both particles (muons and electrons) is filled, KM3MC computes the direct and scattered hits produced by such particles.

In order to make it looks like data, the Monte Carlo output file after KM3MC is connected to the TriggerEfficiency package (triggers, calibrations and electronics features) described in Chapter 4. By means of TriggerEfficiency, the Monte Carlo events are coupled with background hits due to ^{40}K and bioluminescence and the identical trigger criteria defined in the online trigger is applied in order to select candidate events in Monte Carlo samples. The background added to Monte Carlo is extracted from real data acquisition conditions what includes number of active OMs, low efficiency PMTs, baseline rate and bursts due to bioluminescence. In the reconstructed track technique the PMT efficiencies are left with their nominal values in the detector, both for data and Monte Carlo.

Concerning systematics attributed to the physics generators, the uncertainty on the atmospheric neutrino flux considered from the GENHEN package, Bartol's or RPQM prompt neutrino flux is $\sim 15\%$ (138). The uncertainty on the atmospheric muon flux generated with MUPAGE is $\sim 30\%$. The uncertainty on the angular acceptance of the OMs (June 2009, this thesis) is other relevant systematic source of uncertainty for the simulated flux of atmospheric neutrinos and muons (138).

5.1.2 Muon track reconstruction

The track reconstruction in this analysis is done with the so-called "Aafit reconstruction algorithm" (139), which is able to work both for data and Monte Carlo samples. For the track reconstruction, the arrival time of a Cherenkov photon to a PMT and other space parameters associated to the track are computed based on the geometrical inference shown in Figure 5.3. Five parameters are required for the reconstruction of a track coming from a relativistic particle: the zenith θ and azimuth ϕ angles respect to the detector, x and y coordinates to locate the point A defined by the intersection of the perpendicular plane P, and the initial time of the muon track t_0 where it crosses A.

In agreement to Figure 5.3, each photon direction is scanned trying to find an equivalence between the hit times and the ones expected for Cherenkov photons
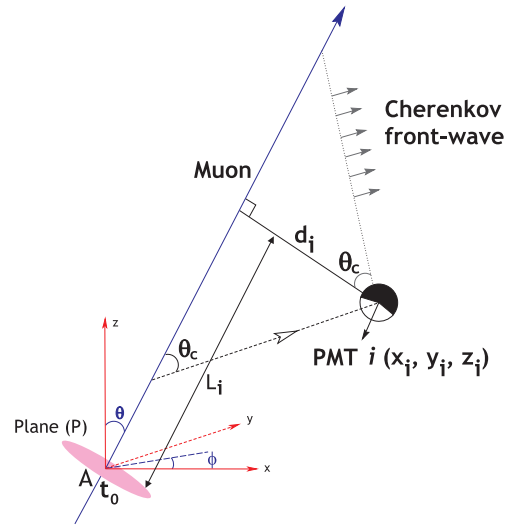
Figure 5.3: Scheme of the geometry used for track reconstruction (i.e., a muon) - A set of five angular, distance and time parameters are needed for the reconstruction of the track by using the `Aafit` algorithm.

emission by a track addressed to that direction. The expected time t^i_{exp} of a hit coming from a Cherenkov photon from a given track can be estimated as

$$t^i_{exp} = t_0 + \frac{1}{c}(L_i - \frac{d_i}{\tan \theta_c}) + \frac{1}{v_g}\frac{d_i}{\sin \theta_c} \quad . \tag{5.1}$$

The second term in Equation 5.1 refers to the time used by the muon for travelling from the initial position to the point where the detected photons are emitted. The last term is just the required time for photons to reach the PMT, where v_g is the group velocity of light. The difference between the true arrival time (t_{hit}) and the expected or theoretical (t_{exp}) time of the hit is known as "time residual" ($t_{res} = t_{hit} - t_{exp}$). The expected arrival time is computed from the muon track time and space parameters as shown, the true arrival time can vary due to photons emitted from secondary electrons or being their path influenced by light scattering. The `Aafit` reconstruction algorithm run along six defined steps:

- **Pre-selection of hits:** the interest is focused to reject as much amount of optical background hits as possible by using a predefined selection algorithm.

- **Linear pre-fit:** it is a first linear fit independent of the starting point, it only uses a sub-sample of the pre-selected hits picked up from local coincidences

(combination of 2 or more hits on one floor in 25 ns) and from hits with amplitudes typically larger than 3.0 photo-electrons.

- **M-estimator fit:** the fit in this step uses the hits which are at distance shorter than 100 m to the initial fitted track and fall on a $\pm$ 150 ns window with respect to the expected time calculated with the parameters of the linear pre-fit. This stage guarantees hits selection with amplitudes larger than 2.3 photo-electrons.

- **Maximum likelihood fit with the original PDF:** here a maximum likelihood fit is done considering time residual from the main fit.

- **Repetition of steps 3 and 4 with different starting points:** the steps 3 and 4 are re-done (9 times) since it improves the efficiency of the algorithm with different starting points concerning the linear pre-fit.

- **Maximum likelihood fit with improved PDF:** the best result obtained in the previous step is used as new starting point for a maximum likelihood fit with an improved PDF (p). In this case, hits are selected with time residual in the [-250, 250] ns interval with amplitudes larger than 2.5 photo-electrons or found in local coincidences. The function p is extracted from Monte Carlo simulations and includes the time residual, the incident angle, the photon path length, and the rate background. Afterwards, p is maximized by using a maximum likelihood function $\mathcal{L}$ which includes the hits with small time residual with respect to the original PDF.

The quality of the reconstruction (Λ) can be estimated as the logarithm of the likelihood function normalized to the degrees of freedom N_{dof}

$$\Lambda = \frac{\log(\mathcal{L})}{N_{dof}} + 0.1(N_{comp} - 1) \quad , \tag{5.2}$$

where N_{comp} represents the number of starting points (number of compatible solutions) result of the track estimation compatible with the preferred result (i.e., which give the same track direction within $1°$). The N_{comp} is also an indicator for rejection of mis-reconstructed tracks. For badly reconstructed events $N_{comp} = 1$ in average, and can reaches up to 9 for well reconstructed events what means that all of the starting points have resulted in the same track. In addition to t_{res}

and Λ, additional track variables can be extracted from the `Aafit` reconstruction algorithm as:

- `beta`: angular uncertainty on the muon track direction such as

$$\beta = \sqrt{\sin^2(\theta_{rec})\sigma_\phi^2 + \sigma_\theta^2} \quad , \tag{5.3}$$

- `tcosth`: cosine of the zenith (θ) of the fitted track,

- `tphi`: azimuth (ϕ) $[-\pi, \pi]$ of the fitted track (not used for single line fit).

Other track parameters not commented before can be easily obtained by a slight modification in the `Aafit` code and suitable treatment of data formats (140) (141).

5.2   Optical properties analysis with reconstructed track

As previously commented, the optical properties studies using reconstructed track are performed comparing distributions of physics quantities associated to the real track, with the same distributions obtained with Monte Carlo samples generated with different inherent optical parameters as absorption length, scattering length and fraction of Rayleigh scattering. A preliminary comparison of quantities such as the quality parameter of the track, the angular error associated to the track, and the zenith angle is performed before the quantification of the uncertainty due to the exact water model (combination of different optical parameters) which describes the data, and the subsequent estimation of the best favoured water model. The preliminary data - Monte Carlo comparison lead as well, to the definition of some quality cuts for tracks used in the analysis. An estimation of the uncertainty associated to the knowledge of the exact water model is performed. The simulated water model that better agrees with the data uses a similar approach as the one used to represented the χ^2-minimization in the OB technique, but considering the mean values (and RMS) of the data - Monte Carlos ratios of muon time residual distributions (t_{res}).

5.2.1 Data run selection

The physics and calibration data in ANTARES are recorded in ROOT format during specific data taking sessions (the so-called runs). The duration of the physics run depends on the number of switched triggers along the acquisition period, thus on the number of triggered hits. Once recorded, the triggered hits are used to reconstruct the particle track which originates them. Two sub-samples (for a preliminary and extended analysis) of the official runs selection used in the ANTARES neutrino point sources searches, have been used for optical properties studies by using the reconstructed track technique.

The first data set is a sub-sample extracted from the official analysis of point-like sources in ANTARES for 2007-2008 data (142) (143). It includes 1044 data files for a 12-lines configuration of the detector in a period defined between 08/05/2008 and 30/12/2008 ($34091 \leq$ run-number ≤ 38216) which means a total lifetime of the data sample of 76.77 days. The second data set (which includes the first one) covers almost two years between 2008 and 2010 ($31051 \leq$ run-number ≤ 54244) with a total lifetime of 618.96 days with about 6000 physics data runs. This second data set was extracted from the last official analysis of point-like sources in ANTARES for 2007-2010 data (144) (35). Both data sets are referred to as official reconstructed data in May 2011. The chosen data sets followed the official quality criteria in ANTARES based on "basic" runs, for which no problems where found during data acquisition. These "basic quality runs" are featured by some minimum requirements as:

- Effective duration of the run larger than 1000 s. This is to avoid runs accidentally started, i.e., by human errors or with the wrong configuration.

- No double frames are present. This is thought in order to reject two data frames (array of hits) coming from the same ID label, i.e., the same ARS, what could mess the configuration, etc.

- No synchronization problems. This is part of consistency checks on the timestamp and index of the timeslices, in order to ensure that no timeslices are lost, or duplicated, or coming in the wrong order.

- Reasonable muon rate between 0.001 Hz and 100 Hz. This is a very loose criterion just to ensure that the 3N trigger rate (Chapter 2) has reasonable

values, i.e., away of recording wrong data as coming from a switched OB
or something messy. It is not supposed to cut any physics event.

Each data run in ANTARES is associated to a specific run setup which defines
the trigger logics and the calibration set to be used in the data taking. For the
time-range when the data taking took place, a mean baseline rate about 70 kHz
with two periods of high optical activity were registered. The whole selected data
is reconstructed by using the `Aafit` algorithm into the official `SeaTray` framework
(145). The reconstruction chain consists of "modules" which interpret the raw
data, apply the calibration and perform the reconstruction. The relevant data
stream is ordered as "frames" storing quantities related to the position, direction,
particle, hit, track and the detector geometry (including OM and PMT features).
Some additional features are set by the user related to the reconstruction, analysis
and simulation if it is the case.

5.2.2 Monte Carlo production (water models)

A reduced range of optical parameters was used for preliminary studies with recon-
structed track. A total of ten Monte Carlo samples were generated following the
"Partic" model (Chapter 3). Such Monte Carlo samples consisted in simulated
and reconstructed physics events in water assuming different water properties, it
is, several combinations of inherent optical properties of the medium as absorption
length, scattering length and fraction of Rayleigh scattering. The absorption and
scattering spectra used for these simulations are depicted in Figure 5.4.
The Monte Carlo samples (water models) were generated in such a way that two
absorption lengths (λ_{abs}) were tested. For each λ_{abs}, three models had the same
effective scattering length (λ_{sca}^{eff}) and different fraction of Rayleigh scattering (η),
and three of them had the same η and different λ_{sca}^{eff} (see Table 5.1 for exact
values).
On the other hand, an extended study was performed producing a larger number
of Monte Carlo water models. This new set consisted of 27 new combinations of
λ_{abs}, λ_{sca} and η. They were constructed from 9 different scattering spectra (3
values of λ_{sca}^{eff} and η) and 3 absorption spectra as represented in Figure 5.5 and
summarized in Table 5.2.
The results from the OB technique on λ_{abs} and λ_{sca} at 470 nm are used as input for
the simulation and reconstruction of tracks. Some water models which minimizes
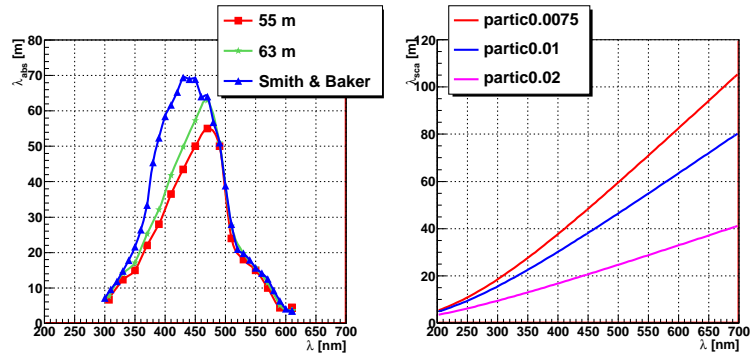
Figure 5.4: Preliminary water models set tested in track reconstruction -
Left: two absorption length spectrum are considered and compared with the Smith
& Baker spectra for the clearest natural waters, the values in the legend correspond
to the maximum. Right: three scattering spectra are used based on the Kopelevich
parametrization. The contributions of large and small scattering centres are assumed
as equal.

λ_{abs} [m]	λ_{sca} [m]	η	λ_{sca}^{eff} [m]
55	53	0.17	227
55	41	0.17	176
55	22	0.17	94
55	41	0.11	227
55	22	0.02	227
63	53	0.17	227
63	41	0.17	176
63	22	0.17	94
63	41	0.11	227
63	22	0.02	227

Table 5.1: The first water models tested comprises ten generated Monte Carlo
samples, to be compared with the preliminary data sample.

λ_{abs} [m]	λ_{sca} [m]	η	λ_{sca}^{eff} [m]
50	17	0.10	100
50	34	0.10	200
50	51	0.10	300
50	26	0.20	100
50	52	0.20	200
50	78	0.20	300
50	55	0.30	100
50	71	0.30	200
50	106	0.30	300
55	17	0.10	100
55	34	0.10	200
55	51	0.10	300
55	26	0.20	100
55	52	0.20	200
55	78	0.20	300
55	55	0.30	100
55	71	0.30	200
55	106	0.30	300
60	17	0.10	100
60	34	0.10	200
60	51	0.10	300
60	26	0.20	100
60	52	0.20	200
60	78	0.20	300
60	55	0.30	100
60	71	0.30	200
60	106	0.30	300

Table 5.2: The water models of the second set comprises 27 Monte Carlo samples chosen uniformly in λ_{abs}, λ_{sca}^{eff} and η, extending the range of study.
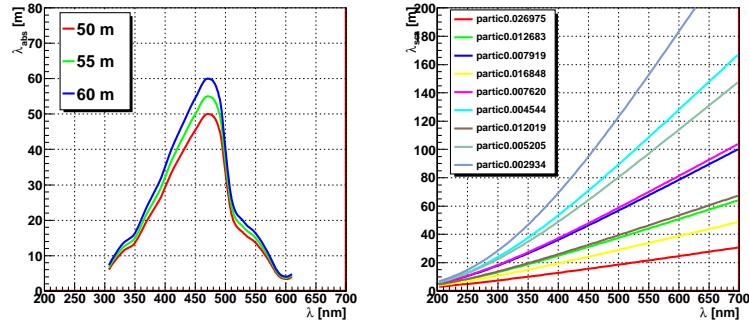
Figure 5.5: Second extended water models set tested in track reconstruction - Left: three absorption length spectra are used. Right: nine scattering spectra based on the Kopelevich parametrization are used. Large and small centres equally contribute.

the data - Monte Carlo discrepancy in the final results of the OB technique (see Table 5.3) were generated as well in the track simulation and reconstruction chain for a full absorption and scattering spectra.

λ_{abs} [m]	λ_{sca} [m]	η	λ_{sca}^{eff} [m]	Run number (OB)
55	70	0.35	175	61518
50	50	0.2	192	58607
50	50	0.3	142	58120

Table 5.3: Additional water models tested in reconstruction. Each combination of optical parameters as λ_{abs}, λ_{sca} and η in Monte Carlo gives the minimal χ^2 when it is compared with the OB run, specified in the last column. The aim of this production is the study of the detector performance, namely angular resolution and effective area.

5.2.3   Influence on the reconstructed track

Once the reconstruction chain is applied for the triggered events both for data and Monte Carlo, several parameters associated to the track can be extracted. This section starts from a qualitative analysis of the influence of the water properties in the distributions of track parameters as the quality parameter, the angular error and the zenith angle. Afterwards, the quantification of this influence is presented and discussed.

As commented before, the quality of the track reconstruction is evaluated by

means of the parameter Λ, or in other words, Λ is used to discriminate good and badly reconstructed events. Figure 5.6 shows the distribution of the reconstruction quality parameter Λ for real data and for different simulated water models (Table 5.1). The plots in the left (respectively right) column correspond to models with $\lambda_{abs} = 55$ m (respectively $\lambda_{abs} = 63$ m). The upper row plots are for $\Lambda > $ -10, while the lower row plots are for $\Lambda > $ -5.4 (a value customarily used to select good reconstructed tracks since it rejects most of the atmospheric muons wrongly reconstructed as up-going). For all the plots, a cut in $\cos\theta > 0$ (tracks reconstructed as up-going) and $\beta < 1°$ (tracks with low angular uncertainty) are applied.
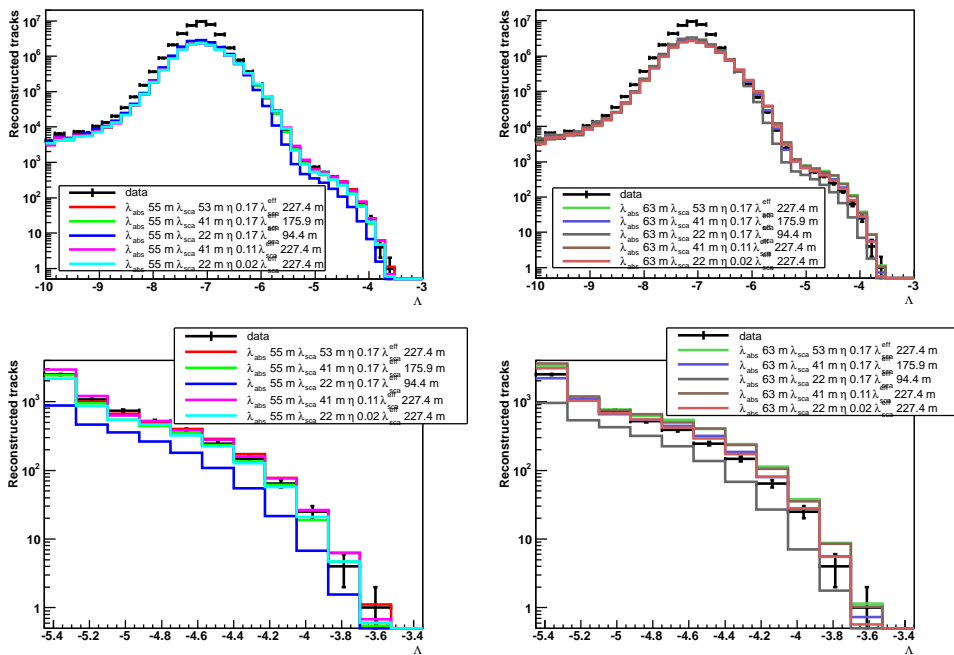
Figure 5.6: Distribution of the quality parameter Λ for data and Monte Carlo generated with different optical parameters. Scattering preliminary checks - In order to see the influence of the scattering, absorption length is fixed in each plot and the scattering parameters are changed. Up-left: distributions with absorption length of 55 m. Up-right: distributions with absorption length of 63 m. Down-left: a zoomed version for the $\lambda_{abs} = 55$ m case. Down-right: a zoomed version for the $\lambda_{abs} = 63$ m case. The quality cuts $\beta < 1°$ and $\cos\theta > 0$ are applied in all the cases.

The first observation in both cases is the poor level of agreement when short λ_{sca}^{eff}

values are assumed, being the corresponding distributions systematically below the data. The water model in red constitutes the ANTARES official water model used on the Monte Carlo simulation of the detector.

On the other hand, Figure 5.7 shows Λ distributions for water models where scattering parameters are fixed and absorption lengths are different (55 m and 63 m). As seen, the favoured models point to large λ_{sca}^{eff} values, while models with low values of λ_{sca}^{eff} ($<$ 100 m) show a large discrepancy with real data and can be discarded. As observed, the shortest absorption length (λ_{abs} = 55 m) seems to agree better with data.
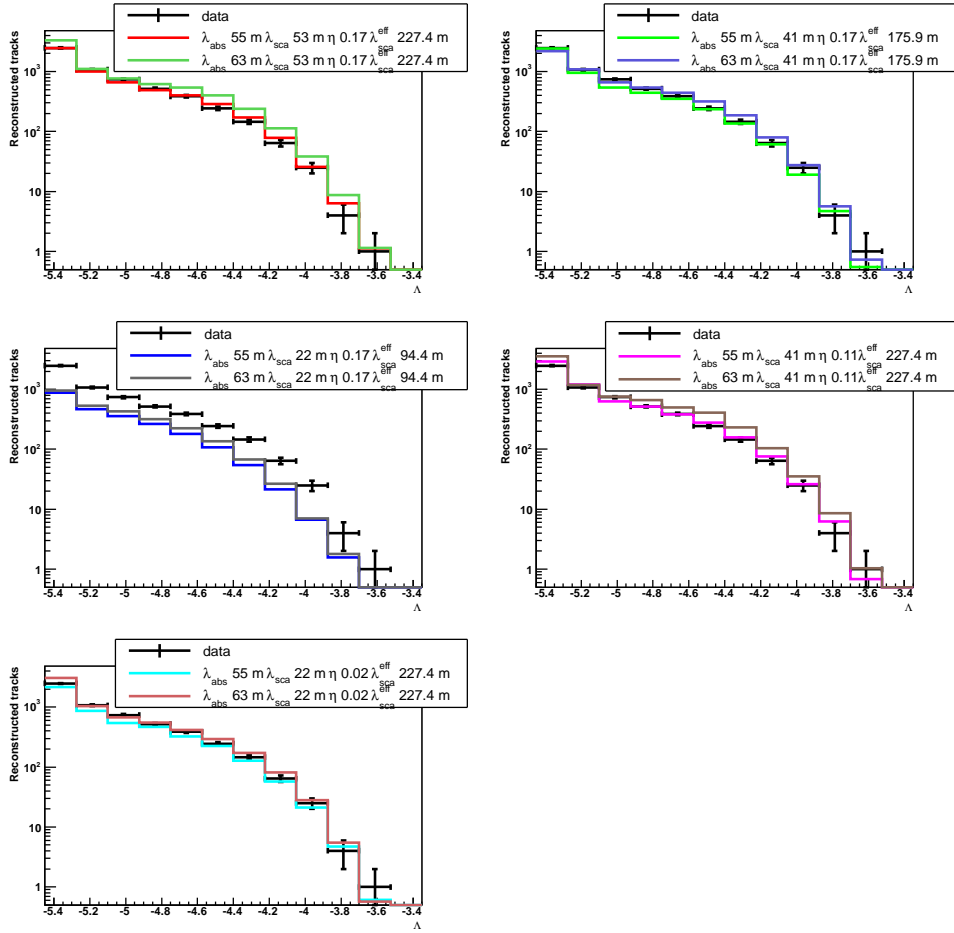
Figure 5.7: Distribution of the quality parameter Λ for data and Monte Carlo generated with different optical parameters. Absorption preliminary checks - In order to see the influence of the absorption, in each plot scattering parameters remain fixed and absorption length is changed. The quality cuts $\beta < 1°$ and $\cos\theta > 0$ are applied in all the cases.

Nonetheless, for combinations of very low values of λ_{sca} and η (i.e. Figure 5.7-bottom-left), a larger $\lambda_{abs}$ can not be totally rejected. There is, apparently, a degeneracy between water models with the same λ_{sca}^{eff}, which is to be expected, since the quality of the fit, Λ, only depends on the time residuals of the track hits. Figure 5.8 shows the Λ distributions of ratios data and Monte Carlo obtained bin-to-bin of all the cases previously presented. By means of the data - Monte Carlo ratios is better seen that $\lambda_{abs} = 55$ m agrees better with data, although the bad agreement for $\lambda_{sca}^{eff} < 100$ m is also clear. Moreover, from these ratio plots a change in the shape for Λ distributions is observed when several combinations of λ_{abs} and λ_{sca} values are considered. The optical properties clearly influence the quality of the reconstructed tracks.

In the track reconstruction the likelihood function near the fitted maximum is assumed to follow a multivariate Gaussian distribution, where the error of zenith and azimuth angles are estimated from the covariance matrix. The angular uncertainty or angular error on the muon track direction, β, can be obtained from these errors, as shown in Equation 5.3. A cut of $\beta < 1°$ ensures a rejection of at least 50% of atmospheric muons which are mis-reconstructed as up-going tracks (144) (35). As previously seen, the changes due to optical properties on the main track reconstruction parameters are better observed from their corresponding data - Monte Carlo ratios. The data - Monte Carlo ratios of β for different water models for up-going $(\cos\theta > 0)$ and well reconstructed $(\Lambda > \text{-}5.4)$ tracks are shown in Figure 5.9.

As a general observation, the distributions with $\lambda_{abs} = 55$ m seems to agree better with data despite a slight overestimation of the expected data - Monte Carlo ratio in some cases. For $\lambda_{abs} = 63$ m underestimations are observed, but the slight flat trend of some models do not clearly allow to discard them. Once again the degeneracy between water models is seen. Additionally, it is observed that changes on the optical properties of the water do not show a strong influence on the determination of the angular error associated to the track, β. There are not significant changes in the shape of the data - Monte Carlo ratio plots, although the normalization in the distributions varies since the number of reconstructed tracks depends on absorption.

The cut in zenith angle governs the selection of up-going $(\cos\theta > 0)$ or down-going $(\cos\theta < 0)$ tracks. Up-going events are those used (naturally) for identification of

Figure 5.8: Ratio between data and Monte Carlo for Λ distributions with different Monte Carlo water models - In the left column, water models with λ_{abs} = 55 m are shown. In the right column the models with λ_{abs} = 63 m are depicted. Each row corresponds to a different value of scattering parameter. The quality cuts $\beta < 1°$ and $\cos\theta > 0$ are applied in all the cases.
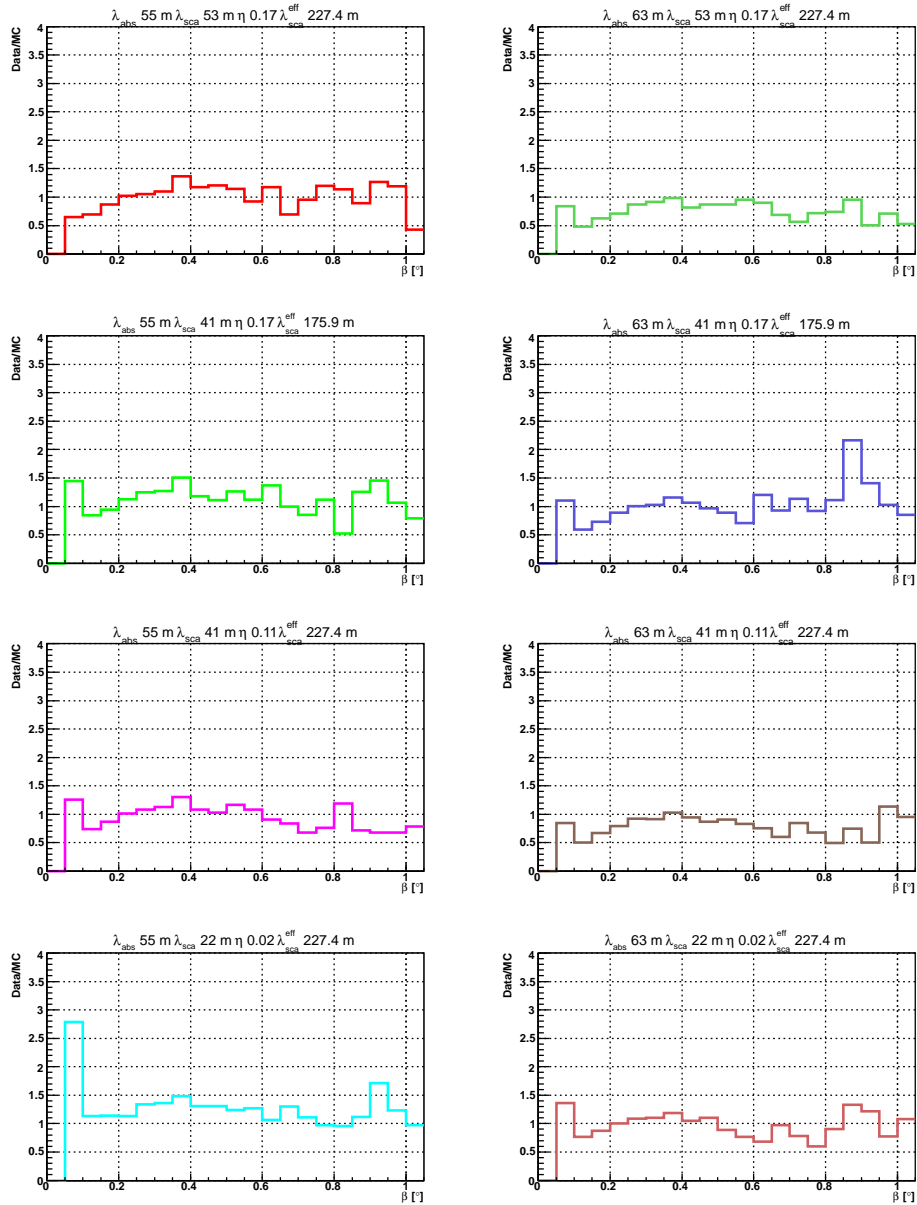
Figure 5.9: Ratio between data and Monte Carlo for β distributions with different Monte Carlo water models - In the left column, water models with λ_{abs} = 55 m are shown. In the right column the models with λ_{abs} = 63 m are depicted. Each row corresponds to a different value of scattering parameter. The quality cuts $\cos\theta > 0$ and $\Lambda > $ -5.4 are applied in all the cases.

neutrino point sources. The data - Monte Carlo ratio for the cosine of the zenith angle distribution for the different water models is shown in Figure 5.10 for $\Lambda >$ -5.4 and $\beta < 1°$ cuts.

As it was seen for β, the data - Monte Carlo ratio for $\cos\theta$ shows that the directional information provided by the zenith angle of the track is not spoiled due to the uncertainty on the water model determination for up-going tracks. The discrepancy between data and Monte Carlo for down-going tracks is to be expected since the reconstruction algorithm is optimized to reconstruct up-going tracks and moreover the OMs are looking downwards, therefore most of the hits collected come from scattered photons. Several combinations of λ_{abs}, λ_{sca} and η do not distort the shape of the data - Monte Carlo ratio distributions and the loss of tracks by absorption effects does not give a sizeable slant on the $\cos\theta$ distributions for up-going tracks. As the atmospheric muon and neutrino events are uniformly distributed in azimuth angle, not any distribution or cut related to azimuth at all were relevant in this analysis.

As general comment, for all the magnitudes showed before, low values of λ_{sca} (i.e., $\leq$ than 35 m) combined with very large values of λ_{abs} could lead to degenerated solutions and both effects can be compensated. It is the reason why a more wide range of optical parameters have been evaluated in this thesis.

Once a first look to the influence of the water properties on the main track reconstruction parameters has been done, a quantification of such influence on the reconstruction quality parameter Λ becomes appropriate. This quantification is done independently for up-going atmospheric neutrinos ($\nu+\bar{\nu}$) and down-going atmospheric muons (μ). The idea is to estimate how much this quality parameter of the reconstruction can change when some optical parameter as λ_{abs} and λ_{sca} are modified as Equation 5.4 indicates

$$\frac{dN_{(\nu,\mu)}}{N_{(\nu,\mu)}} = K \cdot \frac{d\lambda_{(abs,sca)}}{\lambda_{(abs,sca)}} \quad , \tag{5.4}$$

where K is the proportionality constant which quantify the impact of the optical parameter in the quality of the reconstruction.

In Figure 5.11, four cases of distributions of Λ are represented: neutrino and muon distributions with different λ_{abs} and the same scattering parameters (Figure 5.11-up), and neutrino and muon distributions with different scattering parameters and same λ_{abs} (Figure 5.11-down). Only the quality cut at $\Lambda >$ -5.4 was applied.
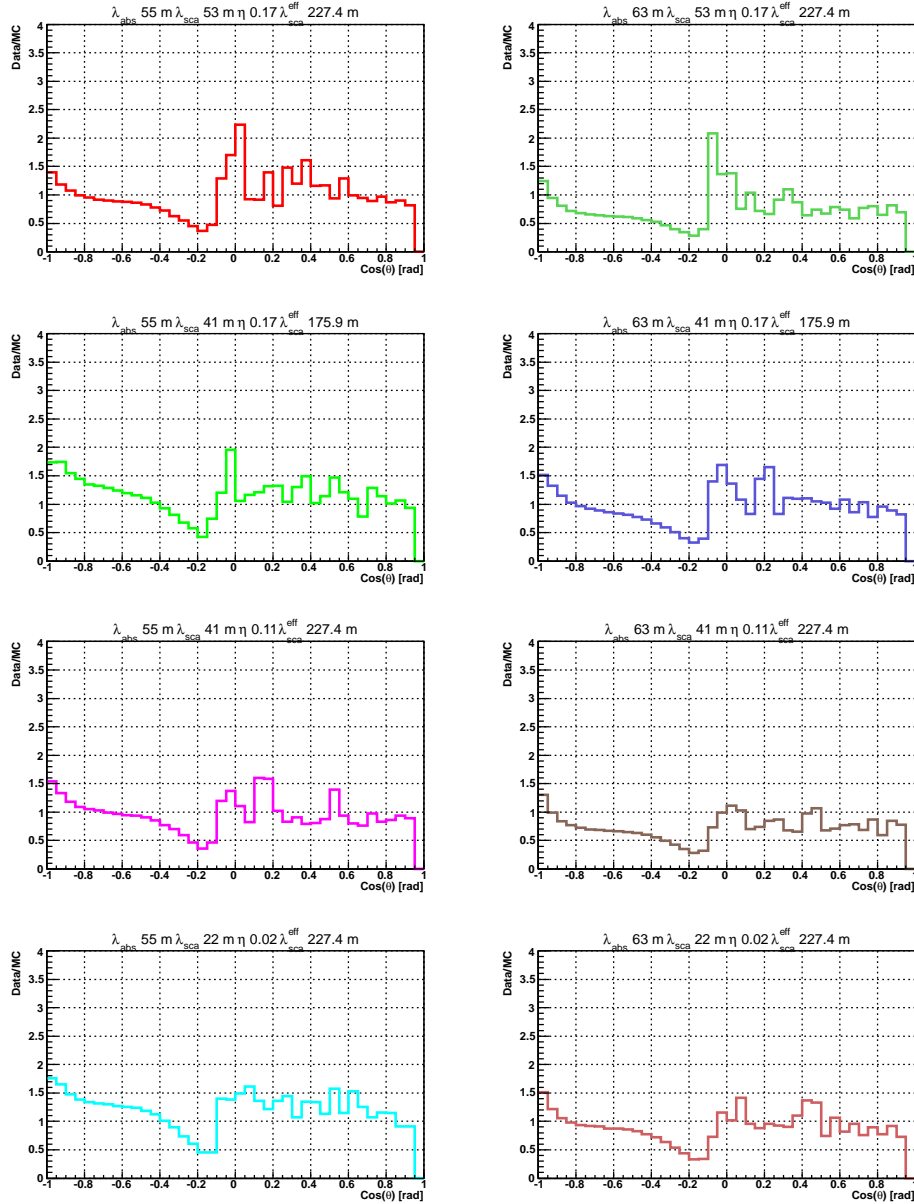
Figure 5.10: Ratio between data and Monte Carlo for the cosine of the zenith angle $\cos\theta$ **distributions with different Monte Carlo water models** - In the left column ,water models with $\lambda_{abs} = 55$ m are shown. In the right column the models with $\lambda_{abs} = 63$ m are depicted. Each row corresponds to a different value of scattering parameter. The quality cuts $\Lambda > -5.4$ and $\beta < 1°$ are applied in all the cases.

Based on Table 5.1, the first two cases correspond to increase λ_{abs} from 55 to 63 m (first and sixth row respectively, 15% of uncertainty) leaving λ_{sca} fixed at 53 m. The second two cases correspond to a fixed value of λ_{abs} at 55 m (or 63 m) decreasing λ_{sca} from 53 m to 41 m (first and second row respectively, 23% of uncertainty).
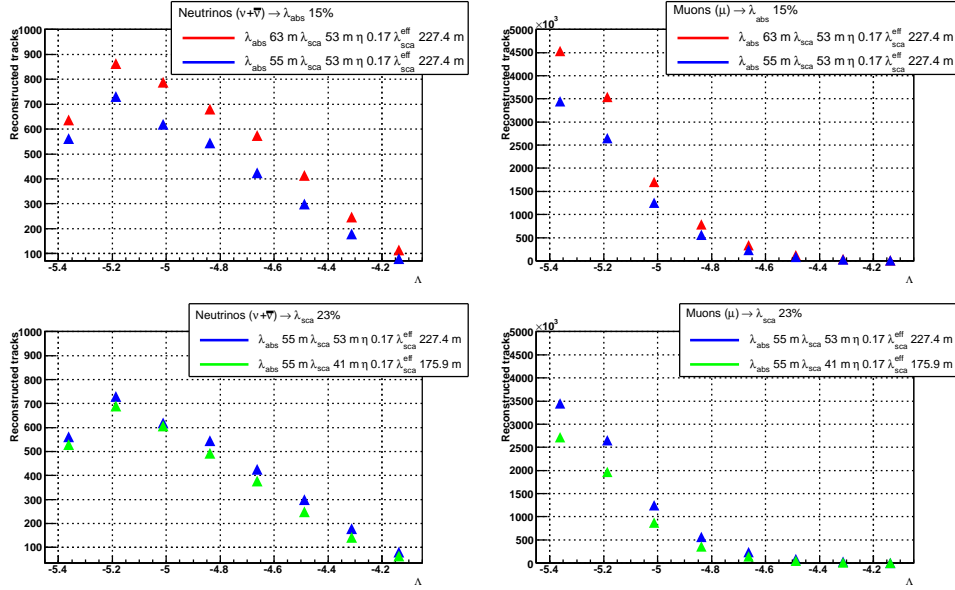
Figure 5.11: Extraction of the uncertainties in Λ distributions due to absorption and scattering - In agreement to Table 5.1, four cases are evaluated. Up-left: neutrino distributions with λ_{abs} non-fixed and fixing λ_{sca}. Up-right: muon distributions with λ_{abs} non-fixed and fixing λ_{sca}. Down-left: neutrino distributions with λ_{sca} non-fixed and fixing λ_{abs}. Down-right: muon distributions with λ_{sca} non-fixed and fixing λ_{abs}. Only the quality cut $\Lambda > -5.4$ is applied in all the cases.

In each case in Figure 5.11, the bin with the maximum occupancy (maximum bin) is determined and the number of reconstructed tracks (bin content) is evaluated for each pair of distributions. Then, Equation 5.4-left can be applied. The Equation 5.4-right represents the uncertainty on the parameter whose influence we want to evaluate, for instance λ_{abs} or λ_{sca}.

By solving the particular case for absorption in Figure 5.11-up for Λ we have for neutrinos and muons respectively

$$\frac{dN_\nu}{N_\nu} = 0.18 \qquad , \qquad \frac{dN_\mu}{N_\mu} = 0.32 \quad . \tag{5.5}$$

In turn, looking for the uncertainties due to scattering in Figure 5.11-down we have for neutrinos and muons respectively

$$\frac{dN_\nu}{N_\nu} = 0.06 \qquad , \qquad \frac{dN_\mu}{N_\mu} = 0.27 \quad . \tag{5.6}$$

As it can be deduced, up-going neutrinos become less affected ($\sim$18%, $\sim$6%) by the optical properties (λ_{abs} and λ_{sca}) than atmospheric down-going muons ($\sim$32%, $\sim$27%) respectively. On the other hand, the absorption has a stronger effect both for neutrinos and muons than scattering. The relative change of the number of tracks as a function of the change in the absorption length is then:

$$\frac{dN_\nu}{N_\nu} = 1.2\frac{d\lambda_{abs}}{\lambda_{abs}} \qquad \frac{dN_\mu}{N_\mu} = 2.2\frac{d\lambda_{abs}}{\lambda_{abs}} \quad , \tag{5.7}$$

while the change as a function of the variation in the scattering length case is:

$$\frac{dN_\nu}{N_\nu} = 0.3\frac{d\lambda_{sca}}{\lambda_{sca}} \qquad \frac{dN_\mu}{N_\mu} = 1.2\frac{d\lambda_{sca}}{\lambda_{sca}} \quad , \tag{5.8}$$

where the proportionality constant is extracted applying Equation 5.4 to neutrino and muon distributions for λ_{abs} and for λ_{sca}. The results obtained with this method are reasonably in agreement within the uncertainties reported by other similar studies performed in ANTARES (146).

5.2.4 Muon time residual. Most favoured water model estimation

As commented before, the difference between the true arrival time (t_{hit}) and the expected time (t_{exp}) of the hit is known as "time residual" ($t_{res} = t_{hit} - t_{exp}$). The muon time residual comparison between data and Monte Carlo is used as a complementary analysis to estimate the water model that agrees better with data. The method is similar to that of the OB technique, but using the mean value (and RMS) of the data - Monte Carlo ratio for muon time residual distributions instead of the χ^2-test. Only the up-going muon tracks with $\Lambda > -5.4$ and $\beta < 1°$ are considered. In this case, the correct selection of events is relevant since bad reconstructed events can spoil the estimation of the water model that better describes the data. Therefore, soft cuts in the quality parameter for up-going tracks have to be applied since less up-going events are expected than down-going ones.

The distribution of the time residual of the hits used in the reconstructed tracks

is computed for the water models listed in Table 5.2 and then compared with the time residual distribution extracted from data. Figure 5.12 shows the comparison of the muon time residual distributions for up-going tracks between data and Monte Carlo distributions for the water models of Table 5.2.

The normalization of the Monte Carlo time residual distributions (among others) in Figure 5.12 depends on two factors: the scaling to the lifetime of the data concerning that of the sample and the generation weight relative to the number of physics events generated for the whole sample. The latter depends of the size of the whole Monte Carlo samples, which is not the same in all the cases and explains the statistical fluctuations for some models seen in Figure 5.12.

As observed in Figure 5.12, the agreement with data gets worst as the scattering length decreases (denoted by "ls"), no matter the absorption length considered (denoted by "la"). This is clearly seen for $\lambda_{sca} < 35$ m (plots P-Z). Such observations were also previously commented for different track parameters. A short scattering length (i.e., $\lambda_{sca} < 35$ m) seems not compatible with data at the ANTARES site. Concerning the remaining models, evident over/under-estimations allows to reject some of them. The models labelled as A, H, K, L, N or O seem to agree better with data. These first assessments from visual inspection can be better quantified from the data - Monte Carlo ratio distributions shown in Figure 5.13.

The most favoured model should be close to the unit (green line) and with low fluctuations along the time residual window (narrow RMS). Table 5.4 shows the mean and RMS values extracted from the data - Monte Carlo ratio distributions from Figure 5.13.

		Data/MC ratio ($\bar{x}\pm$rms)								
		λ_{sca}^{eff} ($\eta = 0.1$) [m]			λ_{sca}^{eff} ($\eta = 0.2$) [m]			λ_{sca}^{eff} ($\eta = 0.3$) [m]		
		100	200	300	100	200	300	100	200	300
λ_{abs} [m]	60	2.28±0.53	1.38±0.42	1.12±0.35	2.20±0.46	0.97±0.39	0.76±0.31	2.35±0.25	0.84±0.35	0.68±0.26
	55	3.04±0.25	1.36±0.61	1.22±0.52	2.34±0.79	1.00±0.41	0.83±0.42	2.21±0.67	0.94±0.41	0.64±0.21
	50	3.73±0.34	1.84±0.65	1.68±0.67	3.51±0.41	1.80±0.70	1.21±0.70	3.43±0.34	2.07±0.64	1.08±0.58

Table 5.4: The table shows the mean and RMS values extracted from the Data/MC ratio distributions for the water models used in the muon time residual analysis. Each three columns the results are grouped by each of the 3 values of η used, and for the 3 different values of the λ_{sca}^{eff}. Each row corresponds to the results grouped by each of the 3 λ_{abs}.
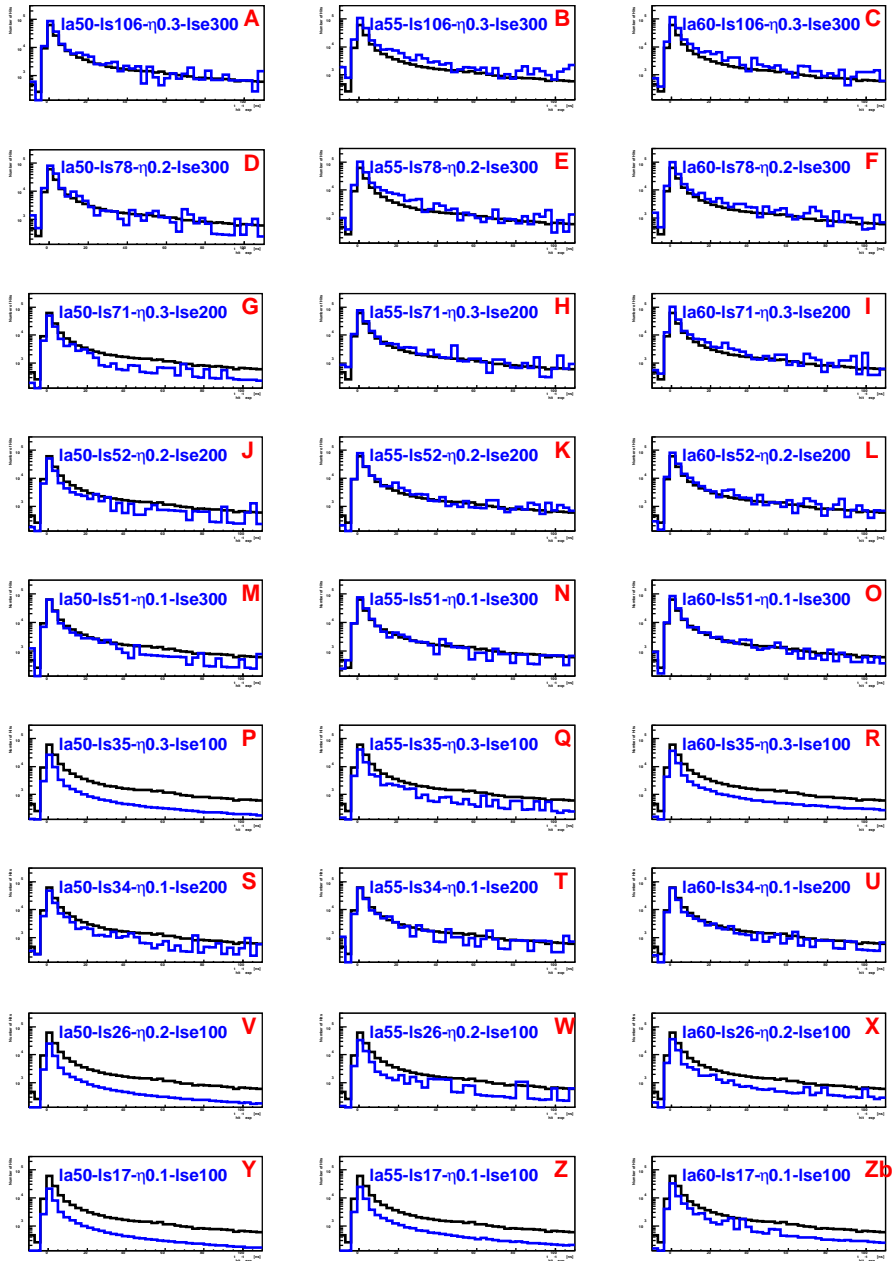
Figure 5.12: Time residual distributions for data and Monte Carlo for up-going tracks - Each Monte Carlo distribution extracted from the 27 models listed in Table 5.2 is compared with that of data. The λ_{abs} ("la") increases (from 50 to 60 m) from left to right column and λ_{sca} ("ls") decreases (from 106 to 17 m) from top to bottom row, λ_{sca}^{eff} is labelled as "lse". In the y-axis the number of hits is represented, the x-axis for the muon time residual. The quality cuts $\cos\theta > 0$, $\Lambda >$ -5.4 and $\beta < 1°$ are applied in all the cases.
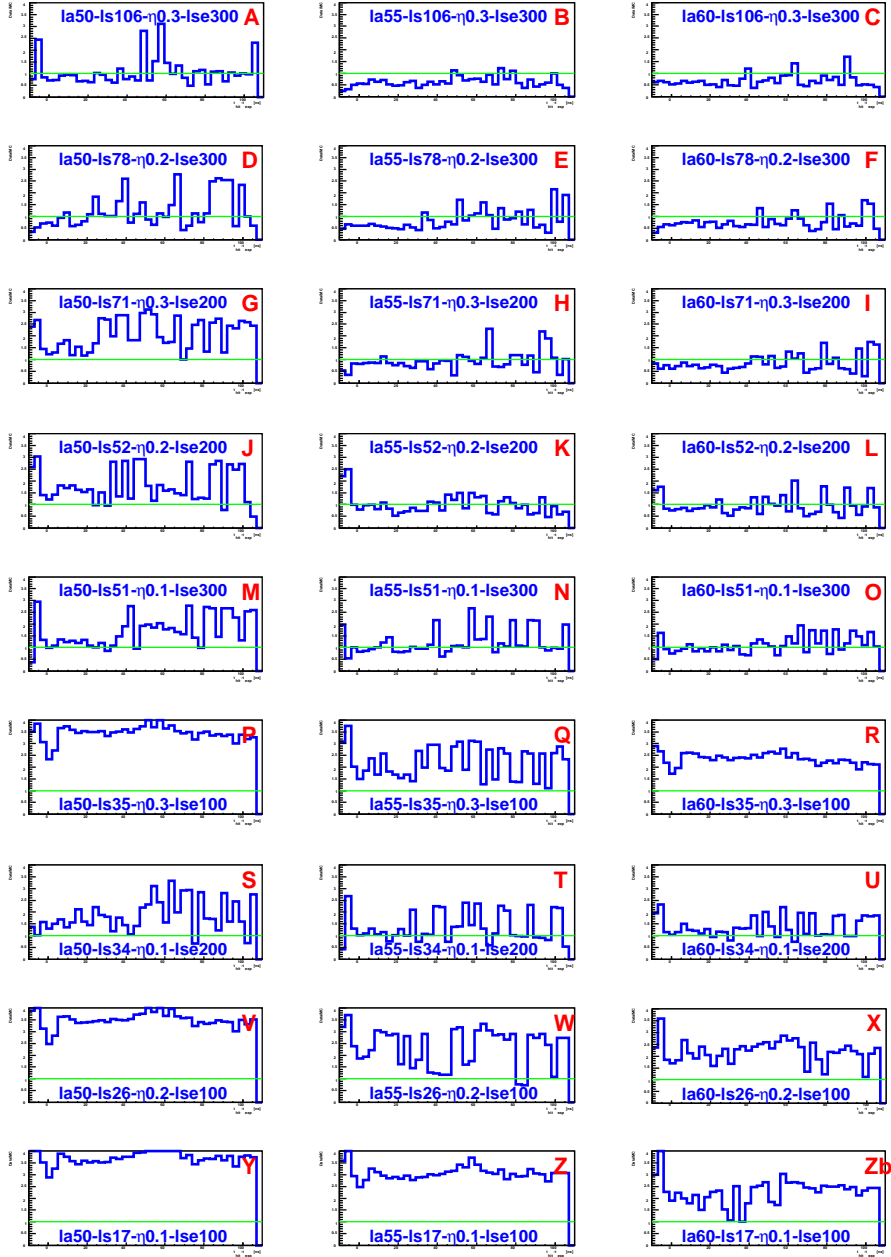
Figure 5.13: Data - Monte Carlo ratios for time residual for up-going tracks - Each plot corresponds to a different water model from Table 5.2. Absorption lengths ("la") increases (50 m - 60 m) from left to right and scattering length ("ls") decreases (106 m - 17 m) from top to bottom, the effective scattering length is labelled as "lse". In the y-axis it is represented the Data/MC ratio, in the x-axis the muon time residual. The quality cuts $\cos\theta > 0$, $\Lambda > $ -5.4 and $\beta < 1°$ are applied in all the cases.

As can be seen, for $\eta \geq 0.2$ similar values for the mean and RMS of the data - Monte Carlo ratios for some models are achieved. From Table 5.4-center ($\eta = 0.2$), the proximity to unity of the mean value of the data - Monte Carlo ratio distributions is something clear only for a pair of water models, those giving 0.97±0.39 and 1.00±0.41. The results for the same pair of water models but with $\eta = 0.3$ are 0.84±0.35 and 0.94±0.41 respectively. Based on the qualitative analysis and results showed in Table 5.4, the most favoured water model searching leads to an educated choice of $\lambda_{abs} = 55$ m, $\lambda_{sca} = 52$ m, $\eta = 0.2$ and $\lambda_{sca}^{eff} = 200$ m, what matches within the uncertainty of the final results of the OB technique (Figure 4.43). However, as it was suggested in the previous section, due to the degeneracy between water models a largest λ_{abs} could not be discarded.

As conclusion, Figure 5.14 compares the most favoured water models extracted from the OB and reconstructed track strategies. In turn, it shows the upper limits for λ_{abs} and λ_{sca} for pure water (90). The reference with predictions for clean sea water for λ_{abs} and λ_{sca} is as well represented (89).
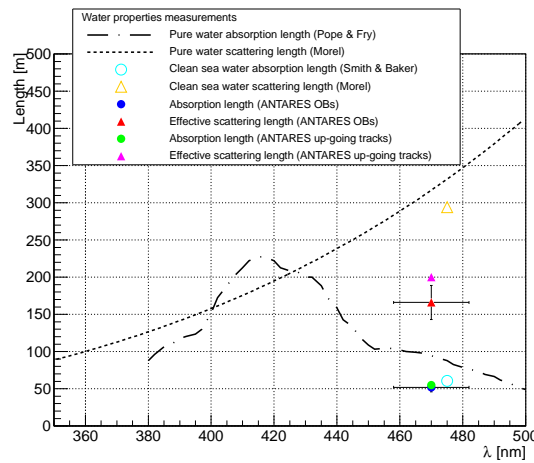
Figure 5.14: Summary of absorption and effective scattering lengths estimations at the ANTARES site (470 nm) - The data - Monte Carlo ratios method for the reconstructed track technique seems to match reasonably with the results of the χ^2-minimization of the OB technique at 470 nm. The upper limits for pure and clearest natural waters are shown for reference.

As seen, the results of λ_{abs} estimations from both methods, OB and reconstructed track, are compatible within the uncertainties. The λ_{sca}^{eff} obtained from the reconstructed track technique differs by a 17% concerning the measurement with the OB technique. The clean sea water absorption estimation from Smith & Baker

(89) seems to agree within the measurements obtained from OB and reconstructed track techniques and below the upper limit set by Pope & Fry measurements for pure water (90). Concerning scattering measurements, the λ_{sca}^{eff} estimations by both techniques differ in about 100 m with the predictions for clean sea water from Morel studies (91) and about 150 m respect to the pure water scattering length upper limit set by Morel (91). The λ_{abs} has the strongest effect in the reconstruction of tracks and it is estimated with less uncertainty than the λ_{sca}^{eff} which has a weaker effect.

5.3   Influence on the detector performance

The angular resolution and the effective area of the detector are the most important parameters concerning the search for point sources of cosmic neutrinos, therefore, the influence of the water properties on such magnitudes has to be known. This study is performed comparing such magnitudes as a function of the neutrino energy. A brief comparison on the number of neutrino events by assuming different weights for atmospheric and cosmic neutrino fluxes is carried out. The study of the influence of the water properties on the detector performance namely angular resolution and effective area is the final subject of this thesis, with special attention to the analysis of such magnitudes based on the water models estimated from the reconstructed track and OB techniques. Such water models and the official ANTARES model are summarized in Table 5.5.

λ_{abs} [m]	λ_{sca} [m]	η	λ_{sca}^{eff} [m]	Method
55	53	0.17	227	ANTARES official
55	52	0.2	200	Reconstructed up-going tracks
55	70	0.35	175	OB `CALIBOB-r61518`
50	50	0.2	192	OB `CALIBOB-r58607`
50	50	0.3	142	OB `CALIBOB-r58120`

Table 5.5: The table shows the most favoured water models obtained from the OB and reconstructed track techniques, which are used to study their influence on the angular resolution and effective area estimations of the detector. The reference ANTARES water model is used for comparison.

5.3.1 Angular resolution

The angular resolution of the detector is defined as the median of the distribution of the difference in absolute value between the reconstructed direction (θ_{rec}) and the true direction (θ_{true}) of the track. As commented in Chapter 2, the angular resolution can be only estimated by Monte Carlo simulations. As starting point, the Figure 5.15 shows the angular resolution of the detector for two water models from Table 5.1, where λ_{abs} has been changed by a 15% keeping fixed λ_{sca} (left) and contrariwise (right), where λ_{sca} is changed by a 23% keeping fixed λ_{abs}.
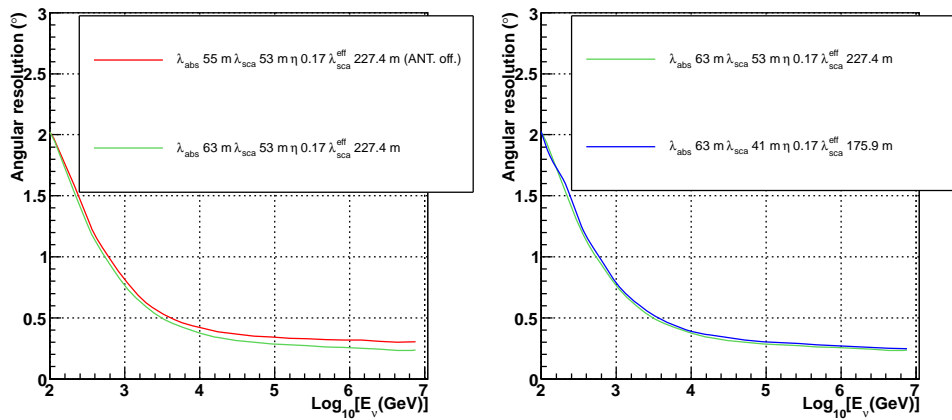
Figure 5.15: Angular resolution as a function of the neutrino energy, water models changing λ_{abs} and λ_{sca} - Left: angular resolution for two different absorption lengths (15%) and λ_{sca} fixed. Right: angular resolution for two different scattering lengths (23%) and λ_{abs} fixed. Quality cuts ($\Lambda > -5.4$, $\beta < 1°$) for tracks defined in the last section are applied for up-going events.

The influence due to both λ_{abs} and λ_{sca} on the angular resolution becomes less than $0.1°$ for the whole neutrino energy range, where λ_{abs} slightly dominates at high energies. The angular resolution at lower neutrino energies is mainly linked to the kinematics as the $\nu - \mu$ angle, and at higher energies governed by the quality of the reconstruction. In general, from medium to higher neutrino energies (i.e. $E_\nu > 10^4$ GeV) the λ_{abs} has a "stronger" influence on angular resolution ($\sim$0.05-0.1°) comparing to λ_{sca} ($\sim$0.05°). At lower energies (i.e. $E_\nu < 10^4$ GeV) both λ_{abs} and λ_{sca} behave similar ($\sim$0.05°). Higher the λ_{abs} and λ_{sca}, better angular resolution is achieved.

On the other hand, the angular resolution estimated for the most favoured water

model from the reconstructed track technique (Up-going tracks) and those from the OB technique (CALIBOB-r*) are compared in Figure 5.16. The ANTARES official angular resolution is also shown which corresponds to that estimated until the release of the last Monte Carlo production done in this thesis.
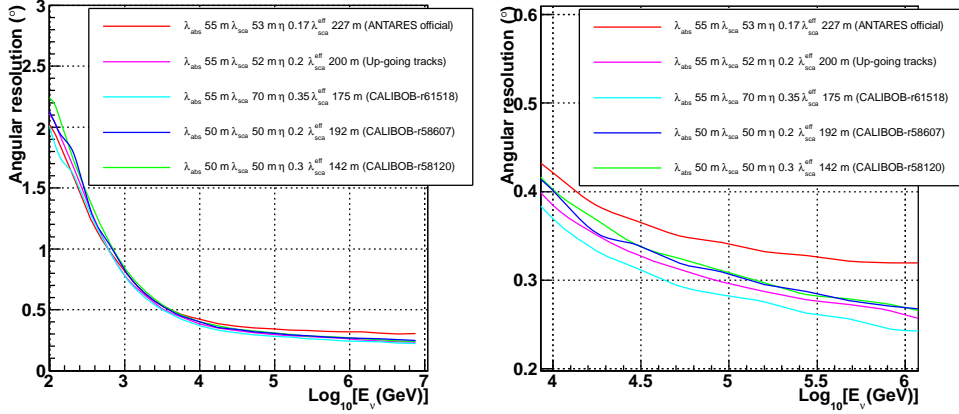
Figure 5.16: Angular resolution of ANTARES compared for the most favoured water models from the reconstructed track and OB techniques - Left: angular resolution as a function of the neutrino energy (full energy range). Right: a zoomed version for intermediate energies. Quality cuts for tracks ($\Lambda > -5.4$, $\beta < 1°$) defined in the last section are applied for neutrino up-going events.

As seen on Figure 5.16, the angular resolution for the water models estimated from the reconstructed track and OB techniques is slightly improved concerning the official one in ANTARES (red curve). The reconstructed track and OB strategies, show similar results on the angular resolution of the detector for the whole neutrino energy range considered. The equivalence of the techniques allows an improvement about $0.05°$ in average concerning the official angular resolution of ANTARES.

5.3.2 Effective area

The effective area can be considered as the ANTARES detection efficiency, and as commented in Chapter 2, can be only calculated by Monte Carlo simulations. The estimation of the effective area for the same uncertainties considered in the study of the angular resolution is depicted in Figure 5.17.

For the λ_{abs}, at lower energies (i.e. $E_\nu < 10^4$ GeV) an overall change of 16% in the effective area of the detector is estimated. This uncertainty decreases down to
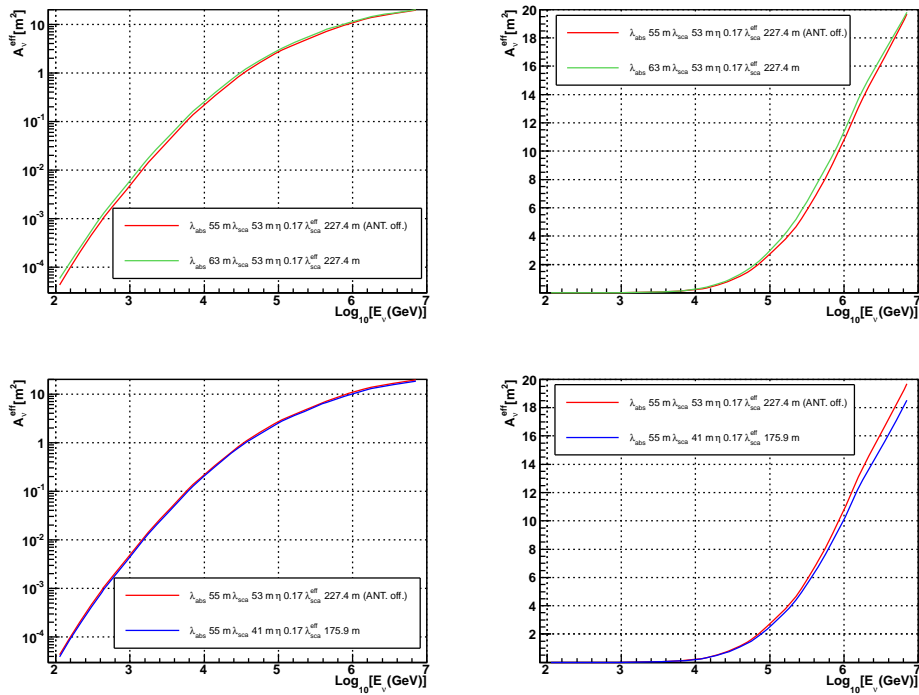
Figure 5.17: Effective area as a function of the neutrino energy, water models changing λ_{abs} **and** λ_{sca} - Up: effective area for two different absorption lengths (15%) and λ_{sca} fixed. Down: effective area for two different scattering lengths (23%) and λ_{abs} fixed. Quality cuts for tracks ($\Lambda > -5.4$, $\beta < 1°$) defined in the last section are applied for up-going events. Right plots in non-log scale.

a 5% at higher energies (i.e. $E_\nu > 10^6$ GeV). Therefore, a change between 16-5% in the effective area is seen due to the uncertainty on the λ_{abs} along the neutrino energy range considered. Concerning λ_{sca}, at lower energies an overall change of 5% in the effective area of the detector is extracted, but slightly increased up to 7% at higher energies. A change between 5-7% in the effective area is seen due to the uncertainty on the λ_{sca} for the whole neutrino energy range considered. Higher the λ_{abs} and λ_{sca}, higher the detector effective area and more neutrinos are detected.

A final look to the influence due to water properties on the effective area based on the selected water models from the reconstructed track and OB strategies is represented in Figure 5.18.
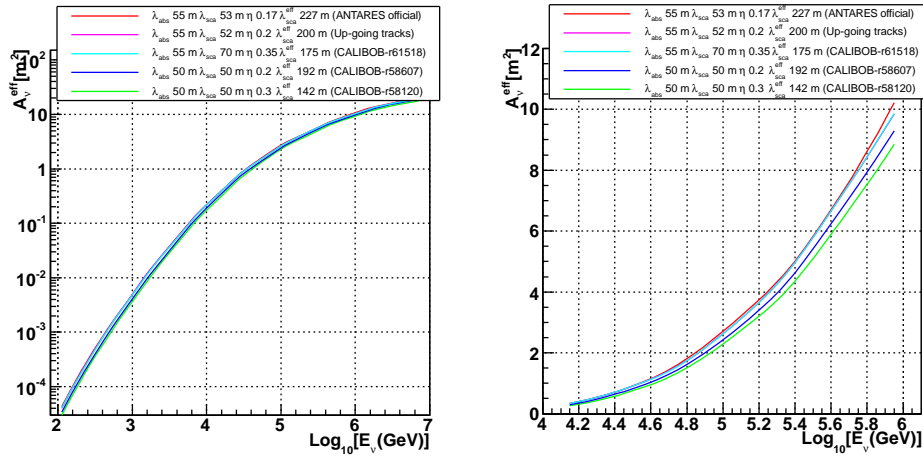
Figure 5.18: Effective area of ANTARES compared with the best favoured water models from the OB and reconstructed track strategies - Left: effective area as a function of the whole neutrino energy range considered. Right: a zoomed version (no-log scale) at intermediate energies. Quality cuts ($\Lambda > -5.4$, $\beta < 1°$) for tracks defined in the last section are applied for neutrino up-going events.

As it can be seen from Figure 5.18, the best model estimated from the reconstructed track technique does not show difference enough concerning the "official" estimations in ANTARES. On the other hand, the water models obtained from the OB technique are compatible among them since no large differences are shown in terms of effective area, what is clearly seen in Figure 5.18-right where a zoom to intermediate energies is represented.

Chapter 6

Summary and Conclusions

6.1 Overview

Neutrino Astronomy aims to scientifically exploit neutrinos as a new cosmic messenger to explore high energy astrophysical phenomena in the TeV–PeV energy range. The very low fluxes and the small interaction cross-section of neutrinos with matter require the construction of massive detectors. When the incoming neutrino direction can be reconstructed with a reasonable angular accuracy, the detector is dubbed "telescope", since the neutrinos, having no electric charge, point back to their source. In the Cherenkov technique, the observation of the neutrino is carried out through the detection of the Cherenkov light induced by the charged relativistic particles produced in the neutrino interaction with matter, mainly the muon in the case of the charged current interactions of muon neutrinos. From the arrival time and position of the detected Cherenkov photons induced by those secondary particles which cross the medium where the detector is located, information on the neutrino direction and energy can be inferred. Since the optical properties of the medium in which the telescope is located determine the transmission of the Cherenkov photons, a proper understanding of the influence of these properties in the track reconstruction and detector performance is required.

The ANTARES deep-sea neutrino detector is the first fully operational undersea neutrino telescope in the Northern Hemisphere. It consists in a three-dimensional layout of 885 photomultipliers (PMTs) arranged in 12 detection lines plus one instrumentation line. Each detection line has 25 storeys, each of them containing

triplets of PMTs housed in optical modules (OMs) and independent modules with the associated electronics. Some of these storeys are equipped with extra devices for time calibration and positioning of the detector. The *Optical Beacon* system, in particular, was designed for the *in-situ* time calibration of the apparatus, i.e. for the proper synchronization of its OMs. Although originally designed to this end, the OB system can be used to have a handle on the optical properties of the surrounding water.

The objective of this thesis is to characterize the ANTARES detection medium. In this sense, some optical properties of the water namely, transmission, absorption and effective scattering lengths are measured with the OB system. Additionally, a complementary study on how such properties influence the reconstruction of tracks and the detector performance is carried out.

To reach this goal, special calibration runs were commissioned and new instruments for water properties measurements were built and operated, e.g. the multiwavelength beacon and the nano-beacons. The tuning of the operating parameters and the handling of such devices once installed in the detector were also tasks performed during this work to achieve the aforementioned goal. Likewise, the development of specialised software codes for calibration and physical analyses together with the production of large simulation samples were, in addition, an important part of this work.

The analysis of the data taken by such devices and of the dependence of the track reconstruction parameters has led to the following results.

6.2   Results on optical properties at the ANTARES site

Two techniques were developed for optical properties measurements: the OB technique (main strategy) and the reconstructed track technique (complementary analysis). The OB technique was used to determine the transmission, absorption and scattering lengths of light. The reconstructed track technique was used to quantify the uncertainty on the reconstruction of tracks due to water properties,

support the OB results for absorption and scattering and quantify their influence on the detector performance.

6.2.1   The OB technique - Systematics

One of the first qualitative results of this work is the realization that the OB system, which is well suited for time calibration, has several important limitations when applied to the investigation of optical properties for which it was not specifically designed. Losses or inefficiencies that do not affect substantially the determination of the time offsets do have, however, an influence on the measurement of optical properties, which are extremely sensitive to instrumental effects. The systematic effects discovered and treated during this work are the following:

- Shadowing

  Intervening material reduces the amount of direct photons that reach the OMs in the same line where the OB is located. This has a negligible influence in time calibration, but has a sizeable effect for optical properties, since forward scattering is large. This problem has been circumvented using OMs in a line different from the one where the OB is located.

- Electronic effects

  The *token ring* mode of the ARS seriously distorts the time distribution of the photons when more than one photon arrives within the ARS time window. This effect is not present for the first arriving photons and therefore does not affect time calibration. The cure to this problem is to operate at the one photo-electron level in the target OMs.

- Source characteristics and its relative location

  The position of the LED inside the OB, the angular distribution of the emitted light and the width of its time distribution are instrumental effects that are convoluted with the light transmission effects to be measured. Likewise, the intrinsic width of the wavelength spectra of the different LEDs change with distance since absorption depends on wavelength, but absorption is in turn one of the optical properties to be measured. Therefore, source effects are inextricably intermingled with the optical properties influencing the final measured quantities, i.e. arrival time and amount of light.

- OM efficiencies

  OM efficiencies have, in general, a negligible effect on timing, but they have to be determined accurately enough for the determination of the optical properties.

These instrumental effects influence each other. For instance, the fact that the shadowing imposes the use of the OMs in neighbouring lines has as a consequence the need to know the angular distribution of the emitted light in regions where its variation with angle is larger and less well determined. Moreover, the symmetry is lost and the actual orientation of the target OMs with respect to the emitting OB has to be known. Likewise, since we are obliged to operate in the one-photoelectron regime, the range of usable OB-OM distances is limited by this requirement and by the need to have sufficient signal over background.

6.2.2   The OB technique - The Transmission Length

The transmission length of light at three different wavelengths (406 nm, 470 nm and 531 nm) was estimated with different OBs in the detector. The method uses a fit to the Beer-Lambert equation of the exponential decrease of signal hits along the neighbouring line with the maximum number of signal hits collected. The *single top-LED* and *all top-LEDs* OB configurations were used. The results for transmission length can be summarised as follows:

$$\lambda_{tr}(406 \text{ nm}) \quad = \quad 31.2 \pm 2.8 \text{ m}$$

$$\lambda_{tr}(470 \text{ nm}) \quad = \quad 39.9 \pm 2.9 \text{ m}$$

$$\lambda_{tr}(531 \text{ nm}) \quad = \quad 20.5 \pm 2.1 \text{ m}$$

Additionally:

- the results are reasonably homogeneous across the detector, without any significant deviation;

- there is a good agreement between the root mean square of the transmission length distribution and the mean value from the distribution of errors from the fits.

  The uncertainties in the transmission length measurements are smaller than

10% and that in the signal intensity by storey smaller than 20%, mainly
due to the loss of symmetry by the flashing neighbouring lines. The un-
certainties in the measurements at 406 nm and 470 nm may be somewhat
overestimated, as indicated by the χ^2 and pull distribution analysis. The
test at 531 nm agrees with expectations;

- the variation with time of the transmission length does not exceed its uncer-
  tainty, therefore this quantity can be considered stable at least in the course
  of these measurements.

6.2.3   The OB technique - The Absorption and Scattering Lengths

The goal of this analysis is the extraction of the theoretical parameters that de-
scribe the transmission of light in water, i.e. the absorption and scattering lengths
and the fraction of Rayleigh scattering, using the amount of photons and their
arrival times at different distances. In this case, the main problems faced were the
following:

- There is no analytical formula of the optical parameters to describe the
  distributions of the measured quantities. Therefore, a set of Monte Carlo
  simulations were generated for a combination of the values of the different
  optical parameters and compared to data.
  The experimental set-up implies a large probability to have several scat-
  terings and the relative values of the optical parameters do not allow to
  neglect absorption or scattering. This prevents any possible simple analyt-
  ical approximation. Therefore, the theoretical expectations to which the
  experimental data are compared have to be produced by means of Monte
  Carlo simulation. A total of 432 water models were generated correspond-
  ing to the combination of 8 absorption lengths, 9 scattering lengths and 6
  fractions of Rayleigh scattering.

- Given the limited amount of information at our disposal, i.e. time and num-
  ber of photons at a few positions with respect to the source, the sensitivity
  to the variation of the parameters is limited and instrumental effects are
  important.
  It is known that forward scattering is large, but due to the shadowing effect

we cannot collect data at low angle. The instrumental effects are large and mixed with the physical phenomena.

- Shadowing effects prevent the use of the OMs located in the same line as the emitting OB. The orientation of the OMs in neighbouring lines changes the amount of light received.

  To tackle this problem, the simulation was performed run-by-run, i.e. the actual conditions of the lines concerning the pointing direction of the relevant OMs was reproduced in the Monte Carlo for each actual data run.

The absorption and scattering lengths at 470 nm were estimated comparing, by means of a modified Pearson's χ^2-test, the arrival time distributions for the data and for Monte Carlo samples produced with different combinations of the optical parameters, for the "*all top-LEDs*" configuration of the OB. The main results obtained were the following:

- the method works well on simulated samples;

  The method was firstly validated on Monte Carlo simulation itself. Two trial simulation models were generated playing the role of real data. From all the models, such with the smallest χ^2 value is chosen.

- the method was applied to a total of 4 different data runs. Taking into account the behaviour of the χ^2 distribution around the minimum the values obtained for different lines were in reasonable agreement. Nevertheless, some instrumental effects were clearly observed in particular for the lines more distant from the OB line.

- An overall minimization was performed using all the available runs for all the lines excluding the most distant ones. The parameters obtained are:

$$\lambda_{abs}(470 \text{ nm}) = 52.1 \pm 5.5 \text{ m}$$

$$\lambda_{sca}(470 \text{ nm}) = 58.7 \pm 8.2 \text{ m}$$

$$\lambda_{sca}^{eff}(470 \text{ nm}) = 166.2 \pm 23.1 \text{ m}$$

The overall minimization used four data runs, each of which employed all the lines excluding the line where the OB was located and those too distant

from the emitting OB, namely: L9 for the OB flashing in L4 (3 runs), and L9, L11, L12 for the OB flashing in L2 (one run). The best values of the absorption and scattering parameters are taking from the Monte Carlo sample with the smallest χ^2. This gives a total of 38 entries for each optical parameter. Since the modified χ^2 function around the minimum has not a parabollic behaviour and the spread of the values obtained hints to a non-statistical origin, it was considered that the root mean square of the distribution of the minimized parameters was an adequate estimator of the uncertainty in the measurements.

6.2.4 The reconstructed track technique - The Absorption and Scattering Lengths

The absorption and scattering results from the OB data analysis were complemented by an independent study based on reconstructed tracks. In this study, the distributions of variables associated to the track as the reconstruction quality parameter, Λ, the angular uncertainty extracted from the track fit, β, the zenith angle, $\cos\theta$, and the muon time residuals, t_{res}, extracted from data and Monte Carlo were compared.

After a preliminary study with 10 water models, an independent set of 27 water models, corresponding to three absorptions lengths ($\lambda_{abs} = 50$ m, 55 m and 60 m) three Rayleigh scattering proportions ($\eta = 0.1$, 0.2 and 0.3) and three effective scattering lengths ($\lambda_{sca}^{eff} = 100$ m, 200 m and 300 m) were finally simulated and the distributions of the aforementioned variables compared to those in data for tracks with $\cos\theta > 0$ (up-going), $\beta < 1°$ (low angular error) and $\Lambda > -5.4$ (well reconstructed). The main results obtained from the reconstructed track technique are summarized as follows:

- From the comparison of the Λ distributions, the main result obtained is the poor level of agreement with data for Monte Carlo samples with $\lambda_{sca}^{eff} \leq 100$ m, $\lambda_{sca} \leq 35$ m and $\eta \leq 0.11$.
  This is in agreement with the expectation of large effective scattering lengths in deep–sea water and a high fraction of forward scattering.

- For good reconstructed tracks, $\Lambda > -5.4$ and $\beta < 1°$, even though the overall normalization changes with the value of the water properties, the

shape of the distributions of the ratio of data over Monte Carlo as a function of the estimated angular error and of the zenith angle does not vary dramatically, i.e. there is no sizeable bias toward any specific region of these variables. This indicates that the uncertainty on the water properties does not induce a bias in the angular determination of the tracks.

- The comparison of the Λ distributions for different water models indicates that for up-going atmospheric neutrinos a relative variation in λ_{abs} induces a variation in the number of reconstructed events 1.2 times larger, while this number of events varies only a factor of 0.3 times the variation in λ_{sca}. For down-going atmospheric muons, the number of reconstructed tracks changes the relative variation in λ_{abs} a factor 2.2 larger, while it is a factor 1.2 the variation in λ_{sca}.

- The model that better agrees with data in the t_{res} distribution has $\lambda_{abs} = 55$ m, $\lambda_{sca} = 52$ m and $\lambda_{sca}^{eff} = 200$ m.
  This is in agreement with the result of the OB technique. However, longer absorption lengths cannot be discarded if the Rayleigh proportion is (somewhat artificially) lowered to very small values. These "degenerate" solutions (with extreme combinations of parameters) can also describe the data and this degeneracy is somehow intrinsic to this method for which only a limited amount of information is available.

Concerning the impact of the water properties on the detector performance, i.e. on the angular resolution and the neutrino effective area, the following statements can be made:

ANGULAR RESOLUTION:

- If λ_{abs} is increased from 55 m to 63 m ($\sim$15% bigger) keeping constant the rest of parameters, the neutrino angular resolution changes by less than $0.1°$ in the neutrino energy range $10^2 - 10^7$ GeV.
  The parameters λ_{sca} and η were fixed to 53 m and 0.17, respectively, but within reasonable limits they should not influence the change of angular resolution with λ_{abs}, which is small in any case.

- If λ_{sca} is decreased from 53 m to 41 m (a $\sim$23% smaller), keeping constant the rest of parameters, the neutrino angular resolution changes by less than 0.05° in the neutrino energy range $10^2 - 10^7$ GeV.

  The parameters λ_{abs} and η were fixed to 63 m and 0.17, respectively, but within reasonable limits they should not influence the change of angular resolution with λ_{sca}, which is small in any case. For a value of $\eta = 0.17$, λ_{sca}^{eff} decreases from 227 m to 176 m, still a very high value and therefore, the change in photon arrival times is expected to be small and not influence sizeably the angular resolution, as this study confirms. This is a known quality of deep–sea water as a medium for neutrino telescopes: the high effective scattering length provides very good angular resolution.

- The angular resolution estimated for the water models preferred by the OB and the reconstructed track techniques is slightly better ($\sim$0.05–0.1°) than the official ANTARES estimation and therefore the latter can be considered a conservative estimate of the angular resolution.

EFFECTIVE AREA:

- If λ_{abs} is increased from 55 m to 63 m ($\sim$15% bigger) keeping constant the rest of parameters, the effective area increases by 16% (5%) in the low (high) end of the neutrino energy range $10^2 - 10^7$ GeV.

  As expected, the absorption length has a non-negligible influence on the effective area. The higher the energy of the neutrino, and therefore the higher the amount of light deposited, the lower the influence of a variation in the absorption length.

- If λ_{sca} is decreased from 53 m to 41 m (a $\sim$23% smaller) keeping constant the rest of parameters, the effective area decreases by 5% (7%) in the low (high) end of the neutrino energy range $10^2 - 10^7$ GeV.

  As expected, the photon loss due to an increase in scattering is smaller than in absorption, since photons do not disappear and a good fraction of them are deviated by small angles.

Chapter 7

Resumen

7.1 Una nueva era en la astronomía

Rayos cósmicos, rayos gamma y astronomía de neutrinos: la astronomía tradicional proviene de la información que proporcionan los fotones, partículas estables y eléctricamente neutras. Sin embargo, existen ciertas limitaciones a la hora de estudiar algunos sistemas astrofísicos ubicados en regiones densas y distantes en el cosmos. Los fotones de alta energía, o rayos gamma, pueden interaccionar con la luz de fondo extra galáctica (*Extragalactic Background Light* ó EBL) restringiendo su alcance a distancias del orden de decenas de Mpc. Igualmente la interacción con el fondo cósmico de microondas (*Cosmic Microwave Background* ó CMB) puede limitar las distancias recorridas a las decenas de kpc. Debido a estas limitaciones, mensajeros cósmicos alternativos como los neutrinos cumplen con las cualidades necesarias para realizar esta "nueva" astronomía. El neutrino es una partícula que solo interacciona débilmente y al no tener carga eléctrica puede proceder de sistemas astrofísicos muy distantes y densos apuntando directamente hacia su fuente de emisión. Desafortunadamente, debido a su baja sección eficaz de interacción y bajo flujo esperado, hacen falta grandes volúmenes de detección para su captura. Actualmente, el enfoque más aceptado para estudiar los fenómenos más energéticos del universo consiste en una astronomía de multi-mensajeros, lo que incluye la astronomía de rayos cósmicos, astronomía de rayos gamma y astronomía de neutrinos.

Astronomía de rayos cósmicos: los rayos cósmicos se clasifican como primarios (aquellos que vienen de la fuente: e^-, p^+, He, Fe, etc.) y secundarios (resultado

de la interacción de los primarios con el gas estelar o la atmósfera de la tierra).
A pesar de haber sido descubiertos hace más de 100 años, el origen (partículas,
energía y sitio de aceleración) de los rayos cósmicos permanece aún sin resolverse.
El mecanismo más aceptado de aceleración de rayos cósmicos es el "Mecanismo de
aceleración de Fermi", procesos de dispersión iterativa de partículas cargadas en
una onda de choque a lo largo de sus trayectorias dentro de los campos magnéticos
cósmicos. Los principales sitios de aceleración basados en la teoría de Fermi están
representados en el "gráfico de Hillas" e incluyen: explosiones de rayos gamma
(*Gamma Ray Bursts* ó GRBs), remanentes de supernovas (*Super Nova Remnants*
ó SNRs) y núcleos de galaxias activas (*Active Galactic Nuclei* ó AGNs).

Astronomía de rayos gamma: la astronomía de rayos gamma utiliza fotones
con energías superiores a los 100 keV para estudiar sistemas astrofísicos exóticos.
Actualmente, dos tipos de mecanismos de aceleración que dan lugar a este tipo de
partículas son comúnmente referenciados: el mecanismo de aceleración leptónico y
el mecanismo de aceleración hadrónico. El tipo leptónico da lugar a rayos gamma
por dispersión Compton inversa (*Inverse Compton* ó IC), mientras en los mode-
los hadrónicos los rayos gamma se producen a partir de procesos de decaimiento
de piones neutros producidos por la interacción de protones muy energéticos con
materia o radiación de la fuente, implicando, por otra parte, producción de piones
cargados y consecuentemente neutrinos de alta energía.

Astronomía de neutrinos: el objetivo de la astronomía de neutrinos es extender
el conocimiento de la astronomía tradicional usando como mensajeros cósmicos
neutrinos en el rango de energías del TeV en adelante. Las únicas fuentes de
neutrinos de origen extraterrestre conocidas actualmente son el sol y la Super
Nova SN1987A. Sin embargo, a finales de 2013, la colaboración IceCube ha pub-
licado la primera evidencia firme de neutrinos procedentes de fuera del sistema
solar. Un total de 28 eventos con una energía superior a 30 TeV y con una signif-
icancia $>4\sigma$, son inconsistentes con lo esperado para fondos de muones y neutri-
nos atmosféricos. A su vez, estas propiedades son consistentes con predicciones
genéricas para una componente adicional de origen extraterrestre. Se habla de
fuentes candidatas galácticas (SNRs, Micro-quásares, Galaxias Starburst o Cen-
tro galáctico) capaces de acelerar protones hasta el rango de los PeV o extra

galácticas (AGNs, GRBs) asociadas al origen de las partículas más energéticas jamás detectadas. Además de astronomía, los telescopios de neutrinos pueden realizar estudios sobre materia oscura y búsqueda de partículas exóticas como monopolos, nuclearidades y defectos topológicos, etc.

Los detectores de neutrinos son considerados como telescopios cuando la dirección del neutrino puede ser reconstruida con una resolución angular de unas decimas de grado. Básicamente, consisten en redes 3-D de sensores de luz siguiendo un patrón geométrico, buscando la detección de luz Cherenkov inducida por partículas cargadas resultado de la interacción del neutrino con el entorno a su paso por el detector. Las técnicas más investigadas actualmente en detección de neutrinos cósmicos incluyen: detección de luz Cherenkov a través de entornos basados en agua-hielo-roca, detección a través de cascadas aéreas, detección radio y detección acústica. Los telescopios Cherenkov son la mejor opción para estudiar eventos de neutrinos con energías superiores al GeV (*Gigaelectron volt*), como lo es el telescopio de neutrinos ANTARES objeto de esta tesis. Las prestaciones de un telescopio de neutrinos pueden ser analizadas en términos de resolución angular y el área efectiva del detector. El impacto de las propiedades ópticas del medio de detección en dichas magnitudes es el objetivo final de esta tesis.

7.2 El telescopio de neutrinos ANTARES

Arquitectura del detector: ANTARES es actualmente el telescopio de neutrinos submarino más grande del hemisferio norte. Está ubicado a una distancia de 40 km de la costa francesa de Toulon y 2.5 km de profundidad en el Mar Mediterráneo. ANTARES está conectado a una estación de control en la costa a través de un cable principal electro-óptico (*Main Electro-Optical Cable* ó MEOC) de 40 kms de longitud. Básicamente, el detector consiste en una red tridimensional de 885 fotomultiplicadores (*Photo-Multiplier Tubes* ó PMTs) distribuidos a lo largo de 12 líneas de detección. Cada línea de detección en ANTARES se compone de 25 pisos donde están ubicados los PMTs en tripletes. Cada línea está anclada al lecho marino a través de un peso muerto colocado en el anclaje inferior de la línea (*Bottom String Socket* ó BSS). En la parte inferior de cada línea se encuentra también el módulo de control de la línea (*String Control Module* ó SCM) donde se recoge todo el flujo de información de la línea y se envía a la estación de control

de la costa a través del MEOC, comunicados por la caja de unión (*Junction Box* ó JB) donde convergen todas las líneas del detector. Cada PMT (10", 14 dínodos) está dentro de una estructura llamada módulo óptico (*Optical Module* ó OM), que consiste en una esfera de vidrio altamente resistente a la presión. La separación entre pisos es de aproximadamente 15 m y la distancia entre líneas de unos 60 m. Cada piso cuenta además con un contenedor de titanio donde se encuentra la electrónica asociada y se conoce como módulo de control local (*Local Control Module* ó LCM). Algunos pisos contienen además dispositivos para la calibración temporal (balizas ópticas) y espacial (hidrófonos). Cada 5 pisos (o sector) se encuentra el módulo de control local maestro (*Master Local Control Module* ó MLCM) el cual está equipado con dispositivos extra para la multiplexación (combinación de dos o más canales de información en un solo medio de transmisión) de la señal, comunicación y conversión electro-óptica a través de complejas tarjetas eléctronicas. El módulo de energía de la línea (*String Power Module* ó SPM) está ubicado en la parte inferior de cada línea y proporciona a cada sector hasta 400 Voltios. El MLCM y los LCM de ese sector se alimentan en paralelo, donde la caja de alimentación local (*Local Power Box* ó LPB) en el LCM distribuye voltajes de baja energía hacia las tarjetas electrónicas.

Señales de fondo en el detector: dos tipos de fondo están presentes en un detector submarino como ANTARES: uno proveniente de la actividad óptica del entorno (fondo óptico) y otro resultado de procesos físicos en la atmósfera que dan lugar a muones y neutrinos atmosféricos (fondo físico). El fondo óptico procede de dos tipos de fuente: la emisión de bioluminiscencia por parte de micro y macro organismos, y los dos modos de decaimiento radiactivo del ^{40}K. La emisión por bioluminiscencia tiene dos componentes: una continua (aunque variable entorno a 60 kHz) y otra componente aleatoria de emisión espontánea (hasta 1 MHz) no constante en el tiempo. Los modos de decaimiento del ^{40}K dan lugar a la emisión de partículas β y γ a través de procesos de desintegración-β (liberando un electrón de cerca de 1.3 MeV) y captura-electrónica (liberando fotones de cerca de 1.46 MeV). El umbral Cherenkov en el sitio de ANTARES está estimado en 0.25 MeV. El ^{40}K contribuye a la parte continua (línea base) de la componente del fondo óptico.

Por otro lado, dos clases de fondo físico están presentes: un "fondo reducible" que

proviene de los muones atmosféricos y un "fondo irreducible" procedente de los neutrinos atmosféricos. Los muones atmosféricos se producen en la interacción de los rayos cósmicos de alta energía con la atmósfera terrestre, llegando a producir una traza a su paso por el detector. Un muon generado por un neutrino atmosférico no puede ser distinguido de un muon creado por un neutrino cósmico (señal). El fondo de muones atmosféricos se puede reducir al ubicar los OMs del detector orientados a $45°$ hacia abajo y con un algoritmo de reconstrucción de la dirección de la traza que discrimine los muones hacia abajo de manera que solo los muones hacia arriba son seleccionados. Por otro lado, debido a que el flujo difuso de neutrinos atmosféricos tiene un espectro energético más suave que el esperado para neutrinos cósmicos, la distribución energética de los eventos constituye una herramienta para separar la señal del fondo. En el caso de fuentes puntuales de neutrinos cósmicos, la única forma de separarlos del fondo es através de la búsqueda de agrupaciones (*clusters*) de eventos en una determinada y reducida dirección en el cielo.

El sistema de adquisición de datos: la digitalización de las señales analógicas registradas en los PMTs/OMs se lleva a cabo mediante un chip electrónico llamado ARS. Las señales de cada PMT (tiempo y carga) son digitalizadas *in-situ* por dos ARS funcionando en una configuración "*token ring*", con el objetivo de disminuir el tiempo muerto de la electrónica. El ARS tiene dos modos de operación: modo foto-electrón (*Single Photo-Electron* ó SPE) o modo muestreo (*Wave-Form* ó WF). La información temporal se realiza mediante un convertidor Tiempo-Voltaje (*Time-to-Voltage Converter* ó TVC), mientras que la medida de la carga se lleva a cabo mediante un convertidor Amplitud-Voltaje (*Amplitude-to-Voltage Converter* ó AVC) en tres pasos: integración, memorización y borrado de la carga. El esquema de transferencia de datos se conoce como "*all-data-to-shore*", donde todas las señales que excedan un umbral de 0.3 foto-electrones (p.e.) son digitalizadas, enviadas a la estación de control en la costa y procesadas en tiempo real por una granja de ordenadores.

Sistemas de calibración: en términos generales, los sistemas de calibración en ANTARES pueden resumirse en: sistema de calibración de la carga, sistema temporal y sistema de posicionamiento.

Sistema de calibración de la carga (amplitud): la precisión en la calibración de la carga resulta determinante en la estimación de la energía del neutrino. La calibración de la carga se basa en la medida del correspondiente pico del p.e. y el valor del pedestal del canal del AVC.

El sistema de calibración temporal: la calibración temporal hace referencia tanto a una calibración absoluta como a una calibración relativa. La calibración absoluta está vinculada al tiempo requerido para correlacionar eventos en el detector con eventos astrofísicos. La precisión necesaria es de 1 ms lo cual está dentro de las especificaciones o requisitos de ANTARES. La calibración relativa se lleva a cabo para medir los desfases temporales entre OMs. La precisión al nivel del nanosegundo (~ 0.5 ns) permite al detector alcanzar una resolución angular por debajo de los $0.5°$ para energías mayores a 10 TeV. La calibración temporal en el detector se realiza primero antes de la inmersión de las líneas en el mar en un cuarto oscuro a través de un laser pulsado y un sistema de reloj. Posteriormente, una vez las líneas han sido desplegadas en el sitio de operación del detector, las constantes relevantes medidas anteriormente son re-calculadas con el sistema de balizas ópticas (*Optical Beacons* ó OBs) el cual consiste en un conjunto de fuentes de luz pulsadas ubicadas estratégicamente a lo largo del detector. El sistema de OBs puede utilizarse también como una herramienta para estudiar las propiedades ópticas del agua. De este modo, la luz emitida por los OBs es detectada por los OMs vecinos donde el efecto de atenuación de la luz se hace presente.

Sistema de calibración de la posición: la calibración de la posición se realiza con un transceptor/receptor en la parte inferior de las líneas y 5 hidrófonos por línea que reciben la señal a determinadas alturas, junto con un conjunto de transpondedores autónomos anclados en posiciones conocidas en el lecho marino. También se cuenta con velocímetros de sonido (*Sound Velocimeters* ó SV) (uno por piso) que determina localmente la velocidad del sonido, y un sistema de brújulas e inclinómetros. Las medidas se hacen por triangulación del tiempo de llegada de las señales acústicas intercambiadas entre los hidrófonos receptores y los transpondedores emisores. El sistema cuenta con una precisión mejor de 10 cm, suficiente para los objetivos físicos del detector.

7.3 La descripción del medio de detección

Propagación de la luz e interacción con la materia: la luz Cherenkov inducida por las partículas cargadas que atraviesan el medio de detección de un telescopio de neutrinos tiene una región óptica de interés entre 320 y 620 nm. Por debajo de 320 nm la luz es absorbida por el vidrio y el gel de acoplamiento del PMT al OM. Por encima de los 620 nm la eficiencia cuántica del PMT no es lo suficientemente alta. La propagación de la luz en el agua está principalmente descrita por la convolución de dos efectos: absorción (desaparición de los fotones) y dispersión (cambio de dirección de los fotones), la suma de ambos efectos se conoce como transmisión. Dichos efectos suelen ser cuantificados en términos de coeficientes, cuyos inversos se conocen como longitudes. De esta forma, la longitud de absorción representa la distancia promedio recorrida por los fotones antes de ser absorbidos, la longitud de dispersión es la distancia promedio entre dos eventos consecutivos de dispersión de fotones. Por lo tanto, el número total de fotones Cherenkov detectados va a depender de cuantos fotones son absorbidos y del tiempo de llegada desde el punto de emisión en la traza hasta los OMs. La ley de Beer-Lambert describe el cambio en la intensidad de la luz con la distancia debido a efectos de atenuación/transmisión de la luz, por tanto involucrando efectos de absorción y dispersión. Las propiedades ópticas del medio se clasifican en propiedades ópticas inherentes (*Inherent Optical Properties* ó IOP) cuando dependen solamente del medio y propiedades ópticas aparentes (*Aparent Optical Properties* ó AOP) cuando dependen tanto del medio como de la estructura geométrica del campo de luz del entorno. Las longitudes de transmisión, absorción y dispersión son las IOP estudiadas en esta tesis.

Absorción, dispersión y velocidad de grupo de la luz en aguas naturales: varios factores son responsables de la absorción de la luz en el agua de mar: moléculas de agua, materia orgánica disuelta y diferentes clases de moléculas de clorofila. El coeficiente de absorción en aguas naturales es función de la longitud de onda de la luz y se puede expresar como la suma de cada coeficiente de absorción debido a los factores comentados anteriormente. La absorción de la luz por el agua pura está asociada a las transiciones electrónicas dentro de las moléculas de agua. La verdadera absorción de un fotón se traduce en un esquema de energía no radiativa, en el que la energía del fotón se convierte en energía térmica. Dos de

los espectros de absorción más referenciados son las medidas de Smith & Baker para las aguas naturales más claras, y las medidas de Pope & Fry para el agua pura.

En el caso de los fenómenos de dispersión en el agua de mar, el efecto puede describirse globalmente en términos de dos contribuciones. La primera de ellas se debe a las fluctuaciones de densidad de las moléculas de agua y se conoce como "dispersión Rayleigh" o de "Einstein-Smoluchowski", típica de partículas cuyo radio es más pequeño que la longitud de onda ($\sim \lambda/20$). La segunda contribución se debe a la concentración de partículas suspendidas en el agua, cuyos tamaños son más grandes que la longitud de onda de la luz ($> \lambda/20$) y se conoce como "dispersión Mie". La proporción de la dispersión Rayleigh respecto a la dispersión total (Rayleigh+Mie) se expresa como η. La dependencia de la longitud de dispersión con la longitud de onda se puede describir aceptablemente mediante el formalismo de Kopelevich (30% de incertidumbre).

Por otro lado, un modelo que describe razonablemente bien el índice de refracción de la luz en función de la longitud de onda y diferentes funciones termodinámicas como la presión, la temperatura y la salinidad, es el modelo de Quan & Fry.

Propiedades ópticas en experimentos de astronomía de neutrinos. La fase de investigación y desarrollo de ANTARES: para la detección de fuentes de neutrinos cósmicos y llevar a cabo los programas de física trazados por un telescopio de neutrinos, es necesario conocer el impacto de las propiedades ópticas del medio en las prestaciones del detector. Como prestaciones del detector se entenderá de aquí en adelante, el estudio de la resolución angular y área efectiva del detector. Las propiedades ópticas en lagos, océanos y hielo no son equivalentes. La longitud de dispersión efectiva, función del coseno promedio de la distribución global de dispersión, es grande para el caso de los océanos en aguas profundas, pero la longitud de absorción es un orden de magnitud más pequeña con respecto a la estimada para el hielo profundo.

En el caso de ANTARES, el llamado test 3' fue una campaña marina totalmente enfocada en el estudio de las propiedades ópticas del sitio a través de fuentes de luz pulsadas. Las medidas obtenidas para la longitud de transmisión, absorción y dispersión mostraron grandes variaciones asociadas a errores sistemáticos, por lo que se planteó la necesidad de realizar un seguimiento online de tales magnitudes

con la propia instrumentación del detector, en lo cual consiste gran parte el trabajo desarrollado en esta tesis.

7.4   Estimación de propiedades ópticas con la técnica de los OB

La medida de los parámetros de propagación de la luz en el entorno del detector, significa tener un control muy estricto de las condiciones del ambiente y del detector. En este sentido, los principales sistemáticos descubiertos y tratados en el análisis incluyen:

- el efecto "sombra" (*shadowing*), responsable de la reducción de fotones directos debido a componentes del detector localizados entre el OB y el OM de la misma línea,

- efectos de la electrónica como el modo "*token ring*" del chip ARS que distorciona la distribución temporal de los fotones cuando más de un fotón llega dentro de la ventana temporal del ARS,

- las características de emisión de la fuente y su ubicación relativa respecto a los OMs,

- las eficiencias de los OMs.

Estos efectos instrumentales estan influenciados unos a otros, por lo tanto, las medidas a realizar resultan extremadamente sensibles a dichos efectos. De hecho, algunas de las discrepancias en la literatura muestran que este tipo de medidas están lejos de ser triviales cualquiera que sea el método empleado.

El trabajo llevado a cabo en esta tesis fue concebido con el propósito de determinar algunas IOP del sitio de ANTARES usando la propia instrumentación del detector y evaluar su impacto en las prestaciones del mismo. Dos técnicas han sido desarrolladas para alcanzar estos propósitos: la técnica de los OBs (técnica principal) cuyos resultados se presentan a continuación, y la técnica de las trazas reconstruidas (estudios complementarios) cuyos resultados se presentan en la siguiente sección.

Estimación de la longitud de transmisión de la luz: la longitud de transmisión de la luz ha sido medida para tres diferentes longitudes de onda (406, 470 y 531 nm) usando diferentes OBs ubicados en diferentes líneas del detector. El método está basado en el ajuste a la ley de Beer-Lambert de la disminución de los hits de señal con la distancia. Para evitar el efecto "sombra" se utilizaron los datos de los OBs situados en las líneas adyacentes a la línea donde se ubicaba el OB emisor. Los datos de OBs utilizados fueron en la configuración "*single top-LED*" y "*all top-LEDs*". Los valores de la longitud de transmisión obtenidos conducen a:

$$\lambda_{tr}(406 \text{ nm}) = 31.2 \pm 2.8 \text{ m}$$

$$\lambda_{tr}(470 \text{ nm}) = 39.9 \pm 2.9 \text{ m}$$

$$\lambda_{tr}(531 \text{ nm}) = 20.5 \pm 2.1 \text{ m}$$

La RMS en cada caso resulta ser compatible con el valor medio extraído de la distribución de errores de los ajustes, el error relativo de la medida es $\leq 10\%$. El error relativo de la intensidad de señal en cada piso es $\leq 20\%$, principalmente asociado a la pérdida de simetría al registrar la luz en líneas vecinas. Las incertidumbres en las medidas a 406 nm y 470 nm pueden estar algo sobreestimadas, como lo indica el análisis de las distribuciones de $P(\chi^2)$ y pulls. No obstante, se concluye la correcta descripción de los datos por la ley de Beer-Lambert. A 531 nm el resultado de ambos test se corresponde con las expectativas. La estabilidad en el tiempo y la concordancia con otras medidas en el Mar Mediterráneo fueron alcanzadas.

Estimación de la longitud de absorción y dispersión de la luz: las longitudes de absorción y dispersión de la luz han sido estimadas únicamente a 470 nm, pero se espera ser extendida a otras longitudes de onda después de la conclusión de esta tesis. El método está basado en la comparación de distribuciones de tiempo de llegada de fotones para datos y muestras Monte Carlo generadas con diferentes IOP (modelos de agua) para la configuración "*all top-LEDs*" del OB. La simulación Monte Carlo ha sido desarrollada a partir del paquete general de simulación de trazas en ANTARES, pero con una sola longitud de onda representando eventos de OB. La cuantificación del acuerdo entre datos y Monte Carlo se realiza a través de

la aplicación de un test de χ^2 de Pearson modificado para histogramas pesados, aplicado para cada OM pero extendido a toda la línea para poder apreciar los efectos de las propiedades ópticas del agua. Para esto, una simulación "run-a-run" fue obligatoria, reproduciendo las mismas condiciones de adquisición que para los datos. En esos runes de OBs, pulsos de luz son emitidos desde un conjunto de LEDs o un LED sencillo de un determinado OB, siendo los pulsos de luz grabados por todos los OMs a lo largo del detector. El evento de OB es identificado a través de un algoritmo que busca la referencia de las señales que provienen del OB emisor. Antes de aplicar el test a los datos, se realiza una prueba con muestras Monte Carlo, para lo cual se elije un modelo de prueba que hace el papel de "datos reales", generándose copias aleatorias de sus distribuciones temporales, comprobándose de este modo la validez del método. Tanto para la prueba realizada en muestras Monte Carlo, como para su aplicación en datos, es necesario seleccionar un rango fijo en las distribuciones temporales donde aparentemente el pico y la cola de la señal están bien definidos para cada piso de la línea. Esta comparación se realiza con todas las distribuciones de los OMs de una misma línea. Seguidamente, aquellas "buenas" distribuciones para cada piso son agrupadas para cada línea (exceptuando aquella donde está el OB emisor) formando con ellas un "súper-histograma" sobre el que se aplica posteriormente el test de χ^2. Los mejores valores para los parámetros de absorción y dispersión corresponden a los valores utilizados en las muestras Monte Carlo con el valor más pequeño de χ^2. A partir de las distribuciones de estos valores, para los runes de datos considerados, se obtienen los resultados que se presentan a continuación:

$$\lambda_{abs}(470 \text{ nm}) = 52.1 \pm 5.5 \text{ m}$$

$$\lambda_{sca}(470 \text{ nm}) = 58.7 \pm 8.2 \text{ m}$$

$$\lambda_{sca}^{eff}(470 \text{ nm}) = 166.2 \pm 23.1 \text{ m}$$

Como puede observarse, los errores relativos en la medida son $\leq 14\%$. En este caso, el tratamiento de la contribución de la dispersión Rayleigh se realiza asumiendo dicho parámetro como un parámetro libre (no dependiente de la longitud de onda), resultando un valor de $\eta = 0.3$ para el presente análisis. Sin embargo, estudios que se están llevando a cabo actualmente en ANTARES podrian llevar a reconsiderar este comportamiento para η.

7.5 Estudios complementarios de propiedades ópticas con trazas reconstruidas

Los resultados obtenidos en la medida de parámetros de absorción y dispersión de la luz mediante la técnica de los OBs, se complementan mediante un estudio independiente basado en la reconstrucción de trazas en el detector. En este caso, se generan un gran número de muestras Monte Carlo con diferentes espectros de absorción y dispersión y se comparan las distribuciones de magnitudes físicas asociadas a la traza como el parámetro de calidad, Λ, el error angular, β y el ángulo cenital, $\cos\theta$, así como los residuos temporales, t_{res}, del ajuste de trazas de muones, tanto para datos como para Monte Carlo. El objetivo consiste en cuantificar el impacto en la reconstrucción de trazas debido a las propiedades ópticas del agua, estimar el modelo de agua que más se ajusta a los datos, y estudiar el impacto en las prestaciones del detector.

Influencia de parámetros de absorción y dispersión en la traza reconstruida:
de las principales observaciones extraídas del análisis, se puede concluir el pobre nivel de acuerdo para longitudes de dispersión efectiva, dispersión y la fracción de dispersión Rayleigh menores a 100 m, 35 m y 0.11 respectivamente. Para trazas bien reconstruidas ($\Lambda > $ -5.4 y $\beta < 1°$), a pesar de que la normalización global de las distribuciones cambia con el valor de las propiedades ópticas, la forma de las distribuciones de la proporción entre datos y Monte Carlo como una función del error angular estimado y el ángulo cenital no varian drásticamente. Esto indica que la incertidumbre en las propiedades ópticas del agua no influyen en la determinación angular de las trazas.

El impacto de las propiedades ópticas en la reconstrucción de trazas en el detector es cuantificado por medio de las variaciones relativas en el número de trazas. En este método, se comparan distribuciones de muones atmosféricos y neutrinos atmosféricos independientemente, que coincidan sus parámetros de dispersión pero no su longitud de absorción, y viceversa, 4 casos en total resultan para su evaluación en la distribución del parámetro de calidad de la traza Λ. Para cada caso se evalúa la variación en el número de trazas reconstruidas (dN/N) debida a cada incertidumbre ($d\lambda/\lambda$) en absorción (15%) y dispersión (23%). De esta manera, un factor de proporcionalidad K tal que dN/N $= K$dλ/λ se usa para cuantificar

el impacto, el cual se calcula fácilmente usando las estimaciones anteriores, lo que lleva a deducir unas incertidumbres debido a las propiedades ópticas de:

- Neutrinos atmosféricos: $\lambda_{abs} \Rightarrow 18\%$, $\lambda_{sca} \Rightarrow 6\%$,

- Muones atmosféricos: $\lambda_{abs} \Rightarrow 32\%$, $\lambda_{sca} \Rightarrow 27\%$.

Como puede observarse, los neutrinos atmosféricos se ven menos afectados por las propiedades ópticas que los muones atmosféricos. Por otra parte, la longitud de absorción tiene un efecto más considerable en ambos casos que la longitud de dispersión. Estos resultados son consistentes con breves estudios realizados previamente en ANTARES.

Para determinar el modelo Monte Carlo o modelo de agua que más se ajusta a los datos reconstruídos, se realiza una comparación entre distribuciones de residuos temporales de muones para datos y un conjunto de modelos de agua estratégicamente generados. A partir de las distribuciones obtenidas de la proporción o razón entre datos y Monte Carlo, se extraen los valores medios y la raíz cuadrática media para todos los casos, el valor medio más cercano a 1 y con la raíz cuadrática media más pequeña es finalmente seleccionado. Este procedimiento lleva a concluir educadamente que el modelo de agua que mejor se ajusta a los datos ha sido generado a partir de una $\lambda_{abs} = 55$ m, $\lambda_{sca} = 52$ m and $\lambda_{sca}^{eff} = 200$ m. Dichos resultados son compatibles dentro de las incertidumbres obtenidas desde los resultados de la técnica de los OBs. No obstante, longitudes de absorción mayores no pueden ser descartadas si la proporción de dispersión Rayleigh llega a tener valores muy pequeños. Estas soluciones "degeneradas", con combinaciones extremas de parámetros, pueden describir también los datos y esta degeneración es de cierto modo intrínseca al método donde solo cierta cantidad de información está disponible.

Influencia de parámetros de absorción y dispersión en las prestaciones del detector: las prestaciones del detector en términos de resolución angular y área efectiva solo pueden estudiarse mediante simulaciones Monte Carlo. Las estimaciones de dichas magnitudes para diferentes casos de modelos de agua y para aquellos modelos sugeridos por los resultados de las técnicas de los OBs y trazas reconstruidas, se han estudiado cuidadosamente.

Para una incertidumbre del 15% en la longitud de absorción y un 23% en la longitud de dispersión, la resolución angular del detector se ve afectada en menos de $0.1°$ a lo largo de un intervalo de 10^2-10^7GeV para la energía del neutrino siendo más impactante la longitud de absorción. La resolución angular para los modelos de agua extraídos de la técnica de OBs y trazas reconstruidas, se encuentra ligeramente mejor que las estimaciones oficiales en ANTARES, entre 0.1-0.05°, mostrando similares resultados entre ellas.

Respecto al área efectiva del detector, para una variación del 15% en la longitud de absorción se obtiene un cambio entre el 16-5% desde bajas a altas energías (10^2-10^7GeV). Sin embargo, para una variación del 23% en la longitud de dispersión se obtiene un cambio entre el 5-7%. La estimación de área efectiva para los modelos de agua obtenidos con las técnicas de los OB y trazas reconstruidas, son cercanamente equivalentes a las estimaciones para el modelo oficial de las simulaciones en ANTARES, siendo compatibles entre ellos.

References

[1] V. F. Hess. Über beobachtungen der durchdringenden strahlung bei sieben freiballonfahrten. *Physikalische Zeitschrift 13: 1084–1091*, 1912.

Referenced on page: 2

[2] http://www.auger.org/.

Referenced on page: 3, 7

[3] C.C.H. Jui. Cosmic ray in the northern hemisphere: Results from the telescope array experiment. *Journal of Physics: Conference Series 404 (2012) 012037*, 2012.

Referenced on page: 3, 7

[4] Francis Halzen. The search for the sources of the cosmic rays one century after their discovery. *XVI International Symposium on Very High Energy Cosmic Ray Interactions, ISVHECRI 2010, Batavia, IL, USA*, 2010.

Referenced on page: 3, 21

[5] J. Hörandel. Models of the knee in the energy spectrum of cosmic rays. *Astropart. Phys., vol. 21, p. 241*, 2004.

Referenced on page: 4

[6] M. Ackermann et al. Detection of the characteristic pion-decay signature in supernova remnants. *Science 15 February 2013. Vol. 339 no. 6121 pp. 807-811*, 2013.

Referenced on page: 4

[7] K.Greisen; G. T. Zatsepin, V.A.Kuzmin; R. J.Gould, and G. P. Schreder. *Phys. Rev. Lett. 16 (1966) 748; JETP Lett. 4 (1966) 78; Phys. Rev. Lett. 16 (1966) 252*.

Referenced on page: 4, 5

[8] E. Fermi. On the origin of the cosmic radiation. *Physical Review 75*, 1949.

Referenced on page: 5

[9] Federico Fraschetti. On the acceleration of ultra-high-energy cosmic rays. *Phil. Trans. R. Soc. A 366*, 2008.

Referenced on page: 5, 5

[10] J. Abraham et al. Properties and performance of the prototype instrument for the pierre auger observatory. *Nucl. Instrum. Meth. A523*, 2004.

Referenced on page: 7

[11] I. Allekotte et al. The surface detector system of the pierre auger observatory. *Nucl. Instrum. Meth. A586*, 2008.

Referenced on page: 7

[12] Hans P Dembinski. Latest results from the pierre auger observatory. *Nuclear Physics in Astrophysics V, Journal of Physics: Conference Series 337, 012068*, 2012.

Referenced on page: 8

[13] D. Ikeda. Results from the telescope array experiment. *Astrophys. Space Sci. Trans., 7, 257–263*, 2011.

Referenced on page: 8, 8

[14] M. Véron-Cetty and P. Véron. A catalogue of quasars and active nuclei: 12th edition. *Astron. Astrophys. 455*, 2006.

Referenced on page: 9, 9

[15] The Pierre Auger Collaboration. Update on the correlation of the highest energy cosmic rays with nearby extragalactic matter. *Astroparticle Physics 34 (2010) 314–326*, 2010.

Referenced on page: 9

[16] F. Aharonian et al. High energy astrophysics with ground-based gamma ray detectors. *Rep. Prog. Phys., 71:096901*, 2008.

Referenced on page: 10

[17] F. Halzen and D. Hooper. High-energy neutrino astronomy: the cosmic ray connection. *Rep. Prog. Phys., 65:1025–1078*, 2002.

Referenced on page: 10

[18] http://www.mpi hd.mpg.de.

Referenced on page: 10

[19] http://magic.mppmu.mpg.de/.

Referenced on page: 11

[20] Borla-Tridon D. et al. for the MAGIC Coll. Measurement of the cosmic electron spectrum with the magic telescopes. *proc. 32nd ICRC, Beijing*, 2011.

Referenced on page: 11

[21] http://veritas.sao.arizona.edu/.

Referenced on page: 11

[22] J. HOLDER FOR THE VERITAS COLLABORATION. Veritas: Status and highlights. *proc. 32nd ICRC, Beijing*, 2011.

Referenced on page: 12

[23] http://www.cta observatory.org/.

Referenced on page: 12

[24] The FERMI-LAT collaboration. Fermi large area telescope second source catalog. *The Astrophysical Journal Supplement, Volume 199, Issue 2, article id. 31*, 2012.

Referenced on page: 13

[25] http://www-sk.icrr.u-tokyo.ac.jp/sk/index e.html.

Referenced on page: 14

[26] http://www-personal.umich.edu/ jcv/imb/imb.html.

Referenced on page: 14

[27] http://www.nu.to.infn.it/exp/all/baksan/.

Referenced on page: 14

[28] https://icecube.wisc.edu/.

Referenced on page: 14

[29] The IceCube collaboration. Evidence for high-energy extraterrestrial neu-
     trinos at the icecube detector. *Science, Vol. 342 no. 6161 (22 November
     2013)*, 2013.
     Referenced on page: 14, 37

[30] http://www donut.fnal.gov/.
     Referenced on page: 16

[31] K. Nakamura and S.T. Petcov. Neutrino mixing section in the lepton particle
     listings: neutrino mass, mixing and oscillations. *RPP*, 2012.
     Referenced on page: 16, 17, 17

[32] http://dayabay.ihep.ac.cn/twiki/bin/view/Public/.
     Referenced on page: 17

[33] J. Learned and K. Mannheim. High-energy neutrino astrophysics. *Ann. Rev.
     Nucl. Part. Sci., vol. 50*, 2000.
     Referenced on page: 18, 29

[34] K. Bays et al. (Super-Kamiokande Collaboration). Supernova relic neutrino
     search at super-kamiokande. *Phys. Rev. D 85, 052007 (2012)*, 2012.
     Referenced on page: 19

[35] S. Adrián-Martínez et al. Search for cosmic neutrino point sources with
     four year data of the antares telescope. *The Astrophysical Journal Letters,
     arXiv:1207.3105*, 2012.
     Referenced on page: 19, 39, 40, 68, 173, 180

[36] The IceCube collaboration. An absence of neutrinos associated with cosmic-
     ray acceleration in γ-ray bursts. *Nature 484, 351–354 (19 April 2012)*, 2012.
     Referenced on page: 19, 23

[37] Ch. Spiering U.F. Katz. High-energy neutrino astrophysics: Status and
     perspectives. *arXiv:1111.0507v1 [astro-ph.HE]*, 2011.
     Referenced on page: 20, 23, 32, 33, 34, 36, 37, 38

[38] http://www.physics.ucla.edu/ moonemp/public/.
     Referenced on page: 20

[39] S.I. Syrovatsk V.L. Ginzburg. Origin of cosmic rays. *Moscow*, 1964.
Referenced on page: 23

[40] Francesco Lorenzo Villante Francesco Vissani. Cosmic rays and neutrinos from supernova remnants (or: the time when h.e.s.s. met ginzburg and syrovatskii). *Nuclear Instruments and Methods in Physics Research A 588 (2008) 123–129*, 2008.
Referenced on page: 23

[41] W. Bednarek. Neutrinos from the pulsar wind nebulae. *Astronomy & Astrophysics*, 2011.
Referenced on page: 24

[42] K. A. et al. Cosmic rays and particle physics. *The astrophysical journal 656*, 2007.
Referenced on page: 24, 26

[43] M Bartosik W. Bednarek. Gamma-rays and neutrinos from the pulsar wind nebulae. *Il Nuovo Cimento B, vol. 120, Issue 6, p.751*, 2005.
Referenced on page: 24

[44] Salvatore Galata. A time dependent search for neutrino emission from microquasars with the antares telescope. *Ph.D. thesis, Universite d Aix-Marseille*, 2012.
Referenced on page: 25

[45] A. Levinson and E. Waxman. Probing microquasars with tev neutrinos. *Physical Review Letters 87.17, 171101, p. 171101*, 2001.
Referenced on page: 25

[46] G. E. et al. Romero. Hadronic gamma-ray emission from windy microquasars. *AAP 410, pp. L1-L4*, 2003.
Referenced on page: 25

[47] Fulvio Melia Roland M. Crocker and Raymond R. Volkas. Neutrinos from the galactic center in the light of its gamma-ray detection at tev energy. *arXiv:astro-ph/0411471v4*, 2005.
Referenced on page: 25

[48] R. M. Crocker and F. Aharonian. The fermi bubbles: Giant, multibillion-year-old reservoirs of galactic center cosmic rays. *arXiv:1008.2658v3*, 2010.
Referenced on page: 26

[49] Dan Hooper and Joseph Silk. Searching for dark matter with neutrino telescopes. *arXiv:hep-ph/0311367v2*, 2004.
Referenced on page: 26

[50] D.I. Olive P. Goddard. Magnetic monopoles in gauge field theories. *Rep. Prog. Phys. 41 1357*, 1978.
Referenced on page: 26

[51] V. Popa. Nuclearite search with the antares neutrino telescope. *Proceedings of the 32ND INTERNATIONAL COSMIC RAY CONFERENCE, BEIJING*, 2011.
Referenced on page: 27

[52] R. Gandhi et al. Ultrahigh-energy neutrino interactions. *Astrop. Phys. 5 81*, 1996.
Referenced on page: 28, 28

[53] P. A. Cherenkov. Visible radiation produced by electrons moving in a medium with velocities exceeding that of light. *Phys. Rev., 52:378*, 1937.
Referenced on page: 28

[54] Jackson JD. Classical electrodynamics. *New York: Wiley. 638 pp. 3rd ed*, 1996.
Referenced on page: 29

[55] Particle Data Group. Phys. rev. d66. 2002.
Referenced on page: 29

[56] N.V. Mokhov D.E. Groom and S.I. Striganov. Muon stopping power and range tables 10mev–100tev. *Atom. Data Nucl. Data Tabl. 78-183*, 2001.
Referenced on page: 30

[57] T. Chiarusi and M. Spurio. High-energy astrophysics with neutrino telescopes. *arXiv:0906.2634*, 2009.
Referenced on page: 30

[58] Francis Halzen. Lectures on high-energy neutrino astronomy. *arXiv:astro-ph/0506248v1*, 2005.

Referenced on page: 30, 31

[59] Carlo Alessandro Nicolau. From nemo to km3net-italy. *RICAP-13 Roma International Conference on AstroParticle Physics*, 2013.

Referenced on page: 34

[60] KM3NeT. Conceptual design report (cdr). *www.km3net.org*.

Referenced on page: 35

[61] Juan-Jose Hernandez-Rey. The km3net neutrino telescope: Status and prospects. *RICAP-13 Roma International Conference on AstroParticle Physics*, 2013.

Referenced on page: 35, 36

[62] Naoko Kurahashi Neilson Nathan Whitehorn, Claudio Kopper. Results from icecube. *Talk on IceCube Particle Astrophysics Symposium, University of Wisconsin, Madison*, 2013.

Referenced on page: 37

[63] Zhan-Arys Dzhilkibaev. Prototyping phase of the baikal-gvd project. *RICAP-13 Roma International Conference on AstroParticle Physics*, 2013.

Referenced on page: 38

[64] Garabed Halladjian. Recherche de neutrinos cosmiques de haute-energie emis par des sources ponctuelles avec antares. *PhD thesis*, 2010.

Referenced on page: 38, 40, 55

[65] Jürgen Brunner. Updated tag list for the new antares event format. *ANTARES-SOFT-1999-003 internal note*, 1999.

Referenced on page: 40

[66] M. Ageron et al. Performance of the first antares detector line. *Astropart. Phys. 31 277-283*, 2009.

Referenced on page: 41

[67] M. Ageron et al. Antares : The first undersea neutrino telescope. *Nucl. Instrum. Meth. A 656 11-38*, 2011.

Referenced on page: 43, 44, 46, 46, 47, 48, 54

[68] P.Amram et al. The antares optical module. *Nucl. Instrum. Meth. A484 369-383*, 2002.

Referenced on page: 44, 46

[69] http://www.nautilus gmbh.de/.

Referenced on page: 46

[70] Mark A. Moline Steven H.D. Haddock and James F. Case. Bioluminescence in the sea. *Annu. Rev. Marine. Sci. 2010.2:443-493*, 2010.

Referenced on page: 49

[71] Dmitry Zaborov. The k-40 calibration method. *ANTARES internal notes, ANTARES-CALI/2011-001*, 2011.

Referenced on page: 49, 69, 120, 121

[72] J.A. Aguilar et al. Performance of the front-end electronics of the antares neutrino telescope. *Nucl. Instrum. Meth. A622 59-73*, 2010.

Referenced on page: 51, 52, 53, 62, 63

[73] J.A. Aguilar et al. Time calibration of the antares neutrino telescope. *Astropart. Phys. 34 539-549*, 2011.

Referenced on page: 55, 65, 65, 66

[74] H. Yepes-Ramirez. Water absorption length measurement with the antares optical beacon system. *Nucl. Instrum. Meth. A 626-627 S118*, 2011.

Referenced on page: 55, 104

[75] M. Ageron et al. The antares optical beacon system. *Nucl. Instrum. Meth. A 578 498-509*, 2007.

Referenced on page: 57, 60, 61, 62

[76] ANTARES technical notes. *ANTARES private communications*.

Referenced on page: 58, 59

[77] Umberto Emanuele. Time calibration of the km3net neutrino telescope. *Physics procedia, Volume 37, Pages 1179–1184*, 2012.

Referenced on page: 59

[78] H. Yepes-Ramirez. Characterization of the optical properties of the site of the antares neutrino telescope. *Nucl. Instrum. Meth. A 725, 203-206*, 2013.
Referenced on page: 60, 61, 104

[79] Ocean Optics. Hr4000cg spectrometer: Uv-nir. *http://www.oceanoptics.com/products/hr4000cg.asp*, —.
Referenced on page: 60, 127

[80] Nanolase. Ng-10120-120. *http://www.photonics.com/Company.aspx?CompanyID=10006*, —.
Referenced on page: 60

[81] S. Adrián-Martínez et al. The positioning system of the antares neutrino telescope. *arXiv:1202.3894v1 [astro-ph.IM]*, 2012.
Referenced on page: 71

[82] David J.L Bailey. Monte carlo tools and analysis methods for understanding the antares experiment and predicting its sensitivity to dark matter. *PhD thesis*, 2002.
Referenced on page: 74, 104, 111, 168

[83] Wolfgang H. Schuster. Measurement of the optical properties of the deep mediterranean - the antares detector medium. *PhD thesis*, 2002.
Referenced on page: 74, 87, 104, 105, 111

[84] C.D. Mobley. Light and water. radiative transfer in natural water. *Academic Press, New York*, 1994.
Referenced on page: 75, 78, 78, 79, 79, 79, 80, 81, 81, 81, 82, 82, 83, 86, 86, 86, 88, 89, 90, 90, 91, 92, 108, 168

[85] Miroslaw Jonasz and Georges R. Fournier. Light scattering by particles in water: theoretical and experimental foundations. *Elsevier academic press: ISBN-13: 978-0-12-388751-1, ISBN-10: 0-12-388751-8*, 2007.
Referenced on page: 77, 86, 87, 87, 92, 92, 93

[86] Vladimir I. Haltrin. Light scattering reviews, chapter 10: absorption and scattering of light in natural waters. *Springer praxis books, 2006 part III, 445-486, DOI: 10.1007/3-540-37672-0-10*, 2006.
Referenced on page: 79, 79, 80, 81, 85, 87, 88, 90, 168

[87] Shuba Sathyendranath Jasmine S. Bartlett, Kenneth J. Voss and Anthony Vodacek. Raman scattering by pure water and sea water. *Applied Optics, Vol. 37, No 15*, 1998.

Referenced on page: 79

[88] Deric Gray W. Scott Pegau and J. Ronald V. Zaneveld. Absorption and attenuation of visible and near-infrared light in water: dependence on temperature and salinity. *Applied Optics, Vol. 36, Issue 24, pp. 6035-6046*, 1997.

Referenced on page: 81

[89] Raymond C. Smith and Karen S. Baker. Optical properties of the clearest natural waters (200-800 nm). *APPLIED OPTICS, Vol. 20, No. 2*, 1981.

Referenced on page: 81, 81, 83, 190, 191

[90] Robin M. Pope and Edward S. Fry. Absorption spectrum (380–700 nm) of pure water. ii. integrating cavity measurements. *APPLIED OPTICS, Vol. 36, No. 33*, 1997.

Referenced on page: 83, 84, 190, 191

[91] A. Morel. Optical properties of pure water and pure sea water. *Optical aspects of Oceanography, N.G. Jerlov and E.S. Nielsen (eds.), Academic Press, New York, 1974, Chap 1, pp 1-24*, 1974.

Referenced on page: 86, 191

[92] Andre Morel and Hubert Loisel. Apparent optical properties of oceanic water: dependence on the molecular scattering contribution. *APPLIED OPTICS, Vol. 37, No. 21*, 1998.

Referenced on page: 89

[93] O. V. Kopelevich and O. A. Gushchin. Statistical and physical models of the light scattering properties of sea water. *Izvestiya USSR AS, Atmos. Ocean Physics, 14, 680–684*, 1978.

Referenced on page: 90

[94] L.A. Kuzmichev. On the velocity of light signals in the deep underwater neutrino experiments. *Nucl. Instr. Meth. A, 482, 304-306*, 2002.

Referenced on page: 92

[95] Xiaohong Quan and Edward S. Fry. Empirical equation for the index of refraction of seawater. *Vol. 34, No. 18, APPLIED OPTICS*, 1995.
Referenced on page: 92, 93, 93, 110

[96] R.C. Millard and G. Seaver. An index of refraction algorithm over temperature, pressure, salinity, density and wavelength. *Deep - Sea Res. 37 (12) : 1909*, 1990.
Referenced on page: 92

[97] David J.L Bailey. The effect of the group velocity and dispersion on photon arrival times in the antares detector. *ANTARES internal notes, ANTARES-PHYS/2001-005*, 2001.
Referenced on page: 93

[98] Jürguen Brunner. The refraction index at the antares site. *ANTARES internal notes, ANTARES-Site/2000-001*, 2000.
Referenced on page: 93

[99] H. Bradner and G. Blackinton. Long base line measurements of light transmission in clear water. *Appl. Opt. 23, 1009–1012*, 1984.
Referenced on page: 94, 94

[100] G. Riccobene et al. Simultaneous measurements of water optical properties by ac9 transmissometer and asp-15 inherent optical properties meter in lake baikal. *Nuclear Instruments and Methods in Physics Research A 498 (2003) 231–239*, 2003.
Referenced on page: 94, 95, 95, 96, 101

[101] P. Buford Price. Implications of optical properties of ocean, lake, and ice for ultrahigh-energy neutrino detection. *20 March 1997, Vol. 36, No. 9, APPLIED OPTICS*, 1997.
Referenced on page: 94, 94, 103

[102] Belolaptikov I.A. et al. In situ measurements of optical parameters in lake baikal with the help of a neutrino telescope. *Applied Optics 33, 6818*, 1999.
Referenced on page: 95

[103] Vasilij Balkanov et al. In situ measurements of optical parameters in lake baikal with the help of a neutrino telescope. *Applied Optics, Vol. 38, Issue 33, pp. 6818-6825 (1999)*, 1999.

Referenced on page: 96

[104] et al Ackermann, M. Optical properties of deep glacial ice at the south pole. *J. Geophys. Res., 111, D13203, doi:10.1029/2005JD006687*, 2006.

Referenced on page: 97, 97, 98, 98, 99

[105] P. Buford Price and Lars Bergstrom. Optical properties of deep ice at the south pole: scattering. *20 June 1997, Vol. 36, No. 18, APPLIED OPTICS*, 1997.

Referenced on page: 97

[106] IceCube collaboration. Measurement of south pole ice transparency with the icecube led calibration system. *Nucl. Instrum. Meth. A 711 73-89*, 2013.

Referenced on page: 98, 99

[107] Syunsuke Kasuga. Observation of a small ν_μ/ν_e ratio of atmospheric neutrino in super-kamiokande by the method of particle identification. *PhD thesis*, 1998.

Referenced on page: 101

[108] WETLabs. Wetlabs ac9 manual. *www.wetlabs.com*, —.

Referenced on page: 101

[109] G. Riccobene et al. Deep seawater inherent optical properties in the southern ionian sea. *Astropart. Phys. 27 1-9*, 2007.

Referenced on page: 101, 102

[110] E.G. Anassontzis et al. Water transparency measurements in the deep ionian sea. *Astroparticle Physics 34 187–197*, 2010.

Referenced on page: 102, 103

[111] N. Palanque-Delabrouille et al. Transmission of light in deep sea water at the site of the antares neutrino telescope. *Astroparticle Physics 23 131–155*, 2005.

Referenced on page: 104, 104, 105, 106, 106, 107, 108, 111, 168

[112] S. Adrián-Martínez et al. Measurement of the group velocity of light in sea water at the antares site. *Astropart. Phys. 35 552-557*, 2012.
Referenced on page: 104, 110, 115

[113] N. Palanque-Delabrouille. Light transmission in the antares site. blue or uv light. (analysis of test 3' data). *ANTARES internal notes, ANTARES-SITE-2000-002*, 2000.
Referenced on page: 106, 108, 113

[114] Juan Antonio Aguilar. Measurements of the attenuation length in antares with the optical beacon system. *ANTARES internal notes, ANTARES-SITE/2007-001*, 2007.
Referenced on page: 111

[115] W.H.W Schuster and David J.L Bailey. Optical properties at the antares site: what we know and we don't know from test 3'. *ANTARES internal notes, ANTARES-SITE/2002-001*, 2002.
Referenced on page: 111

[116] Juan Antonio Aguilar. Analysis of the optical beacon system and search for point like sources in the antares neutrino telescope. *PhD thesis*, 2008.
Referenced on page: 113

[117] O. Skjeggestad A.G. Frodesen. Probability and statistic in particle physics. *Columbia University Press*, 1979.
Referenced on page: 132, 141

[118] Christian Walk. Handbook on statistical distributions for experimentalists. *Universitet Stockholms, Internal Report, SUF-PFY/96-01*, 2007.
Referenced on page: 132

[119] Luc Demortier and Louis Lyons. Everything you always wanted to know about pulls. *The Rockefeller University and University of Oxford. CDF/ANAL/PUBLIC/5776.*, 2002.
Referenced on page: 141

[120] N.D. Gagunashvili. Pearson's chi-square test modifications for comparison of unweighted and weighted histograms and two weighted histograms. *PoS*

(ACAT) 054, 2007.

Referenced on page: 147

[121] David J.L. Bailey. Km3 v2r1: User guide. *ANTARES internal notes, ANTARES-Software/2002-006*, 2002.

Referenced on page: 148, 165, 167

[122] Sergio Navas and Lee Thompson. Km3 v2r1 user guide and reference manual. *ANTARES internal notes, ANTARES-Soft/1999-011*, 1999.

Referenced on page: 148, 165, 167

[123] M. de Jong. The triggerefficiency program. *ANTARES internal notes, ANTARES-SOFT-2009-001*, 2009.

Referenced on page: 148

[124] M. de Jong. The antares trigger software. *ANTARES internal notes, ANTARES-SOFT-2005-005*, 2005.

Referenced on page: 148

[125] C.W. James. Km3 release v4r4. *ANTARES internal notes, ANTARES-SOFT-2012-007*, 2012.

Referenced on page: 155

[126] T. Montaruli K. Kuzmin and I. A. Sokalski. Genhen v6r3: implementation of the glashow resonance and of music transport code. *ANTARES internal notes, ANTARES-SOFT-2004-012*, 2004.

Referenced on page: 165

[127] E. V. Korolkova and L. Thompson. Monte carlo simulation of cosmic ray muons at sea level with corsika. *ANTARES internal notes, ANTARES-SOFT-2003-002*, 2003.

Referenced on page: 165

[128] A. Margiotta M. Spurio G. Carminati, M. Bazzotti. Atmospheric muons from parametric formulas: a fast generator for neutrino telescopes (mupage). *Comput. Phys. Commun. 179, 915-923 (2008)*, 2008.

Referenced on page: 165

[129] Giada Carminati. Study of diffuse flux of high energy neutrinos through showers with the antares neutrino telescope. *PhD thesis*, 2010.

Referenced on page: 165

[130] M.Sioli M.Spurio Y.Becherini, A.Margiotta. A parameterisation of single and multiple muons in the deep water or ice. *Astrop.Phys.25 (2006) 1–13*, 2006.

Referenced on page: 165

[131] Sergio Navas. A comparison between geasim and km3 generators. *ANTARES internal notes, ANTARES-SOFT-1999-002*, 1999.

Referenced on page: 165

[132] A. Edin G. Ingelman and J. Rathsman. Lepto 6.5 - a monte carlo generator for deep inelastic scattering. *Comput. Phys. Commun., vol. 101, p. 108, 1997*, 1997.

Referenced on page: 165

[133] G. Barr. The separation of signals and background in a nucleon decay experiment. *Ph.D. Thesis, Keble College, University of Oxford*, 1987.

Referenced on page: 165

[134] T. Sjöstrand. High-energy physics event generation with pythia 5.7 and jet-set 7.4. *Compt. Phys. Commun., vol. 82, p. 74, 1994*, 1994.

Referenced on page: 165

[135] V. Agrawal et al. Atmospheric neutrino flux above 1 gev. *Phys. Rev. D53, 1314-1323 (1996)*, 1996.

Referenced on page: 165

[136] E.V. Bugaev et al. Prompt leptons in cosmic rays. *Nuovo Cimento 12, 41-73 (1988)*, 1988.

Referenced on page: 165

[137] C. Forti et al. Simulation of atmospheric cascades and deep-underground muons. *Phys. Rev. D42, 3668-3689*, 1990.

Referenced on page: 166

[138] Simone Biagi. Search for a diffuse flux of astrophysical muon neutrinos in the antares telescope. *PhD thesis*, 2010.
Referenced on page: 169

[139] Adriaan Jacob Heijboer. Track reconstruction and point source searches with antares. *Ph.D. thesis, Universiteit van Amsterdam*, 2004.
Referenced on page: 169

[140] Giulia Vannoni Fabian Schüssler, Kevin Payet. Data summary trees for reconstructed and simulated antares events. *ANTARES internal notes, ANTARES-SOFT-2010-003*, 2010.
Referenced on page: 172

[141] Giulia Vannoni Fabian Schüssler, Kevin Payet. Analysis utilities for antdst. *ANTARES internal notes, ANTARES-SOFT-2010-004*, 2010.
Referenced on page: 172

[142] Aart Heijboer Claudio Bogazzi, Joris Hartman. Point source search with 2007 and 2008 data. *ANTARES internal notes, ANTARES-PHYS-2010-008*, 2010.
Referenced on page: 173

[143] S. Adrián-Martínez et al. First search for point sources of high-energy cosmic neutrinos with the antares neutrino telescope. *The Astrophysical Journal Letters, 743:L14 (6pp)*, 2011.
Referenced on page: 173

[144] Juan-Pablo Gomez-Gonzalez. Search for point sources of high energy neutrinos with 2007-10 data. *ANTARES internal notes, ANTARES-PHYS-2011-006*, 2011.
Referenced on page: 173, 180

[145] C. Kopper Th. Eberl. The seatray software framework. *ANTARES internal notes, ANTARES-SOFT-2009-013*, 2009.
Referenced on page: 174

[146] C.W. James. Private communications. *ANTARES collaboration*, 2013.
Referenced on page: 186